

**INVESTIGATIONS IN CARDIAC SURGERY:
PHYSICAL ASPECTS OF LASER ANASTOMOSIS,
THERMAL BONDING AND ARTERIAL DILATION.**

by

John Wesley Fenner

Presented as a thesis for the degree of PhD in the University of Glasgow

**Department of Cardiac Surgery
and
Department of Clinical Physics and Bioengineering**

**Faculty of Medicine
July 1993**

ProQuest Number: 13833373

All rights reserved

INFORMATION TO ALL USERS

The quality of this reproduction is dependent upon the quality of the copy submitted.

In the unlikely event that the author did not send a complete manuscript and there are missing pages, these will be noted. Also, if material had to be removed, a note will indicate the deletion.



ProQuest 13833373

Published by ProQuest LLC (2019). Copyright of the Dissertation is held by the Author.

All rights reserved.

This work is protected against unauthorized copying under Title 17, United States Code
Microform Edition © ProQuest LLC.

ProQuest LLC.
789 East Eisenhower Parkway
P.O. Box 1346
Ann Arbor, MI 48106 – 1346

Thesis
9660
copy 1



ABSTRACT

The work of this thesis examines the application of lasers to cardiac surgery in two areas - laser assisted anastomosis and laser balloon angioplasty. Both techniques utilise laser interactions with tissue, particularly with the blood vessel wall. Modification of the collagen component is a recurring feature of such interactions, frequently determining the general response of the vessel as a whole. Hence an introduction to collagen structure and biochemistry is presented in Chapter 2.

Laser Anastomosis

Our own exploration of Argon laser anastomosis in vivo is discussed in Chapter 3. This establishes our experience in this area and highlights the shortcomings of the technique (namely inconsistent bonding). In vitro work was undertaken (Chapter 4) to investigate the nature of the bonding process. Tissue bonds were successfully created without the use of a laser, implicating dehydration as an important factor. These bonds were christened 'dry bonds' and a bonding theory based on dehydration was proposed to explain the phenomenon.

The results of investigation into the wide variation of the strength of dry bonds (Chapter 5) were in agreement with the dry bonding theory. The work of Chapter 6 undertook a comparison of laser and dry bonds in which the properties of the two bond types were found to be very similar, further implicating dehydration as the mechanism responsible for Argon laser anastomosis. This hypothesis is examined on a theoretical basis in Chapters 7 and 8, the former providing the groundwork of laser tissue interactions and the latter applying a numerical model to describe the bonding process. A theoretical description based on dehydration is shown to account for experimental observations and indicates that dehydration is the mediator of Argon laser anastomosis. The work as a whole is summarised in Chapter 9 to conclude that dehydration is the mechanism of Argon laser bonding.

Laser Balloon Angioplasty

Chapter 10 introduces the technique of balloon angioplasty applied to coronary artery disease with consideration of laser recanalisation and laser balloon angioplasty. The latter is an experimental technique designed to 'fix' a stenosed vessel in an expanded state by laser irradiation during balloon inflation. However the temperature dependent processes responsible for this action are not well defined since vessel temperature is difficult to obtain during radiative balloon

inflation. In response to this, Chapter 11 describes a technique to simulate the thermal effects of the laser balloon while simultaneously providing accurate vessel temperature. In addition, a technique permitting repeated angiography on an excised section of myocardium is described, enabling analysis of vessel diameter pre- and post angioplasty. Application of the technique to non-diseased coronary arteries in vitro is related in Chapter 12. The results of this work reveal acutely altered vessel diameters and indicate that the technique is both viable and useful. Chapter 13 draws the work to a conclusion and considers its future application.

CONTENTS

	Page No.
Title Page	i
Abstract	ii
Contents	iv
Tables & Illustrations	xii
Acknowledgements	xvi
Chapter 1: Lasers in Cardiac Surgery	
1.1 INTRODUCTION	1
1.1.1 Directionality	1
1.1.2 Monochromaticity	1
1.1.3 Intensity	2
1.1.4 Coherence	2
1.2 TYPES OF LASER	2
1.3 DANGERS OF LASER RADIATION	3
1.4 APPLICATIONS OF LASERS TO MEDICINE	4
1.5 APPLICATIONS OF LASERS TO CARDIAC SURGERY	4
1.5.1 The Heart, Vasculature and Problems	4
1.5.2 The Laser in Cardiac Surgery	5
1.5.3 Technique	6
1.5.4 Results	7
1.5.5 Mechanism	9
1.5.6 Complications	9
1.5.7 Advantages	9
Chapter 2: Collagen	
2.1 INTRODUCTION	13
2.2 VESSEL STRUCTURE	13
2.2.1 Arteries	16
2.2.2 Veins	16
2.3 COLLAGEN	16
2.3.1 Molecular Structure	17
2.3.2 Fibrous Structure	17

	Page No.
2.3.3 Extra-Fibrillar Matrix	21
2.3.4 Mechanical Properties	21
2.4 ELASTIN	23
2.5 HISTOLOGICAL TECHNIQUES	23
2.5.1 Picrosirius Red F3BA	24
Chapter 3: Laser Bonding In Vivo	
3.1 INTRODUCTION	27
3.1.1 Argon Laser	27
3.1.2 Coupling Optics	29
3.1.3 Fibreoptic Cable	29
3.1.4 Delivery Handpiece	29
3.1.5 Micromanipulator	31
3.1.6 Camera	31
3.2 EXPERIMENTAL PROCEDURE	31
3.2.1 Introduction	31
3.2.2 Method	34
3.2.3 Post Mortem	37
3.2.4 Variations in Technique	39
3.2.5 Pressure Testing	39
3.3 RESULTS	41
3.3.1 Group 1	41
3.3.2 Group 2	41
3.3.3 Group 3	41
3.4 DISCUSSION	44
3.5 CONCLUSION	46
Chapter 4: Dry Bonds In Vitro	
4.1 INTRODUCTION	48
4.2 EXPERIMENTAL DESIGN: Principal Concerns	49
4.2.1 Tissue Preparation	49
4.2.2 Tissue Bonding	50
4.2.3 Tissue Bond Strength	50
4.3 EQUIPMENT	50
4.3.1 Bonding	50

	Page No.
4.3.2 Temperature Uniformity of Approximator	52
4.4 TEMPERATURE GRADIENTS ACROSS THE THICKNESS OF THE APPROXIMATOR	52
4.4.1 Method	52
4.4.2 Results	52
4.4.3 Discussion	55
4.5 TEMPERATURE GRADIENTS ACROSS THE FACE OF THE APPROXIMATOR	55
4.5.1 Method	55
4.5.2 Results	55
4.5.3 Discussion	55
4.6 SHEAR STRENGTH OF TISSUE BONDS AS A FUNCTION OF BONDING TEMPERATURE	58
4.6.1 Method: Dry Bonds	58
4.6.2 Wet Bonds	64
4.7 RESULTS	64
4.8 DISCUSSION	71
4.8.1 Scatter	72
4.8.2 Equivalence	72
4.9 POSSIBLE BONDING MECHANISM	73
4.10 CONCLUSION	75
Chapter 5: Scatter of Dry Bonds	
5.1 INTRODUCTION	76
5.2 MODIFICATION OF APPROXIMATOR TO PERMIT APPLICATION OF INCREASED PRESSURE TO OVERLAPPED BONDING SLICES	76
5.2.1 Method	77
5.2.2 Results	77
5.2.3 Low Pressure	79
5.2.4 Medium Pressure	81
5.2.5 High Pressure	81
5.2.6 Discussion	81
5.3 SHEAR STRENGTH OF TISSUE BONDS AS A FUNCTION OF TISSUE APPPOSITION	83
5.3.1 Method	83
5.4 RESULTS	88

	Page No.
5.4.1 Comparison of Mean Bond Strength	88
5.4.2 Comparison of Scatter	88
5.5 DISCUSSION	91
5.6 CONCLUSION	92
Chapter 6: Laser/Dry Bond Equivalence	
6.1 INTRODUCTION	93
6.2 METHOD	94
6.2.1 EXPERIMENT 1: Bond Strength	94
6.2.1.1 Tissue Preparation	94
6.2.1.2 Tissue Bonding	96
6.2.1.3 Bonding Parameters	96
6.2.1.4 Preparation for Strength Testing	99
6.2.1.5 Strength Testing	99
6.2.1.6 Tracking Speed & Bonding Time	102
6.2.1.7 Histology	102
6.2.2 EXPERIMENT 2: Rehydration	102
6.2.3 EXPERIMENT 3: Natural Breaking Strength of Unbonded Tissue	106
6.2.3.1 Statistics	106
6.3 RESULTS: Comparison of Laser and Dry Bonds	106
6.3.1 Non-Denatured Samples	106
6.3.2 Denatured Samples	108
6.3.3 Rehydration	108
6.3.4 Natural Tissue Breaking Strength	108
6.3.5 Histology	108
6.4 DISCUSSION	117
6.4.1 Breaking Strength of Tissue Bonds	119
6.4.2 Tracking Speed & Bonding Time	119
6.4.3 Breaking Strength of Natural Tissue	120
6.4.4 Histology	120
6.4.5 Experimental Technique	120
6.5 CONCLUSION	123

	Page No.
Chapter 7: Laser Tissue Interactions	
7.1 INTRODUCTION	124
7.2 TEMPERATURE MEASUREMENT	125
7.2.1 Contact Probes	125
7.2.2 Remote Sensing	125
7.2.3 Model	126
7.3 MATHEMATICAL MODEL	127
7.3.1 Introduction	127
7.4 LIGHT DISTRIBUTION	127
7.4.1 Beer's Law	127
7.5 THE KUBELKA-MUNK MODEL	128
7.6 MODIFIED 1-DIMENSIONAL MODEL WITH SCATTERING	132
7.6.1 Contribution From Advancing Wavefront	132
7.6.2 Contribution of Scatter to Absorption	132
7.6.3 Three Dimensions	139
7.7 CONCLUSION	141
Chapter 8: Numerical Model of Laser Bonding	
8.1 INTRODUCTION	142
8.1.1 Heat Flow and the Heat Equation	142
8.2 NUMERICAL EXPRESSION OF THE HEAT EQUATION	143
8.2.1 Simple Analytical Validation: The Hotspot Problem	144
8.2.2 Cylindrical Polar Co-ordinates	147
8.3 CALCULATION OF TISSUE TEMPERATURE DISTRIBUTION	147
8.3.1 Matrix Granularity	147
8.3.2 Boundary Conditions	149
8.3.3 Conditions at Tissue Surface	149
8.3.4 Symmetry Condition at Beam Axis ($r = 0$)	150
8.3.5 Boundary Condition for Large r	150
8.3.6 Energy Distribution	150
8.3.7 Conical Beam Profile	152
8.3.8 Chromophore	153
8.3.9 Parameters	153
8.4 VALIDATION OF MODEL	154
8.4.1 Detailed Experimental Validation of Model	154
8.5 VALIDATION EXPERIMENT	163

	Page No.
8.5.1 Lasing ~600 μ m Thick, Chromophored Tissue Sections	163
8.5.2 Discussion	165
8.6 DEHYDRATION	171
8.7 CONCLUSION	177
 Chapter 9: Laser Bonding - Conclusions	
9.1 INTRODUCTION	180
9.1.1 Chapter 3 - Laser Bonding In Vivo	180
9.1.2 Chapter 4 - Dry Bonding In Vitro	181
9.1.3 Chapter 5 - Scatter of Dry Bonds	181
9.1.4 Chapter 6 - Laser/Dry Bonding Equivalence	181
9.1.5 Chapters 7&8 - Theory	182
9.2 OVERALL ASSESSMENT OF WORK	183
9.3 IMPLICATIONS	184
9.4 CONCLUSION	187
 Chapter 10: Laser Balloon Angioplasty	
10.1 INTRODUCTION	188
10.2 HISTORY	188
10.3 BALLOON ANGIOPLASTY IN PRACTICE	190
10.3.1 Complications	192
10.4 MODIFICATIONS	193
10.5 THE LASER IN ANGIOPLASTY	193
10.5.1 Recanalisation	194
10.5.2 Laser Balloon Angioplasty	195
 Chapter 11: Thermal Simulation of Laser Balloon	
11.1 INTRODUCTION	199
11.2 A MODIFIED BALLOON TO SIMULATE THERMAL EFFECTS OF LASER BALLOON ANGIOPLASTY	200
11.2.1 Standard Balloon Angioplasty Catheter	200
11.2.2 Laser Balloon Angioplasty Catheter	200
11.2.3 Modified Balloon Angioplasty Catheter - 'Thermal Balloon'	202
11.3 SUPPORTING EQUIPMENT	202

	Page No.
11.3.1 Peristaltic Pump	204
11.3.2 Heat Exchanger	204
11.3.3 Non-Return Valve and Compliance Chamber	204
11.3.4 General Notes	207
11.4 COMPARISON OF THERMAL AND LASER BALLOON CATHETERS	209
11.5 APPLICATION	211
11.6 A TECHNIQUE FOR THE SEALING OF MYOCARDIAL SECTIONS TO PERMIT IN VITRO ANGIOGRAPHY OF THE CORONARY VESSELS	212
11.7 CONCLUSION	217
Chapter 12: In Vitro Application of Thermal Balloon	
12.1 INTRODUCTION	218
12.2 METHOD	219
12.2.1 Standard X-ray Procedure	219
12.2.2 Application of the Cold Balloon	220
12.2.3 Application of Hot Balloon	222
12.2.4 X-ray Analysis	222
12.3 HISTOLOGY	225
12.4 ADDITIONAL EXPERIMENTS	226
12.4.1 Reproducibility	226
12.4.2 Vessel Response to Heat (No Balloon)	226
12.5 STATISTICAL ANALYSIS	226
12.6 RESULTS	227
12.6.1 Reproducibility	227
12.6.2 Vessel Response to Heat (No Balloon)	227
12.6.3 Vessel Response to Cold and Hot Balloon Angioplasty	227
12.6.4 Histology	231
12.7 DISCUSSION	237
12.7.1 Technique	237
12.7.2 Results	238
12.8 CONCLUSION	240
Chapter 13: Laser Balloon Angioplasty - Conclusions	
13.1 INTRODUCTION	241
13.2 EXPERIMENTS	241

	Page No.
13.3 FUTURE STUDY	242
13.3.1 Vessel Elasticity	242
13.3.2 Atheromatous Vessels	243
13.3.3 In Vivo	243
13.4 CONCLUSION	243
References	244

TABLES & ILLUSTRATIONS

	Page No.
Chapter 1: Lasers in Cardiac Surgery	
Table 1.1 A range of lasers and powers used for anastomosis.	8
Table 1.2 Absorption and scattering coefficients.	11
Chapter 2: Collagen	
Fig. 2.1 Stay sutures.	14
Fig. 2.2 Three layered arrangement of vessel structure.	15
Fig. 2.3 Gly-X-Y sequence of tropocollagen.	18
Fig. 2.4 Characteristic banding of collagen under E.M.	19
Fig. 2.5 Heirarchical structure of collagen.	20
Fig. 2.6 Collagen crimp and non-linear stress-strain curve.	22
Fig. 2.7 Arterial wall stained with Elastic Van Gieson.	25
Fig. 2.8 Arterial wall stained with Picrosirius Red.	26
Chapter 3: Laser Bonding In Vivo	
Fig. 3.1 Equipment for laser bonding in an animal model.	28
Fig. 3.2 Coupling optics.	30
Fig. 3.3 Micromanipulator.	32
Fig. 3.4 Thermal camera.	33
Fig. 3.5 Argon laser is tracked along incision for bonding.	35
Fig. 3.6 A series of still photographs showing successful anastomosis.	36
Fig. 3.7 Radiographic images of anastomosed vessels.	38
Fig. 3.8 Pressure testing equipment.	40
Fig. 3.9 Histological section of laser anastomosis.	42
Fig. 3.10 Histological section of laser anastomosis.	43
Chapter 4: Dry Bonds In Vitro	
Fig. 4.1 Construction of perspex approximator.	51
Fig. 4.2 Irradiation of approximator by 120W lamp.	53
Fig. 4.3 Approximator temperature as a function of heating time.	54
Fig. 4.4 Approximator and thermocouple array.	56

	Page No.	
Table 4.1	Temperature distribution recorded by thermocouple array.	57
Fig. 4.5	Wet and dry overlap bonding procedure.	59
Fig. 4.6	Creating aortic slices approximately 0.5mm thick.	60
Fig. 4.7	Approximator with overlapped tissue and radiation shields.	61
Fig. 4.8	Opaque white tissue slice before dehydration.	62
Fig. 4.9	Translucent brown tissue bond created by dehydration.	63
Table 4.2	Dry bond strength as a function of bonding temperature.	65
Fig. 4.10	Dry bond strength as a function of bonding temperature.	66
Fig. 4.11	Dry bond strength as a function of rehydration time.	68
Fig. 4.12	Wet bond strength as a function of bonding temperature.	69
Fig. 4.13	Summary of wet and dry bond strengths with temperature.	70
Fig. 4.14	Proposed bonding model.	74

Chapter 5: Scatter of Dry Bonds

Fig. 5.1	Measurement of force applied by approximator elastic bands.	78
Fig. 5.2	Force as a function of vernier position - low pressure.	80
Fig. 5.3	Force as a function of vernier position - moderate pressure.	82
Fig. 5.4	Experimental procedure for dry bond scatter assessment.	84
Fig. 5.5	Bond strength for the five groups of the experimental series.	89
Table 5.1	Results summary for the five groups of the experimental series.	90

Chapter 6: Laser/Dry Bond Equivalence

Fig. 6.1	Experimental approach for laser and dry bond comparison.	95
Fig. 6.2	Laser bonding technique.	97
Fig. 6.3	Dry (oven) bonding technique.	98
Fig. 6.4	Trimming bond prior to strength testing.	100
Fig. 6.5	Equipment to measure bond strength.	101
Fig. 6.6	Typical trace of strength tested bond.	103
Fig. 6.7	Bond strength as a function of tracking speed.	104
Fig. 6.8	Bond strength as a function of oven bonding time.	105
Fig. 6.9	Strength comparison of non-denatured laser and dry bonds.	107
Fig. 6.10	Strength comparison of denatured laser and dry bonds.	109
Table 6.1	Laser and dry bond strengths.	110
Fig. 6.11	Laser bond strength as a function of rehydration time.	111
Fig. 6.12	Natural breaking strength of unbonded tissue slices.	112

	Page No.
Fig. 6.13	EVG and PSR stained sections of 65mW laser bond. 113
Fig. 6.14	EVG and PSR stained sections of 100mW laser bond. 114
Fig. 6.15	EVG and PSR stained sections of 36 deg.C. dry bond. 115
Fig. 6.16	EVG and PSR stained sections of 70 deg.C. dry bond. 116
Fig. 6.17	Examples of excellent and poor apposition. 118
Fig. 6.18	Dry bond strength under different cutting conditions. 122

Chapter 7: Laser Tissue Interactions

Fig. 7.1	3-dimensional plot showing $r(\mu, \gamma) < 1$. 131
Fig. 7.2	The scattering function $A'_s(X)$ for different scattering coeffs. 135
Fig. 7.3	The scattering function $A'_s(X)$ and sub-surface maximum. 136
Fig. 7.4	Forward scattered (g_f) component of $A'_s(X)$. 137
Fig. 7.5	Backward scattered (g_b) component of $A'_s(X)$. 138
Fig. 7.6	Comparison of standard and modified Kubelka-Munk models. 140

Chapter 8: Numerical Model of Laser Bonding

Fig. 8.1	Cooling of hotspot in an infinite cooler medium. 146
Fig. 8.2	Beam profile measured with 0.17mm aperture. 151
Fig. 8.3	Temperature versus time for 65mW beam. 155
Fig. 8.4	Temperature versus radius for 65mW beam. 156
Fig. 8.5	Temperature versus depth for 65mW beam. 157
Fig. 8.6	3-dimensional time-temperature plot for 65mW beam. 158
Fig. 8.7	Temperature versus time for 100mW beam. 159
Fig. 8.8	Temperature versus radius for 100mW beam. 160
Fig. 8.9	Temperature versus depth for 100mW beam. 161
Fig. 8.10	3-dimensional time-temperature plot for 100mW beam. 162
Fig. 8.11	PSR stained serial sections lased at 230mW. 164
Fig. 8.12	Denatured tissue section with model prediction superimposed. 166
Fig. 8.13	Denatured tissue section with model prediction superimposed. 167
Fig. 8.14	Denatured tissue section with model prediction superimposed. 168
Fig. 8.15	Denatured tissue section with model prediction superimposed. 169
Table 8.1	Calculated and recorded peak temperatures. 170
Fig. 8.16	Temperature vs time for 65mW beam switched off at 10 secs. 173
Fig. 8.17	3-dimensional plot for 65mW beam switched off at 10 secs. 174

	Page No.
Table 8.2	Table of temperature for 65mW beam switched off at 10 secs. 175
Fig. 8.18	Tracking speed and theoretical maximum bond strength. 178
 Chapter 9: Laser Bonding - Conclusions	
Fig. 9.1	Proposed overlap bonding technique. 185
 Chapter 10: Laser Balloon Angioplasty	
Fig. 10.1	Action of angioplasty balloon. 189
Fig. 10.2	Deflated and inflated angioplasty balloon. 191
Fig. 10.3	Action of the Spears laser balloon. 196
 Chapter 11: Thermal Simulation of Laser Balloon	
Fig. 11.1	Construction of a standard angioplasty balloon catheter. 201
Fig. 11.2	Construction of modified angioplasty balloon catheter. 203
Fig. 11.3	Equipment required to drive thermal angioplasty balloon. 205
Fig. 11.4	Pump force proportional to square of tube radius. 206
Fig. 11.5	Photograph of equipment to drive angioplasty balloon. 208
Fig. 11.6	Angiogram of heart showing coronary vessels. 213
Fig. 11.7	Myocardial section is excised from the heart. 214
Fig. 11.8	Sealing of myocardial section with contrast-gel. 216
 Chapter 12: In Vitro Application of Thermal Balloon	
Fig. 12.1	Angiography of myocardial section with Urografin 325. 221
Fig. 12.2	Angiogram of myocardial section perfused with Urografin. 223
Fig. 12.3	Angiogram of myocardial section perfused with Urografin. 224
Fig. 12.4	Vessel diameter reproducibility with intravascular pressure. 228
Fig. 12.5	Vessel diameter shrinkage after perfusion with boiling water. 229
Fig. 12.6	Vessel diameter changes with hot and cold angioplasty. 230
Fig. 12.7	Diameter-pressure graph with pre and cold balloon angioplasty. 232
Fig. 12.8	Diameter-pressure graph with hot and cold balloon angioplasty. 233
Table 12.1	Diameter with intravascular pressure and angioplasty type. 234
Fig. 12.9	Vessel section prior to angioplasty. 235
Fig. 12.10	Vessel section after thermal balloon angioplasty. 236

ACKNOWLEDGEMENTS

This work would not have been possible without the excellent and enthusiastic supervision of both Dr. H. Moseley and Dr. W. Martin, to whom I am most grateful. Equally I would like to thank Prof. D. Wheatley, who has overseen the project as a whole, and furthermore has patiently let me proceed at my own pace. My thanks go to Mr. J Morrison (MSc - distinction) who has ably provided general technical support and processed all the histological specimens. In addition, my colleagues Dr. T. McKay and Dr. G. Bernacca have been a ready source of encouragement and ideas. Surgical expertise was provided by Dr. D. Taggart and additional assistance came from Mr. W. Dunn.

I am grateful to the engineering workshop of the Department of Clinical Physics and Bioengineering who manufactured the approximator, and the Glasgow Abattoir Co. Ltd. for their co-operation in supplying the sheep hearts. The image analysis system used to process and present much of the data was provided by the Scottish Home and Health Department. The PhD project itself was funded by the British Heart Foundation.

Last but not least, I must thank my wife for her patience and unstinting support over these last few years - thank you...

Chapter 1

Lasers in Cardiac Surgery

1.1 INTRODUCTION

Townes and Schawlow utilised the principle of stimulated emission to develop the microwave MASER (1,2), extended shortly thereafter to the optical spectrum by T H Maiman (Hughes Research Laboratories) using a thin ruby rod a few inches long with silvered ends, illuminated by a helical flash lamp (3,4). Thus the LASER (Light Amplification by Stimulated Emission of Radiation) was born. The device consists of a lasing medium pumped to population inversion by an energy source (which can be radiant energy, electrical discharge etc.), which induces stimulated emission. The radiation is confined between two mirrors. With one mirror slightly less than perfectly reflecting, the non-reflected component emerges as a fine laser beam. A brief discussion of its qualities is given below.

1.1.1 Directionality

The thin thread of light that emerges from a laser is an indication of the way in which it was created. The highly reflective mirrors of the laser cavity cause the photons to be reflected many times (typically 100) before they emerge from the output mirror. The output thus incurs minimal divergence, equating to a few milliradians.

1.1.2 Monochromaticity

The beam of a laser is highly monochromatic. The frequency spread of the 632.8nm output of a HeNe laser is less than 0.005nm, predominantly caused by Doppler broadening (ie. Doppler shifted light from the motion of emitting atoms moving towards and away from the observer). The monochromaticity results from the resonant phenomenon of stimulated emission, the radiation oscillating within what is essentially a tuned cavity.

1.1.3 Intensity

The inexpensive low powered 1mW HeNe laser produces a beam of intensity many times greater than the sun (5). This is the result of amplification due to repeated stimulated emissions.

1.1.4 Coherence

The distinct speckle pattern of a laser beam on a surface is a manifestation of its coherence. Coherence is a quality that refers to the ordered nature of the light, and defines to what extent the electro-magnetic (EM) field in one part of the beam can be related to another. The nature of stimulated emission keeps all emitted photons in phase and therefore the state of the EM field at one point within the emitted beam can be used to calculate the field elsewhere, up to quite large distances (several metres). Along the axis of the beam, this is known as longitudinal coherence, or coherence length. In the radial plane, the large number of reflections within the cavity creates an output that approximates a plane wave and thus the EM field is well defined across it - a property known as transverse or spatial coherence. The significance of coherence is that it defines a distance over which a stationary interference pattern can be expected to occur. It is the overall coherent nature of the laser beam which creates interference patterns on a surface visible as laser speckle.

1.2 TYPES OF LASER

By February of 1961, Javan, Bennet and Herricut were reporting successful operation of a CW (ie. Continuous Wave output) HeNe gas laser at 1152.3nm (1), and indeed the red HeNe laser is today the most popular device, being easy to construct, inexpensive and reliable. All the noble gases have been made to lase, the population inversion being created by ionisation in an electrical discharge. The most extensively studied is Argon, operating CW at several Watts in the visible spectrum (488nm, 514nm), although examples have been driven as hard as 150W CW.

The CO₂ laser is another gas laser but its output is derived from vibrational modes of the CO₂ molecule. The beam is infra-red (10.6 μm) and its efficiency can be unusually high (15%) when the CO₂ gas is combined with nitrogen and hydrogen. With such a mixture, outputs of 60kW CW can be achieved.

The Nd:YAG laser relies on the optical transitions of the ionic rare earth element neodymium (Nd³⁺) which is embedded within an yttrium-aluminium-garnet crystal. It lases at 1.06μm (infra-red), but the neodymium can also be made to lase in other hosts such as glass.

A semiconductor laser is reliant upon stimulated transitions between the conduction and valence bands of a p-n junction. The first example was GaAs (gallium-arsenide), constructed in 1962. These devices can be very small and can be fabricated with techniques familiar to the semiconductor industry.

Lasing in the ultra-violet part of the spectrum is possible with the Excimer laser, which uses rare-gas molecules or atoms in combination with halide atoms pumped to an ionised state called an excited state dimer (from which the name excimer is derived). The large energies involved are responsible for the high frequency UV output.

Other laser sources include the chemical laser which requires no external power source but is driven by a chemical reaction, dye lasers (for frequency tuneable output) and metal vapour lasers. However, it is inappropriate to list these in further detail here, and the reader is referred to other texts for further accounts of these devices (5).

1.3 DANGERS OF LASER RADIATION

The greatest danger posed by a laser is its extreme intensity, with possible accidental exposure of the eye. The sheer number of photons generated by the stimulated amplification process is such that even the feeble 1mW laser is extremely bright. This is exacerbated by the fact that the eye focuses the beam onto a small spot on the retina which can increase power density by a factor of up to 10^5 . With many lasers capable of generating substantially more than 1mW a real hazard is evident - direct viewing of the beam has considerable potential to blind. Good advice states simply that an observer should NEVER look directly into the beam of a laser - a discussion of various accidents can be found in the reference (6).

A classification system has been created to quantify the danger posed by various systems. This is related to a quantity called the maximum permissible exposure (MPE), above which a specified organ (principally the eye, but also has provision for other organs - skin) cannot be safely exposed (6,7,8,9). Such a quantity takes account of not only intensity, but also laser frequency and the period of time over which it is delivered.

Class 1 lasers are very low power and inherently safe, since any exposure will not exceed the MPE. Classes 2 and 3a lasers are more powerful and potentially harmful, but the viewer is protected by the blink reflex and other natural aversion responses. Intrabeam viewing of class 3b lasers will cause blindness and class 4

lasers are yet more hazardous with even diffuse reflections proving dangerous. Burns to the skin are possible, and these lasers represent a fire hazard.

In order to protect the user from accidental exposure, laser protective eyewear can be worn. Eyewear is classified according to wavelength and optical density (OD). The OD details how many orders of magnitude the offending wavelength is attenuated in passing through the goggle lens. Technically

$$OD = \log_{10} \frac{\text{Incident intensity}}{\text{Transmitted intensity}}$$

However, this figure takes no account of the damage threshold of the lens, which therefore may melt at high enough intensities even though the transmitted intensity is below the MPE (10,11). The monochromatic nature of laser light permits the construction of goggles that attenuate one particular wavelength but leave the rest unaffected. This allows clear (if a little coloured) vision, but it is obviously important that the goggle is suitable for the wavelength in use. Use of the wrong wavelength goggle provides no protection at all.

1.4 APPLICATIONS OF LASERS TO MEDICINE

Although the laser has found many applications (communications, guidance systems, generation of fusion neutrons, welding, cutting, surveying, holography, computer data storage etc. (5)) since its description by Schawlow as an "invention in search of an application", the interest of this thesis is its medical utilisation.

In medicine, the dangerous aspects of the laser beam can be turned to medical advantage under carefully controlled conditions (12-17). Its intensity can be used for cutting. Its coherence is appropriate for eye testing. Its monochromaticity can be used to induce localised frequency dependent reactions (18).

1.5 APPLICATIONS OF LASERS TO CARDIAC SURGERY

Use of the laser in medicine is widespread and its list of applications grows daily, however the opportunity is now taken to examine its role in cardiac surgery. A brief description of the heart is given below followed by a discussion of the potential of the laser in cardiac therapy.

1.5.1 The Heart, Vasculature and Problems

The adult human heart is typically the size of a loosely clenched fist, weighing approximately 0.25kg in females and 0.3kg in males (19). It is a four-stage pump with a two-stage low pressure side on the right side, and a two-stage high pressure

side on the left. De-oxygenated blood returning from the venous system to the right atrium is pumped at low pressure by the right ventricle through the lungs to re-oxygenate the blood. Oxygenated blood returns to the left atrium to be pumped at higher pressure by the left ventricle through the systemic circulation where it eventually returns to the right atrium. The heart muscle itself (myocardium) requires oxygenated blood to function and is supplied by a vascular network on its exterior surface. The main supplying vessels are called the coronary arteries. This supply is tapped from the root of the aorta, immediately beyond the left ventricular aortic valve.

Apart from abnormalities in contraction and rhythm (bradycardia, tachycardia, fibrillation - corrected by drugs or pacing) major problems of the heart that can occur involve failure of a valve or inadequate blood supply to the myocardium, both compromising function and ultimately leading to heart failure. The cardiac surgeon attempts to rectify these problems.

With valve failure, replacement is possible (20), and with chronic heart failure transplantation may be an option (21,22). However the bulk of the work of the cardiac surgeon involves rectifying poor blood supply to oxygen starved myocardium caused by blockages in the arterial network. The blockages result from steady deposition of fats and minerals over a period of time which form atheromatous plaques that obstruct the bore of the vessel. Significant blockage of the larger supplying vessels (coronary arteries) is the more critical condition since this affects blood flow to all myocardium downstream of it. The traditional surgical approach attempts to bypass the blockage by anastomosing a patent vessel across the blocked artery so that an alternative route for the blood is provided, restoring the supply.

1.5.2 The Laser in Cardiac Surgery

The use of the laser in cardiac surgery has been directed towards attempted alleviation of some of the difficulties encountered in bypass surgery. One aspect of this is balloon angioplasty in which, as an alternative to surgery, a small deflated balloon is inserted into the obstructed artery and then inflated to increase the bore of the vessel by squashing the plaque outwards into the vessel wall (23). Unfortunately the restenosis rate is high, but it is felt that introduction of the laser to help thermally remodel the ballooned artery may reduce restenosis. This topic is examined in detail in the latter part of this thesis (Chapters 10, 11, 12, 13). In conditions where balloon angioplasty is not suitable, bypass surgery is an alternative option. In this case the laser has been proposed as a potential tool to improve surgery by replacing sutured anastomoses with a laser bond (24). The

technique involves apposing (ie. butting together) the vessels to be anastomosed and tracking a laser beam (Argon, Nd:YAG or CO₂ with powers of typically several hundred mW) along the length of the joint. Such bonds are simple to make and can be very effective (25).

The non-sutured anastomosis of vessels predates the laser by many years, since in 1963 (26) Sigel et al. demonstrated tissue anastomosis using a process of high frequency electrocoagulation, the tissue apparently bonding as the result of heating from the high frequency electric current (27). Using this technique, end-to-end and end-to-side vessel anastomoses were created, the incisions being up to 25mm long. For closure of small incisions (<7mm) the success rate was high, but for incisions larger than this, the failures outnumbered the successes. Histology revealed welds of varying degrees of damage, with the best showing only moderate tissue coagulation with preservation of fibre structure. These examples were capable of withstanding internal pressures of 600-900mmHg. It was noted that excessive heat created an amorphous coagulum, eventually resulting in disintegration and carbonisation - poor bond strength was the result. In conclusion, successful bonding required minimal tissue coagulation with carefully and accurately aligned bonding faces.

The electrocoaptive work never proceeded further, perhaps due to the technical difficulties of creating these bonds. It was not until some 14 years later that Jain and Gorisch reported similar results, but in their case a laser was used for bonding (24). Although it was recognised that sutured anastomoses of vessels of diameter less than 0.5mm were very difficult (if not impossible) using conventional techniques, it appeared that the laser provided a simple non-contact method for achieving this goal. Using vessels of 0.3mm to 1mm diameter and a Nd:YAG laser at 17W, incisions were sealed in 0.5mm sections with single 1/20 second bursts (0.5mm spot diameter). Histology was encouraging, with the laser results reported to be superior to that of electrocoagulation because of the cleaner, more precise energy source. Jain and Gorisch concluded that the results warranted further investigation, including the use of alternative lasers and some assessment of temperatures induced in the vessel wall.

Their work spawned a whole series of investigations by other groups which successfully produced similar results. Details are given below:

1.5.3 Technique

Quality of apposition was readily recognised as being of importance to the success of a bond (25,28). To this end, apposing vessel faces were pulled together with a few well placed stay sutures (29,30). In some cases it was felt that the adventitia

should be stripped from the vessel at the bond edge so as not to hinder apposition (31), whereas others attempted to incorporate the adventitia into the bond (32). Equally ambiguous was the attitude held towards the presence of blood between the bonding faces. Vessel faces were left in their natural state in Jain's experiment (24) but extra blood was applied in the experiments of Kreuger et al. (33) to enhance any fibrin induced adhesion. However the presence of fibrin is generally accepted to impede adhesion by replacing true laser bonds with weaker fibrin-based bonds.

Although the work of Jain (24) used a Nd:YAG laser at 9kWcm^{-2} , a wide range of other laser types and power densities have been used to successfully bond vessels (Table 1.1). Nd:YAG output up to 38kWcm^{-2} has been utilised (34), with the CO_2 laser covering the middle ground at several hundred Wcm^{-2} (25,35,36). The Argon laser is used at lower power densities which typically equate to 10Wcm^{-2} (37). The CO_2 laser is the most common device for bonding purposes, particularly for smaller vessels only a few millimetres diameter. The temperatures achieved during bonding vary widely, with estimates in excess of 100deg.C. for the CO_2 laser (38), $70\text{-}80\text{ deg.C.}$ for the Nd:YAG (39) and less than 50 deg.C. with the Argon laser (40).

Beyond the basic technique, many modifications have been tried in an attempt to improve the laser bond. Pulsed laser output has been utilised (41). Laser absorbing dyes (chromophores) have been used to localise and increase absorption of laser energy in the bond area (42,43,44,45). Air has been blown onto the lased tissue to keep it cool, and others have tried drops of cool saline to achieve the same end (46,47). Glues have been used in an attempt to reinforce the bond (45,48). Some prefer the use of absorbable sutures to minimise interference with the vessel wall (49,50). Alternative laser sources have also been tried (51,52).

The exposure period suitable for a successful bond has been loosely defined as requiring continuous lasing until certain changes are observed at the lased vessel surface (53,54). The changes are usually described in terms of tissue discolouration (37,55) or in one case as slight dehydration and shrinkage (56).

1.5.4 Results

The results of laser bonding are well documented. There have been many animal studies, most of which have involved anastomosis of vessels a millimetre or two in diameter. Lased vessels demonstrate superior long term patency, but patency rates struggle to equal to those of sutures (57-61). The frequency of postoperative aneurysms and pseudoaneurysms (30%) has caused concern (32,62) and appears

GROUP	DATE	LASER	POWER	SUTURES	COMMENTS
Sigel	1963	--	N/A	No	Electrocoagulation
Sigel	1965	--	N/A	No	Electrocoagulation
Jain	1979	YAG	17W	No	Small vessels
Gomes	1983	Ar	0.8-1.5W	Yes	
Okada	1985	CO2	0.02-0.04W	Yes	Clinical use
Pribil	1985	Ar	15W	Yes	Small vessels
White	1986	CO2	1-2W	Yes	
		YAG	7W	Yes	
		Ar	1.5W	Yes	
Quigley	1986	CO2	0.07W	Yes	Aneurysms
Schober	1986	Ar	0.3W	Yes	SEM
Godlewski	1986	Ar	0.3W	Yes	Small vessels
Neblett	1986	CO2	0.08W	Yes	Small vessels
Badeau	1986	CO2	0.07-0.15W	Yes	Thermography
Vance	1986	Ar	0.4W	Yes	Chromophore
McCarthy	1986	CO2	0.06-0.1W	Yes	
Negro	1986	CO2	0.3W	Yes	
Vale	1986	CO2	0.1W	Yes	
White	1986	CO2	1W	Yes	
		YAG	1W	Yes	
Kopchok	1986	Ar	0.5W	Yes	
White	1987	Ar	0.5W	Yes	Temperature
Nijima	1987	YAG	20W	No	Temperature
Kopchok	1988	Ar	0.5-1W	Yes	Intervascular splint
Ulrich	1988	YAG	12.5W	Yes	Temperature
Ruiz-Razura	1988	CO2	0.8W	Yes	Long term follow up
Kopchok	1988	Ar	0.5W	Yes	Strength
		CO2	0.15W	Yes	Temperature
Travers	1988	CO2	0.03-0.04W	Yes	
Flemming	1988	CO2	0.1W	Yes	240 anastomoses
Fujitani	1988	Ar	0.5W	Yes	
Shapiro	1989	YAG	5W	Yes	
Unno	1989	Diode	0.06W		Pulsed
Chuck	1989	Ar	0.3W	Yes	
Nakata	1989	CO2	0.065W	Yes	Chromophore
Shiia	1989	CO2	0.035W	Yes	Small vessels
Ninomiya	1989	YAG	1-1.5W	Yes	
Murray	1989	Ar	0.5W	Yes	Contact method
Jacobowitz	1990	CO2	0.08W	Yes	
White	1990	Ar	0.5W	Yes	Pulsed
Flemming	1990	CO2	0.1W	Yes	Absorbable sutures
Ruiz-Razura	1990	CO2	0.07-0.08W	Yes	Strength
Gennaro	1991	CO2	0.1W	Yes	
Ashton	1991	Diode	4.8 Wcm-2	Yes	Strength
Basu	1991	CO2	0.2W	Yes	

Table 1.1

A range of lasers at various powers have been used to successfully anastomose vessels.

to be associated with use of the CO₂ laser rather than Argon or Nd:YAG, being attributed to poor apposition or interruption of the elastic lamina and its inability to adequately regenerate. Endothelial damage by laser or suture is similar. Re-endothelialisation following laser surgery has been observed to be complete within 7 days (56), but is more widely reported to require 2 weeks (30,54). Although intimal hyperplasia is similar in both cases, lased arteries heal more quickly, having a reduced inflammatory reaction and a more organised collagen/elastin response.

Testing of bond strength after lasing reveals that bursting pressure of a lased vessel exceeds systemic pressure (63,64,65). Although the laser bond appears to be less strong than a sutured anastomosis initially, the two become equal 2 weeks or more post-operatively, with Hartz (66) reporting superior laser bond strength at 6 weeks.

1.5.5 Mechanism

The wide range of bonding conditions reported makes it difficult to determine a single mechanism responsible for the laser bonding effect - many mechanisms have been proposed. Some have attributed bonding to enhanced fibrin clotting (48) and others to thermal fusion of vessel proteins (61,67). Some groups have talked more specifically of fusion of collagen fibres and collagen-collagen bonds (68). Schober (34) reports interdigitation of lased collagen fibres suggesting that this might be an important requirement for bonding.

1.5.6 Complications

Although laser bonding has much to commend it, it is not without problems. The extent and degree of vessel coagulation is difficult to control while lasing. This directly affects bond strength, which is further complicated by the problem of poor apposition (37,69). The failure rate of bonds has not been widely reported, but Frazier (70) talks of weld disruption in 40% of samples while Godlewski (37) reveals that 25% of his bonds ruptured within hours to days of lasing. It is also recognised that adequate experience is required before consistent bonding can be achieved (71).

1.5.7 Advantages

In spite of these complications, there are advantages of laser bonding as compared to sutures. The time to create bonds is less, in a manner which reduces trauma and distortion of the vessel wall (54,35). The technique is non-tactile and more sterile, and the increased precision obtainable with a laser beam makes it applicable to small vessels not amenable to sutures (24,72).

In summary, it became apparent that typical qualities of laser assisted anastomoses included improved healing, reduced foreign body response and potentially superior long term patency, all from a technique that required less dexterity than sutures. The CO₂ laser produced good bonds, especially with smaller vessels of only a few millimetres diameter, but also had a tendency to create aneurysms around the area of the joint. The greater tissue penetration of the Argon beam (Table 1.2) was credited with producing superior bonds in thicker walled vessels (diameter > 4mm) with no signs of aneurysm (73). The Nd:YAG had its proponents, but neither it nor the Argon laser were considered the equal of the CO₂ laser in the realm of small and average sized vessels.

Closer examination has attempted to characterise bonding conditions and laser parameters in order that they might be correlated with the strength and quality of the bond. Mechanical properties have been examined (74,75,76). Light and electron microscopy have been utilised (77,78,79,80). Thermal cameras were used to analyse the temperature conditions induced within the lased tissue (36,47,81,82). The result is a consensus of opinion (principally from the CO₂ and Nd:YAG work) that concludes bonding is a thermal effect similar to that observed by Sigel et al., the tissue proteins (major component - collagen) being heated to a temperature sufficient to cause denaturation, creating a protein coagulum which subsequently sets to bind the tissue faces together. Certainly this was supported by the histology which showed thermally denatured tissue bonds along with evidence of interdigitated collagen fibres (34).

It was the work of White et al. with the Argon laser that cast doubt on this theory, since he asserted that bonds could be created with the Argon laser at temperatures in the region of 40 - 50 deg.C. (40,46,47,68), temperatures rather less than that required to denature the tissue (62 deg.C.). In reality these temperatures were barely above normal body temperature which prompted White to suggest that the bonding effect was unlikely to be thermal and was possibly photochemical in nature (40,79). This would imply some direct, closely coupled interaction between the photons of the laser and the molecules of the collagen fibres. However, with bonding conditions being so different to that of the CO₂ and Nd:YAG bonds, it was recognised that the photochemical mechanism may not apply to these. Hence it was proposed that the low temperature Argon mechanism may be fundamentally different to that of the high temperature bonds created with the CO₂ and Nd:YAG lasers.

In addition to experimental work, a theoretical framework was constructed, describing the nature of the laser interaction with tissue and the resultant heat flow and temperature distributions that would arise (83-90). The introduction of a

	Argon Laser	Nd:YAG Laser	CO2 Laser
	514 nm	1.06 μm	10.6 μm
Linear Attenuation			
Coefficient (per cm)	10	4	200
Kubelka-Munk Absorption			
Coefficient (per cm)	11	0.9	
Kubelka-Munk Scatter			
Coefficient (per cm)	11	2.8	

Table 1.2 Absorption and scattering coefficients of vessel wall at various laser wavelengths.

thermal camera to monitor tissue temperature while lasing provided potential experimental validation of the theoretical model (36,47,82). The details of this work are more fully discussed in Chapters 7 and 8. The aim of the theoretical approach is to obtain as much information as possible about the flow of energy within the lased tissue, which can then be correlated with bond strength and histology in the hope of enhancing understanding of the bonding mechanism. It attempts to answer such fundamental questions as: 'Is the process photochemical?', 'To what extent is thermal denaturation responsible for the creation of a tissue bond?'.

Unfortunately, these issues are still currently unresolved. The mechanism of laser tissue bonding is not yet understood. It is important to understand the mechanism because as yet the success of laser bonding does not equal that of sutures (it varies from group to group) and although laser bonds show potential they are not yet consistent enough to be trusted in patients (although there is the occasional report of clinical application (91,92)). As a result, each group has its own way of doing things and yet is unable to justify why they think their method is better than that of another group. The picture has become confused by the large number of alternative approaches that have been tried. Despite the wealth of data collected, many fundamental questions remain unanswered:

- What tissue temperature should be achieved?
- Is there an appropriate power or exposure?
- Is the bonding mechanism photochemical?
- Is denaturation required?

This thesis attempts to establish some of the ground rules necessary for the creation of laser tissue bonds. It starts with a necessary introduction to collagen (Chapter 2), followed by a series of in vivo experiments with the Argon laser, used to establish the problems and techniques of laser assisted vascular anastomoses (Chapter 3). The following two chapters (Chapters 4 and 5) describe a fundamental investigation of the bonding mechanism which leads to numerous conclusions about the nature of the Argon bond. Chapter 6 attempts to validate these conclusions with a number of laser experiments and the theoretical background is dealt with in Chapters 7 and 8. Finally an overview of the work performed and its clinical implications are discussed in Chapter 9. Chapters 10 onwards are concerned with the related application of laser balloon angioplasty.

Chapter 2

Collagen

2.1 INTRODUCTION

Laser assisted vessel anastomosis involves apposing the faces of the vessels to be joined (usually achieved with two or three stay sutures (Fig. 2.1)) and carefully tracking a laser beam along the length of the joint. The bonding process has been attributed to the creation of collagen-collagen bonds induced by the laser (34,79). It is therefore appropriate at this stage to consider the structural components of the vessel wall and particularly the role played by collagen. These issues are considered below, concluding with a summary of histological techniques used to identify collagen within the vessel wall.

2.2 VESSEL STRUCTURE

A simple but inclusive system applicable to all vessels is used to classify components of the vessel wall (93). However, the generality of this model is also its weakness. Classifications can not be pressed too strongly since the adaptive nature of vessels inevitably blurs sharp delineations between components. The classification system considers vessel structure to consist of three concentric layers (tunica intima, tunica media, tunica adventitia) each with its own cellular orientation (Fig. 2.2).

The innermost layer (tunica intima) is a delicate layer of connective tissue organised longitudinally which merges with the media. At the luminal surface of the vessel the intima supports the endothelium. This is a smooth layer of cells only one cell thick which presents a smooth surface to the circulating blood. This lining coats the whole of the vascular system from the smallest vessel to the largest. In contrast the components of the media (the middle layer) are arranged in circumferential fashion, consisting of muscle cells and connective tissue. Beyond the media lies the adventitia - longitudinally organised connective tissue - which acts as an interface with surrounding tissue. These components act together to balance the internal pressures presented by the circulation (94).

Stay sutures:

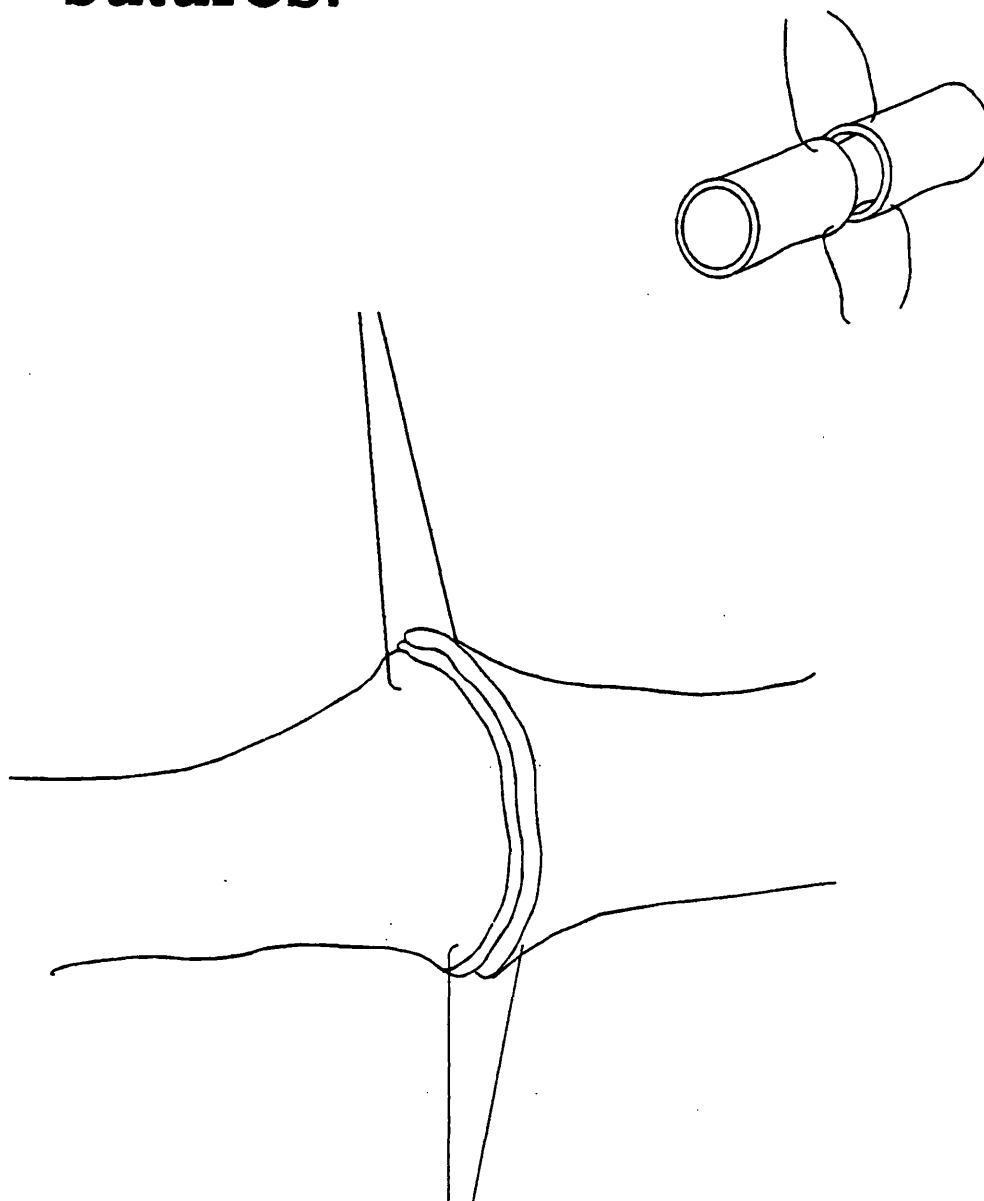


Figure 2.1 Stay sutures are used to pull the vessel faces together for good apposition prior to bonding.

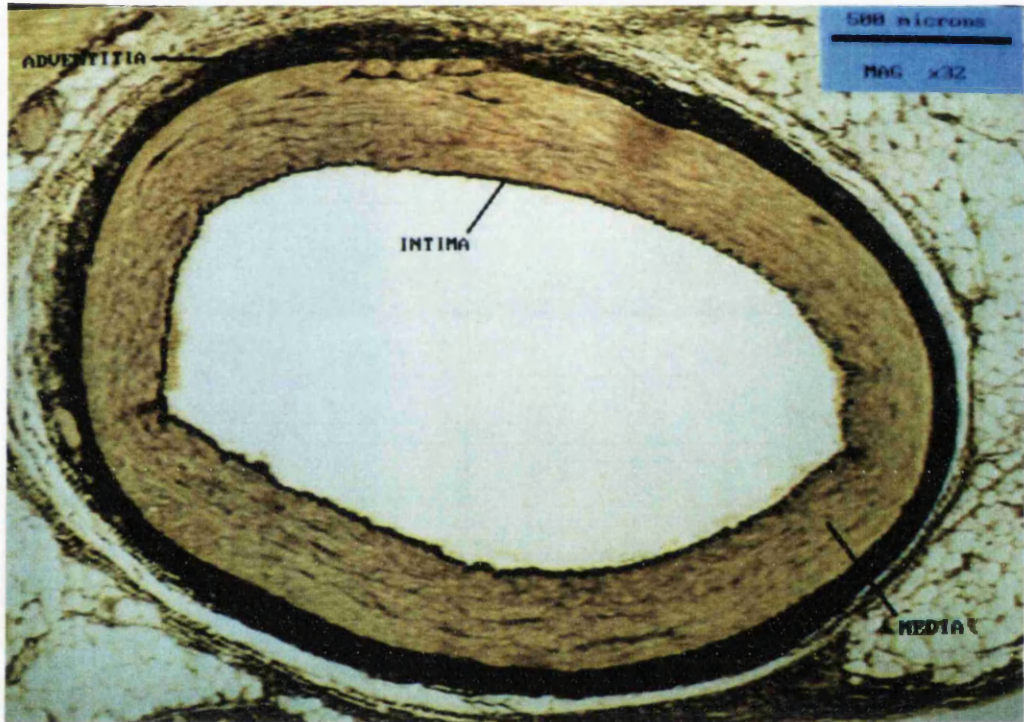


Figure 2.2 Vessel cross-section showing three layered arrangement of vessel structure.

Peripheral resistance is primarily dictated by the internal bore of the vessel and controlled by the muscular cells of the vessel wall. Their response time is slow in comparison to the pulsing of the circulation, and therefore vessel response at this frequency is determined by the elasticity of the vessel wall. Vessel elasticity not only provides compliance but also renders the pulsatile flow of the heart rather more continuous in the peripheral vessels.

2.2.1 Arteries

Arteries can be identified by their thick media, containing muscle cells interspersed with elastin and collagen fibres. In addition, a dense layer of elastin tends to be sandwiched between endothelium and media. The larger arteries are more elastic than small ones.

2.2.2 Veins

Veins are also composed of the three layered structure. A vein of the same internal bore as an artery has a thinner media which is mainly muscular but with much reduced content of both muscle and elastin. The adventitia consists of longitudinal elastic and muscle fibres and is much thicker than for an artery. The adventitial thickness of the largest veins can exceed that of the media.

2.3 COLLAGEN

Collagen is an abundant protein accounting for nearly a third of body proteins. It is part of the connective tissue matrix whose function it is to maintain the structural integrity of tissue. This results from the highly ordered manner in which collagen is packed conferring great tensile strength on the matrix. Collagen is itself a fibrous matrix, the fibres being embedded within an amorphous gel-like substance (the extra-fibrillar matrix) whose content critically affects the properties of collagen as a whole (95). Subtle changes in the protein sequence of the collagen molecules and extra-fibrillar matrix creates collagens with a range of differing properties, so that to date at least 13 types have been identified (96). Collagen type I is the most prevalent, being found in interstitial tissues, skin, tendon and bone (97). Type III is similar but less abundant. Type II is found in hyaline cartilage and type IV is not fibrous - it is present in the vitreous humour of the eye. Our interest is in the fibrous type I and III collagens present in the walls of blood vessels.

2.3.1 Molecular Structure

The basic building block of collagens is a triple amino acid sequence which can be described as glycine-X-Y, where X and Y may be any amino acid but are most frequently proline and hydroxyproline (96,97,98). The glycine-X-Y sequence repeated many times (Fig. 2.3) forms a left handed helical rod (pitch 0.9nm) some 338 triplets long. This α -chain is terminated at both ends by a non-triplet amino acid called a telopeptide. Three α -chains (α_1 , α_2 , and α_3 , of which α_1 and α_2 are identical for type I collagen) are wrapped around each other to form a right handed triple stranded thread with a length of approximately 300nm, a diameter of 1.4nm and a pitch of approximately 9nm. This molecule - tropocollagen - has a molecular weight of 300,000. The α -chains of the helix are bound together by covalent links along the length of the molecule. There is also space for a single hydrogen bond within each triplet which acts in conjunction with the covalent links of the telopeptides to bind to other neighbouring tropocollagen molecules. In this case the hydrogen bonds are bridged by water molecules (96). The distribution of forces between each tropocollagen molecule stacks them in a quarter-staggered array (ie. although aligned in parallel, each is shifted axially from its neighbour by one quarter of the molecular length) held stable by both polar and anionic interactions. This repeated longitudinal stacking gives rise to periodic charge concentrations responsible for the characteristic banding pattern of period 67nm (Fig. 2.4) visible under the electron microscope (67nm x 4 equals approximate length of tropocollagen). The lateral interaction between rods creates a structure of pentagonal cross-section approximately 3.6nm in diameter. The result is a long thin micro-fibril consisting of a highly ordered pentagonal array of tropocollagen molecules.

2.3.2 Fibrous Structure

Micro-fibrils pack in a tetragonal lattice (95) to form sub-fibrils of some 30nm diameter (Fig. 2.5). Further aggregation occurs as sub-fibrils form collagen fibrils which have a wide range of diameters from 50nm to 500nm. It is believed that fibril formation results from growth into very long filaments which then aggregate laterally. The distribution of fibril sizes is related to the stresses the collagen must sustain (99). Fibrils embedded within the extra-fibrillar matrix align to form collagen fibres.

Throughout this structure, the molecular cross-links are responsible for forming both inter- and intra-molecular bonds. Inter-fibrillar bonds although

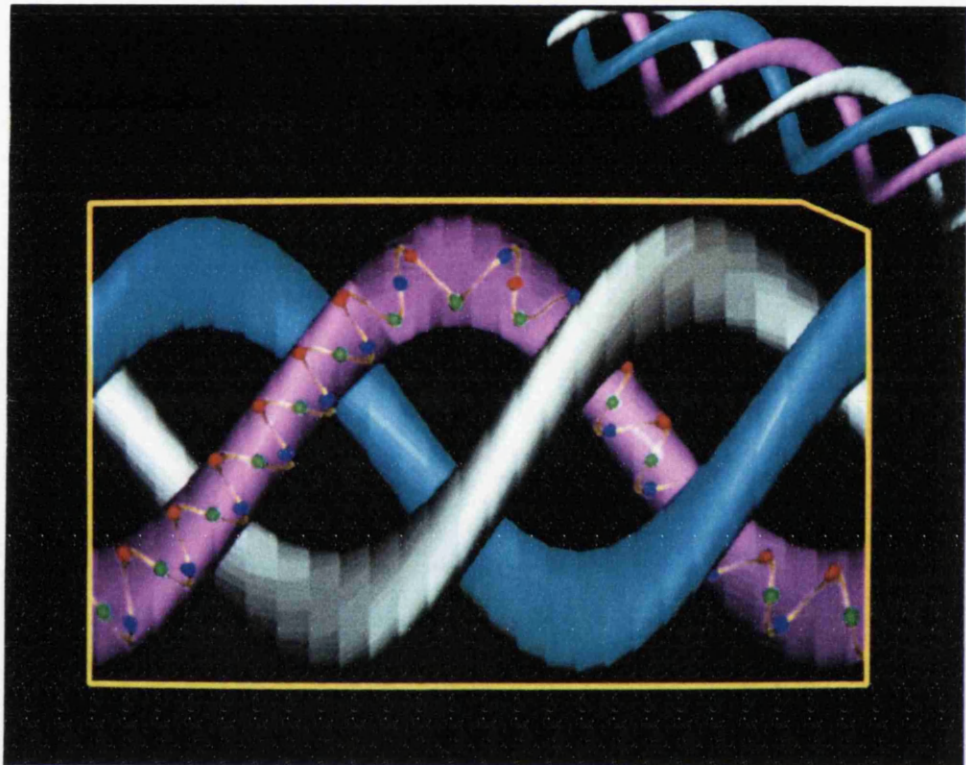


Figure 2.3 Tropocollagen constructed from three intertwining helices (pink, white and blue). Each thread is itself a helix based on the Gly-X-Y sequence, represented by the red, green and blue dots.



Figure 2.4

The characteristic banding of collagen under the electron microscope (top picture). This is destroyed by denaturation (bottom picture). (Reprinted from Schober 1989)

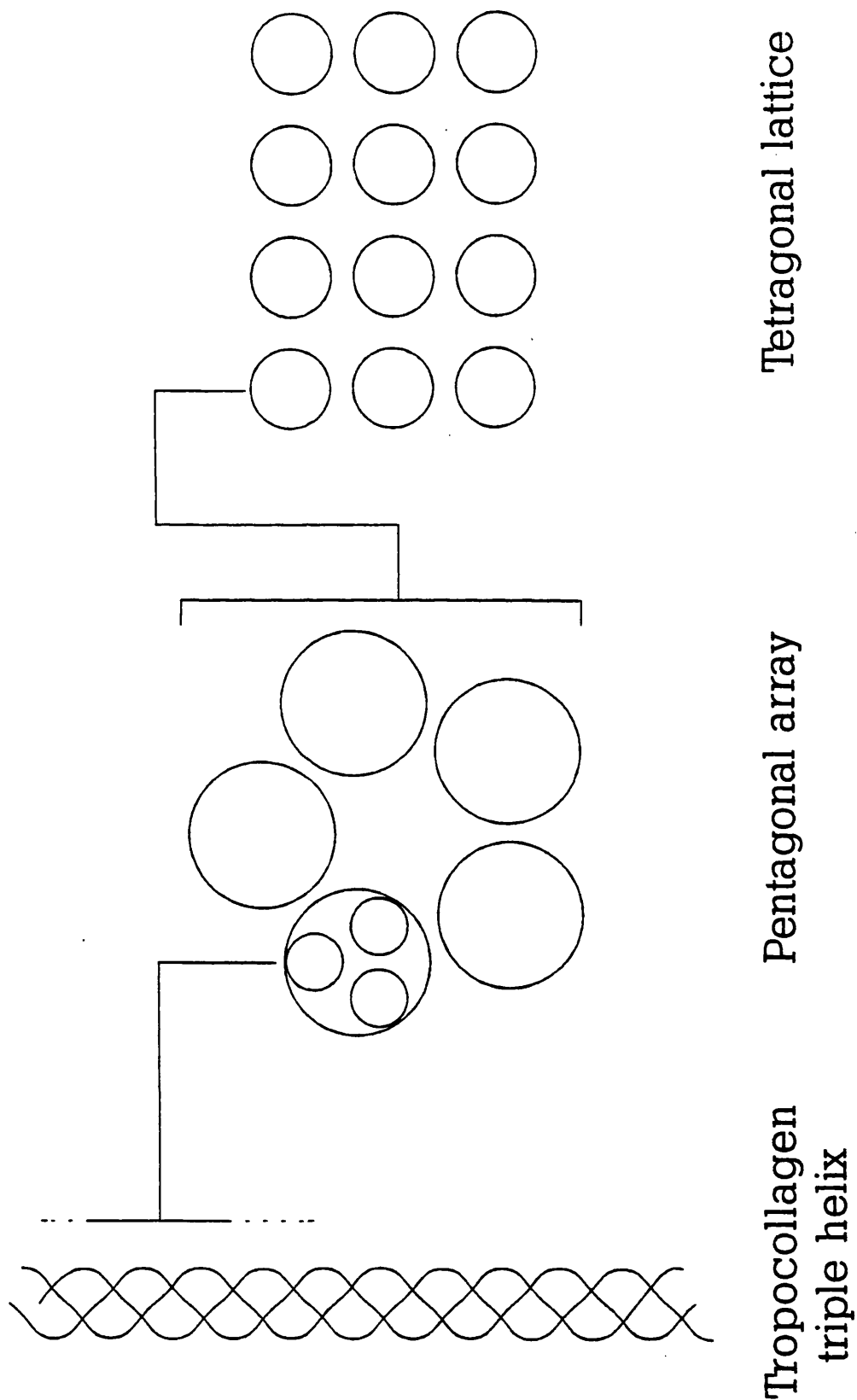


Figure 2.5 Hierarchical structure of collagen.

containing an anionic component are predominantly polar in nature, and thus water content plays an important role in determining the properties of collagen.

2.3.3 Extra-Fibrillar Matrix

The gel-like amorphous substance in which the fibrils are embedded consists of proteoglycans and water (95). Proteoglycans are a high molecular weight hyaluronic acid with associated mucopolysaccharides. These maintain the fibrous hierarchy of the collagen structure, its properties being a strong function of water content.

2.3.4 Mechanical Properties

It is clear that water, by virtue of its ability to form cross-links, plays an important part in the conformation of collagen fibres (100). Hence it is instructive to consider the sequence of events in the rehydration of dehydrated collagen (95).

The first 7% of water by weight is incorporated into the tropocollagen structure. From 7% to 25%, water molecules bind to tropocollagen side chains and are adsorbed between the helices of the micro-fibrils. 25% to 45% represents a transition region in which not all water is bound, but some is free to be sorbed within the extra-fibrillar matrix. Above 45% rehydration, water freely rehydrates the matrix. The density of hydrated collagen is a little greater than the dehydrated sample because it is thought that water induced cross-links pull the fibre components more closely together. It is not surprising to find that tensile strength is a function of water content with maximum strength achieved above 33% rehydration. However, excessive accumulation of water ultimately leads to a reduction in strength as excess molecules squeeze between and force apart bonding sites, reducing molecular attraction.

Collagen fibril orientation is an important factor in determining the mechanical properties of the tissue, the fibrils generally being aligned with the axis of stress. They exhibit a crimped structure (crimp length 1-100 μ m, crimp angle 5-25 degrees) which acts as a compliance mechanism as the collagen is stretched (95). At low strains (Fig. 2.6) a non-linear stress-strain relationship exists (the 'toe' of the curve) as the fibrils uncrimp independently of each other. Having uncrimped all fibres, higher strains provide a linear elastic region due to elastic deformation of the fibrils. At yet higher strains a yield point is reached as inter-fibrillar cross-links start to break, and beyond this a second yield point indicates breaking of intra-fibrillar links.

Collagen fibres - with crimp

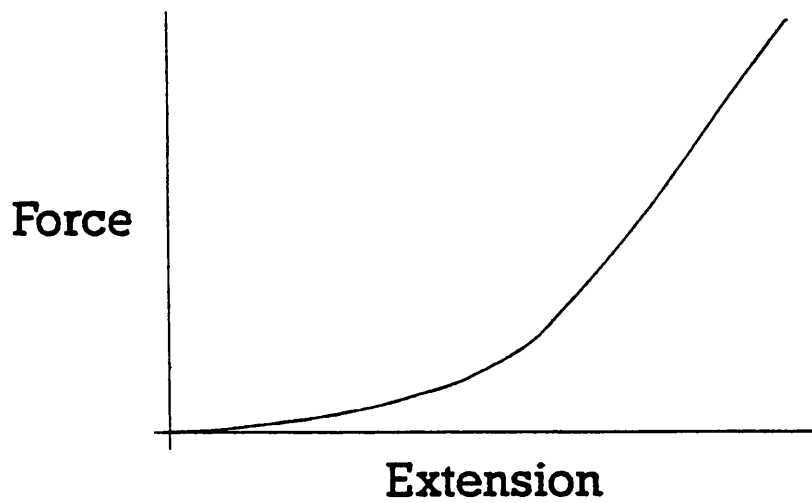
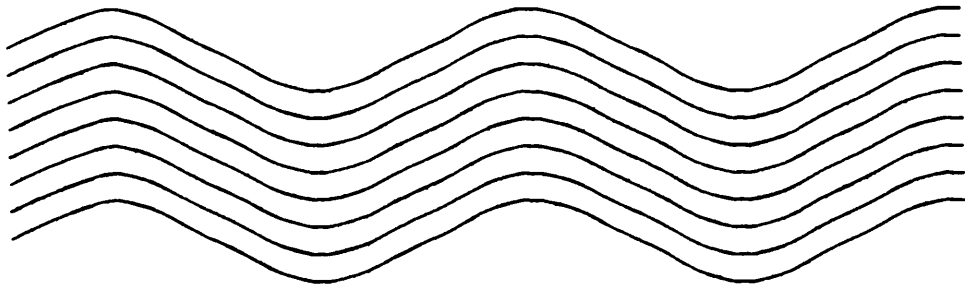


Figure 2.6 Diagram demonstrating the periodic crimp of collagen fibres. This is responsible for the non-linear 'toe' region of the stress-strain curve.

The linear elastic region has a stiffness directly related to the proportion of collagen in relation to the matrix. Therefore a bimodal distribution of fibril diameters is associated with a stiffer material since the smaller diameter fibrils can fit between the larger inter-fibrillar gaps. In contrast, the extra-fibrillar matrix is considered to be the factor controlling the creep and viscoelastic properties of the material.

It is the nature of the cross-links that provide collagen fibres with their high tensile strength, and equally that they display little resistance to flexion or torsion.

The cross-links can be disrupted through heating (101), this occurring at a temperature of approximately 62 deg.C. under normal circumstances (ie. conditions of normal acidity, hydration and stress). This process is called thermal denaturation. Intermolecular cross-links are broken to the extent that the banding pattern under electron microscopy is no longer visible. The ordered structure of collagen is lost and it becomes a jumble of random coils. This change remains on cooling and is essentially irreversible. Denaturation also affects the physical properties of collagen - it shrinks and the elastic modulus is much reduced. The high degree of symmetry of non-denatured collagen makes it optically active, but this birefringence is lost with denaturation.

2.4 ELASTIN

A brief note on the structure of elastin is merited since it is also present in the vessel wall and forms a major component of the connective tissue matrix (97). Although elastin lacks distinct periodicity, it does aggregate to form long parallel fibrous threads, constructed of 5nm diameter rods aligned in parallel to form a 5-6 μ m core surrounded by a sheath of micro-fibrils which are approximately 10-12 μ m in diameter. Elastin has a much lower modulus of elasticity than collagen (ie. its not so stiff) and is more resistant to denaturation (its temperature of thermal denaturation is higher).

2.5 HISTOLOGICAL TECHNIQUES

Identification of collagen within tissue structure is achieved with histological techniques. This is an established method in which prepared tissue is cut into tissue sections a few microns thick, and stained with a chemical specific for a particular protein sequence. The slice is thin enough to be translucent, with the coloured stain localising in only those components for which it is specific. Viewed through a microscope, the colouring of the stain permits ready and accurate

identification of particular structures, which contrast against the rest of the material.

Paraffin wax processing was used to prepare the tissue for staining. This is a process in which fresh tissue is initially 'fixed' in formaldehyde (glutaraldehyde may also be used) thus cross-linking the sample, effectively stopping its decomposition. The fixed tissue is stiffened so that it can be cut cleanly by embedding it in and replacing its water content with wax. A microtome (effectively a bacon slicer on a small scale) is used to cut sections a few microns thick. The reverse of the wax dehydration process is used to rehydrate the tissue, at which juncture it is chemically stained. The section is mounted on a glass slide and covered with a cover slip to stop it drying out. The coverslip glue is refractive index matched with the glass for distortion free viewing.

Throughout this study the Elastic van Gieson stain was used to identify general components of a vessel. Elastin is stained black, other connective tissue purple/red and muscle yellow (Fig. 2.7).

The stain specific for collagen is Picrosirius Red, discussed in some detail below.

2.5.1 Picrosirius Red F3BA

Sirius red is a strongly anionic dye whose rod like molecules are of short length in comparison to those of tropocollagen (4.6nm). The sulphonic acid groups along its length react with the base groups of collagen, the molecules of both aligning themselves. Approximately 120 sirius red dye molecules are known to associate with each tropocollagen molecule. The result of this union is enhanced birefringence (in excess of 7 times that of collagen itself (102,103)). Viewed under the microscope with the sample placed between crossed polarisers, the collagen-sirius red combination is readily visible as areas of brightness against a dark non-birefringent background (Fig 2.8). Since the natural birefringence of collagen types I and III are slightly different, their difference is enhanced with staining, visible by their different colours (104). The presence of picric acid within the dye is important since it stops the indiscriminate staining of non-collagenous components.

If denatured collagen is stained with picrosirius red, it displays no birefringence because of the essentially random orientation of the proteins due to breaking of molecular cross-links (105).



Figure 2.7 A section of an arterial vessel wall stained with Elastic Van Gieson. Muscle stains yellow (media), collagen stains red/pink and elastin dark gray or black (intima).

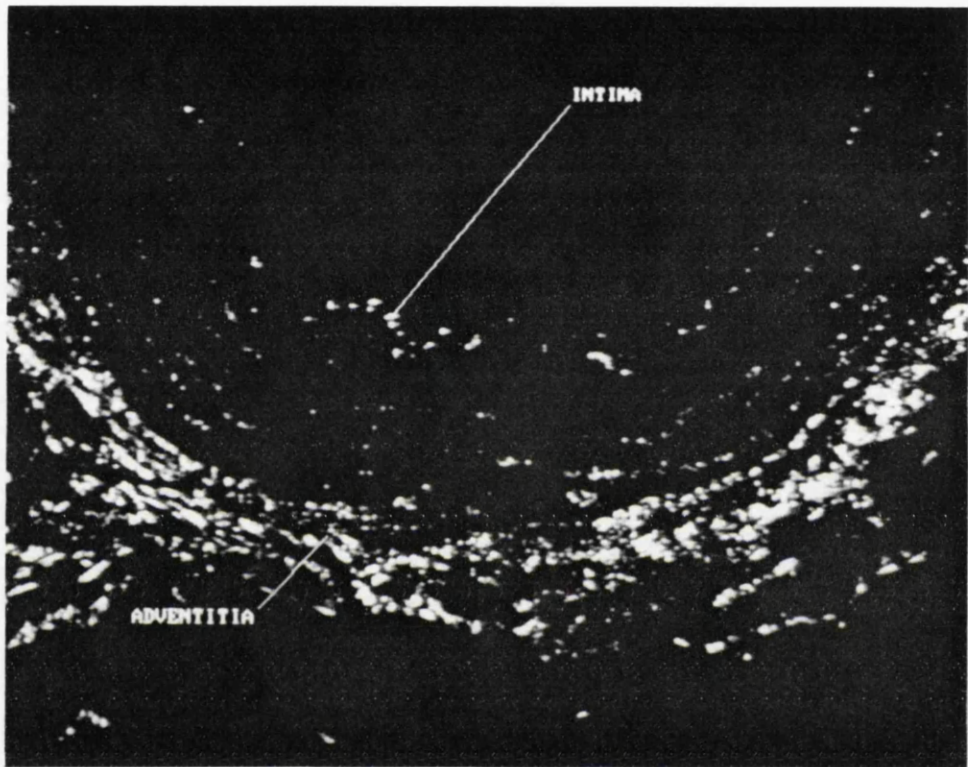


Figure 2.8 The collagen component of a vessel wall is readily observed (the white areas) when stained with Picrosirius Red and viewed between crossed polarisers.

Chapter 3

Laser Bonding In Vivo

3.1 INTRODUCTION

The creation of Argon laser tissue bonds in an animal model required the equipment specification shown in the diagram (Fig. 3.1). The Argon laser provides the beam to bond the tissue, with the output being switched on or off by the electro-mechanical shutter. The low power HeNe beam bypasses the shutter arrangement and is therefore always present. Mirrors are used to coaxially combine both beams which are coupled to the optical fibre by a focusing lens. The fibre transports the light and allows flexible positioning of the handpiece, which produces a small diameter, collimated output beam for lasing the vessel. This arrangement was augmented by two items of additional equipment, namely, a thermal camera to monitor vessel temperature during bonding and a micromanipulator (ie. a vernier clamp) to hold the laser handpiece, enabling accurately controlled movement during lasing. Each item is discussed in detail below:

3.1.1 Argon Laser

A Spectra Physics 2000 Argon ion laser was used, providing continuous wave (CW) output in the blue-green part of the spectrum, with variable power output to a maximum of 10 Watts. The Argon lasing process is only 0.1% efficient, with the result that large amounts of energy are required to produce moderate amounts of laser light. This necessitates a 3-phase electrical supply and the laser tube has to be water cooled to dissipate the large quantity of energy (heat) not converted to light. Argon gas within the tube is ionised by electrical discharge. The Argon ions become further excited by multiple electron collisions perpetuated by the intense electric field across the tube. This creates the population inversion necessary for the active medium to lase. The laser transitions are complex, but primary lines are 514.5nm and 488.0 nm. The reader is referred to other texts (5) for the fundamentals of laser action.

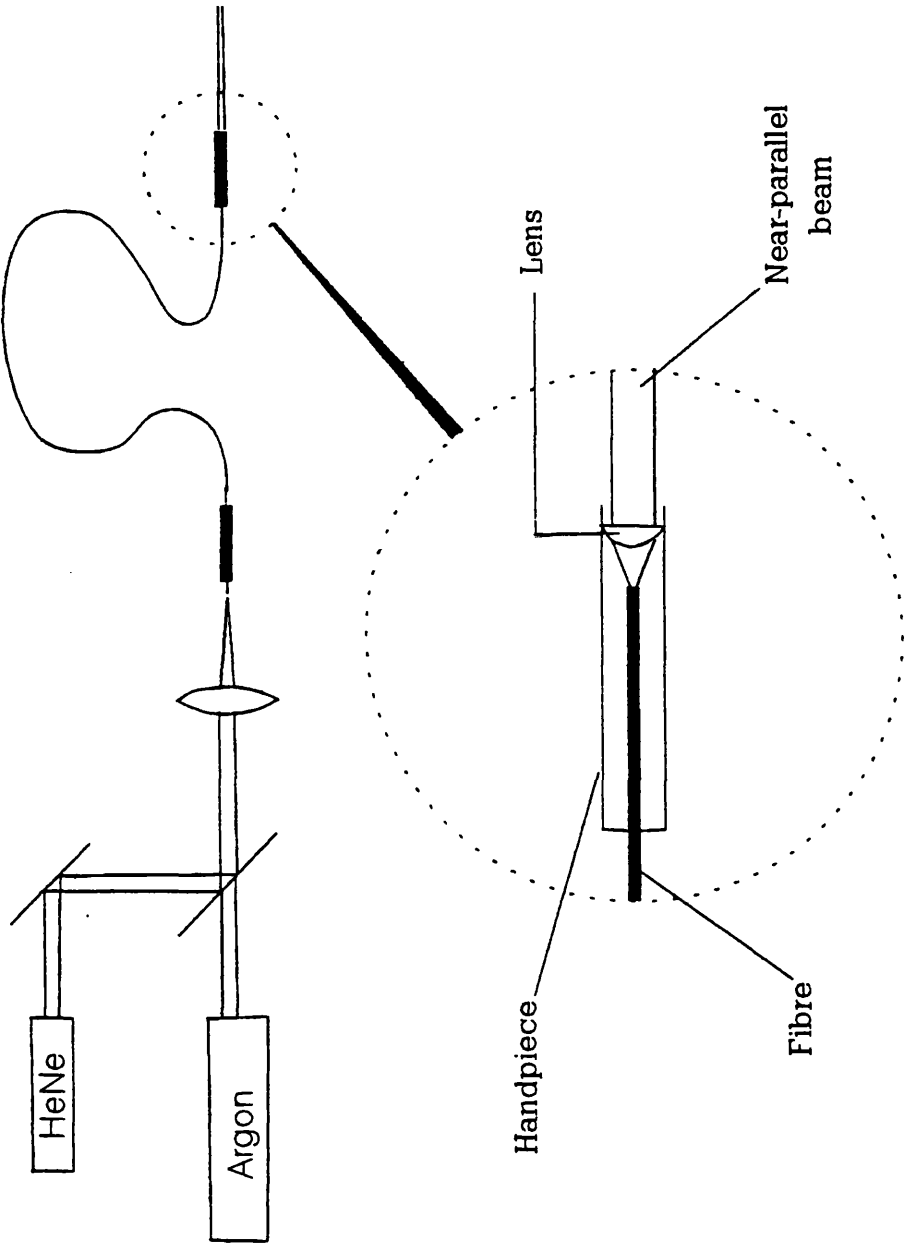


Figure 3.1 Equipment set-up required for laser bonding in an animal model.

3.1.2 Coupling Optics

A mirror and transparent glass plate combine the red HeNe (632.8nm) aiming beam coaxially with the Argon beam (Fig. 3.2). A single lens focuses both beams onto the cleaved face of a fibreoptic cable.

3.1.3 Fibreoptic Cable

The fibreoptic cable (100 μ m fibre - Optical Fibres 100/140B) consists of a fine glass core surrounded by plastic cladding, protected by an outer jacket strengthened by the integration of Kevlar strands. (Kevlar is a tough protective material used in bullet proof jackets). The sharp refractive index change at the core/cladding boundary confines light travelling within the glass core by total internal reflection. Light that exceeds the critical angle for total internal reflection is lost to the sheath. Light that catches the boundary at a more glancing angle is bent towards the core centre and can undergo multiple total internal reflections along its length with minimal losses and is thus 'conducted' along the length of the fibre. It is apparent that, for successful transmission, light entering the cable must fall within a cone narrow enough to satisfy the condition for total internal reflection - this is the acceptance angle of the fibre. Similarly, rays emerging from the other end of the fibre will also be contained within such a cone. Thus for effective coupling the focusing lens must have a long enough focal length for the outer edges of the focused beam to fall within the acceptance angle of the fibre. In addition it is also desirable that the diameter of the focused spot at the face of the fibre should be comparable to the diameter of the fibre core itself - a function of the quality of the focusing lens.

In our experiments, the laser power required for bonding was typically less than 100mW. With 10W of output available, there was no real need to optimise the coupling, since inefficiencies could be easily compensated by simply increasing the Argon laser output. However, with experience, it was found that the condition of the fibre faces critically affected the amount of light that could enter and leave the fibre, and therefore particular care was taken to cleave the faces cleanly before aligning the optics.

3.1.4 Delivery Handpiece

The handpiece essentially reverses the action of the coupling optics, converting the emerging cone of light from the fibre, into a parallel beam. A small diameter beam is required in order to localise its effects during the bonding of 2mm diameter vessels. Parallel output is desirable since this provides an irradiance that is invariant with the distance from the handpiece, giving a constant exposure at the surface of

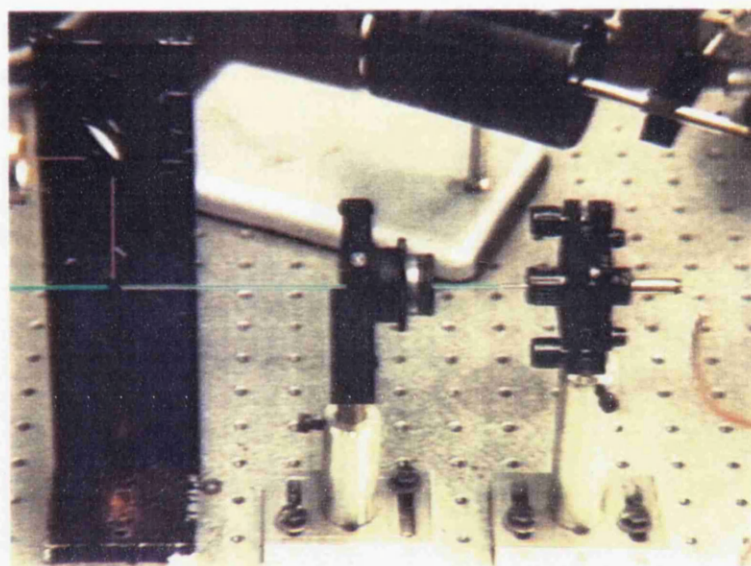


Figure 3.2 Coupling optics. The HeNe and Argon beams are combined and focused on the optical fibre (right of picture).

the vessel. A simple solution used a single hemispherical lens placed close to the fibre face to intercept the expanding cone of light while it was still of small diameter. The small radius of curvature (2mm) of the lens provided the short focal length required, but this produced non-linear effects which degraded the desired parallel output to a near-parallel beam of half angle divergence less than 2 degrees. A typical working distance from lens to vessel surface was between 5 and 10mm, the 2 degree divergence producing a nominal variation in power density of the order of 20% during our experiments.

3.1.5 Micromanipulator

Bonding a vessel with the laser involves tracking the beam along the length of the vessel joint. A delicate 2mm diameter vessel requires precision delivery of the laser energy. The micromanipulator (Newport Corp - Fig.3.3) forms an accurate and stable platform suitable for the purpose. A clamping arm grasps the delivery handpiece, which can be translated manually along 3 orthogonal axes. Movement is controlled with three rotary knobs, each of which can move the arm independently along an axis. A set of vernier scales permits accurate measurement of movement to within 0.1mm.

3.1.6 Camera

The thermal camera (Fig. 3.4) is an infra-red imaging device. A germanium lens focuses the infra-red scene onto a pyroelectric vidicon, which translates the thermal image to a raster scan suitable for viewing on a television monitor. The lens is transparent to radiation in the 8-14 μ m band, a range in which maximum radiant energy is emitted from objects at near ambient temperature. Under optimum conditions the camera is capable of resolving temperatures of as little as 0.2 deg.C. Spatial resolution can be better than 0.5mm. In our case the camera was used to monitor tissue temperature during lasing.

3.2 EXPERIMENTAL PROCEDURE

3.2.1 Introduction

In cardiac surgery, laser bonding would be directed towards anastomosis of vessels of the heart (eg. coronary artery bypass grafts) currently performed with suture techniques. In vivo work in humans was not possible at this early experimental stage, but a suitable alternative proved to be in vivo anastomosis of the carotid vessels in the neck of the rabbit, whose size and structure are similar to those of coronary arteries in humans. The rest of this chapter describes in vivo anastomosis

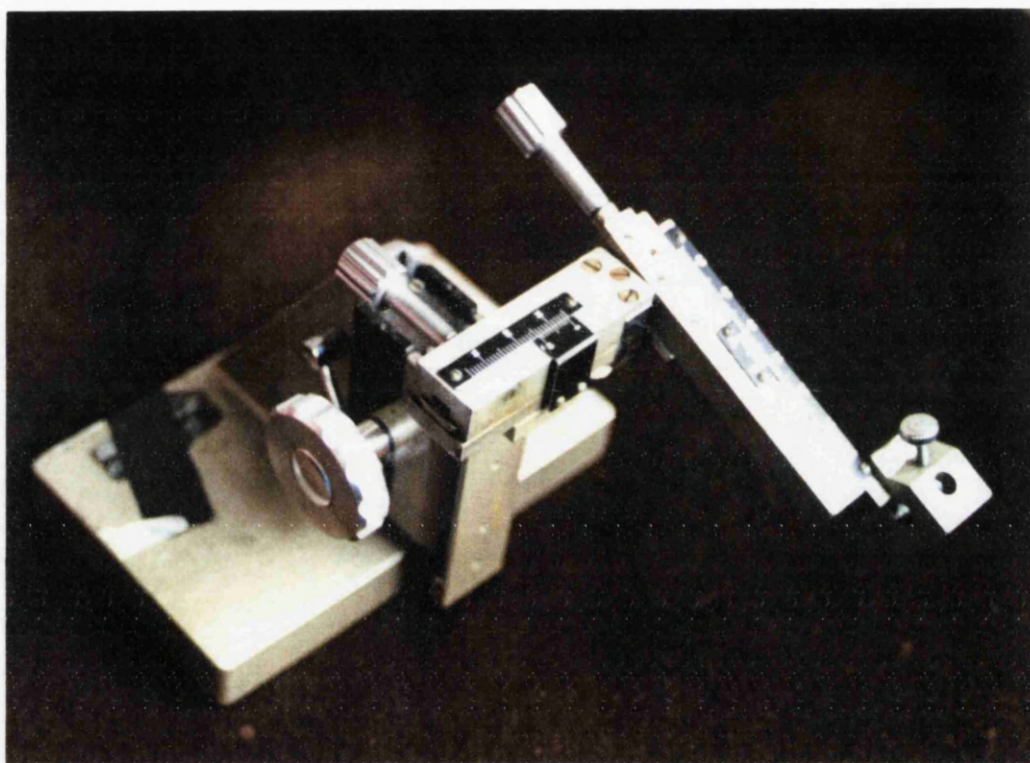


Figure 3.3 The micromanipulator - used for accurate movement of the laser handpiece during lasing.

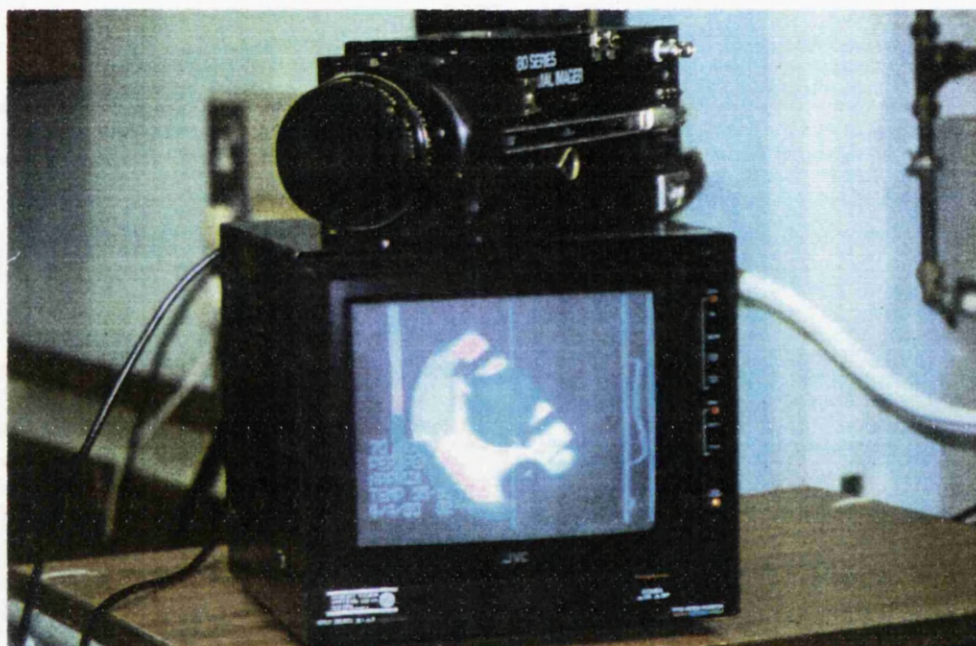


Figure 3.4 Thermal camera and monitor, with a thermal image on the screen.

of carotid arterial vessels in an animal model followed by a discussion of the merits and problems of the technique.

3.2.2 Method

A New Zealand White Rabbit was anaesthetised (halothane, nitrous oxide and oxygen) supine on the operating table. A vertical midline incision was made along the anterior length of the neck, and opened to expose the left and right carotid arteries (typically 1-2mm diameter with a wall thickness of approximately 0.15mm). Blood viscosity was reduced by an injection of 500 units of heparin to prevent clotting. The left carotid artery was clamped at 2 points approximately 2cm apart to isolate a section of the vessel. This action does not cause the animal distress since a plentiful blood supply can reach the brain via the other carotid artery. A 6mm longitudinal incision was made along the isolated section of the vessel using microvascular scissors. The separated vessel edges fell together naturally to form a butt joint along which the laser beam could be run to form a bond. In this experiment no stay sutures were used. Chromophore (a solution of 1% fuchsin ethanol) was applied along the length of the vessel edges using a fine glass capillary tube. The power of the Argon beam at the handpiece was set to the desired output (approximately 100mW) with reference to a Scientech 362 laser power meter. With a 2mm diameter spot, average power density at the vessel surface was approximately 3Wcm^{-2} . The Argon beam was switched off to allow the HeNe aiming spot to be placed over the incision and the micromanipulator manoeuvred so as to align one of its translational axes parallel with the bond line. As a result, the beam could be tracked along the bond line by the turning of a single micromanipulator knob, giving smooth and accurate delivery of the lasing beam. An attempt was also made to align other axes so that the handpiece remained equidistant from the vessel over its length.

Alignment of the thermal camera involved placing a small piece of card (1cm x 0.5cm) with a thin black line down its centre, over the vessel with the line lying on top of the incision. The Argon beam was switched on and tracked up and down the artery in a manner similar to that used for bonding the vessel. Heated by the beam, the black line presented a moving localised temperature spot to the camera, which was used to set up the orientation and focus of the camera.

With the Argon beam absent, the card was removed and the HeNe spot placed at one end of the incision. The working distance (ie. the distance between the base of the handpiece and the vessel surface) was set to between 5 and 10mm. The Argon beam was switched on and the spot tracked slowly (0.2 mms^{-1})

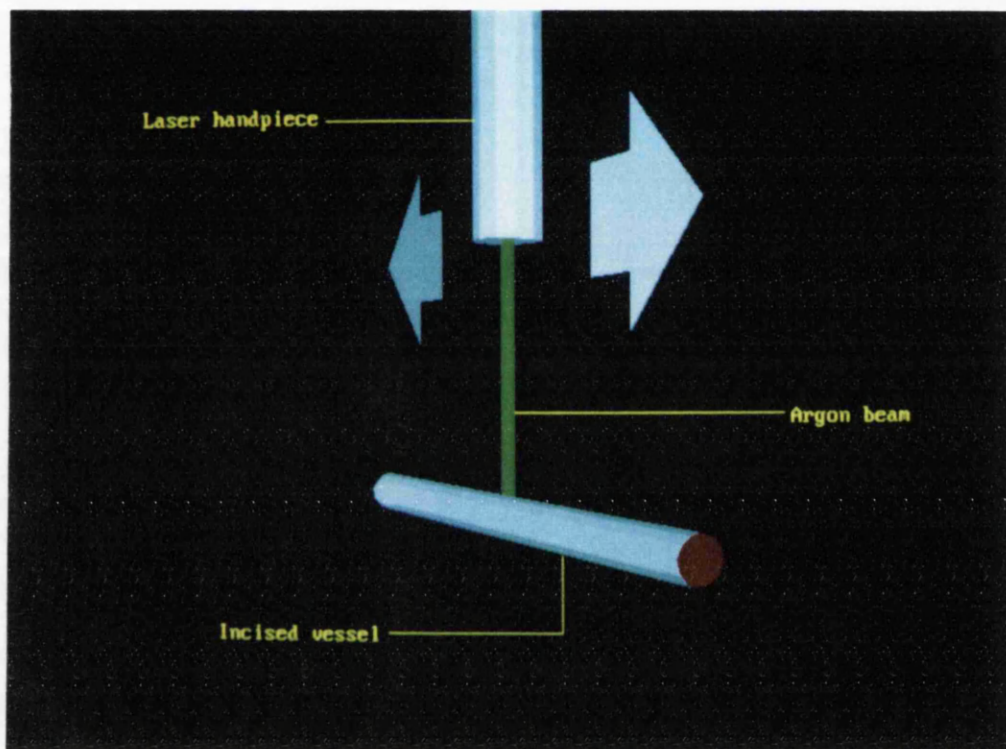


Figure 3.5 Argon laser bonding requires steady tracking of the beam, along the length of the incision.

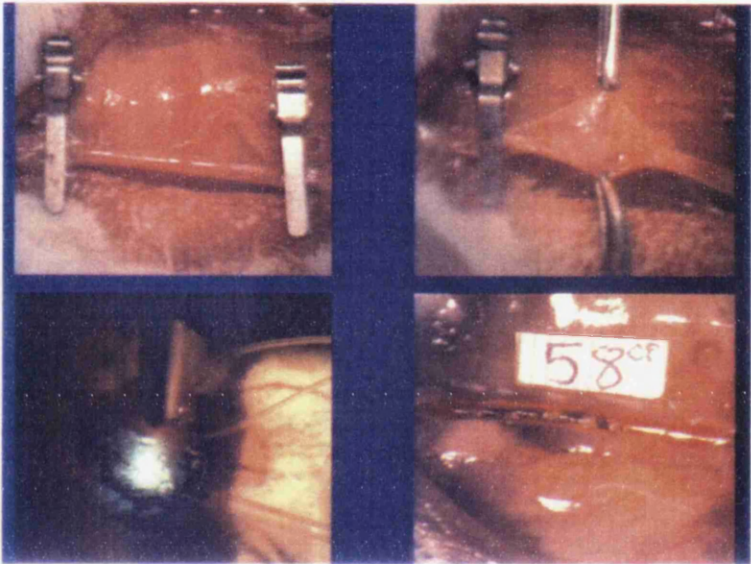


Figure 3.6 A series of stills showing an isolated vessel (top left), with longitudinal incision (top right), lased (bottom left) and successful anastomosis (bottom right).

up and down the length of the incision (Figs 3.5 & 3.6) until slight discolouration of the bond line was visible. Tracking speed affected the bonding temperature observed through the camera and hence it was possible to crudely control the bonding temperature by altering the speed at which the beam was moved. A scan line analyser interfaced to the thermal imager permitted accurate measurement of the temperatures recorded by the camera. The infra-red images captured by the camera were recorded on video tape for subsequent analysis.

After lasing, the vessel clamps were removed and the bonded joint examined for leaks. If leaking blood was visible, the clamps were re-applied and the area treated again with the laser in an attempt to stop the leak. In the majority of cases this sealed the vessel. Those cases in which the leak persisted were deemed a technical failure and the failed anastomosis excised, the exposed ends of the vessel in vivo being closed with sutures.

Following removal of the clamps after successful anastomosis (no leaks), the position of the bond was marked by attaching a small (5mm) clip to neighbouring tissue to aid identification of the bond area during radiography and at post mortem. The experimental procedure was repeated on the right carotid artery to provide 2 laser assisted vascular anastomoses per rabbit - one on the left, one on the right. The neck of the rabbit was sutured back together and the revived animal returned to its cage for observation.

Examination of the vessels was performed at post mortem. Providing the animals did not die first, the rabbits were electively sacrificed at between 1 and 14 days of the post operative period. A small proportion were sacrificed at 3 or 4 months to assess longer term survival.

3.2.3 Post Mortem

Immediately following death or elective sacrifice, a vertical midline incision along the anterior length of the neck was made to expose the anastomosed carotid vessels. Location of the position of each anastomosis was aided by locating the metal clip placed next to the vessel for the purpose. Vessels were examined by low power stereo-microscopy. Each artery was cannulated 1cm proximal to the anastomosis and white contrast medium injected. Those bonds that had developed a leak subsequent to the operation were evident by the presence of white contrast medium spilling out of the vessel. For the anastomoses that remained in tact, radiography revealed the presence of a blocked or patent vessel (Fig 3.7).

The vessels were excised, cut into lengths of approximately 3mm and fixed in glutaraldehyde. The fixed tissue was processed, embedded in paraffin wax and cut into 3 μ m thick sections. The sections were stained with haematoxylin/eosin

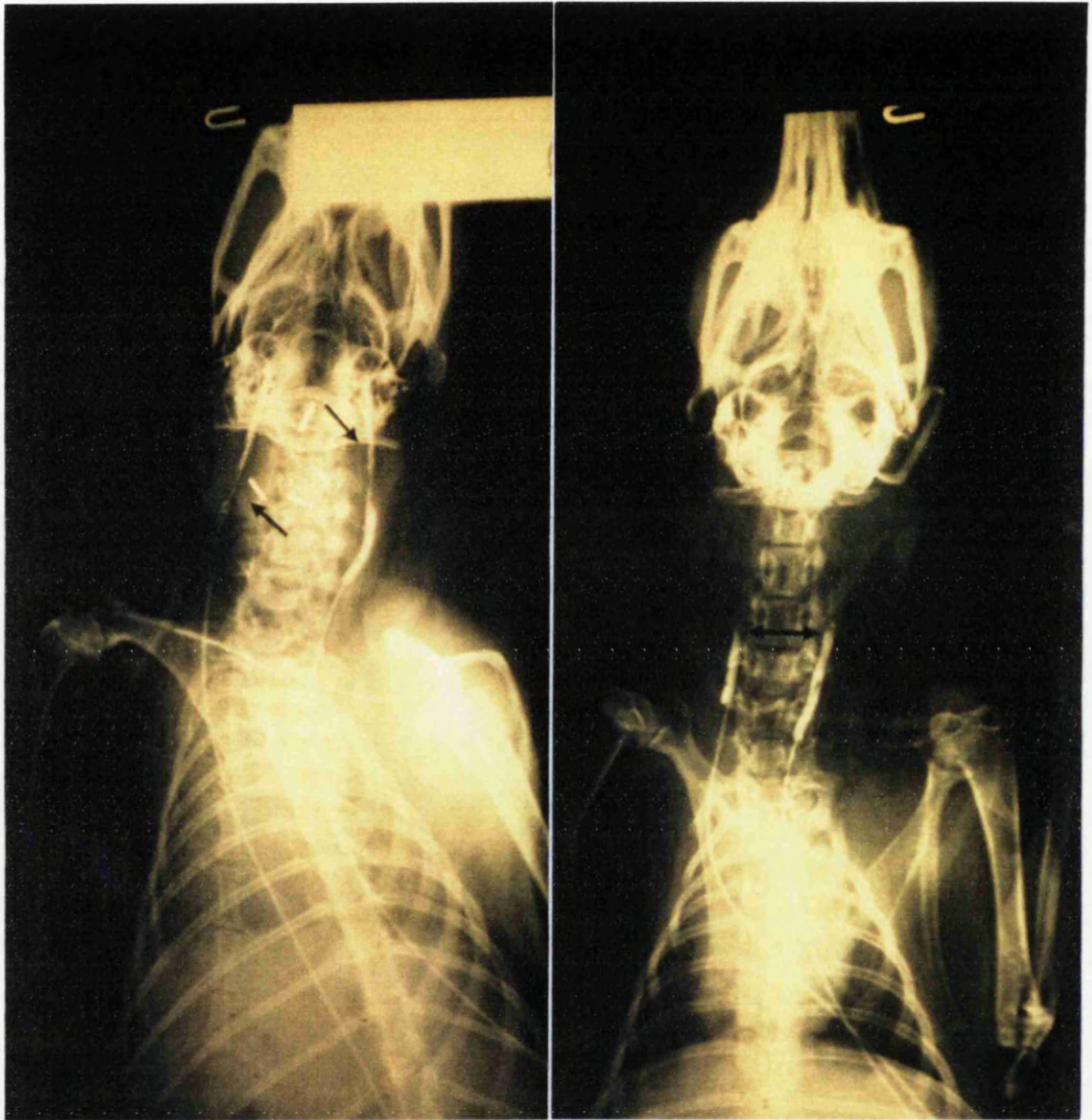


Figure 3.7 Arrows indicate the area of anastomosis on the two carotid vessels. Thrombosis is visible on the image on the right by lack of flow distal to these sites.

(nuclear and cytoplasmic stain) and Millers elastic (elastin stain) counterstained with Martius Scarlet Blue (muscle and collagen stain) for histological evaluation.

3.2.4 Variations in Technique

The preceding description describes the basic techniques on which all the experiments were based. However, small variations in bonding technique were employed throughout the series in response to the findings of results as they arose. The group variations in experiments are listed below:

Group 1

Bilateral LAVA were performed on 6 animals, and laser output was set to 100mW.

Group 2

Bilateral LAVA were performed on 25 animals, and laser output was set to 80mW. At the conclusion of each successful anastomosis, cyanoacrylate gel (ie. superglue) was smeared around the vessel over the length of the anastomosis, so as to encase the vessel in an attempt to reinforce the bond.

Group 3

This formed a control group in which 10 vessels were neither incised nor lased, but simply smeared with the cyanoacrylate gel.

3.2.5 Pressure Testing

At post mortem, a small proportion of the anastomosed vessels were excised and set aside to test their strength by subjecting the 2cm long section to a steadily increasing internal pressure until the vessel ruptured. The equipment is shown in figure 3.8.

A purse string suture was used to bind the excised vessel tightly to the cannula - an effective water-tight seal. The other end of the vessel was sealed shut with several liga clips. The cannula was connected to a saline-filled syringe via a T-piece where a pressure transducer measured fluid pressure, its output being recorded on an X-Y plotter. Care was taken to remove all air from the system. A linear motor was used to slowly advance the plunger of the syringe, the speed being set to cause a steady increase in pressure of approximately 10mmHg per second. The X-Y plotter recording the pressure increase, ideally reveals a sharp visible pressure drop when the anastomosis bursts.

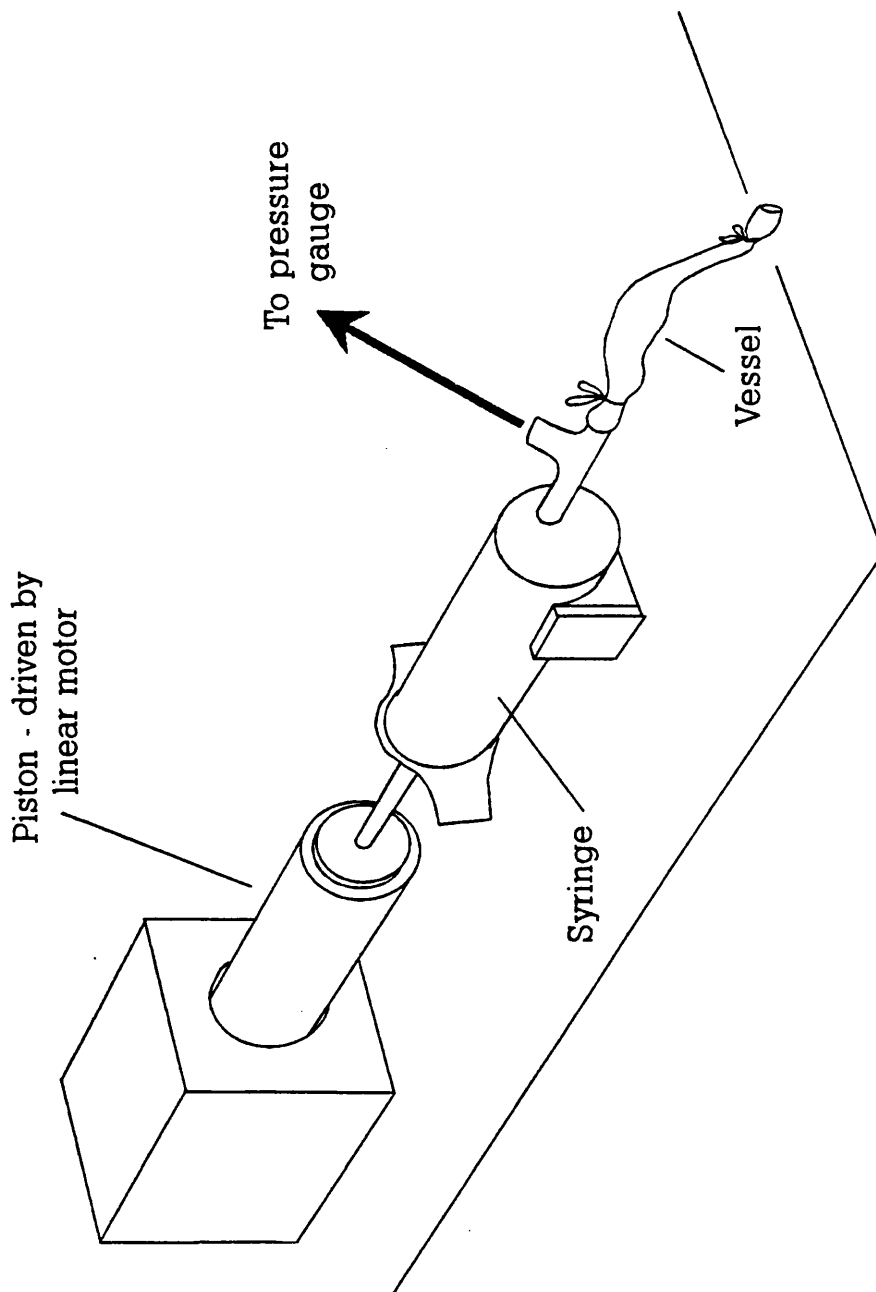


Figure 3.8 Equipment for pressure testing anastomosed vessels.

3.3 RESULTS

3.3.1 Group 1

Bilateral LAVA were performed on 6 animals with laser output set to 100mW. Continuous lasing times varied from 2 to 16 minutes, with a mean of 6 minutes. Typical bonding temperatures averaged 60 - 70 deg.C. as observed by the camera. None of the animals survived the initial 24 hour period. Two died from bilateral thrombosis, and the other 4 from unilateral leaks. All of the non-leaking vessels were patent. Histologically, these suffered from substantial medial necrosis involving of the order of 50% of vessel circumference. The adventitia showed mild acute inflammation with several vessels containing thrombi (Figs. 3.9 & 3.10).

3.3.2 Group 2

25 animals received bilateral LAVA, with laser output set to 80mW. Continuous lasing times varied between 1 and 4 minutes. Typical bonding temperatures averaged less than 50 deg.C. as observed by the camera. In this group, the bonded vessel was reinforced with a superglue shell after lasing in an attempt to reduce the number of leaks. Of 50 anastomoses (bilateral x25), 4 were technical failures, but all 4 rabbits survived the operation since the other carotid artery in each case was anastomosed satisfactorily. Of the 46 anastomoses remaining, 2 rabbits died within 24 hours as a result of unilateral leaks, leaving 42 anastomoses available for examination after the first day. 37 of these vessels were examined at elective sacrifice between 4 and 14 days post operatively - 12 were patent and 25 thrombosed. 5 LAVA were left for long term evaluation, 2 of which were examined at 3 months - 1 vessel was patent, the other thrombosed.

Under histological examination, the vessels of group 2 had a greater degree of medial necrosis than group 1, with a marked increase in adventitial inflammation. These would be important contributing factors to the degree of thrombosis encountered. A proportion of vessels were made available for destructive pressure testing. Catastrophic bursting pressures varied widely, ranging from 100mmHg up to 1000mmHg.

3.3.3 Group 3

5 animals formed the control group, in which cyanoacrylate glue was smeared over the vessel (bilateral), but no laser was used and no incision made. Explanted between 4 and 14 days, none of the 10 vessels showed evidence of thrombosis.



Figure 3.9 Histology - vessel cross-section. This vessel has thrombosed following anastomosis. The swollen region on the left is a hyperplastic response to the laser bonding in that area.

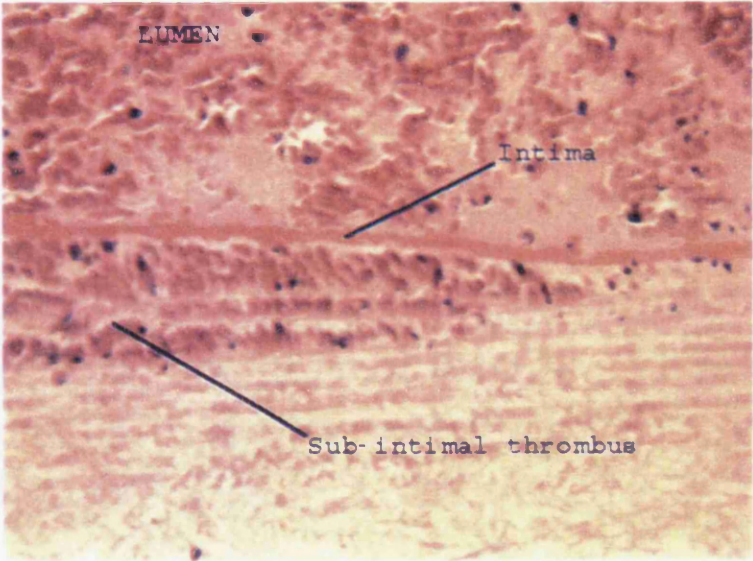


Figure 3.10 At higher magnification the section shows the presence of sub-intimal thrombus.

3.4 DISCUSSION

Most laser tissue bonding to date has been performed with the CO₂ laser which has proved quite successful when used with stay sutures (106,107,108). Other lasers have been used, the strongest proponent of the Argon laser being White et al. in the USA (50,79). Their experimental protocol includes cooling the vessel with drops of saline while the vessel is being lased, and they maintain that this yields results superior to CO₂ bonds. In particular, the problem of pseudo-aneurysms associated with CO₂ bonds does not appear to occur with those vessels bonded under the conditions reported by White (73). Additionally, while bonding in the presence of a thermal camera, it is reported that bonds were created at temperatures below 50deg.C. (46,68) - a value well below the denaturation temperature of the tissue. This has important implications with respect to the currently accepted mechanism for laser bonding (Chapter 1) which points to collagen denaturation as being responsible. Denaturation is known to occur with the relatively high temperatures produced by CO₂ laser bonding (greater than 100deg.C. (36,38)), and thus it has been suggested that a different mechanism may be active with the low temperatures encountered by White.

Furnished with similar equipment to White, our group has been able to confirm his findings. Successful bonds were created at recorded temperatures below 50deg.C., even although significant differences exist between the respective experiments. White employed greater power density, applied for a longer period (energy fluence approximately 1300Jcm⁻² (47,58)). The vessel was simultaneously cooled with drops of saline. In contrast, the use of chromophore in our experiments permitted a reduction in incident laser energy, which when combined with reduced lasing times resulted in a mean energy fluence of 70Jcm⁻². White used stay sutures to pull the vessel faces together, whereas we simply left the incised vessel faces to fall into natural apposition. Comparison of results reveals that a higher percentage of satisfactory bonds without leaks was obtained by White, despite our own confidence in our experimental method and execution. A case for technical incompetence could be argued had we failed to produce bonds in the first place, but in nearly all cases, leak-free bonds were successfully created. Rather, failure of the bonds occurred in the ensuing 24 hour period without glue, or by thrombosis over a longer period if glue was used. It seems likely that the stay sutures used by other groups would confer greater strength on the anastomosis while reducing the stress on the laser bond itself, resulting in improved long term survival. This can be envisaged as creation of a primary bond with the laser, subsequently reinforced by other measures - sutures in the case of White and superglue in ours. The use of superglue produced a dramatic fall in the number of animals dying from ruptured

vessels, but introduced a marked increase in death through thrombosis. Since the presence of glue on the non-incised vessels produced no thrombosis, it may indicate that the aggravated thrombogenic reaction was the result of contact between the blood components and the glue, possibly mediated by a pin-point leak confined within the superglue shell.

Conflict exists between the histological results and the bonding temperatures indicated by the thermal camera. The widespread medial necrosis apparent histologically is not consistent with the low temperatures displayed by the imaging device. Such findings throw doubt on the temperature recorded by the camera during the bonding process. A possible explanation contends that the small diameter of the temperature spot induced by the laser exceeds the resolution of the camera. This would be expected to cause the imager to underestimate the true temperature value. Resolution tests under conditions similar to those while bonding, would yield important information regarding the limitations of the camera and may provide a suitable correction factor. This is the subject of another investigation. Application of mathematical techniques to model the energy exchange and heat flow processes within the lased tissue would provide a theoretical temperature map that could be correlated with that seen by the camera. Consistent agreement between the resolution adjusted camera temperatures and those predicted by the mathematical model would provide a sound basis on which to assess temperature related effects.

Further inaccuracies may be caused by the presence of thin films of water on the vessel surface, since water is highly absorptive in the infra-red region (8-12 μ m) in which the camera is sensitive. Again, this would cause it to under-read.

Previous work in our department (unpublished), in which bonding was carried out with a laser output of 300mW and a similar experimental protocol (without glue), produced vessels with increased adventitial inflammation and more medial necrosis than those examined here using 100mW. It is clear that the lower laser energy resulted in reduced vessel damage. However, vessels lased at 300mW showed reduced thrombosis as compared to vessels in this experiment, which is the converse of what would be expected.

As a general observation, damage to the vessel wall was widespread, encompassing the whole circumference. Such widespread destruction could be expected to greatly inhibit the healing processes, due to lack of viable tissue components within the damaged area capable of acting as a nucleus for healing. This widespread effect is probably the result of a large lasing spot, encompassing most of the vessel and causing tissue disruption beyond the area of the bond line.

Shrinking of the spot size to localise its effects to the area immediately surrounding the bond line may prove advantageous.

Bonding at temperatures below denaturation if possible, has advantages: the proportion of viable tissue would greatly increase and improved healing would probably result. Of course, this has essentially been the approach of White, by cooling the vessel during lasing. Alternative strategies could involve the blowing of cold air over the bonding area or using a pulsed beam to allow a short period of cooling between pulses.

The pressure testing system proved less than successful. Rarely was a marked loss in pressure recorded as the vessel ruptured. Too often, 'rupture' took the form of a pin-point leak, which at higher pressures sprayed a fine jet of saline several feet. The compliance of the vessel wall was able to compensate for the small water volume loss caused by the leak with resultant minimal change in recorded pressure. In addition, since saline was being pumped into the vessel at a rather greater rate than was being lost by the leak, intravascular pressure still steadily increased but at a slightly reduced rate. The combination of the two meant that the change in gradient of the pressure trace was so small as to be indiscernible. In one or two cases however, the above did not occur, and the vessel burst uniformly and catastrophically at high pressure, marked clearly by a sudden loss of recorded pressure on the X-Y plotter. Such cases revealed bursting pressures of up to 1000mmHg.

3.5 CONCLUSION

In conclusion, we have successfully mastered the techniques of laser bonding, acquiring invaluable first hand knowledge of the problems and limitations of the procedures involved. Successful bonds were created at apparent temperatures below the denaturation temperature of the tissue. Unfortunately, the presence of a leak free bond immediately after lasing was no guarantee that it would stay that way over the next 24 hours. Without glue to reinforce the bond, many vessels ruptured several hours after the operation. However, a small proportion of vessels maintained structural integrity to provide patent vessels in the long term with excellent healing characteristics. Unfortunately, there was no visually apparent difference following lasing, between those vessels that would last and those that would not. It thus becomes clear that although successful laser bonds are feasible, we were not in a position to be able to produce such bonds consistently. The application of secondary measures - whether it be sutures or glue

- to reinforce the bond, significantly improves survival, but in our case the glue produced a strongly thrombogenic reaction. Our lack of success in the creation of robust patent bonds gives little hope for general application of the technique elsewhere. Sutured anastomoses may be time consuming, but they do create bonds that work consistently. Laser bonds will have to be at least their equal before they can be proposed as a viable alternative.

Chapter 4

Dry Bonds In Vitro

4.1 INTRODUCTION

Although much of the bonding work to date has been performed with the CO₂ laser, other lasers have been used (Nd:YAG, Argon) to produce similar results: improved healing; reduced foreign body response; superior long term patency etc. (50,76,108). This similarity suggests a common bonding mechanism. Experimental observations have led to the proposition that thermal coagulation of the vessel proteins is the primary mechanism, and that this forms a glue which binds the tissue faces (61). However, the Argon laser can apparently produce bonds at temperatures well below that required for denaturation (40), indicating a different mechanism. White has suggested that the mechanism may be photochemical (79). However, in our experience (Chapter 3), temperatures measured by thermal camera cannot be considered accurate since they appear to conflict with histological evidence. Thus it is further uncertain whether bonding is primarily thermal or photochemical in nature. The exact mechanism is important, since a photochemical bond would be specifically light dependent, being affected by properties such as wavelength, coherence and intensity. In contrast, a bond produced by a thermal stimulus would not necessarily require the use of a laser, which simply acts as a convenient source of energy to heat the tissue.

The photochemical/thermal issue has not been resolved, but the majority opinion is towards a thermal effect for several reasons. Firstly, there is little direct evidence to suggest that bonding is photochemical. Should such an effect exist, it would be expected to be the result of resonances between particular laser wavelengths and protein molecules. However, bonding occurs over a wide wavelength range spanning from Argon (488nm) in the visible spectrum to CO₂ (10600nm) in the far infra-red. Such a wide bandwidth resonance would be an unusual phenomenon. Secondly, thermal bonding was attributed to the work of Sigel et al. in 1963 (26) where a high frequency electric current was used to fuse apposed tissue. Their description of the resultant bond and subsequent healing is strongly reminiscent of bonds created by laser.

A reasonable starting assumption is that laser bonding is a thermal effect. This implies that viable tissue bonds could be created without the use of a laser. Experimental verification of this was attempted using pieces of sheep aorta as follows:

i) Two separate pieces of aortic tissue were held together using a scissor clamp and immersed in constant temperature water or saline for several minutes over temperatures ranging from 20 to 100 deg.C. No bonds resulted.

ii) The experiment was repeated at higher temperatures by replacing the water with vegetable cooking oil. At temperatures in the region of 120 deg.C. and above, tissue bonds did seem to form. The tissue sizzled vigorously.

iii) At temperatures of about 120 deg.C. and above, individual aortic slices appeared to bond to most things eg. metal plates, glass ..., all accompanied by sounds of sizzling. Furthermore, if the tissue was removed from the surface, and the previously bonded face reapplied to the hot surface, bonding did not occur, and neither was sizzling heard.

iv) It was noticed that slices of aorta left on a glass plate at room temperature, stuck to the plate as the tissue dried out. Application of water rehydrated the sample, and with time it floated off relatively easily.

These preliminary observations indicate that both temperature and dehydration are factors contributing to a form of bonding. Hence a more detailed experiment was devised to create a series of in vitro bonds (without a laser) over a range of constant temperatures in both wet and dry (ie. dehydrating) conditions. The quality of the resultant bonds was assessed by destructive testing.

4.2 EXPERIMENTAL DESIGN: Principal Concerns

4.2.1 Tissue Preparation

The difficulty of handling small rabbit carotid vessels in vitro meant that they were unsuitable for this experiment. A ready supply of sheep aorta was available from the abattoir, and this was felt to be a suitable analogue of the rabbit carotid and human coronary arteries for the terms of this experiment.

4.2.2 Tissue Bonding

Bonding at constant temperature presents problems. Accurate knowledge of bond temperature is required, but the temperature distribution or apposition of tissue must not be disturbed by the insertion of probes or sensors. Remote temperature sensing can be employed, but as has been seen, the resulting temperature data is difficult to interpret. Such difficulties can be overcome by placing the tissue in thermal equilibrium with an object of large thermal mass of known temperature. Since a stable low temperature oven was not available, suitable equipment had to be designed and built in the laboratory.

4.2.3 Tissue Bond Strength

Breaking strength can be used as an indicator of the quality of a bond, thus permitting comparison between samples. Strength testing involves attaching the sample to a force balance. The sample is progressively stressed, and the force at which the bond breaks is noted.

4.3 EQUIPMENT

4.3.1 Bonding

Good tissue bonding requires adequate apposition, a condition most easily met by overlapping slices to create an overlap bond. The overlapped tissue was gently held between the jaws of a temperature stabilised clamp (approximator). Approximator temperature was readily monitored by thermocouple, and the bond temperature assumed to be the same by conduction. The approximator was constructed from perspex and figure 4.1 shows its dimensions.

Although better designs can be envisaged, this particular device was cheap, simple to make, reliable and available. It was heated to a steady temperature by the infra-red radiation from a 120W spotlight. The distance between the radiative source and the approximator could be varied to alter the equilibrium temperature. A thermocouple attached to the rear of the approximator close to the area which held the tissue recorded the clamp temperature, also assumed to be the temperature of the tissue. Direct radiative heating of tissue was prevented by the use of radiation shields. A passive reflector was placed a short distance behind the approximating jig to reflect excess radiation back onto the jig thus providing a more even energy distribution.

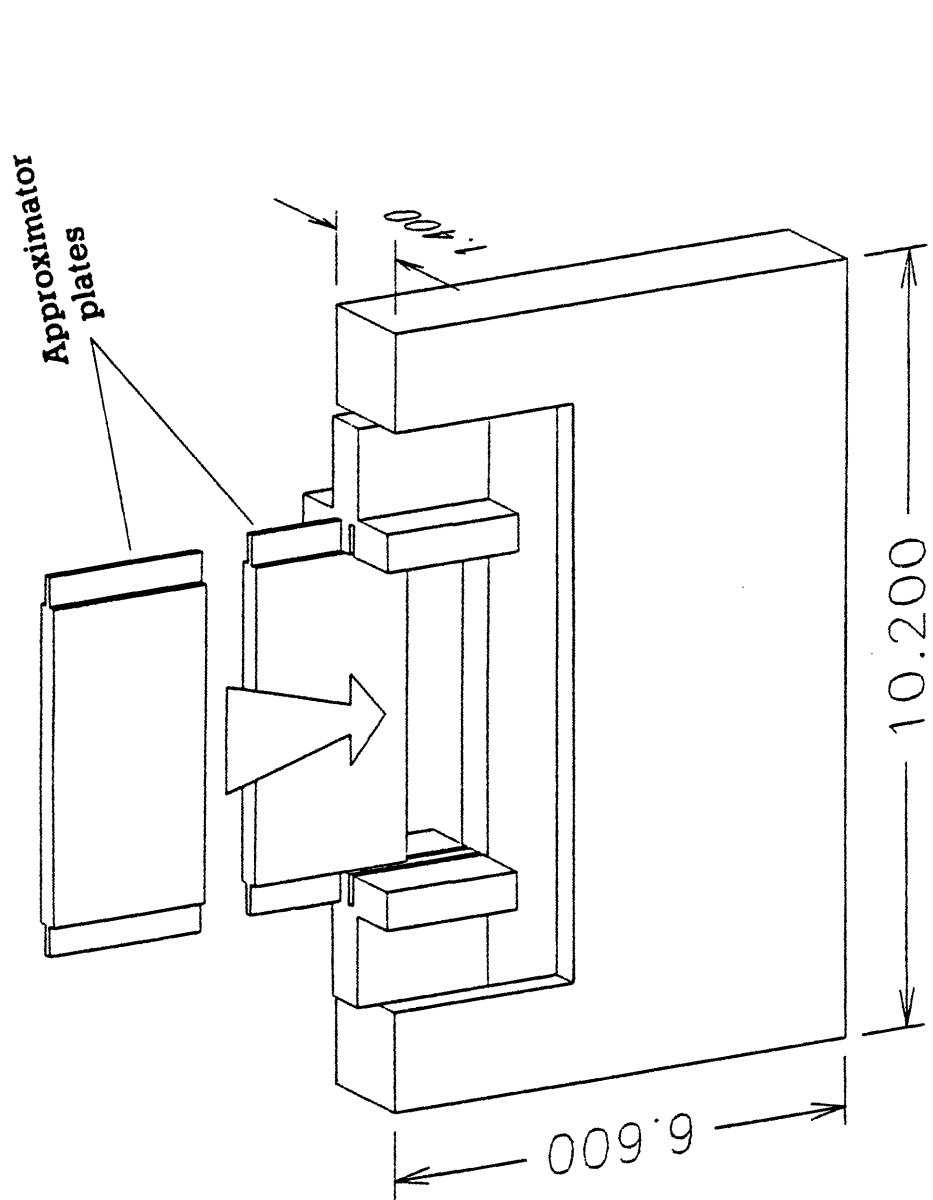


Figure 4.1 Construction of perspex approximator. Dimensions in centimetres.

4.3.2 Temperature Uniformity of Approximator

The following describes two short experiments designed to assess the suitability of the clamp as a temperature stabilised approximating device, by investigating the volume distribution of temperature when the clamp was heated. The experiments consist of evaluating the temperature gradient across the thickness of the approximator, and also the variation in temperature across the approximator face in the region where tissue would be held.

4.4 TEMPERATURE GRADIENTS ACROSS THE THICKNESS OF THE APPROXIMATOR

This experiment establishes the presence of minimal temperature gradients across the thickness of the approximator in the region where the tissue is held.

4.4.1 Method

The experiment was arranged as shown in figure 4.2. The conductive housing of the thermocouple was shielded from direct radiative effects with tin-foil. The face of the thermocouple was held in contact with the front approximator plate by a thin elastic band and the temperature recorded. The 120W spotlight was switched on and the temperature and time recorded at frequent intervals. After an hour the spotlight was switched off and the approximator left to cool to room temperature.

The thermocouple was removed and held in a similar position on the rear face of the approximator. The lamp was switched on, and again temperature was recorded as a function of time for a one hour period. After the clamp had cooled, the whole experiment was repeated to get a measure of reproducibility.

Data was plotted graphically, showing recorded temperature rise of the approximator as a function of time.

4.4.2 Results

Figure 4.3 plots the temperature rise of the approximator as a function of time. The estimated error of the thermocouple reading was 0.2 deg.C, with timing accurate to 0.1 minutes. All graphs are very similar, with temperatures differing little over the 1 hour period. The mean temperature rise of all 4 experiments at one hour equalled 24.5 deg.C with a standard deviation of 0.7 deg.C. Clamp temperature was the same as room temperature at the start of each experiment, varying by up to 2 deg.C. This did not affect the eventual temperature rise of the clamp which appeared to be relatively independent of room temperature.

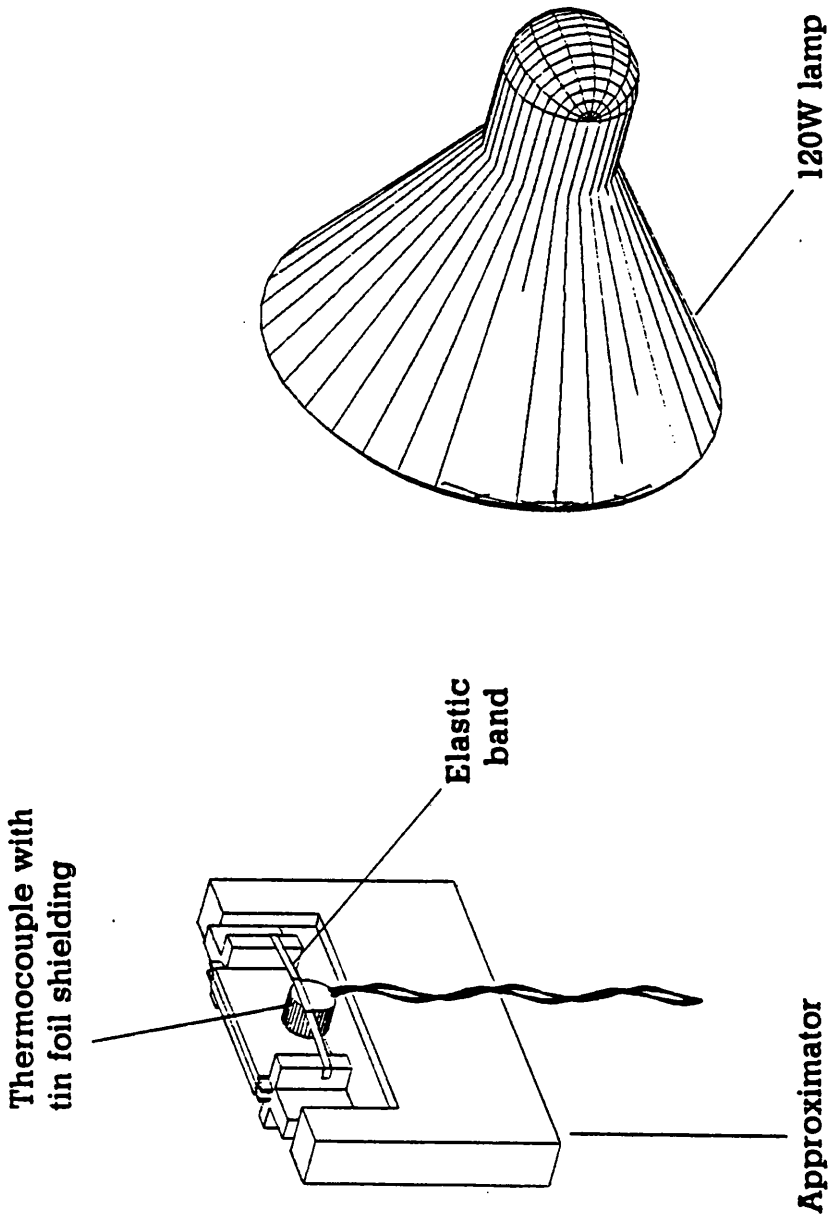


Figure 4.2 The approximator is irradiated by the 120W lamp. Temperature is recorded by the shielded thermocouple.

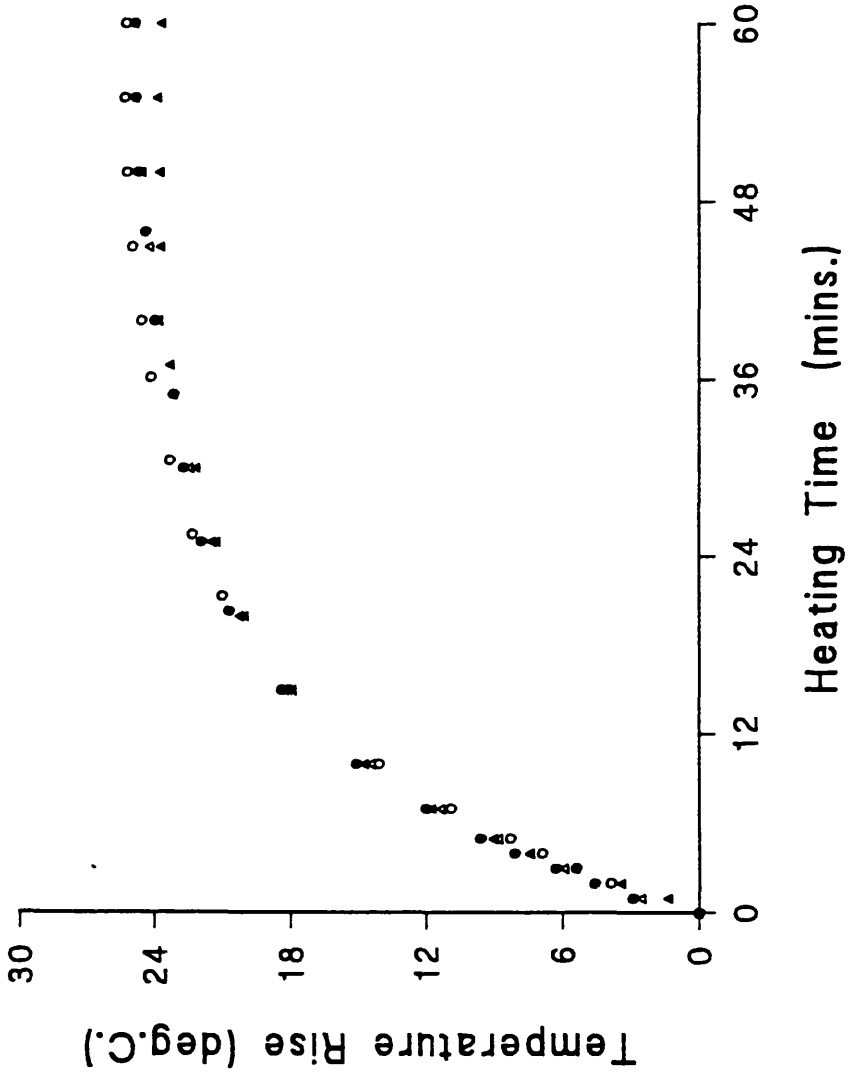


Figure 4.3 Approximator temperature as a function of heating time. Unfilled symbols show temperature on the lamp side of the approximator, with filled symbols showing the temperature on the opposite face. Circles - 1st run, Triangles - 2nd run.

4.4.3 Discussion

Insignificant temperature gradients were found across the thickness of the clamp during heating, even though the experiment was performed without a passive rear heat reflector. Inclusion of this item would further improve temperature uniformity. The exponential nature of the curves is reminiscent of Newtonian cooling.

4.5 TEMPERATURE GRADIENTS ACROSS THE FACE OF THE APPROXIMATOR

This experiment establishes the presence of minimal temperature gradients across the face of the approximator in the region surrounding the bonding area.

4.5.1 Method

The experiment was set up as shown in figure 4.4, arranged to simulate tissue bonding at 55 deg.C., with radiation shields closed and reference thermocouple attached to the rear approximator plate. No tissue was used. Pin-head thermocouples were placed where the overlapping tissue would have been, and the approximator plates were lowered to within 1mm of the thermocouple heads. Three other pin-head thermocouples were taped to the approximator below the others as shown, providing a thermocouple array to monitor temperature. The 120W spotlight was switched on to start heating, and the temperature of all thermocouples recorded after approximately 55 minutes.

4.5.2 Results

The temperature data is tabulated in table 4.1. Apart from the hotspot at the approximator centre (thermocouple 4 - exceeds the reference thermocouple temperature by 4.2 deg.C.) temperatures across the approximator face differed by less than 3 deg.C. and the temperatures at the tissue positions closely matched that of the reference thermocouple to within 1 deg.C.

4.5.3 Discussion

The results of the above experiments show that temperature is acceptably uniform in the volume of the approximator surrounding the tissue bonding area. From these results it is reasonable to quote tissue bonding temperatures as being within ± 3 deg.C. of that recorded by the reference thermocouple.

The following section describes application of the above equipment to the bonding of tissue slices without a laser.

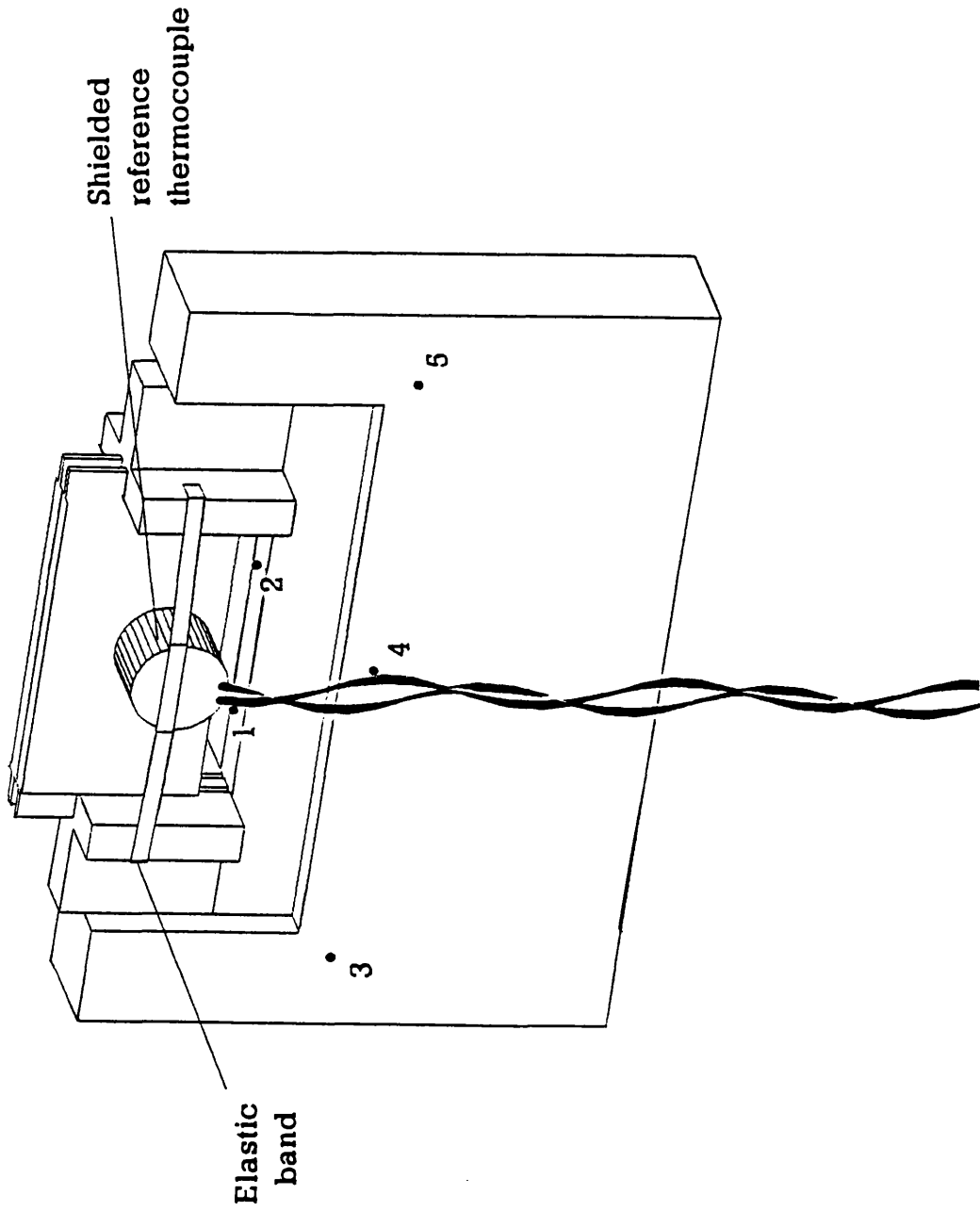


Figure 4.4 Thermocouple array used to assess temperature gradients across the approximator face.

COMMENTS	REFERENCE THERMOCOUPLE (deg.C.)	THERMOCOUPLE TEMPERATURE (deg.C. +/- 0.3)				
		1	2	3	4	5
Heated for 58 minutes with shields open.	57.5 +/- 0.3	60.8	59.9	60.0	60	58
Heated for 50 minutes with shields closed.	56.0 +/- 0.3	55.2	56.4	57.7	60.2	56.2

Table 4.1 Distribution of temperatures recorded by thermocouple array.

4.6 SHEAR STRENGTH OF TISSUE BONDS AS A FUNCTION OF BONDING TEMPERATURE

The bonding equipment described above enables accurate assessment of bonding temperature. Since Argon bonds appear to be created in the region of 40 - 50 deg.C. and denaturation occurs between 60 and 65 deg.C., a suitable temperature range for investigation was taken as 20 - 90 deg.C.

4.6.1 Method: Dry Bonds

Normal sheep hearts were obtained fresh from the abattoir, and 2 - 3cm of aorta in the region of the aortic root excised. Each aortic piece was stored in refrigerated saline and used within 7 days.

A longitudinal cut enabled the piece to be laid flat, and a rectangle of tissue approximately 2.5 x 1cm was cut from the centre (Fig. 4.5). A small nick was made at the half thickness point of one corner of the rectangle, and the slice gently peeled apart to provide 2 thinner slices approximately 0.5mm thick (Fig. 4.6). The peeled face of each slice was marked and designated the bonding face. After washing in distilled water, slice thickness was measured with a Mitutoyo tissue gauge. This instrument gently holds the tissue between two flat pads (approximately 1cm²) the distance between them being the thickness measurement. Rather than a spot measurement, this represents thickness averaged over the pad area.

One of the peeled slices was taken, cut in half and laid onto the preheated approximator base plate with its bonding face upward. The other half of the cut slice was placed on top to form an overlap, with the peeled bonding face downward, so that the peeled faces of both halves were in contact/apposition. This exercise was repeated with the other peeled slice, giving 2 sets of overlapped slices, one at either end of the approximator base plate. The clamping approximator plates were gently lowered onto the overlapped slices, and secured by two thin rubber bands to apply a gentle pressure of 5 ± 2 kPa to the slices (Fig. 4.7). This arrangement ensured good thermal contact throughout the heating phase of the experiment, the pressure helping to take up any slack if tissue shrinkage occurred. With radiation shields in place, the approximator was heated by the 120W lamp for as long as was necessary to completely dehydrate both samples. This was discernible by a change in the consistency of the tissue from a floppy opaque white to a brittle translucent brown (Figs. 4.8 & 4.9). The process took 2 hours at 70 deg.C. and 5 hours at 40 deg.C. Equilibrium temperature recorded by the reference thermocouple, was monitored throughout the experiment, and was seen to vary by less than 2 deg.C. in all cases.

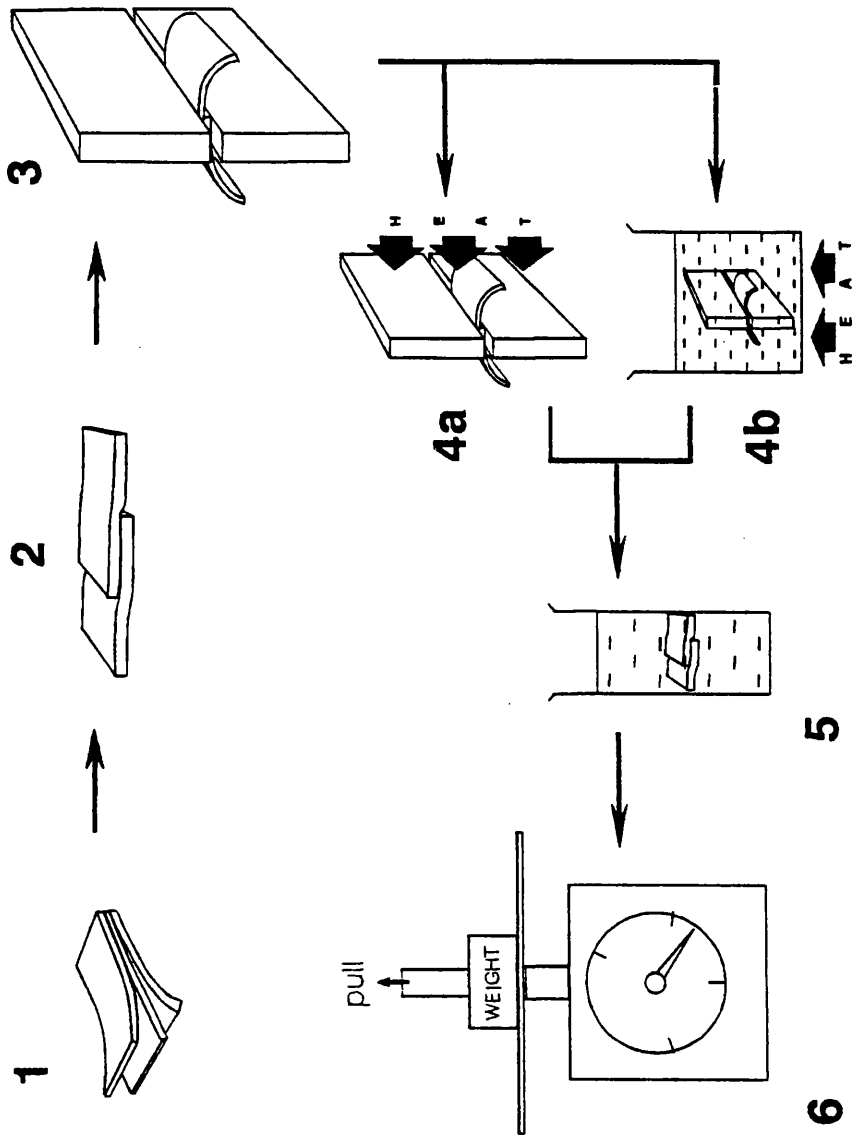


Figure 4.5 Experimental procedure: aortic wall separated into slices approximately 0.5mm thick (1), overlapped (2), and placed in perspex jig (3). Heat by irradiation from 120W spot-light (4a), or immerse in temperature controlled water bath (4b). The bond formed is rehydrated (5), and strength tested to breaking point (6).

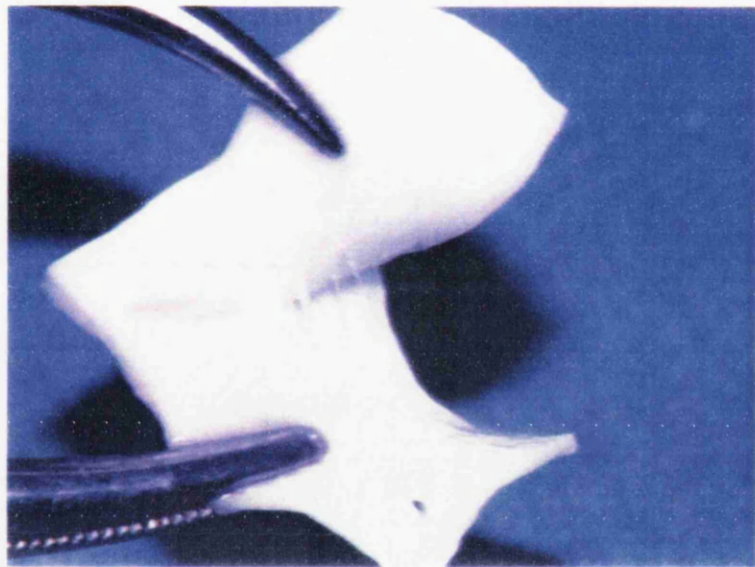


Figure 4.6 Separating the aortic wall into slices approximately 0.5mm thick.

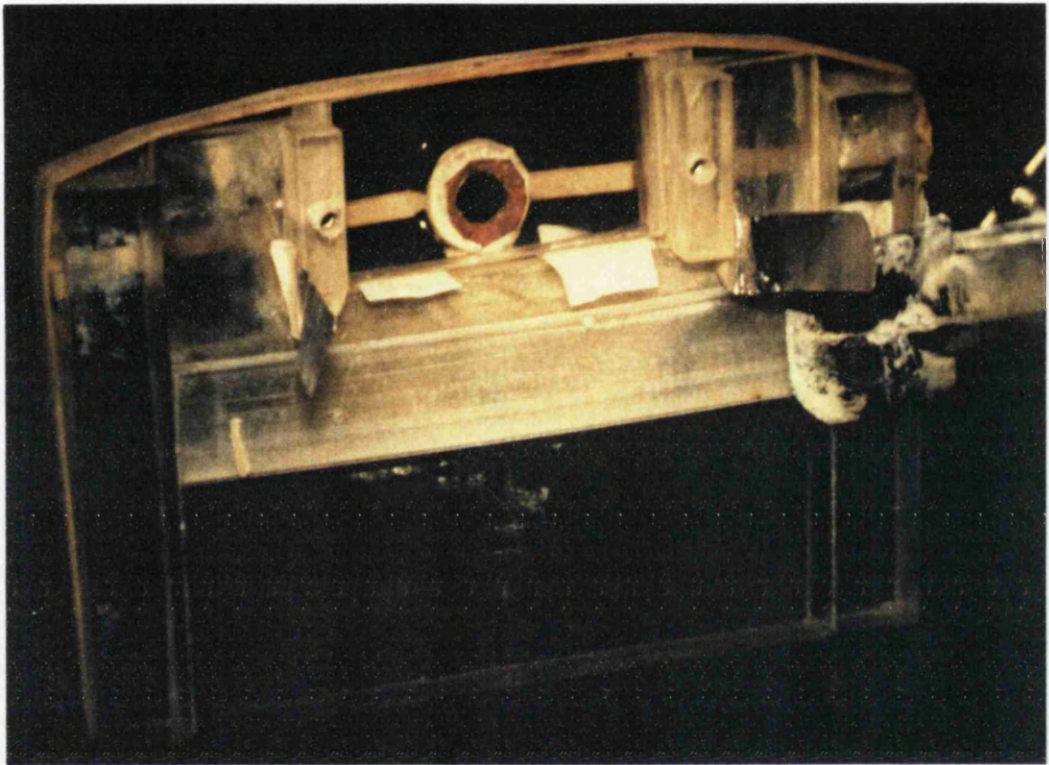


Figure 4.7 Picture of approximator. Thermocouple and white tissue slices are clearly visible. The tin foil to the left and right of the slices are radiation shields in the open position. During the experiment they are closed in front of the slices to protect them from direct radiative effects.



Figure 4.8 The opaque white tissue slice before dehydration.



Figure 4.9 The slice turns translucent brown after dehydration in the approximator.

When heating was finished, the lamp was switched off, the tissue removed from the approximator and rehydrated in room temperature saline for 10 minutes. The tissue regained its colour, opacity and floppy nature within the first 3 minutes of rehydration.

4.6.2 Wet Bonds

The procedure for tissue bonding under wet (ie. non dehydrating) conditions was similar to that already described. Tissue was prepared and overlapped on the approximator as before, which was then immersed in a temperature controlled water bath full of saline. The bonds were heated by immersion for the same period as the dry bonds were irradiated at the same temperature (ie. 2 hours at 70 deg.C., 5 hours at 40 deg.C.). After heating, the tissue bonds were immersed in room temperature saline for 10 minutes (as per the dry bonds) to minimise procedural differences between bonds created under wet or dry conditions.

Both types of bonds were subsequently tested to destruction to evaluate their breaking shear strength. The extent of the overlap area actually bonded by the approximator could be seen by examining the edges of the bond. The resultant bond length and breadth was measured with calipers to calculate bond area, ideally, equating to the full area sandwiched by the approximator. The bonded slice was held between the jaws of two clamps, one of which was attached to a force balance, the other held by hand with a scissor clamp. The jaws of both clamps were aligned parallel to the edge of the bond to minimise off-axis forces. The tissue was steadily stretched and the force at which the bond suddenly broke (ie. the breaking shear strength) was noted. The breaking shear strength per unit area was calculated.

The experiment was performed at the following approximator temperatures - 20, 40, 55, 70 and 90 deg.C. Several bonds were created and evaluated at each temperature. Breaking shear strength per unit area was plotted as a function of bonding temperature. Non-parametric statistical methods (Mann-Whitney U) were applied to the data sets since the data was not established as having come from a normal distribution.

4.7 RESULTS

Figure 4.10 plots the breaking shear strength of dry bonds as a function of bonding temperature (also tabulated in Table 4.2). In the interests of clarity, the errors of the individual points are not shown, but the error in bond strength per unit area is estimated to be $\pm 30\%$ and bonding temperature is accurate to ± 3 deg.C. The

Bond strength at 21 ± 3 deg.C. (g cm-2 ± 30%)	Bond strength at 41 ± 3 deg.C. (g cm-2 ± 30%)	Bond strength at 55 ± 3 deg.C. (g cm-2 ± 30%)	Bond strength at 70 ± 3 deg.C. (g cm-2 ± 30%)	Bond strength at 90 ± 4 deg.C. (g cm-2 ± 30%)
630	544	206	169	408
190	120	321	258	627
124	109	245	1260	329
285	300	79	308	708
39	39	908	238	389
59	11	156	94	320
40	193	106	255	614
0	163	148	857	557
39	150	385	520	383
116	83	413	408	654
891	247	187	916	408
157	53	538	365	210
79	670	245	479	475
106	275	79	256	709
225	258	400		574
267	1270	237		476
131	358	222		692
202	188	284		
	250	298		
	132	557		

Table 4.2 Recorded dry bond strength as a function of the temperature at which bonds were created.

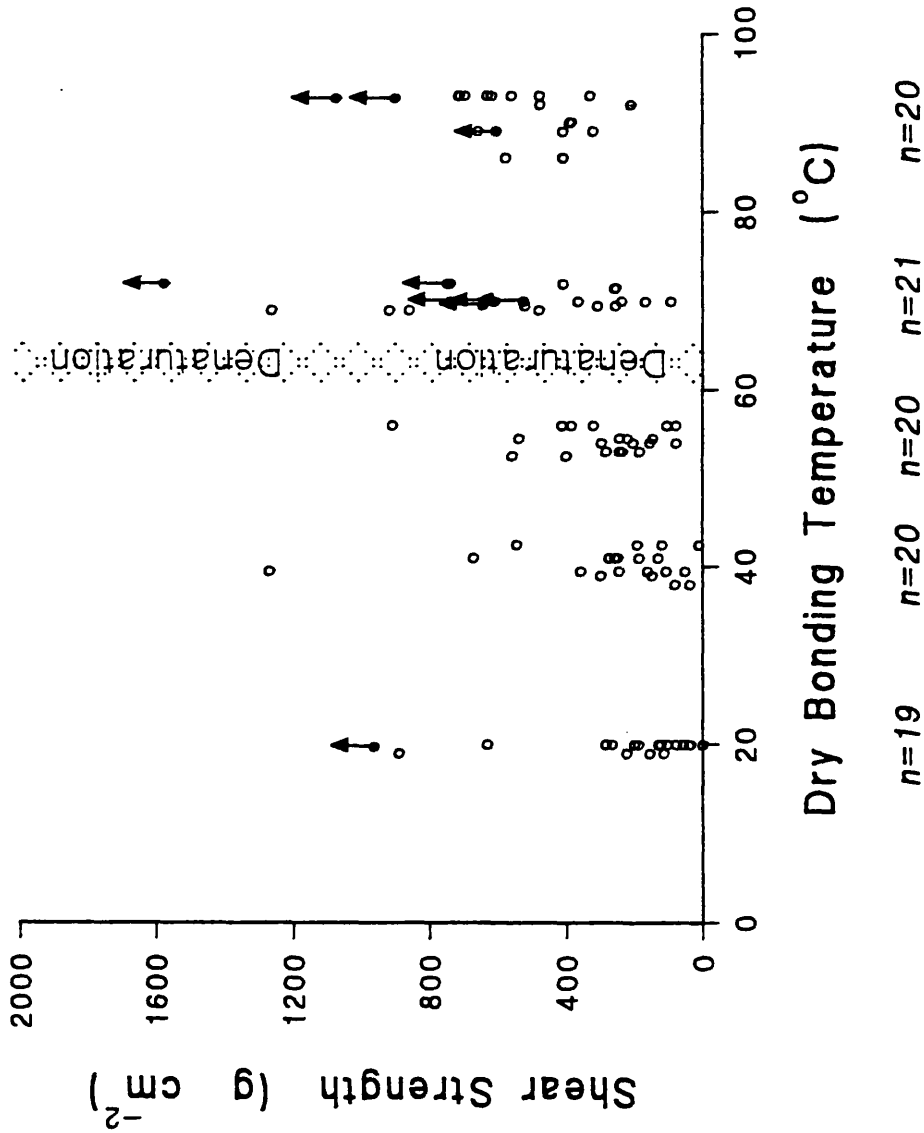


Figure 4.10 Dry bond shear strength as a function of bonding temperature. Points with arrows attached indicate that the bonds did not break, and true breaking strength exceeds this value.

points with arrows attached, denote those samples that did not break while being strength tested, but simply slipped out and pulled free from the clamps. In these cases, the shear stress at the time the tissue slipped from the clamp was recorded and plotted, but clearly, the breaking shear strength exceeds this value. These samples were returned to saline to be rehydrated for a further 4 to 5 hours before being strength tested again.

With regard to the results of figure 4.10, the non-parametric Mann-Whitney U test was applied to determine differences between groups. No significant difference in mean group strength was found for temperatures ranging from 20 to 55 deg.C. ($p > 0.1$). Neither was there any significant difference between mean strength of bonds created at 70 or 90 deg.C. ($p > 0.1$). A significant difference was recorded however between those bonds created at 55 deg.C. and those created at 70 deg.C. ($p < 0.01$). On this basis the 20, 40 & 55 deg.C. data was assimilated to form one group representing bonds created at temperatures below the denaturation temperature of the tissue (mean strength = $271 \pm 254 \text{ gcm}^{-2}$, $n=59$), and the data at 70 and 90 deg.C combined to represent bonds created above the denaturation temperature (mean strength = $563 \pm 300 \text{ gcm}^{-2}$, $n=40$). The two groups were significantly different with $p < 0.01$.

The data for those bonds rehydrated for a further 4 - 5 hours is plotted in figure 4.11, the values at 10 minutes showing the point at which the tissue pulled free of the clamp. The breaking shear strength after extended rehydration was significantly reduced as compared to the values at 10 minutes ($p < 0.01$).

The results of bonding under wet conditions is shown in figure 4.12. Although rather fewer points are shown, the data appears to follow a trend similar to that of figure 4.10, in which mean bond strength increases above the denaturation temperature. Hence the results were collated into 2 groups - bonds created below denaturation (20, 40, 55 deg.C: mean strength = $23 \pm 15 \text{ gcm}^{-2}$, $n=9$) and those created above denaturation (70, 90 deg.C: mean strength = $51 \pm 18 \text{ gcm}^{-2}$, $n=7$). The mean bond strength of the two groups was found to be significantly different ($p < 0.01$).

Bond strength data is summarised in the graph of figure 4.13, the points showing dry bond strength means and standard deviation. The summarised wet bond means are depicted by the dotted line. The wet bonds were considerably weaker than any of the dry bond groups ($p \leq 0.02$) at all temperature points.

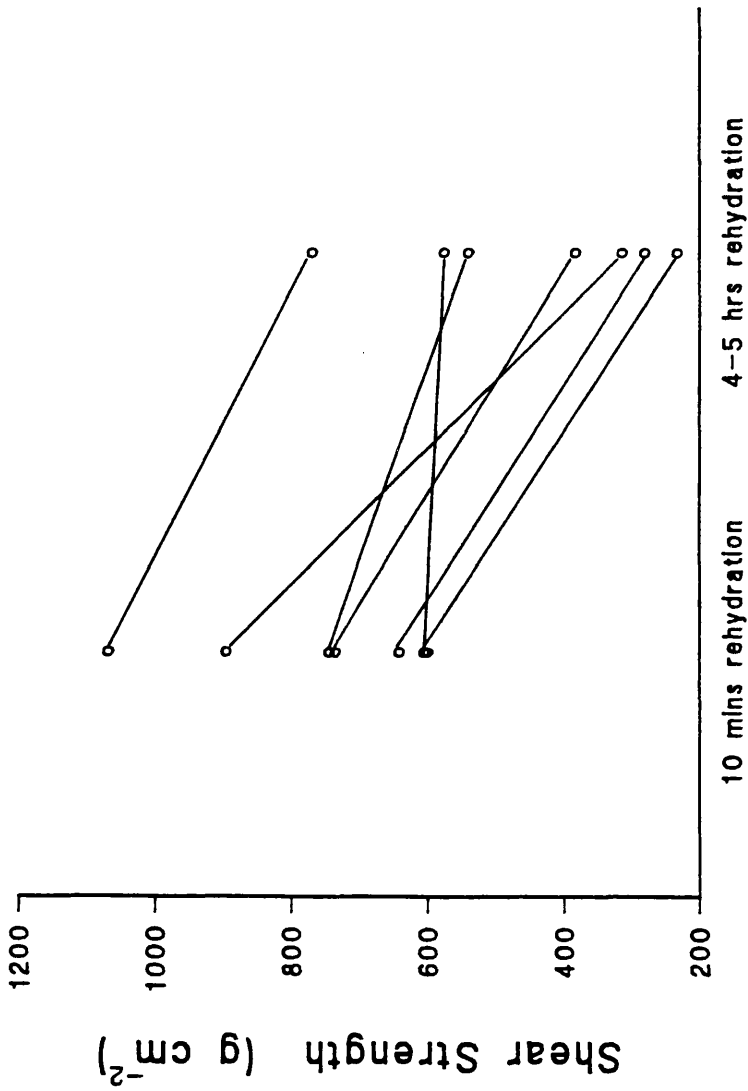


Figure 4.11 Bond strength as a function of rehydration time.

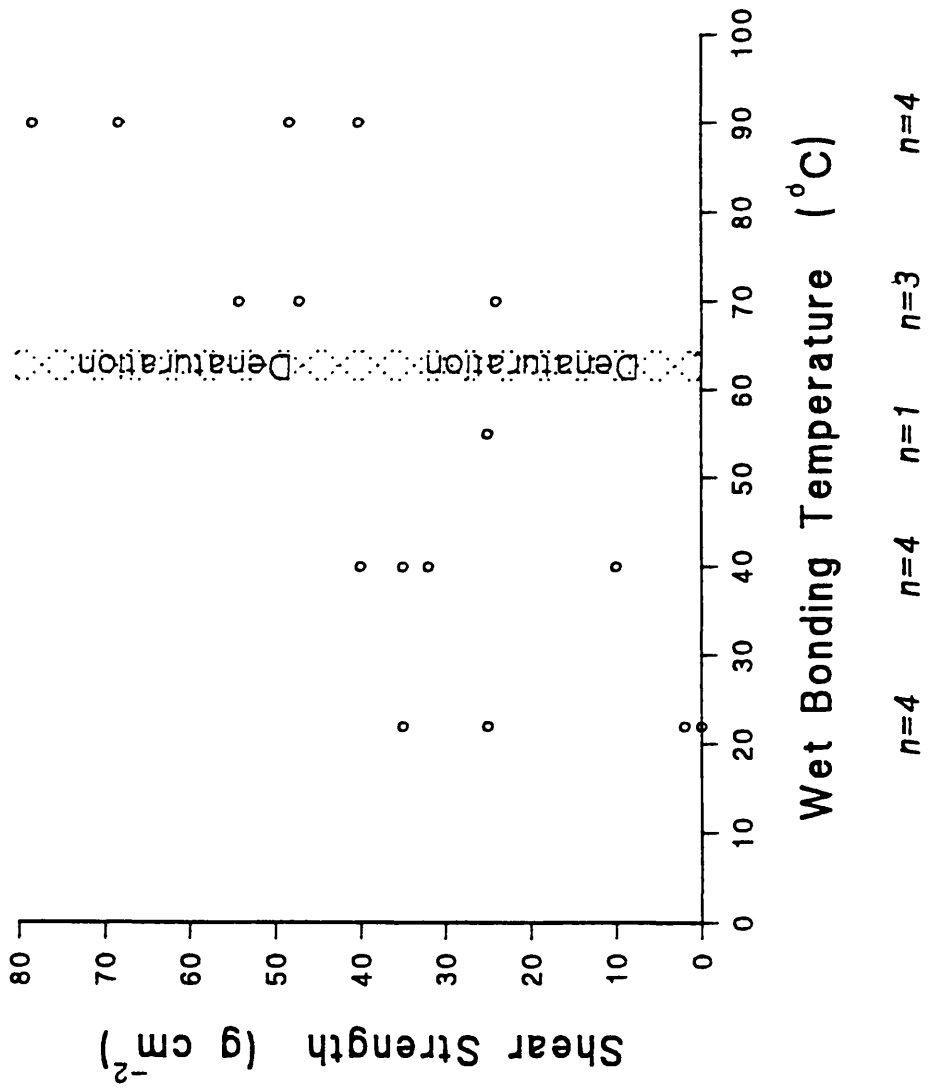


Figure 4.12 Wet bond shear strength as a function of bonding temperature.

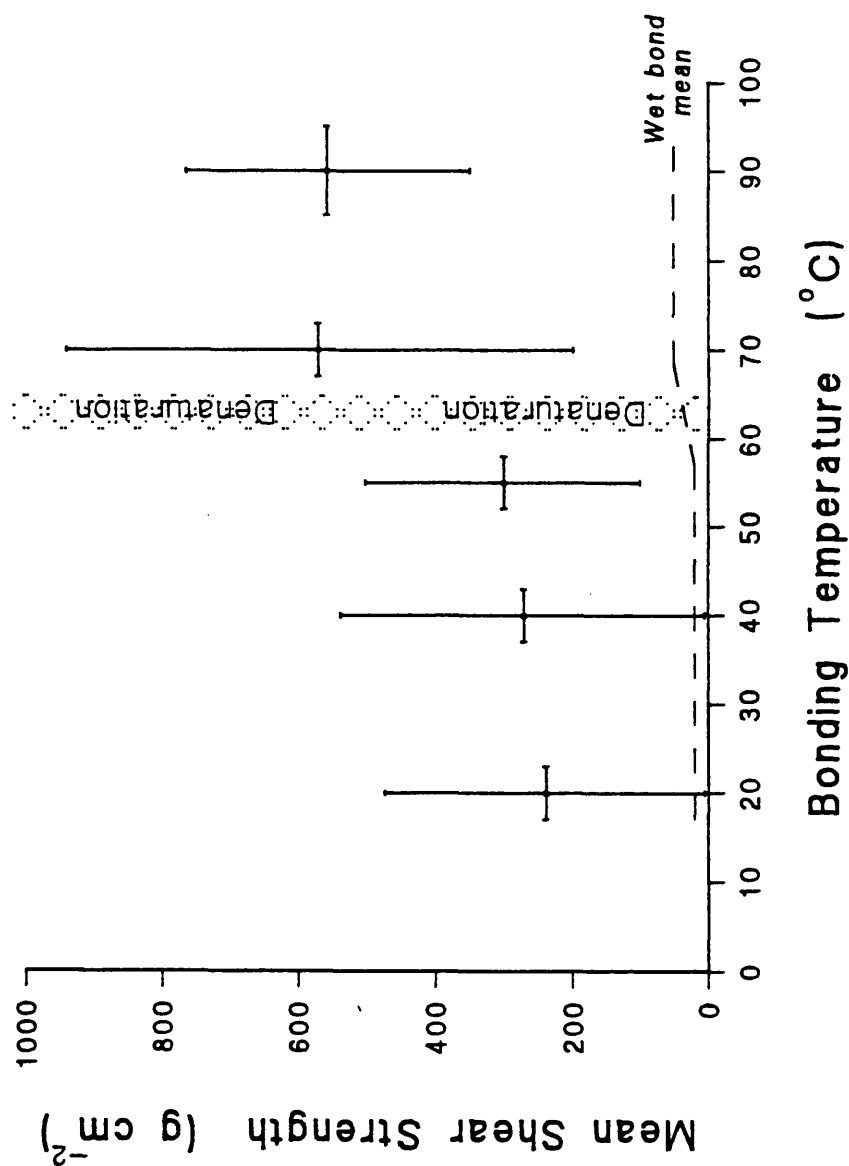


Figure 4.13 Summary of wet and dry bond strength as a function of temperature. Crosses refer to dry bond mean and standard deviation. Dotted line refers to wet bond mean.

4.8 DISCUSSION

Although the issue of whether bonding is a photochemical or thermal effect has not been resolved, current discussion tends to focus on whether denaturation is required. Evidence from CO₂ work (72,106), Sigel et al. (26,2,7) and Schober (who reported changes in collagen structure as a result of bonding (34)) suggests that denaturation may be necessary. The work of White and Gorisch (47,79) however casts doubt on this. The conclusion must be that either the 45 deg.C. temperatures quoted by White et al. are wrong (and at this temperature nothing is expected to happen to collagen, so why does it bond? - hence the photochemical suggestion); or the temperatures as measured by White are correct and a different mechanism exists below denaturation; or the same bonding mechanism is active in both the CO₂ and Argon cases but denaturation is not a necessary condition. The denaturation question is important, and is the impetus for accurate knowledge of bonding temperatures. The biggest disadvantage of the laser is this lack of temperature information, for although tissue temperature can be measured (directly or remotely), it must be asked to what extent such readings provide a true reflection of the temperature at the bond faces. This is particularly true of the thermal camera, the readings of which are resolution limited and compromised by the presence of water. An error of less than 5 degrees would be sufficient to completely misdiagnose the denaturation state of the collagen. Furthermore, it is not known to what extent micro hotspots may be occurring within the bonding faces, causing localised denaturation with associated tissue bonding. Such rises in temperature would be undetectable because of their small size.

The advantages of the non laser heating of tissue bonds described in this experiment are: tissue temperature can be gauged to within a few degrees; denaturing hotspots cannot be occurring because the bond and approximator are in thermal equilibrium. The results show that tissue bonds of significant strength can be produced by purely thermal effects and thermal denaturation is not required. But it appears that dehydration is the more important factor, as bonds created under wet conditions proved very weak in comparison to those created by dehydration. A strong thermal dependence was also seen, since bonds created at temperatures below denaturation were almost half the strength of those created above denaturation. Those bonds that did not break after 10 minutes rehydration suffered considerable reduction in bond strength following further rehydration. This may be a result of the bond being weakened by the first strength test, or perhaps may be a strength degrading effect of rehydration alone. The latter is supported by the preliminary experiments in which partially dehydrated tissue which had adhered to a glass surface could be more easily removed if left to soak in water.

Although the data has provided some interesting results, two major areas remain to be addressed:

- i) Scatter - The spread of strength data at any particular temperature is considerable.
- ii) Equivalence - It is not known to what extent the dry bonds created in this experiment are in any way the same as those created by laser.

4.8.1 Scatter

The spread of results in each temperature group makes it difficult to be certain that true differences in bond strength exist. Looking at the raw data of figure 4.10, it is not immediately obvious that those bonds created at temperatures above denaturation have distinctly different bond strengths to those created at 20 - 55 deg.C. The results would be more acceptable if the scatter in bond strength were reduced. Pockets of air trapped between the apposed tissue faces seem the most likely cause of the scatter. The tissue faces were not perfectly smooth since they had been peeled apart by hand. Air gaps could be seen between the dehydrated tissue faces as speckled areas that scattered the light differently to the translucent, well apposed regions. These air gaps were difficult to measure, especially if spread diffusely across a bond. Their effect is to reduce bond strength due to decreased contact between slices. In addition, a reduction in the calculated strength per unit area results because the simple measurement of bond area described in this experiment does not effectively account for the true loss in bonding area due to air gaps. This is further complicated by a standard result of stress analysis which states that bond strength is a function of bond geometry, which in our case is determined by the air gaps present. A two step solution is appropriate:

- i) Improve intimacy and consistency of apposition.
- ii) Improve assessment of bonded area, to more accurately account for losses in bond area due to air gaps.

These ideas are explored in the next chapter.

4.8.2 Equivalence

To what extent are the dry bonds created in this experiment the same as those created by laser? At this stage it is not clear, but similarities do exist. Firstly, our work with the rabbits (in agreement with White) suggested bonding temperatures of 40 - 50 deg.C., and this has been shown possible by the dry bonding. Secondly, when bonding with the laser, lasing was continued until the incision became

slightly discoloured which has been described by some groups in terms of dehydration (56). Thirdly, in our experience laser bonds were inconsistent: some apparently strong, lasting several weeks; others weak, rupturing a few hours after lasing. This parallels the scatter in the strength of dry bonds. Furthermore, is it possible that the bonds that ruptured in the rabbits several hours after lasing, did so as a result of the bond weakening from rehydration? Rehydration would result from blood within the lumen and the capillaries in the adventitia of the vessel.

There is little data available in the literature pertaining to the strength of overlap bonds. Jenkins (109) did report creating them with a Nd:YAG laser at rather higher temperatures than ourselves (above 100 deg.C., overlap area bonded under pressure of 185kPa). His results show a large amount of scatter with a maximum mean shear strength of 286 gcm⁻² which fits well with the mean strength of non-denatured dry bonds (271 gcm⁻²) in our experiment.

However, dissimilarities between laser and dry bonding also exist. Dry bonding times are very long compared to the laser and the creation of large overlap bonds is rather different to the delicate butt joints most often associated with laser bonding. It is also recognised that the techniques used here are not easily reconciled with the bonding technique advocated by Kopchok, White et al (47) in which drops of saline are used to keep the bonding area moist and cool in an attempt to maintain moisture content so as to encourage improved healing due to minimal thermal damage.

4.9 POSSIBLE BONDING MECHANISM

It was noted earlier that tissue drying on a surface will adhere to it, and rehydration can reverse this process. Similarly, it is common experience that after eating a meal, dirty plates left 'to soak' are much easier to clean. The standard explanation of this process (110) is that food molecules contain locally polarised regions that bond through Van der Waals forces to surrounding water molecules. Should the water be removed by dehydration, the bond sites become free to bond to the plate surface. By immersing the food and plate in water, water molecules preferentially re-occupy the bond sites (depending on how strong the affinity between water and food molecules is) terminating bonding with the plate surface and the food is easily rubbed off.

Given the similarity between laser and dry bonds, the above model of adhesion is extended to explain tissue bonding in terms of dehydration without denaturation being required.

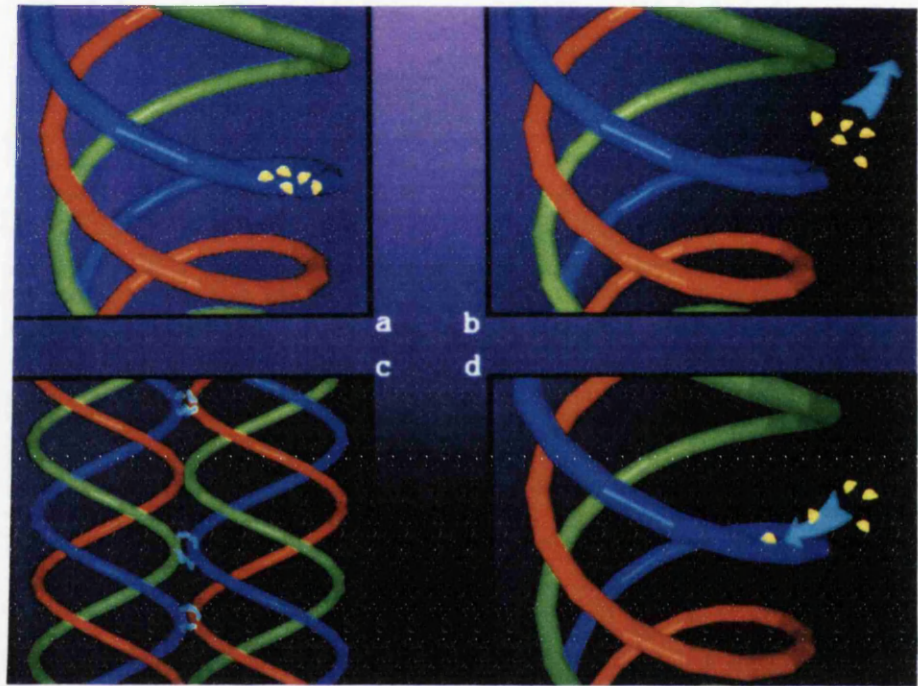


Figure 4.14 Proposed bonding model. Water molecules (yellow) loosely bind to polar regions of the collagen molecules (a). With dehydration the water is lost (b) leaving spare bond sites that allow the collagen molecules to bind to each other (c). Water preferentially re-occupies these sites following rehydration and the collagen-collagen bonds are broken (d).

Collagen is a major component of arterial tissue and is based on a molecular triple helix. Although the molecule is electrically neutral overall, locally polarised regions exist along its length. These regions can form weak hydrogen bonds with surrounding water molecules (Fig. 4.14). Dehydration of the tissue drives the water off, leaving the polarised regions free to bond to surrounding molecules, and collagen-collagen bonds are formed. With rehydration, the water molecules preferentially reoccupy the bond sites and the collagen no longer bonds to itself.

With denaturation, the molecular crosslinks of the triple helix are irreversibly broken. This reveals yet more bond sites that can be used for collagen-collagen bonding when dehydrated, and an increase in bond strength results. The bonding as described, relies on short range Van der Waals forces and thus intimacy of apposed bonding faces would be critical to the strength of any bond.

This model can satisfactorily account for dry bonds created at temperatures below denaturation and provides an explanation for the increase in bond strength as the denaturation temperature is exceeded. It also suggests that bond strength might decrease with rehydration and hints at a possible reason (ie. poor apposition) for the high degree of scatter observed in the experimental results.

If applied to laser bonding, this theory would suggest that the laser creates a localised area of dehydration within the tissue under the area of the beam. The only conditions for a successful bond are that water is driven out of the bond faster than it is replaced (eg. by capillary action) and that apposition of bonding surfaces is good.

4.10 CONCLUSION

The dry bonding experiment answers both the photochemical and thermal denaturation questions in that neither is required to create a satisfactory tissue bond. A model of bonding based on dehydration can account for the experimental results. However, model nor experiment reveal whether such bonds are the same as laser bonds (although there are similarities). Further investigation is required.

Chapter 5

Scatter of Dry Bonds

5.1 INTRODUCTION

The bonding experiment of Chapter 4 highlighted the importance of dehydration in the formation of overlapped tissue bonds. The equivalence of such bonds with those created by laser remains to be established. A stumbling block to acceptance of the interpretation of the dry bond data presented in Chapter 4 is the substantial scatter of data points at any particular temperature. The proposed bonding model suggests that this is the result of poor intimacy at the bonding faces. This seems a plausible explanation given that the apposed tissue faces were not particularly smooth and air gaps could be seen between them.

To investigate this further, a modified re-run of the previous experiment (at one temperature only) was performed, in which surface intimacy of tissue slices was progressively improved through:

- i) introduction of smoothly cut bonding faces;
- ii) careful removal of inter-surface air gaps with improved quantification of any that remained;
- iii) application of increased pressure to the overlapped slices for improved apposition.

Quality of bonds was compared by obtaining their breaking shear strength per unit area. This experiment and the necessary modifications to the approximator are described below.

5.2 MODIFICATION OF APPROXIMATOR TO PERMIT APPLICATION OF INCREASED PRESSURE TO OVERLAPPED BONDING SLICES

The higher pressure apposition of tissue slices during bonding required minimal modifications to the approximator. Dry bonding experiments to date have utilised thin elastic bands wrapped around the approximator to apply a small but steady force to the faces of the overlap bond to assist good apposition. This is particularly important when it is considered that dehydration causes the tissue to shrink and

the overlapped slices get thinner. The pressure applied to the approximator plates ensures good thermal contact as well as keeping the tissue approximated. The pressure applied to the tissue is easily changed by replacing the thin elastic bands with stronger ones. This experiment determines the pressure applied to the tissue with the use of different elastic bands.

5.2.1 Method

The approximator with elastic bands was rigged as for a bonding experiment, with approximator plates removed (Fig. 5.1). It was held inverted by a vernier clamp and attached via the elastic bands to a set of scales as shown in the diagram. The elastic bands were attached to the weighing platform in such a way that raising the approximator extended the bands in a manner similar to that of the approximator plates. Under such conditions, the applied force can be read on the scales. Lowering the approximator relaxes the tension on the bands until no force is exerted on the weighing platform. Further downwards movement of the approximator forcibly depresses the weighing platform. The large spring constant of the scales dictates that a large force is required for a small depression:

From a position of depressing the balance by several millimetres, the approximator was progressively raised by increments of 0.5mm - the displayed weight being recorded at each point - until the band was stretched by several millimetres, supporting a force of hundreds of grams. The recorded force was plotted as a function of vernier position. The elastic band was exchanged for a stronger one, and the experiment repeated.

To conclude the experiment, the elastic bands were removed from the approximator, and the approximator plates fully inserted. The distance the plates protruded above the approximator body was measured. This information in combination with the typical thickness of overlapped tissue provided a value for the expected extension of the bands during a bonding experiment, from which the force applied to the plates could be calculated. Knowledge of overlapped tissue area converts this result to an apposing pressure.

5.2.2 Results

Load-position graphs are plotted for low and moderate pressure configurations, created by the use of weak and stronger elastic bands. Vernier position was accurate to 0.1mm and force accurate to 2 grams.

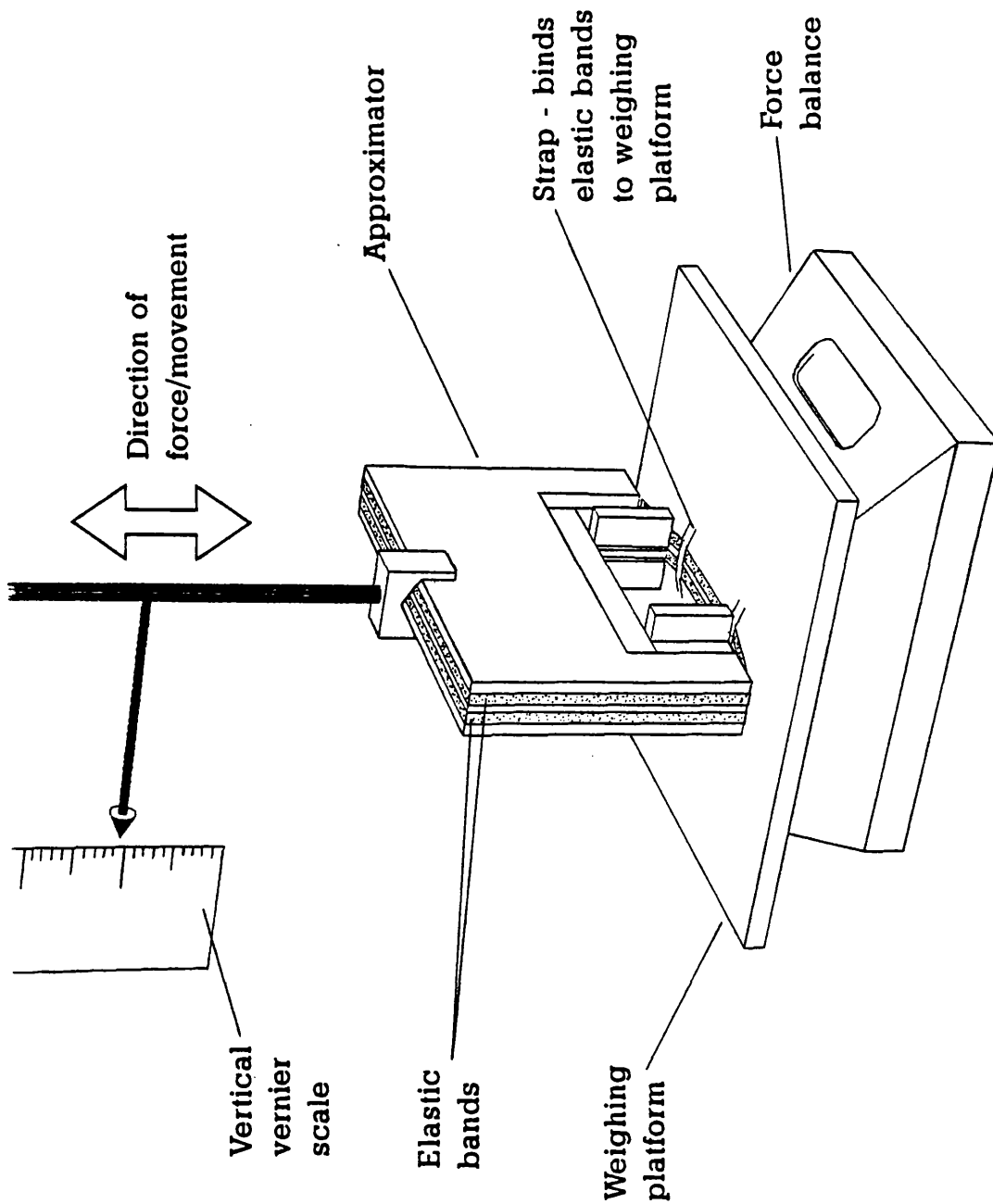


Figure 5.1 Equipment used to measure the force applied by approximator elastic bands to the approximator plates.

5.2.3 Low Pressure

Figure 5.2 shows a curve comprised of two straight lines of different gradients. The line of steeper gradient results from that part of the experiment in which the weighing platform is forcibly depressed (gradient (m_{BAL}) = -424gmm^{-1}). As the applied force changes from balance compression to elastic extension the gradient changes to a gentler slope (gradient (m) = -21.3gmm^{-1} , correlation coefficient = -0.999). The latter is a composite slope consisting of the extension of the elastic band plus the sympathetic extension of the balance, which must be subtracted from the composite result to provide the true elastic gradient:

Combined displacement (D) = band extension (B_E) + balance displacement (B_{AL})

$$\text{ie. } \begin{aligned} D &= B_E + B_{AL} \\ \frac{\delta D}{\delta F} &= \frac{\delta(B_E + B_{AL})}{\delta F} \quad (F = \text{applied force}) \end{aligned}$$

but the force per unit extension ($\frac{\delta F}{\delta D}$) is the gradient (m):

$$\frac{1}{m} = \frac{1}{m_{BE}} + \frac{1}{m_{BAL}} \quad (m_{BE} = \text{Elastic gradient})$$

(m_{BAL} = Balance gradient)

$$\Rightarrow m_{BE} = \frac{m \cdot m_{BAL}}{m_{BAL} - m}$$

It should be noted however, that the gradient of the balance (m_{BAL}) is typically 10-20 times that of the combination (m), and so its contribution to the gradient of the band is insignificant. Therefore the true elastic gradient may be quoted as equal to the gradient of the combination (m):

$$m_{BE} = -21.3\text{gmm}^{-1}$$

The approximator plates were measured as protruding above the approximator body by 2.0mm, which with the addition of a typical overlapped tissue thickness of 0.8mm produces an effective band extension of 2.8mm. The force generated acts upon two overlap bonds of nominal bonding area 60mm^2 each. The resultant pressure becomes

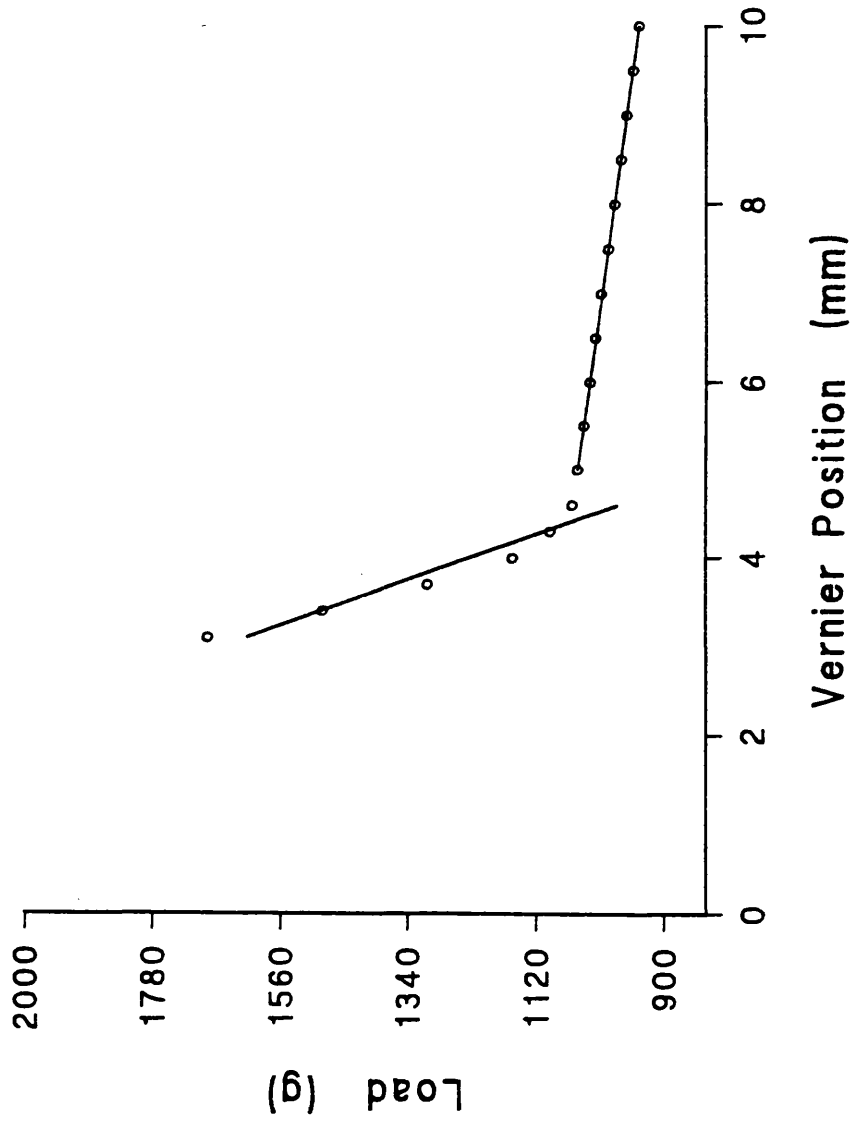


Figure 5.2 Force (recorded by balance) as a function of vertical vernier position - low pressure elastic bands. Two regression lines have been superimposed on the data.

Applied pressure = Applied force per unit area

$$\begin{aligned} &= \frac{2.8 \times 21.3}{(2 \times 60)} \\ &= 0.497 \text{gmm}^{-1} \\ &\approx 5 \text{kPa} \end{aligned}$$

5.2.4 Medium Pressure

In this instance, a stronger elastic band was used and the pressure evaluated over a 60mm^2 area. Again, a two-part linear curve is seen (Fig. 5.3), the gradient at the compression stage of the experiment being $m_{\text{BAL}} = -493\text{gmm}^{-1}$. With the combined extension of elastic band and balance, the gradient becomes $m = -50.1\text{gmm}^{-1}$, $r = -0.999$. As with the low pressure results, the contribution of the balance gradient to the true elastic gradient (m_{BE}) is negligible, and the true elastic gradient can be quoted as:

$$m_{\text{BE}} = -50.1\text{gmm}^{-1}$$

When this result is applied to the extension caused by the raised approximator plates sitting on overlapped tissue, the nominal pressure on each bond is:

$$\text{Nominal medium bonding pressure} \approx 25\text{kPa}$$

5.2.5 High Pressure

No high pressure experiment was performed, since the high pressure configuration consisted of wrapping 2 of the bands used for the medium pressure configuration around the approximator, thus doubling bond pressure.

ie.

$$\text{Nominal high bonding pressure} \approx 50\text{kPa}$$

5.2.6 Discussion

As expected, the gradients of the lines in which the balance was forcibly depressed are similar. They are not identical however, the two differing by more than 15%, indicating the magnitude of error in the experiment. The variability of tissue parameters (eg. bonding area, overlap thickness etc.) in a typical bonding experiment are such that accurate knowledge of applied pressure is unnecessary. Force measurement errors incurred in this experiment are insignificant in comparison

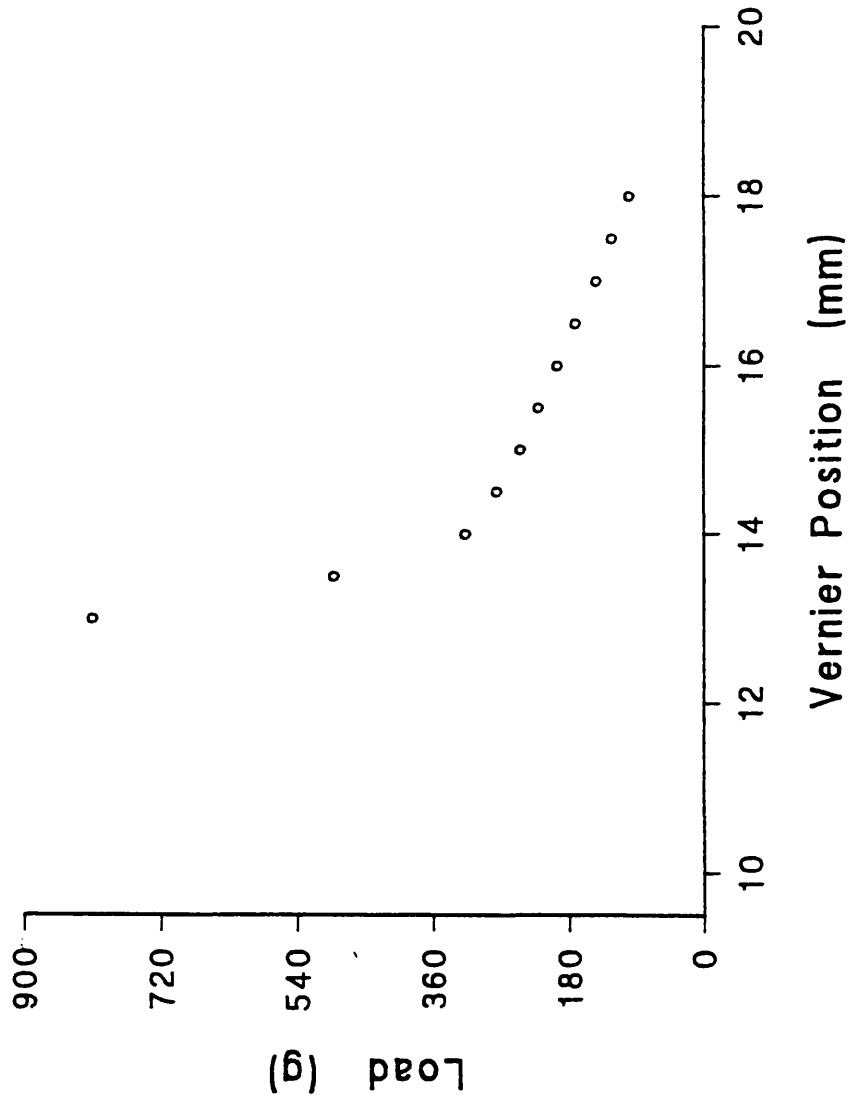


Figure 5.3 Force (recorded by balance) as a function of vertical vernier position - medium pressure elastic bands.

to the inaccuracies introduced by such broad generalisations as 'typical' bonding area and 'typical' tissue thickness. Estimation of bonding area to calculate applied pressure is possible, but overlap tissue thickness is more difficult to assess. This is not only because the pressure of the clamp compresses the tissue (hence changing its thickness, and therefore the applied pressure) but also because as the tissue dehydrates, it shrinks and thickness decreases. This reduces the applied pressure as bonding progresses. The quoted figures then, simply provide an estimate of the pressure apposing the tissue during dry bonding.

The application of the modified approximator, in conjunction with other techniques, to reduce the scatter in the strength of dry bonds will now be discussed in detail.

5.3 SHEAR STRENGTH OF TISSUE BONDS AS A FUNCTION OF TISSUE APPPOSITION

This experiment repeats the technique of dry bonding described in Chapter 4, with the aim of reducing the scatter in the strength of dry bonds. It was performed at 55 deg.C. only, with the addition of a few systematic modifications in terms of tissue preparation and its placement on the approximator. Basic technique is described first, before introducing the modifications employed for each group.

5.3.1 Method

Fresh sheep heart was obtained from the abattoir and a 3-4cm length of aorta excised in the region of the aortic root. The aortic pieces were stored in refrigerated saline and used within 7 days. As described in Chapter 4, a rectangular slice approximately 2.5x1cm was cut from the length of aorta, the adventitia removed, and the slice then peeled in half to produce two half-thickness slices approximately 0.5mm thick. After being washed in distilled water, and thickness measured with a Mitutoyo tissue gauge, each slice was cut in half and overlapped on the approximator which had been preheated to 55 deg.C. (Fig. 5.4). The approximator plates were lowered onto the overlapped slices and thin elastic bands used to apply a pressure of 5kPa to the apposed tissue in order to encourage good apposition and thermal contact. The approximator was heated (with radiation shields in place) for 3 hours at 55 deg.C., during which the tissue dehydrated, becoming brittle and translucent brown in colour.

The slices were removed from the approximator and immersed in room temperature saline for 10 minutes to rehydrate the tissue. It regained its natural

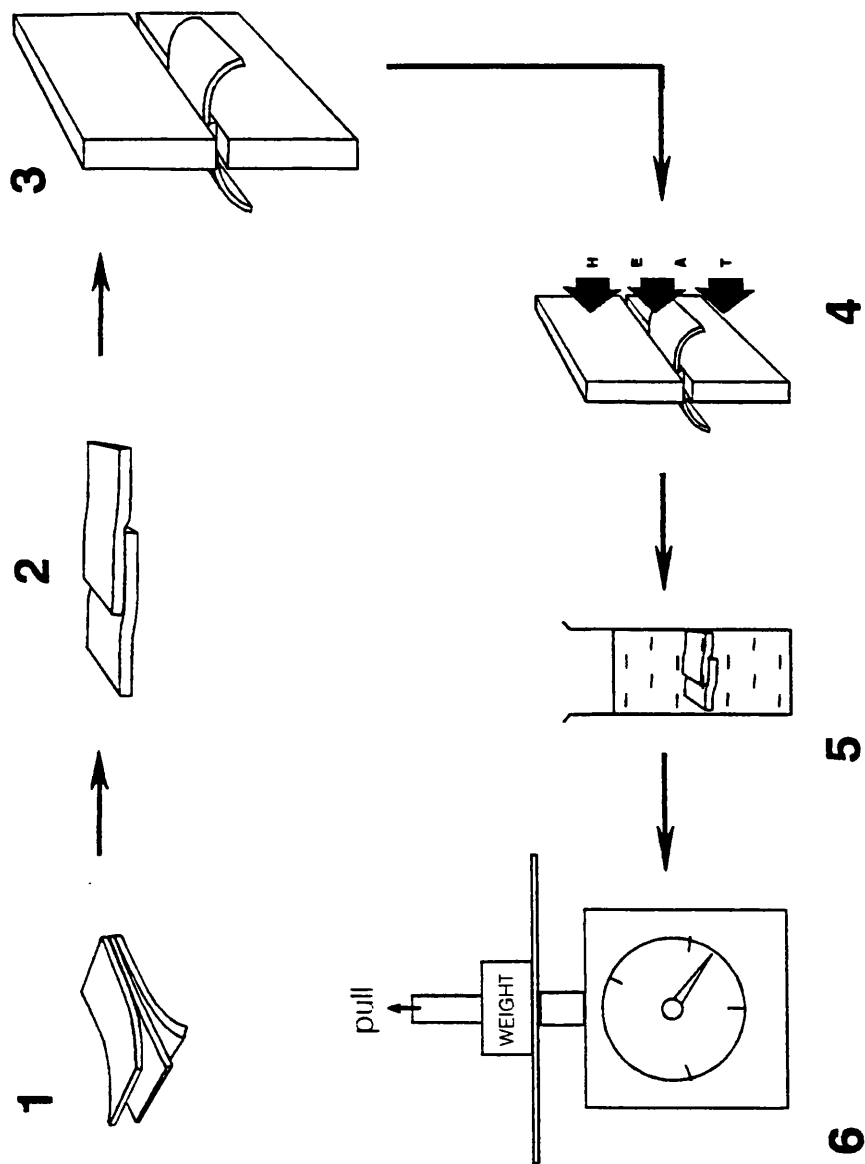


Figure 5.4 Experimental procedure: aortic wall separated into slices approximately 0.5mm thick (1), overlapped (2), and placed in perspex jig (3). Heat by irradiation at 55 deg.C. (4). Rehydrate bond (5), and strength test to breaking point (6).

floppiness and opaque white colour within the first 3 minutes of rehydration. Vernier calipers were used to measure the length and breadth of the bonded area which was then held in a force balance and subjected to increasing stress until the bond suddenly broke. The applied force at the time of breaking was noted, and breaking strength per unit area was calculated.

The systematic differences in technique between groups will now be described in detail. In this series of experiments, no wet bonds were made.

Group 1

This group was created as described above and consists of the 55 deg.C. data obtained in Chapter 4. Experimentally significant points are:

- i) Bonding surfaces were rough since slices were created by peeling tissue apart.
- ii) No attempt was made to remove inter-surface air gaps.
- iii) Quantification of air gaps in the bonded sample was poor.
- iv) Bonding was performed at low pressure (5kPa)

Group 2

This group features the replacement of hand peeled slices with smooth faced slices cut on a rotary microtome (Cambridge Medical Instruments Ltd) and detailed air gap quantification.

A rectangular tissue section (2.5 x 1cm) was excised from sheep aorta as previously described. The adventitia was removed (scraped off) and the slice dabbed dry with a paper towel. The adventitial side of the slice was laid flat and stuck firmly (with superglue) to the face of a cork block whose dimensions were slightly larger (3 x 1cm) than the tissue itself. The glue was left to dry for 2 minutes and then the cork/tissue assembly immersed in dry ice for 10-15 minutes. The cork block was mounted in the jaws of the rotary microtome, presenting the frozen tissue slice for cutting - tissue hardened by freezing can be cut more precisely by microtome. A flat smooth tissue face was created by repeatedly shaving off 25 μ m sections. Several smooth sections approximately 500 μ m thick were then cut from the tissue block and stored in saline. Slice thickness was measured at multiple points across the tissue surface with a Mitutoyo tissue gauge, and those slices whose thickness varied by more than 50 μ m were discarded. An acceptable slice was taken, and one face marked as the bonding face. After cutting in half, the tissue was mounted on the preheated approximator with the designated bonding faces in apposition. The approximator plates were lowered and secured with low pressure elastic bands to apply a force of 5kPa to the bonding faces. With

radiation shields in place, the tissue was heated at 55 deg.C. for 3 hours, by which time the tissue had dehydrated and a bond formed.

The bonded tissue was removed from the approximator and assessed for the presence of air gaps. These were regions in which poor tissue contact scattered the light giving the area a light speckled appearance in contrast to the translucent brown of the well apposed regions. Length and breadth of the perimeter of the bond was measured accompanied by a simple hand drawn sketch of the bond area with air gaps. The tissue was rehydrated in saline for 10 minutes during which it quickly regained its natural opaque colour and consistency. With the tissue in its opaque state, air gaps were not visible and therefore the bond was probed with forceps, using the hand drawn map as a guide, to verify the presence or otherwise, of air gaps trapped within the bond. This exercise was used to update the map to provide a final estimate of the percentage of the bond area lost to air gaps, from which the effective bond area could be calculated.

The bond was connected to the force balance and steadily stretched. The force at which the bond broke was noted, and the breaking shear strength per unit area calculated. Features of note are:

- i) Smooth tissue faces were cut with a microtome.
- ii) No attempt was made to remove inter-surface air gaps.
- iii) The effective bonded area, taking account of loss due to air gaps, was carefully calculated.
- iv) Bonding was performed at low pressure (5kPa).

Group 3

This group features smooth tissue faces cut by microtome, attempted air gap removal, and air gap quantification.

Smooth faced aortic slices approximately 0.5mm thick were prepared as for group 2. One face of the slice was designated the bonding face, cut in half, and one half placed on the approximator base plate. In an attempt to remove any pockets of air between the tissue and base plate, the tissue surface was gently stroked across the whole area with tweezers to force air out past the tissue edges. The bonding face of the other half slice was placed in apposition with the now smoothed slice to form a tissue overlap. Again with the use of forceps, the overlapped area was gently stroked to tease air out of the bond, removing inter-surface air gaps.

The approximator plates were lowered and held in place with low pressure bands (5kPa), the tissue being heated (with radiation shields in place) for 3 hours at 55 deg.C. The experiment proceeded as for group 2, ending with a careful

assessment of air gap corrected bond area, followed by a strength test of the bond. The breaking shear strength per area was calculated. Points to note are:

- i) Smooth tissue faces were cut with a microtome.
- ii) A concerted attempt was made to remove inter-surface air gaps.
- iii) The effective bonded area, taking account of loss due to air gaps, was carefully calculated.
- iv) Bonding was performed at low pressure (5kPa).

Group 4

This group features smooth tissue faces cut by microtome, attempted air gap removal, air gap quantification and bonding performed at an intermediate pressure of 25kPa.

This experiment was performed in a manner identical to group 3 except that the pressure applied to the bonding surfaces by the approximator plates was increased (using stronger elastic bands) from 5kPa to 25kPa. Points to note are:

- i) Smooth tissue faces were cut with a microtome.
- ii) A concerted attempt was made to remove inter-surface air gaps.
- iii) The effective bonded area, taking account of loss due to air gaps, was carefully calculated.
- iv) Bonding was performed at intermediate pressure (25kPa).

Group 5

This group features smooth tissue faces cut by microtome, attempted air gap removal, air gap quantification and bonding performed at a high pressure of 50kPa.

The experiment was identical to the experiments of groups 3 and 4 except that the pressure applied to the bonding faces through the approximator plates was increased (by using strong elastic bands) to 50kPa. Points to note are:

- i) Smooth tissue faces were cut with a microtome.
- ii) A concerted attempt was made to remove inter-surface air gaps.
- iii) The effective bonded area, taking account of loss due to air gaps, was carefully calculated.
- iv) Bonding was performed at high pressure (50kPa).

Bond strength per unit area was plotted in groups, according to the particular methods used to prepare and create the bond. Assessment of differences between groups was determined by comparing means and standard deviations. Means were compared using the non-parametric U statistic since the data appeared to be non-normal. The lack of an appropriate non-parametric test for comparison of group variance required that the parametric F statistic was used instead.

5.4 RESULTS

The grouped data is plotted in figure 5.5, showing the effect on bond strength of successive attempts to improve bond apposition. For reasons of clarity, error bars of individual points have not been included but are estimated to be approximately $\pm 30\%$, the principal contribution coming from estimation of effective bond area correcting for air gaps ($\pm 20\%$), with the error in breaking strength $\pm 10\%$.

5.4.1 Comparison of Mean Bond Strength

Differences between group means were established with the Mann-Whitney U test. No significant difference in mean bond strength was found between groups 1 to 4 ($p > 0.1$). The mean strength of group 5 however was significantly different from groups 3 and 4 ($p < 0.02$), group 5 consisting of those samples bonded at the highest pressure (50kPa). The arrowed points of group 5 indicate those bonds that did not break during strength testing, but slipped from the grip of the clamp in which the bond was being held. Such points represent the force per unit area applied to the bond at the moment it slipped from the clamp. Clearly, the breaking strength of the bond is greater than this, increasing the differences between the groups. In some cases the clamp was tight enough to stop the tissue slipping, but the clamped tissue ripped cleanly across its width instead, the bond remaining whole. In these cases, the bond strength exceeded the natural breaking strength of the tissue.

5.4.2 Comparison of Scatter

The parametric F test was applied to the data to determine differences in group variance (ie. scatter).

No significant difference (Table 5.1) was found between the scatter of groups 1 and 2 ($p > 0.1$), group 2 being a repeat of the group 1 experiment except that tissue slices were cut with a microtome. A significant difference between group 3 and group 2 was found with the coefficient of variation changing from

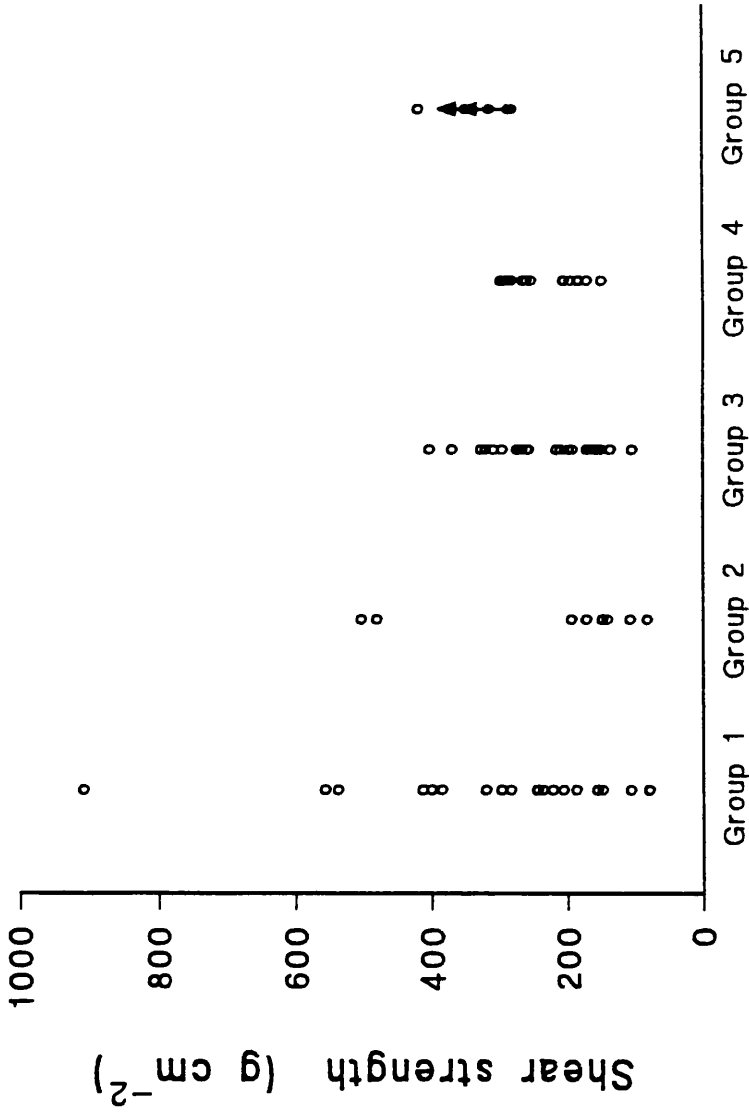


Figure 5.5

Breaking strength per unit area of the five groups in the experimental series.

Group 1 - hand cut, air gaps ignored, low pressure. Group 2 - microtome, air gaps ignored, low pressure. Group 3 - microtome, air gaps removed, low pressure. Group 4 - microtome, air gaps removed, moderate pressure. Group 5 - microtome, air gaps removed, high pressure. Points with arrows attached in group 5 indicate that the bonds did not break and true breaking strength exceeds this value.

EXPT	Microtome	Air Gap Removal	Pressure	Breaking Strength n S.D. Mean	Sig. Diff.
1	No	No	Lo	20 197 301	X MEAN
2	Yes	No	Lo	8 166 244	X SCATTER
3	Yes	Yes	Lo	25 80 227	X MEAN ✓ SCATTER
4	Yes	Yes	Mid	15 52 235	✓ MEAN SCATTER
5	Yes	Yes	Hi	5 -- 328	✓ MEAN SCATTER

X = No significant difference
 ✓ = Significant difference

Table 5.1 Summary of the results of the five groups in the experimental series.

68% to 35% ($p < 0.0025$). The slices of groups 2 and 3 were cut by microtome, but group 3 included attempts to remove inter-surface air gaps. Group 4 was a repeat of group 3 except that bonding was performed at medium instead of low pressure. This produced a significant reduction in the coefficient of variation from 35% to 22% ($p = 0.025$). No comparison of group scatter was possible with group 5, since a large proportion of the bonds did not break.

5.5 DISCUSSION

The bonding experiments of Chapter 4 investigated tissue bonding over a temperature range of 20 - 90 deg.C. The presence of large scatter in the bond strength results required investigation, and this was performed in this experiment at 55 deg.C. which was felt to be a temperature reasonably representative of the 20 - 90 deg.C. range previously used. It is likely that conclusions drawn from this experiment can be generalised to apply to the whole of the 20 - 90 deg.C. temperature range.

The starting point of the experiment (group 1) was the creation of dry bonds at 55 deg.C. with the technique of Chapter 4, involving roughly peeled slices bonded at low pressure with resultant large scatter in bond strength about the mean. A change of approach in group 2, using slices with smoothly cut faces provided statistically indistinguishable results from that of group 1 - ie. no change. However, the combination of smooth tissue faces with removal of inter-surface air gaps, dramatically reduced the scatter in bond strength, leaving the mean strength unchanged. This strongly implicates inter-surface air gaps (ie. poor apposition) as the primary source of scatter in dry bonds. Increasing the bond pressure from 5kPa to 25kPa further reduced the scatter with the mean still unchanged, but a higher pressure of 50kPa did increase bond strength.

Such findings can be well accounted for by the proposed model of bonding based on dehydration. This model suggests that dry bonding is a result of interactions between polarised regions of collagen molecules, which are normally occupied by water but become vacant with dehydration. Such interactions, based on Van der Waals forces, would be very short range and therefore good apposition would be critically important to the creation of tissue bonds. It is difficult to know what accuracy of apposition is required. Our results indicate that visible air gaps need to be removed, but it is not known to what extent (if any) micro-air gaps may be compromising bond consistency and strength. Our experience suggests that surface intimacy to better than $100\mu\text{m}$ is at least required, because as the series of

experiments progressed the approximator began to warp, and deformation of the bonding plates by more than $100\mu\text{m}$ made bonding almost impossible.

The removal of air gaps was not the sole reason for reduced scatter, since the technique was coupled with a much improved assessment of any air gaps that remained after bonding. Smoothing the bond at the time it was first placed on the approximator not only served to remove air gaps but aggregated those that remained, making them easier to see and measure when heating was finished. The improved method of air gap assessment contributes to a more reliable evaluation of bond strength per unit area.

The rise in mean bond strength at a high bonding pressure of 50kPa is not surprising since this is likely to force the tissue faces together, increasing surface intimacy beyond that which would normally be encountered. More bonds can form as a result, and bond strength increases.

5.6 CONCLUSION

Scatter in the strength of dry bonds was progressively reduced through systematic improvement of tissue apposition and improved assessment of inter-surface air gaps. Furthermore, bond strength increased with application of high pressure to the apposed faces. The dehydration model was able to account for these observations.

Chapter 6

Laser/Dry Bonding Equivalence

6.1 INTRODUCTION

The in vivo bonding work of earlier chapters showed laser bonds to be inconsistent. The work was inconclusive in so far as we were unable to draw any clear conclusions as to how to improve the technique, or establish why it sometimes did not work. The most important observation was that a smaller laser spot might be beneficial so as to reduce the extent of damage to surrounding tissue.

Our lack of success with the in vivo work prompted investigation from a different direction to establish some basic mechanism responsible for tissue bonding. This was achieved by the creation of overlap bonds constructed without the laser. The tissue apparently bonded by dehydration. The strength of the resultant bonds was evaluated and revealed that:

- i) Tissue bonds could be created at temperatures below the denaturation temperature of the tissue;
- ii) Dry bonds (ie. bonds created by dehydration) were much stronger than wet bonds;
- iii) A disproportionate jump in bond strength occurred as bonding temperature exceeded the denaturation temperature of the tissue;
- iv) Bond strength decreased with increasing rehydration.

A model was proposed to account for these results, in which bonding was considered the result of expulsion of water molecules from the collagen matrix by dehydration, exposing polarised bond sites suitable for the formation of collagen-collagen bonds. Although creation of the above overlap bonds was rather different to that of the laser bonds in vivo, it was proposed that the mechanism might be relevant to the laser bond. This chapter describes a series of experiments designed to investigate this hypothesis. If laser bonding is mediated by dehydration, the

properties of laser bonds should be indistinguishable from those created by dehydration alone.

Therefore, butt-jointed tissue bonds were created with and without the laser in conditions similar to those created *in vivo* (Fig. 6.1). To establish their similarity, the properties of the bonds were compared in three areas:

- i) Bond strength
- ii) The effect of rehydration.
- iii) Histology

These properties are also compared with the properties of the overlap bonds of Chapter 4 in an attempt to unify all the bonding activity through dehydration.

6.2 METHOD

6.2.1 EXPERIMENT 1: Bond Strength

6.2.1.1 Tissue Preparation

A section of aortic root approximately 2cm in length was isolated from fresh sheep heart obtained from the abattoir. The aortic segment was stored in refrigerated saline and used within 7 days. With a cut parallel to the longitudinal axis the segment was opened and laid flat, after which it was frozen and cut into rectangular sections approximately 140 μ m thick with a microtome. The slices were trimmed to a rectangular shape of approximate dimensions 20 x 10 x 0.14mm. Slice thickness was measured with a Mitutoyo tissue gauge, and was similar to the thickness of the rabbit carotid vessels bonded *in vivo* (Chapter 3).

An incision approximately 15mm long was made down the centre of the tissue section, parallel to the long axis of the rectangle. A clean cut was executed by placing the slice on a curved plastic surface and rocking a new microtome blade once along the desired line of cut to create the incision. The blade had been previously dipped in xylene and alcohol to remove any surface oil. The slice was laid flat on a glass slide, and the faces of the incision carefully dabbed dry with a paper towel. A thin line of chromophore was applied to the faces with a fine, pointed scalpel blade (using it like the nib of a pen) and the faces then dabbed dry to remove excess dye. A drop of saline was applied to the area to keep the tissue hydrated.

The tissue slice was transferred to a flat plastic-coated glass slide. (The presence of the plastic acts as a non-stick surface and minimises any tendency of the slice to adhere to the slide while bonding). Pulling the tissue from one end naturally brought the faces of the incision together which were then further

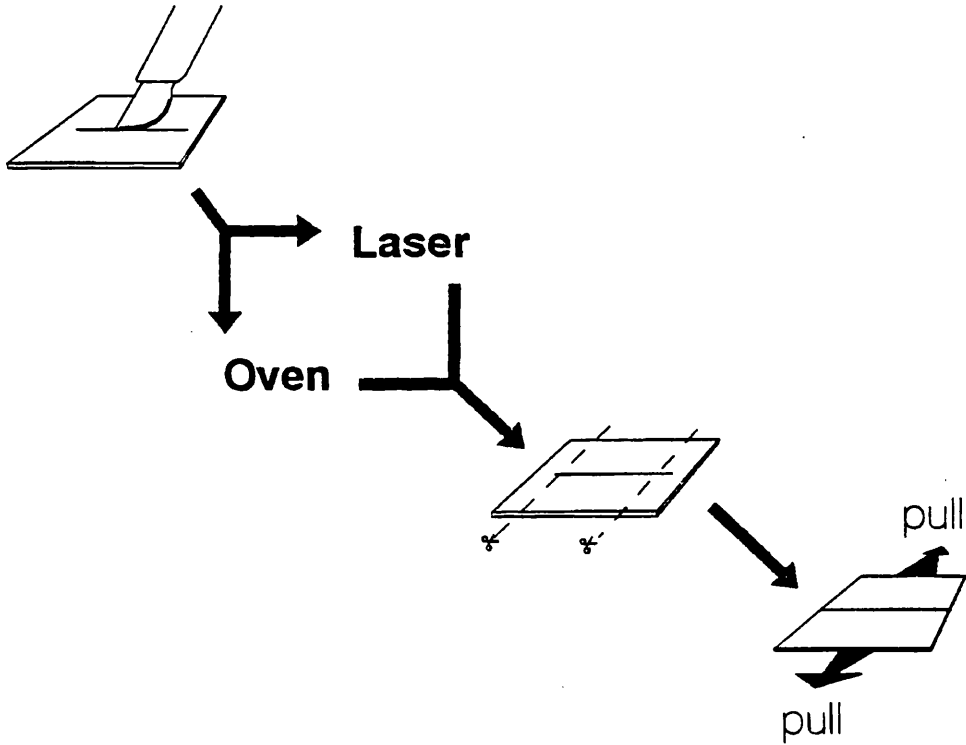


Figure 6.1 An incision was made in a thin tissue slice, and bonded back together by laser or dehydration alone (oven). After trimming, the strength of the bond was evaluated by measuring the force required to pull it apart.

apposed under a microscope (Mag. x10). Care was taken to ensure good apposition along the whole length of the incision. Moving to a higher power microscope (x50), the apposed incision was inspected for any gaps separating the bonding faces. If possible the gaps were removed by gently pushing the faces together. If this failed, the slice was discarded and the experiment started afresh. This approach enabled the removal of all visible gaps down to a diameter of about $2\mu\text{m}$.

To prevent unnecessary tissue dehydration during the bonding process, a long strip of soggy paper towel was placed on either side of the bond line and taped to the slide. The resultant glass/tissue/towel arrangement provided a suitably stable framework on which to perform tissue bonding.

6.2.1.2 Tissue Bonding

Tissue bonding was achieved by one of two methods. The first involved tracking a laser beam along the length of the incision (Fig. 6.2), with the laser handpiece attached to a constant speed linear motor. Several lasing parameters and tracking speeds were used. These are discussed below.

The alternative method placed the glass/tissue/towel assembly in a low temperature oven for 24 hours (Fig. 6.3). However, in order to stop the towel drying out (and hence the tissue beneath it) the slide was placed on a beaker with the towel ends suspended in water contained therein. The towels remained wet throughout the bonding period by capillary action. Details of the oven bonding temperatures used are discussed below.

In both cases (laser and oven) the method exposes only the area to be bonded to the applied bonding influence, with surrounding tissue remaining hydrated by virtue of the towels. Both techniques closely model each other and hence permit direct comparison of their bond strengths.

6.2.1.3 Bonding Parameters

The first group of bonds were created at temperatures below the denaturation temperature of the tissue (later confirmed by histology). For the laser bonds this involved a 65mW beam with a diameter of 1.5 ± 0.1 mm. The beam was tracked along the length of the incision at a constant speed of $1/30$ mm sec⁻¹ (ie. an inverse tracking speed of 30 sec mm⁻¹). The oven bonded slices were heated in a constant temperature oven at 36 deg.C. for 24 hours.

A second group of bonds was created at temperatures above the denaturation temperature of the tissue. Laser power was set to 100mW (1.5 ± 0.1 mm diameter spot) with the same inverse tracking speed as above (30 sec mm⁻¹). The dry bonded slices were heated in a 70 deg.C. oven for 24 hours.

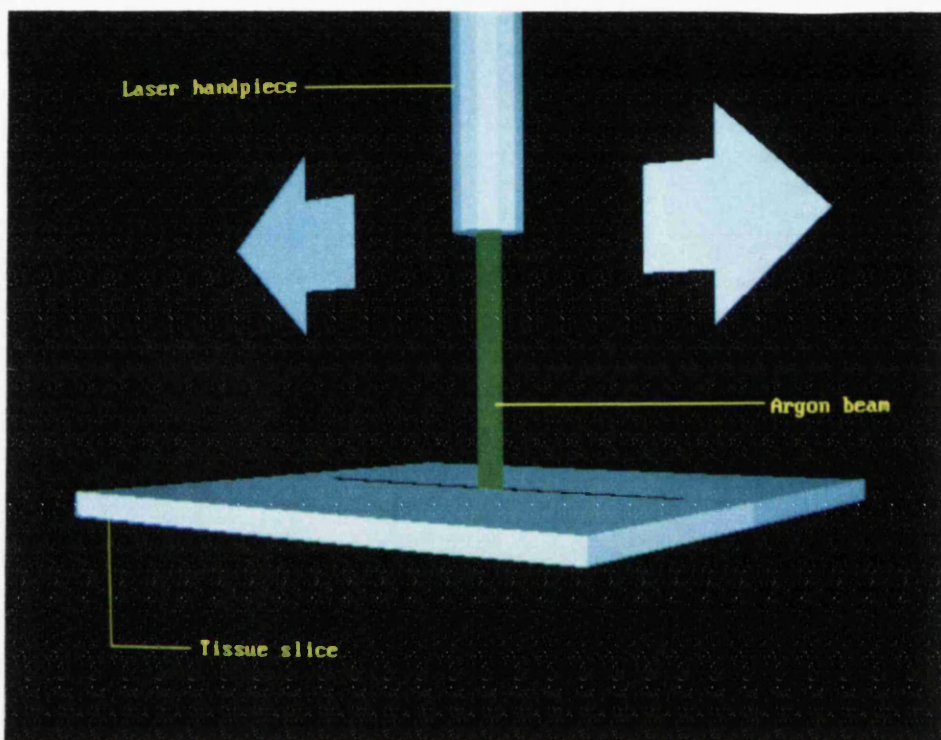


Figure 6.2 Laser bonding was achieved by tracking the beam steadily along the length of the incision.

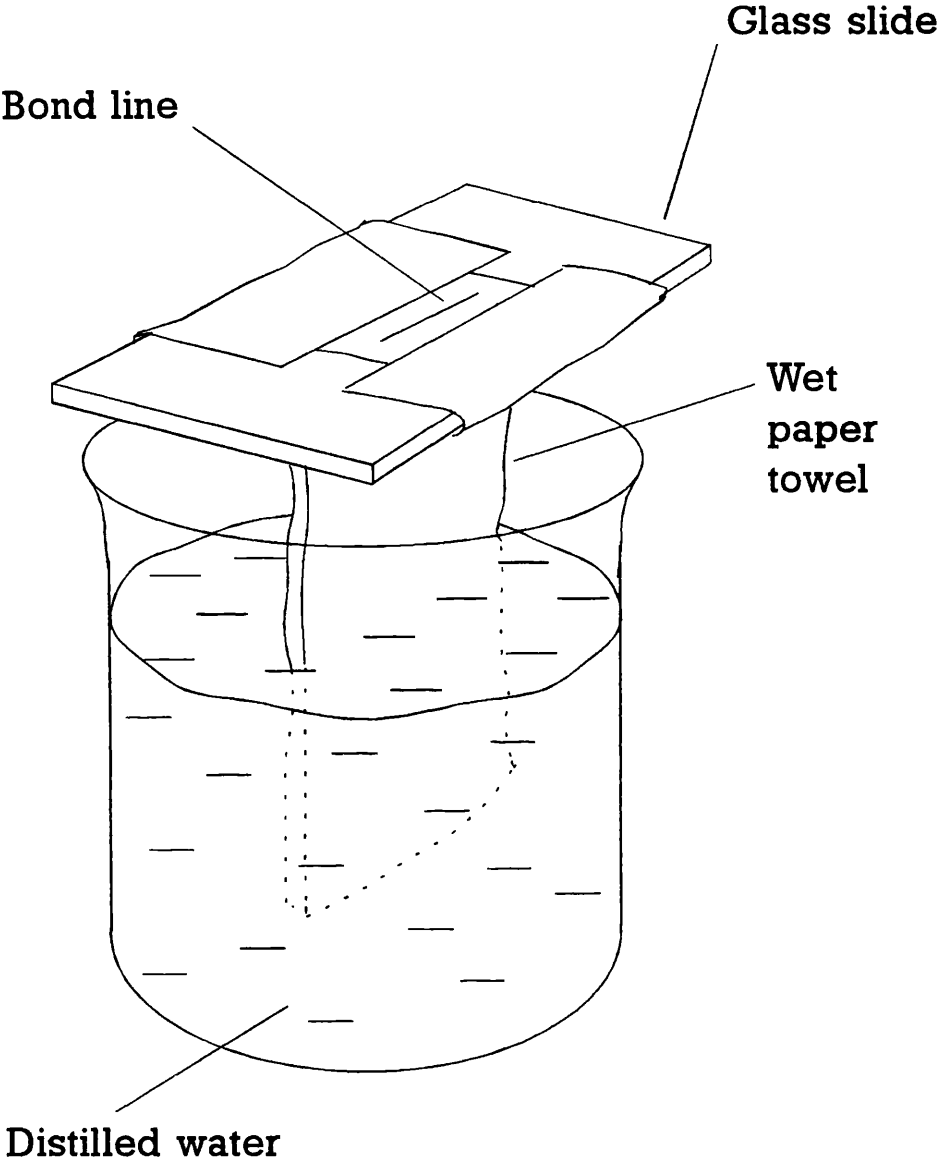


Figure 6.3 Oven bonding confines dehydration to the bond line only. The rest of the tissue is kept moist by the wet paper towel.

6.2.1.4 Preparation for Strength Testing

After bonding, the tissue joint was examined under a microscope (Mag. x50) to see if any gaps were visible along the length of the bonded incision. This was particularly relevant to bonds created in the oven since the more widespread shrinkage caused by oven dehydration tended to pull the apposed faces apart. The position and size of air gaps was noted, but in practice they were rare.

The dehydrated bond area was initially rehydrated with a few drops of saline and the soggy towels removed. More saline was applied, creating a puddle in which the slice was immersed. After 3 minutes, the sample was carefully removed from the glass slide and placed in a jar of saline, allowing ample rehydration of upper and lower surfaces. At 10 minutes, the bond was examined under a microscope (x50) and a note taken of any additional gaps that had opened along the length of the bond as a result of the above manipulations. The tissue was cut across the full width of the slice at each end of the incision by rocking a curved scalpel blade across the sample, placed on a glass slide (Fig. 6.4)). This created clean edges without stressing the bond. A central length of tissue approximately 1cm long is the result, bonded along the whole of its length. Using the rocking blade technique again, a 2-3mm wide section of the bond was removed from one end for histological examination.

The main slice (now a little less than 1cm long) was examined for the final time under the microscope for the presence of any gaps. If any were seen along the length of the incision at this stage, bonding was considered to have been unsuccessful and the slice discarded. However, most bonds were satisfactory, and were then rehydrated for a further 10 minutes, resulting in a total of 23 ± 2 minutes. The bonds were now subjected to strength testing.

6.2.1.5 Strength Testing

All tissue bonds were tested destructively under the same conditions, and the breaking strength of the bonds per unit area calculated. Bond length was measured with a travelling microscope and callipers, thickness having already been obtained. The sample was held between two clamps, both constrained to move in one dimension (ie. perpendicular to the bond line, in the plane of the tissue). The bond line was positioned midway between the clamps, parallel to their straight edges so that when pulled apart, stress was applied uniformly along the length of the bond (Fig. 6.5). One clamp was attached to a slow moving (approximately 0.25 mms^{-1}) hydraulic piston, whose speed of movement was highly reproducible. The other clamp was attached to a strain gauge which recorded the force applied across the bond on an X-Y plotter. As the piston advanced, it slowly pulled the clamps apart,

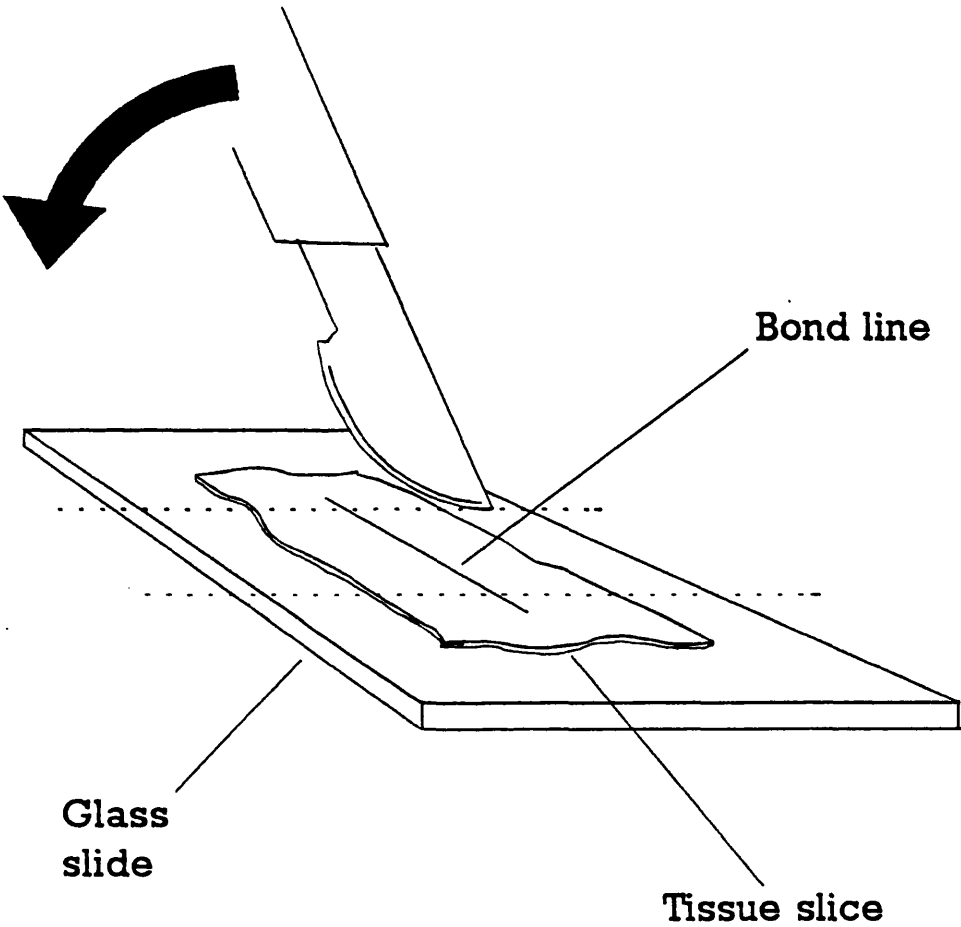


Figure 6.4 Trimming the bond prior to strength testing.

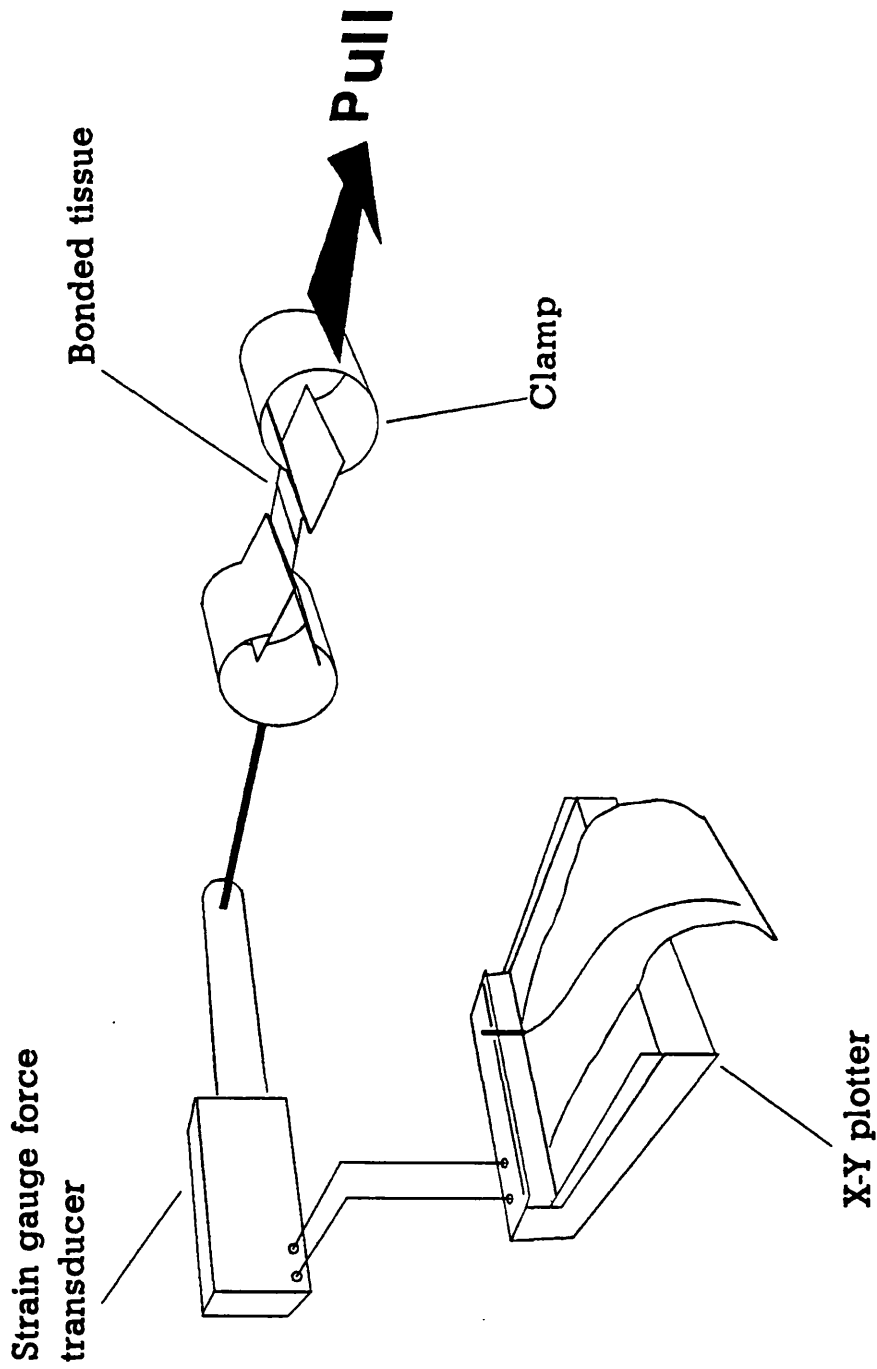


Figure 6.5 A force transducer measures breaking strength as the bonded slice is steadily pulled apart.

with the strain gauge recording the increasing force. Eventually, sudden disruption of the bond occurred (Fig. 6.6), and the breaking force was read off the X-Y plotter. From this, breaking force per unit area of the bond was calculated.

6.2.1.6 Tracking Speed & Bonding Times

It can be readily appreciated that bond strength must depend upon the tracking speed of the laser. If the beam is moved too quickly, an inadequate bond will form, resulting in reduced bond strength. Clearly, it is only valid to directly compare those bonds created at the same tracking speed. This presents potential difficulties with the oven bonded samples because tracking speed is not applicable. However comparison is possible because the dehydration model of bonding predicts a maximum bond strength for slow tracking speeds and long oven exposures. This is a logical result of the model, in which bond strength is related to the dehydration of the bond. Maximum bond strength is expected to occur when the tissue is fully dehydrated, independent of the method used to achieve it. This provides a region in which direct bond strength comparison can occur.

As a result, a series of laser bonds were formed (denaturation temperature not exceeded) with various tracking speeds. Bond strength per unit area was calculated and plotted as a function of inverse tracking speed (Fig. 6.7). In a similar manner, bond strength as a function of dehydration time was plotted for bonds created at 36 deg.C. in the oven (Fig. 6.8).

These graphs were used to determine the necessary bonding times and tracking speeds for direct comparison of bond strength. A choice of 30sec.mm⁻¹ was selected for the laser and an exposure of 24 hours for the oven bonded samples. Both lie on the bond strength plateau and represent maximum achievable bond strengths for both groups.

6.2.1.7 Histology

The small portion (2-3mm) of each bond removed for histology was fixed in 10% formol saline. 10 μ m thick paraffin wax sections were cut and stained with Picrosirius (PSR) and Elastic Van Gieson (EVG), thus enabling sample histology to be compared.

6.2.2 EXPERIMENT 2: Rehydration

In order to assess the effect of increased rehydration on laser bond strength, a series of low temperature (ie. tissue not denatured) laser bonds were created in the

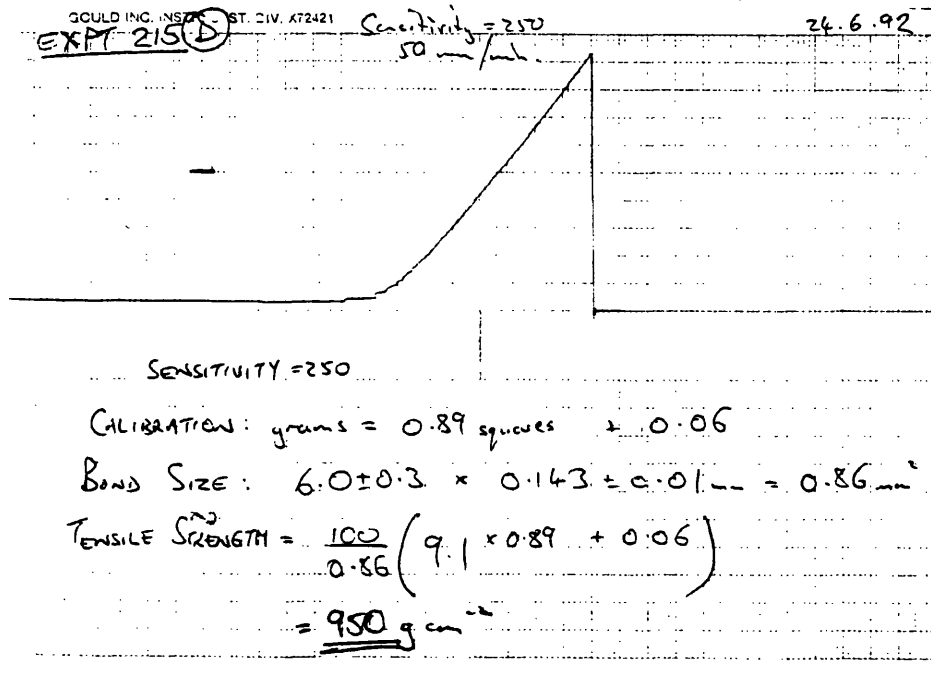
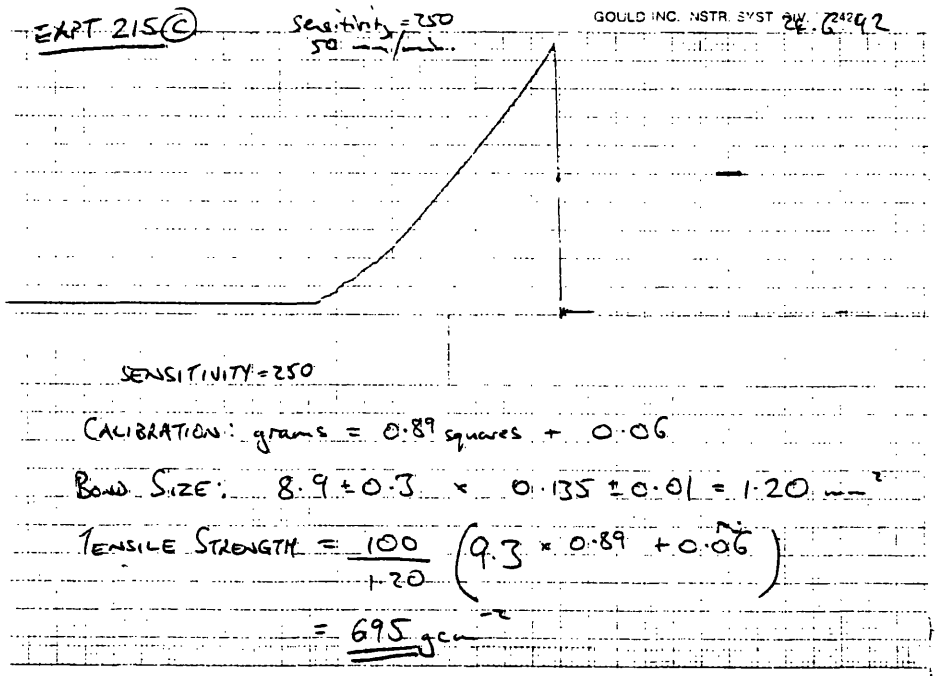


Figure 6.6 A typical trace from the X-Y plotter showing applied force (vertical axis) across the bond, versus time (horizontal axis). The sharp drop to zero is where the bond suddenly broke.

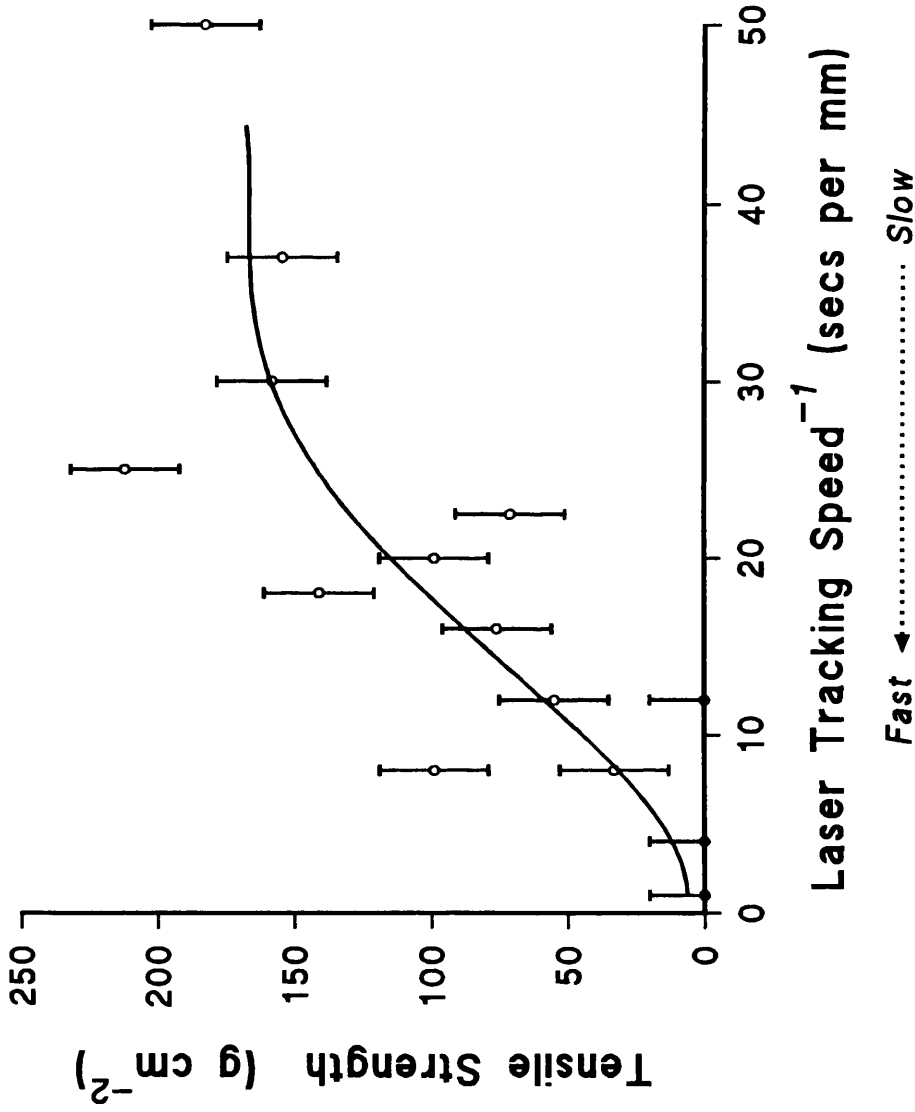


Figure 6.7 Bond strength as a function of tracking speed. The curve is a least squares 4th order polynomial fit to the data.

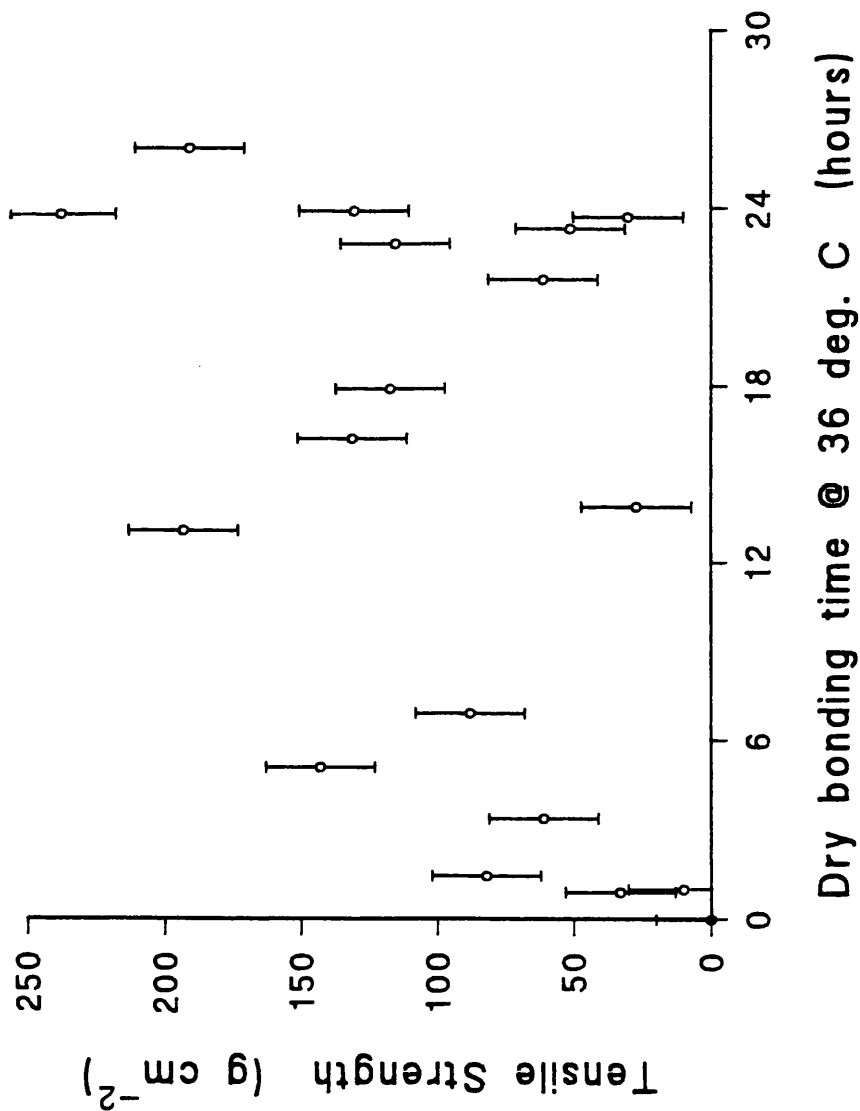


Figure 6.8 Bond strength as a function of oven bonding time at 36 deg.C. Scatter is large, but maximum strength reaches a plateau at large bonding times.

manner described above. However, the period of rehydration prior to strength testing was increased from 23 mins. to 5 or 6 hours. Strength testing was subsequently performed as per normal and the breaking strength per unit area calculated.

6.2.3 EXPERIMENT 3: Natural Breaking Strength of Unbonded Tissue

To help put the breaking strength of tissue bonds into perspective, a set of experiments was performed to evaluate the breaking strength of similar tissue containing no bond.

In the manner earlier described, aortic tissue slices were cut into sections approximately $100\mu\text{m}$ thick, and trimmed to a rectangular shape of the same dimensions as the bonds ready for strength testing. Tissue thickness was measured with a Mitutoyo tissue gauge, and average tissue width obtained by measurement with callipers at several points along its length. Each sample was placed in the strength testing clamps with the same orientation as the bonded samples. The strain gauge recorded the tissue breaking strength on the X-Y plotter, from which the breaking tensile strength per unit cross-sectional area was calculated, using the same method of calculation as for the bonded samples.

6.2.3.1 Statistics

There is no evidence that any of the experimental groups are normally distributed. On this basis, non-parametric statistical methods were used - Mann-Whitney U test (2-tailed) - to establish significant differences between the means of sample populations.

6.3 RESULTS: Comparison of Laser and Dry Bonds

6.3.1 Non-Denatured Samples

Comparison of bond strength per unit area of bonds created at temperatures below denaturation by either method (laser or oven) is shown in the figure (Fig. 6.9). Although not shown, errors in the tensile strength axis equate to $\pm 10\%$. The principal contribution comes from the inaccuracy in measured tissue thickness used to calculate the bonding area. Mean bond strength of the laser group was 234gcm^{-2} with a coefficient of variation (CV) of 47% ($n=10$). The results of the oven bonded group were similar (mean= 288gcm^{-2} , CV=46%, $n=8$), such that no significant difference exists between them ($p>0.1$).

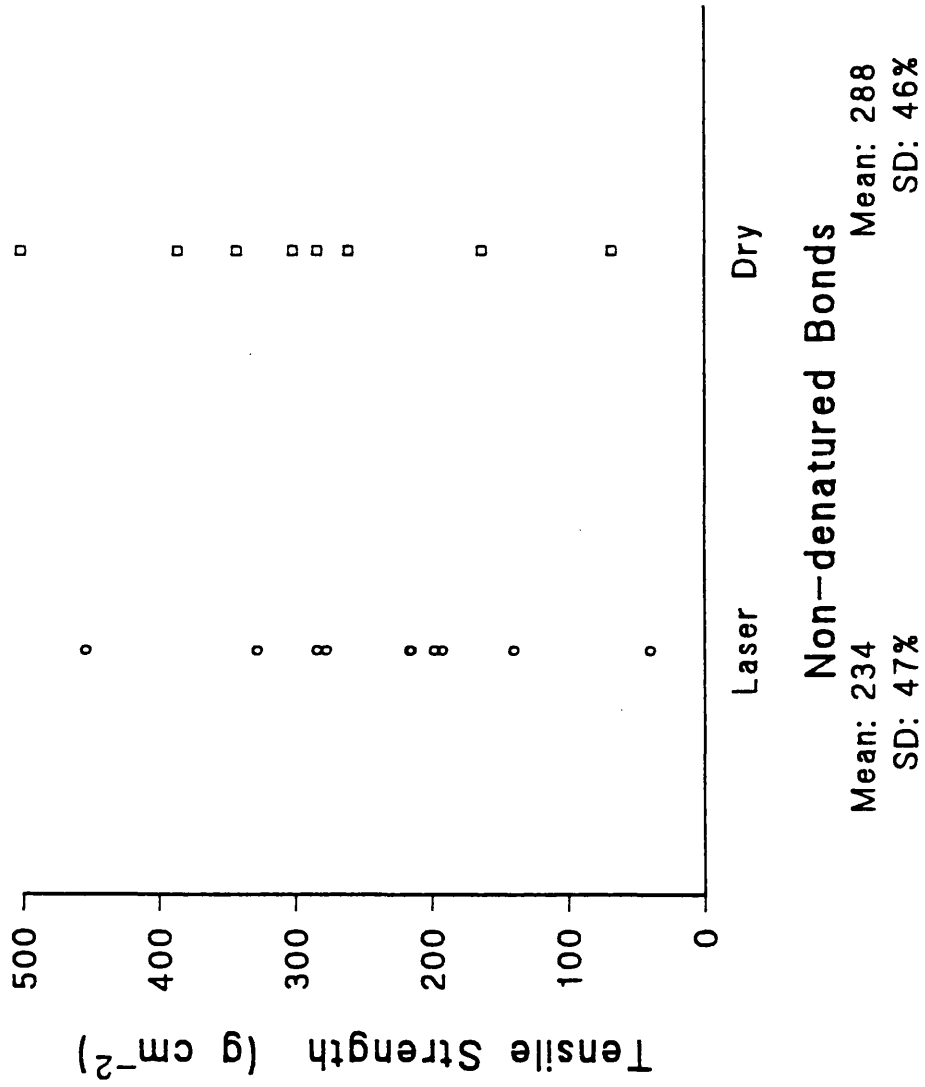


Figure 6.9 Strength of non-denatured laser and oven bonded samples compared.

6.3.2 Denatured Samples

The groups created at temperatures in excess of the tissue denaturation temperature exhibited a much increased bond strength over the non-denatured samples ($p < 0.015$ in both cases - Fig. 6.10). Table 6.1 tabulates the bond strength results. As above, error in each tensile strength measurement was $\pm 10\%$. Denatured laser bonds had a mean bond strength of 548gcm^{-2} ($\text{CV} = 52\%$, $n = 9$). Figures for the oven bonded group are: Mean = 994gcm^{-2} , $\text{CV} = 53\%$, $n = 9$. Unlike the low temperature group, these two have significantly different bond strength means ($p < 0.02$).

6.3.3 Rehydration

The strength of laser bonds created without denaturation and rehydrated for 23mins. or 5-6 hours is plotted in figure 6.11, tensile strength errors being $\pm 10\%$. The mean strength of laser bonded tissue with only 23 minutes rehydration is 234gcm^{-2} ($\text{CV} = 47\%$, $n = 10$). Mean bond strength after 5 hours rehydration falls to 101gcm^{-2} ($\text{CV} = 40\%$, $n = 7$). The two sets of data are significantly different ($p < 0.01$).

6.3.4 Natural Tissue Breaking Strength

The breaking strength of the non-incised/unbonded tissue slices is shown in the figure 6.12. Tensile strength errors equate to $\pm 10\%$, principally due to inaccuracies of the thickness measurement used to calculate the tensile surface area. With $n = 11$, mean breaking strength was 2350gcm^{-2} ($\text{CV} = 29\%$).

6.3.5 Histology

Histology consistently revealed that laser bonds created at 100mW were denatured in the lased area, whereas those created at 65mW were not. Examples are shown in the figures. Figure 6.13 shows EVG and PSR stained sections of a 65mW (non-denatured) laser bond. The connective tissue structure is well defined and the PSR image shows no loss of birefringence in the bonded area. This contrasts with the lased amorphous region of the 100mW EVG stained sample (Fig. 6.14), coupled with a marked loss of birefringence in the PSR stained section. This indicates considerable tissue denaturation.

Similar results were found with the dry bonds. The non-denatured section (Fig. 6.15 - bonded at 36 deg.C.) shows clear differentiation of connective tissue components (EVG) and no loss of birefringence in the PSR stained image. However, the 70 deg.C. bonded sample has lost its birefringence (Fig. 6.16), associated with the amorphous detail of the EVG stained section, indicative of tissue denaturation.

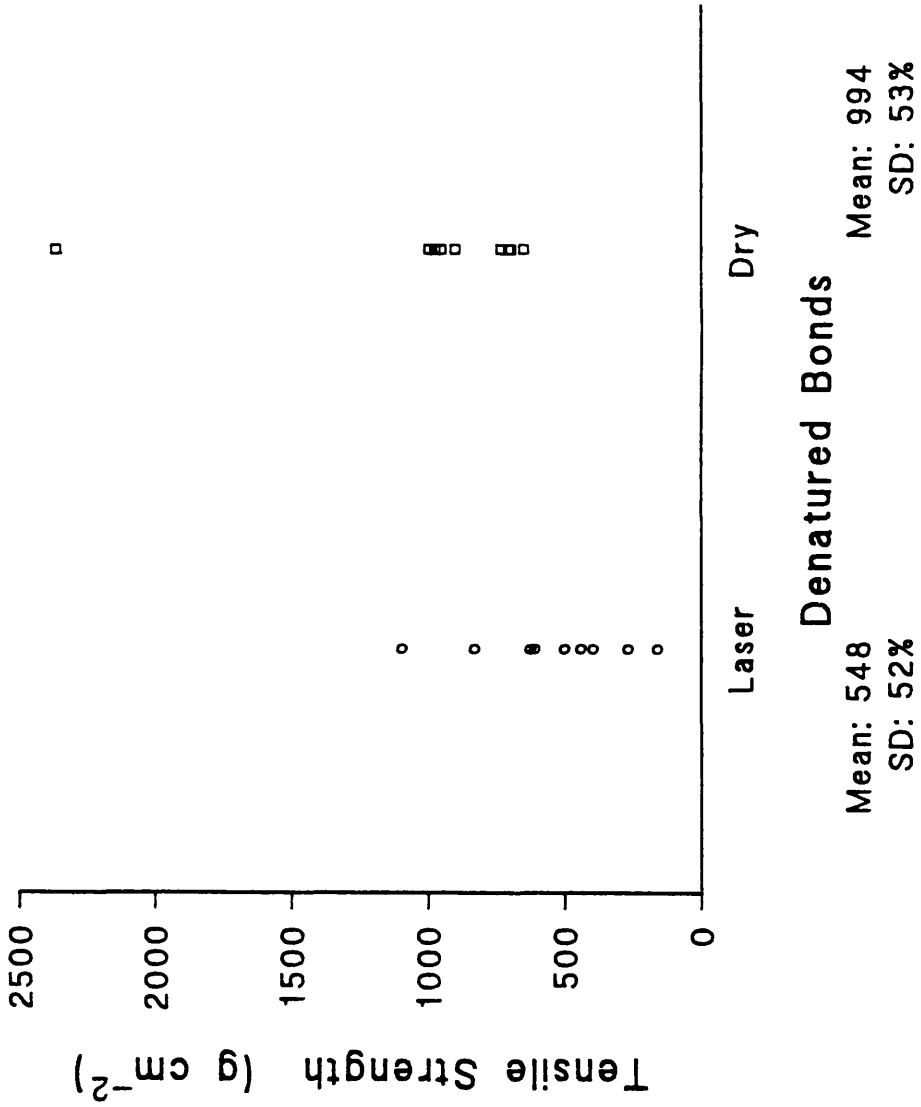


Figure 6.10 Strength of denatured laser and oven bonded samples compared.

BONDING TEMPERATURE: 36 deg.C.		
	Laser bond strength	Dry bond strength
	(g cm-2 ± 10%)	(g cm-2 ± 10%)
	215	301
	140	260
	216	68
	454	283
	192	163
	328	342
	277	385
	198	500
	284	
	40	
BONDING TEMPERATURE: > 70 deg.C.		
	Laser bond strength	Dry bond strength
	(g cm-2 ± 10%)	(g cm-2 ± 10%)
	609	972
	162	730
	397	695
	269	950
	1096	994
	442	898
	501	648
	625	2359
	830	702

Table 6.1 Laser and dry bond strengths.

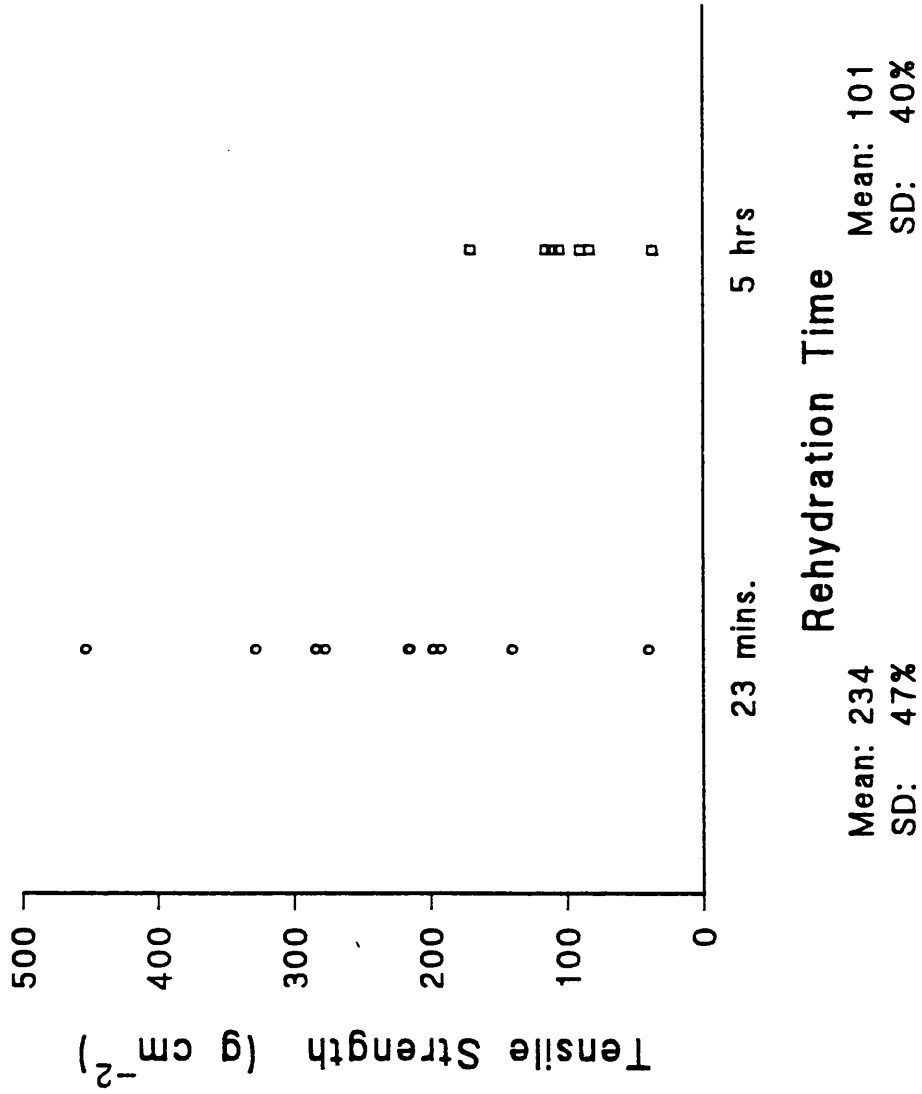


Figure 6.11 Laser bond strength as a function of rehydration time.

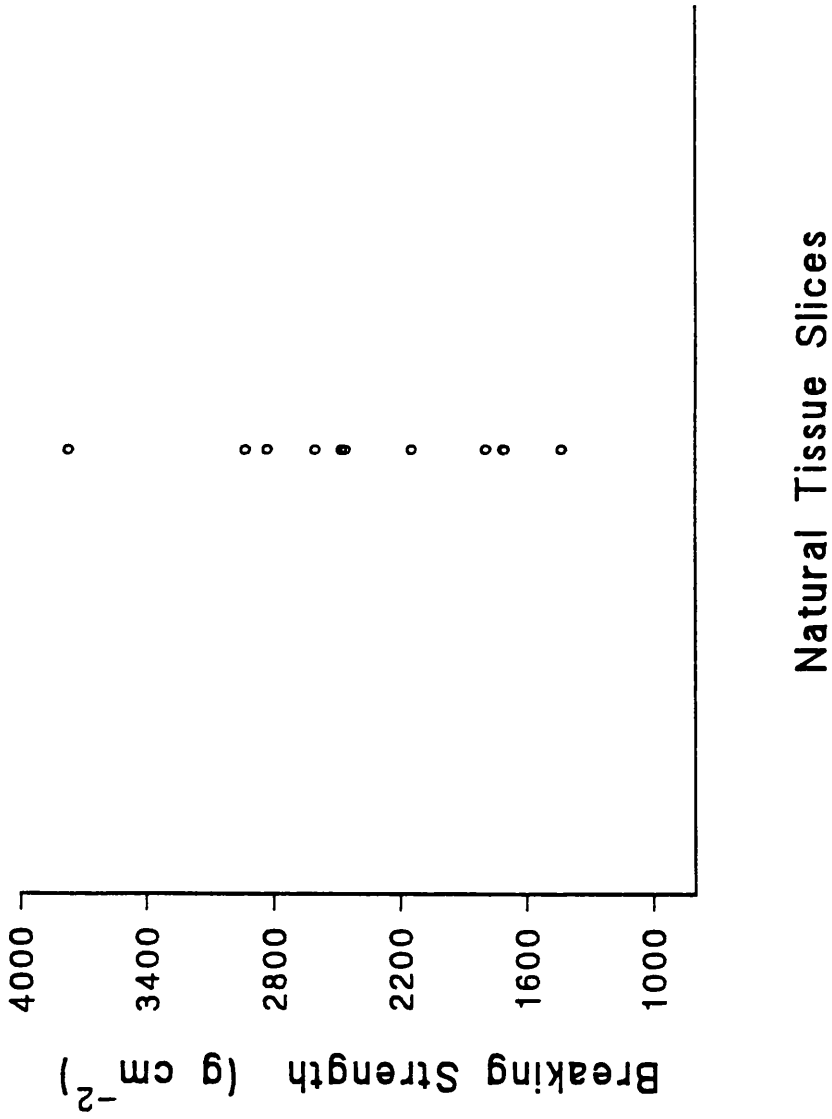


Figure 6.12 Natural breaking strength of unbonded tissue slices.

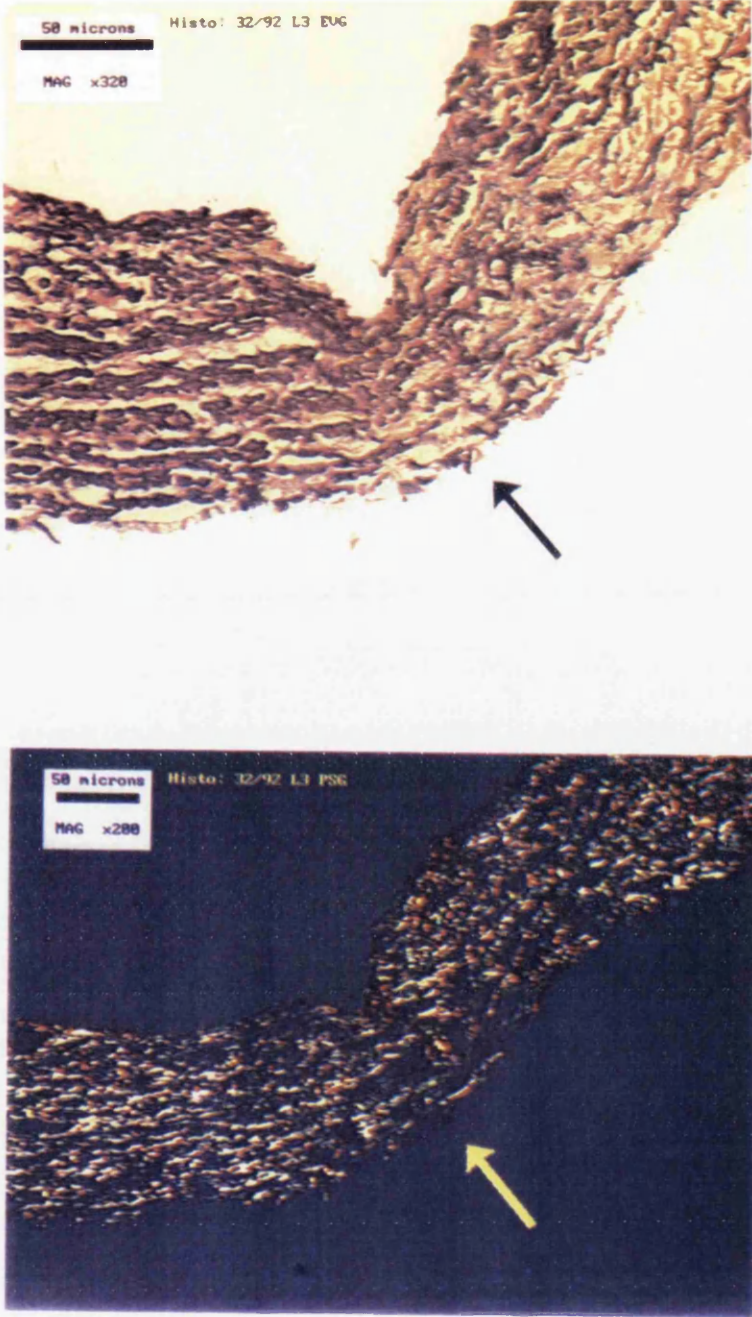


Figure 6.13 EVG (top) and PSR (bottom) stained sections of a 65mW (non-denatured) laser bond. The sections are transverse, perpendicular to the incision. The arrow points to the apposed bonded faces.



Figure 6.14 EVG (top) and PSR (bottom) stained sections of a 100mW (denatured) laser bond. The sections are transverse, perpendicular to the incision. The arrow points to the apposed bonded faces.

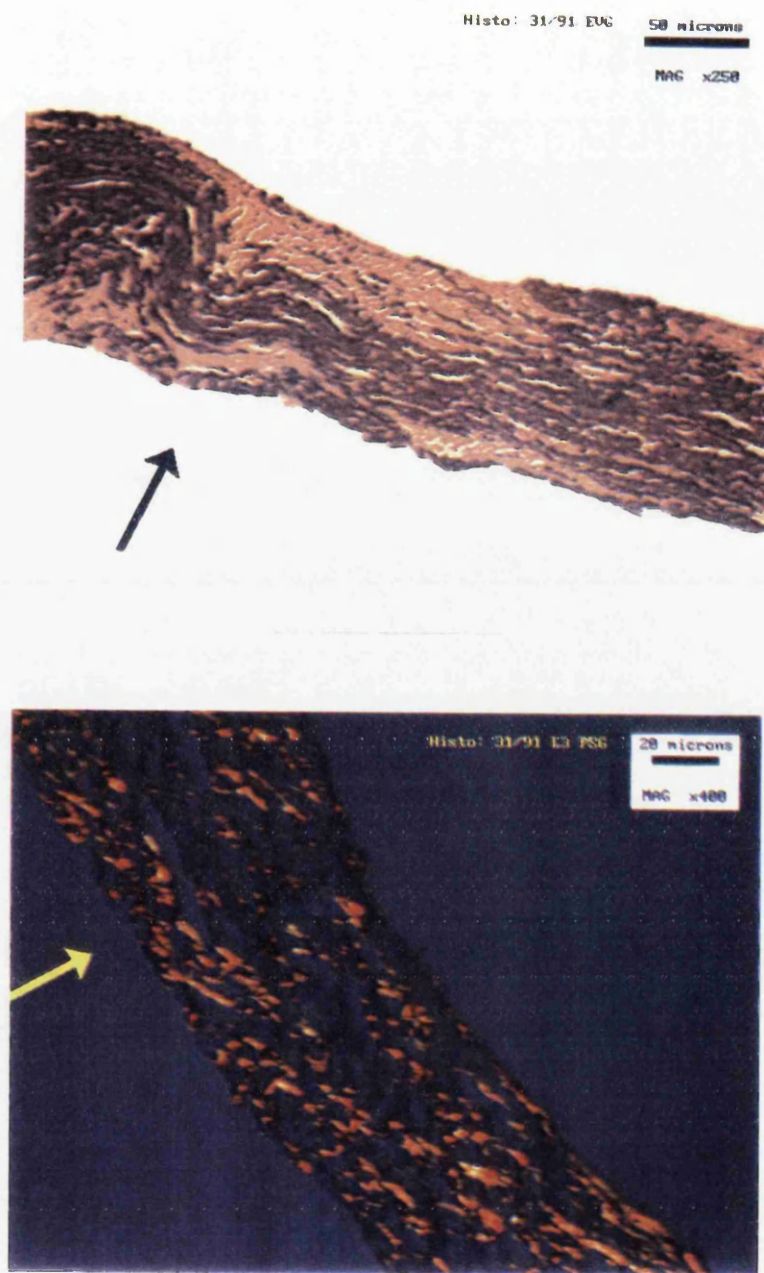


Figure 6.15 EVG (top) and PSR (bottom) stained sections of a 36 deg.C. (non-denatured) dry bond. The sections are transverse, perpendicular to the incision. The arrow points to the apposed bonded faces.

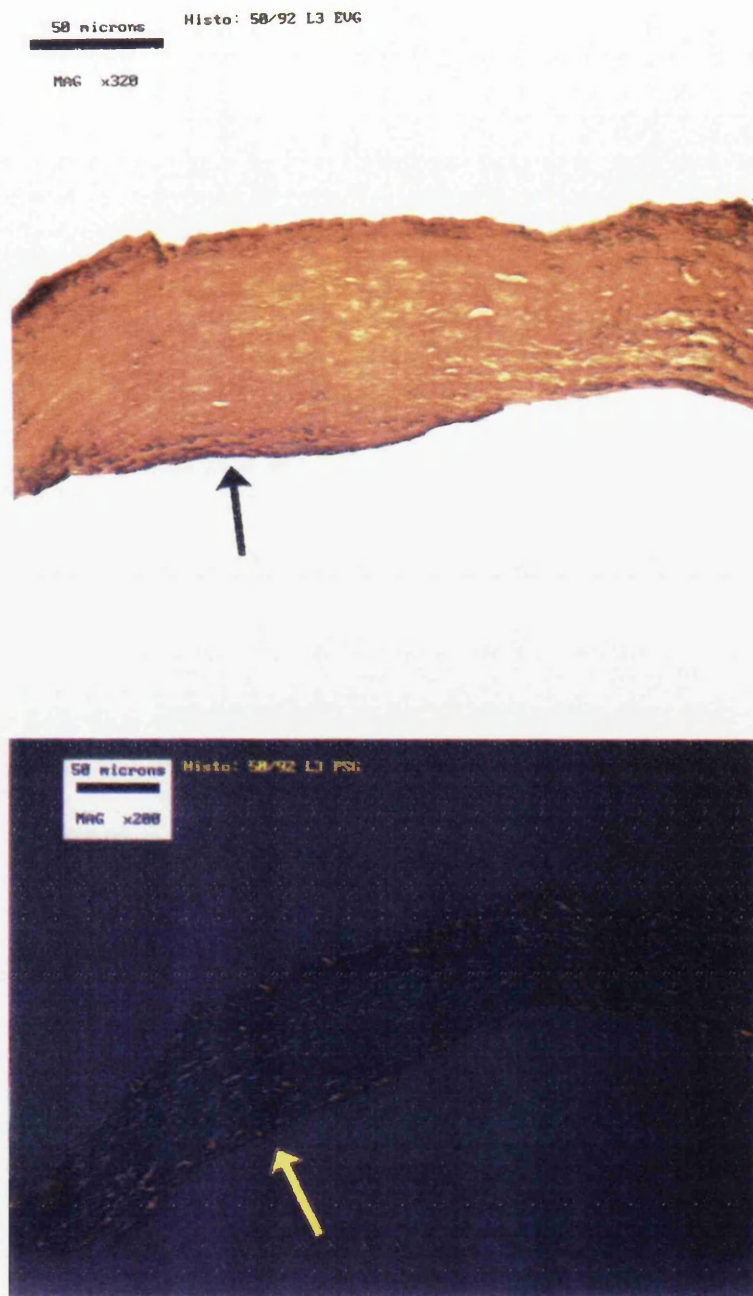


Figure 6.16 EVG (top) and PSR (bottom) stained sections of a 70 deg.C. (denatured) dry bond. The sections are transverse, perpendicular to the incision. The arrow points to the apposed bonded faces.

The histology shows that both dehydration and laser techniques (whether the tissue is denatured or not) can create tissue bonds of very high quality, to the extent that it becomes difficult to identify the bonded area. With the connective tissue stains we used, there was no histologically distinguishing feature to separate the laser group from the dry-bonded group. A macroscopic difference exists in that the extensive dehydration of the dry bonded samples tends to leave the bonded area more compressed after bonding and rehydration, than is generally the case for the laser. As a feature of interest, contrasting states of apposition are shown in the images of figure 6.17, in which both excellent and very poor apposition can be seen.

6.4 DISCUSSION

Earlier work proposed a mechanism for tissue bonding based on dehydration (Chapter 4). With this model, dehydration drives water from the collagen matrix, exposing polarised bond sites which are now free to bond to each other. Collagen binds to collagen, and a tissue bond is formed. The mechanism can be extended to include laser bonds if as has been proposed, movement of the beam along the length of the incision, produces localised dehydration beneath the beam, sufficient to bind the tissue together. On this premise, bonds created by laser are of the same nature as those created by dehydration, and both should exhibit the same properties. Furthermore, the overlap bonding work of Chapter 4 indicates what properties these might be, namely:

- i) Creation of bonds at temperatures above and below the denaturation temperature of the tissue;
- ii) A sharp increase in bond strength if the denaturation temperature is exceeded;
- iii) A reduction in bond strength with increased rehydration.

It is recognised that the large overlap bonds of Chapter 4 were created under rather different conditions to the lased rabbit carotid arteries of Chapter 3, which involved the bonding of butt-jointed, chromophore painted tissue approximately $150\mu\text{m}$ thick. However, the *in vitro* work of this chapter has attempted to correct this by mimicking the *in vivo* bonding conditions as closely as possible.

Since successful laser bonds were created in this experiment it indicates that the *in vivo* conditions have been adequately simulated. The work of this

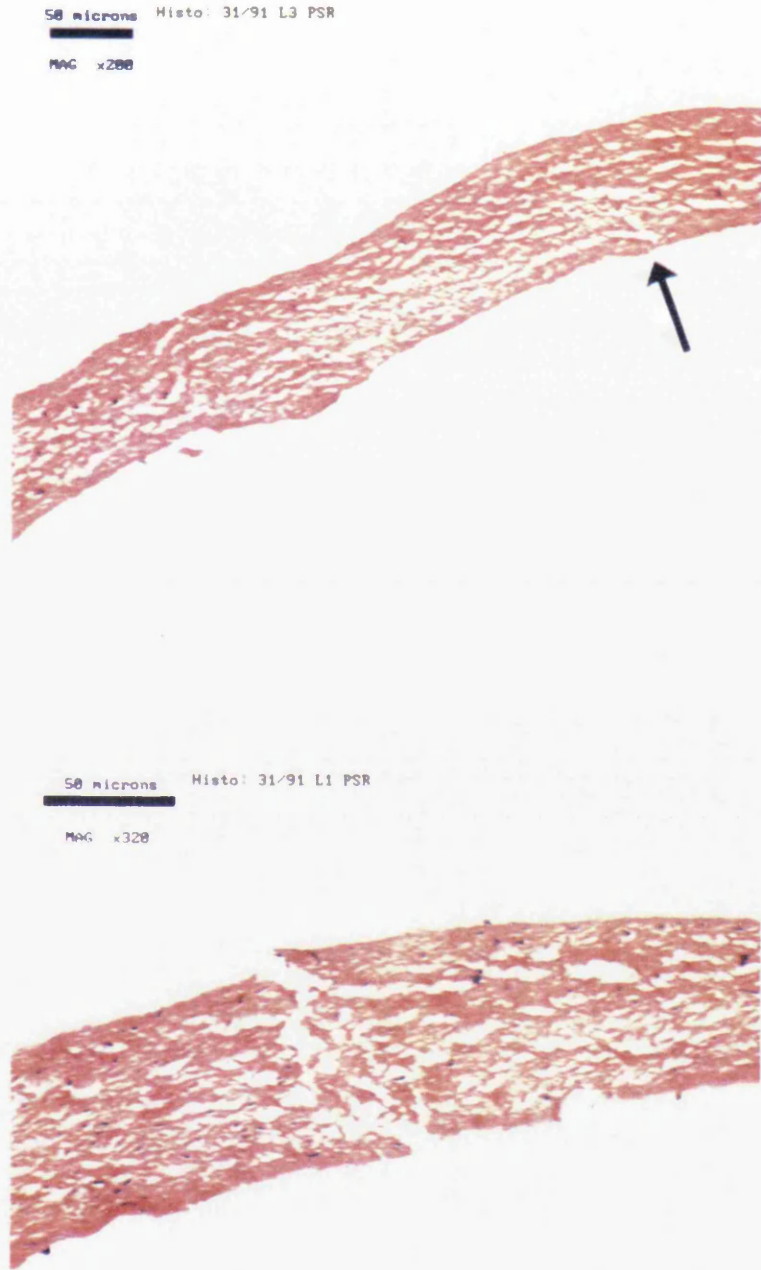


Figure 6.17 Contrasting quality of apposition. The near perfect apposition of the top image makes it difficult to identify the bond line (shown by the arrow). In the image below, the bonded faces barely touch. Both examples come from the same bond.

chapter proceeds to investigate further the properties of these bonds and compares them to the properties of the dry bond. Should they be the same throughout, it provides strong evidence that the laser bond is mediated by dehydration.

6.4.1 Breaking Strength of Tissue Bonds

In agreement with the results of the overlap bonding work, satisfactory bonds were created by both laser and dehydration techniques at temperatures below denaturation. Furthermore, comparison of strength of bonds created by either method revealed them to be statistically indistinguishable. However, the same cannot be said of those bonds in which the denaturation temperature of the tissue was exceeded. In this case although both groups have very similar scatter (also similar to the low temperature group), the mean dry bond strength is approximately 1.5 times that of the laser bonded group. The outlying dry bond point near 2500gcm^{-2} is remarkably strong and presumably due to unusually well apposed bonding faces. The strength testing equipment was unable to apply enough force to break the bond, and hence its actual breaking strength is in excess of this figure, as represented by the arrow attached to the point on the graph. Even if ignored as a freak result, the rest of the group still remains significantly different from the laser group. This result is difficult to explain if the two types of bonds are the same.

Both laser and dry groups mirror the jump in bond strength predicted by the results of the overlap bonding experiment when the denaturation temperature is exceeded. In the case of overlap bonds, mean bond strength increased by a factor of 2.1 (Chapter 4). This is similar to the increase of the laser bond in this experiment (factor of 2.3) which is not as great as the increase in the strength of the butt-jointed dry bonds (factor of 3.4).

Further correlation with the results of the overlap bonding experiment is indicated where rehydration is concerned, since the laser bonds were shown to weaken with increased rehydration, mean bond strength decreasing by a factor of more than 2 over a 5 hour period.

6.4.2 Tracking Speed & Bonding Time

The dehydration model can account for the distribution of the bond strength/tracking speed graph of figure 6.7. The model maintains that bond strength is directly related to the state of dehydration of the tissue, so that when all water is removed, maximum bond strength is achieved. Therefore, reducing the speed at which the beam moves, allows it to increase dehydration of the bond, thus creating more bonding sites and increasing bond strength. This reaches a maximum when all available water is removed. Further exposure by the laser does

not increase bond strength because all available bonds have been used. A similar argument applies to the oven bonded samples, with bond strength increasing to a maximum with increased dehydration time.

Unfortunately, the scatter of the bond strengths is such that these observations are not obvious, but the maximum strengths for a given bonding time or tracking speed do show a trend in the direction described. Fundamentally, the model suggests that as long as the exposure times in either case are long enough, maximum bond strengths will be achieved, permitting their direct comparison.

6.4.3 Breaking Strength of Natural Tissue

The mean breaking strength of the unbonded tissue slices was found to be approximately 10 times that of non-denatured bonds, and less than 5 times greater than denatured bonds. It is interesting to note that the scatter in breaking strength of the natural tissue is quite large (CV = 29%) and perhaps indicates that natural tissue inhomogeneity might also be responsible for the scatter in bond strength, in addition to apposition discussed in the previous chapter.

6.4.4 Histology

All bonds were fixed, stained and sectioned in the same way. The structural component of both types of bonds were shown to be the same when stained with the collagen specific Picrosirius stain, and the more general connective tissue stain Elastic Van Gieson. The only visible difference between the groups was that the more widespread dehydration of the oven bonded tissue (due to the area of dehydration being less localised than the laser beam) caused greater shrinkage of the bond area and thus the dry bonded sections looked compressed in comparison to the laser bonds.

The Picrosirius stain consistently confirmed that the low temperature bonds were created without denaturing the tissue. Laser bond temperature was estimated to be between 40 and 60 deg.C. Similarly, all the higher temperature bonds showed histological evidence of denaturation. Laser bond temperature in this case was estimated to be of the same order of magnitude as the in vivo experiments (ie. 70 ± 10 deg.C.) since lasing conditions were similar.

6.4.5 Experimental Technique

In the bonding of the rabbit carotid (Chapter 3), the vessel edges were left to fall into natural apposition. Such a condition would have been better simulated in this experiment if the tissue had only been supported around its perimeter, rather than placed on a glass slide. This leaves the bond free, exposed to air on both sides. In

reality, this was unworkable because the surface tension of the saline solution in which the tissue had been stored, acted to pull the freely hanging apposed faces apart, giving very poor apposition. In contrast, supported on a glass plate the tissue edges remained wherever they were placed, allowing apposition to be accurately controlled, especially with the use of a microscope.

However, considering the scatter of the bonding results it would appear that apposition was not controlled accurately enough, and experience bore this out. Clearly it is important that the incision be clean and precise in order to create accurate butt-joints. The cut must not damage or squash the abutting edges for poor apposition will be the result. Hence, a scalpel blade was initially used for this purpose, being frequently changed to maintain a sharp edge. However, the resultant bonds displayed a disconcerting amount of scatter considering the highly constrained manner in which the whole of the experiment was performed. This led us to examine the knife blades under a microscope, being one of the few remaining variables outside our control. Examination revealed a sharp edge with occasional non-uniformities along its length. In contrast, examination of numerous Wilkinson Sword Microtome blades showed them all to have a perfect edge. These were used instead of the scalpel blades, with immediate results - mean bond strength changed significantly (Mann Whitney U, 2-tailed; $p < 0.01$) in addition to a reduction in the scatter of the results. The graph (Fig. 6.18) illustrates the effect. Henceforth a new microtome blade was used for each incision that was created.

This result was surprising because all bonds were apposed under the microscope, which enabled removal of visible bond gaps as small as $2\mu\text{m}$. To the observer, all apposed incisions appeared to be of equally high quality, independent of the blade used, since all visible gaps had been removed. But perhaps this method is not as thorough as it first seemed, because a bond gap could only be identified by the tell-tale spot of light resulting from penetration of the microscope illumination through the crack in the incision. It seems reasonable that looking down on tissue $140\mu\text{m}$ thick, a spot may only be visible if there is a non-apposed channel down the full depth of the face. Should apposition occur anywhere throughout the depth of the tissue, the light may be blocked and the tissue appear apposed. Therefore, it could be suggested that at best our checks served to ensure partial apposition along the whole length of the bond. Clearly, exceptional apposition beyond that which can be achieved with a microscope is required for strong consistent bonding.

It was only the oven bonded group that changed bond strength in response to the change in knife blade. This is not surprising when it is considered that the lasing experiment requires stability around the bond area for a few minutes while

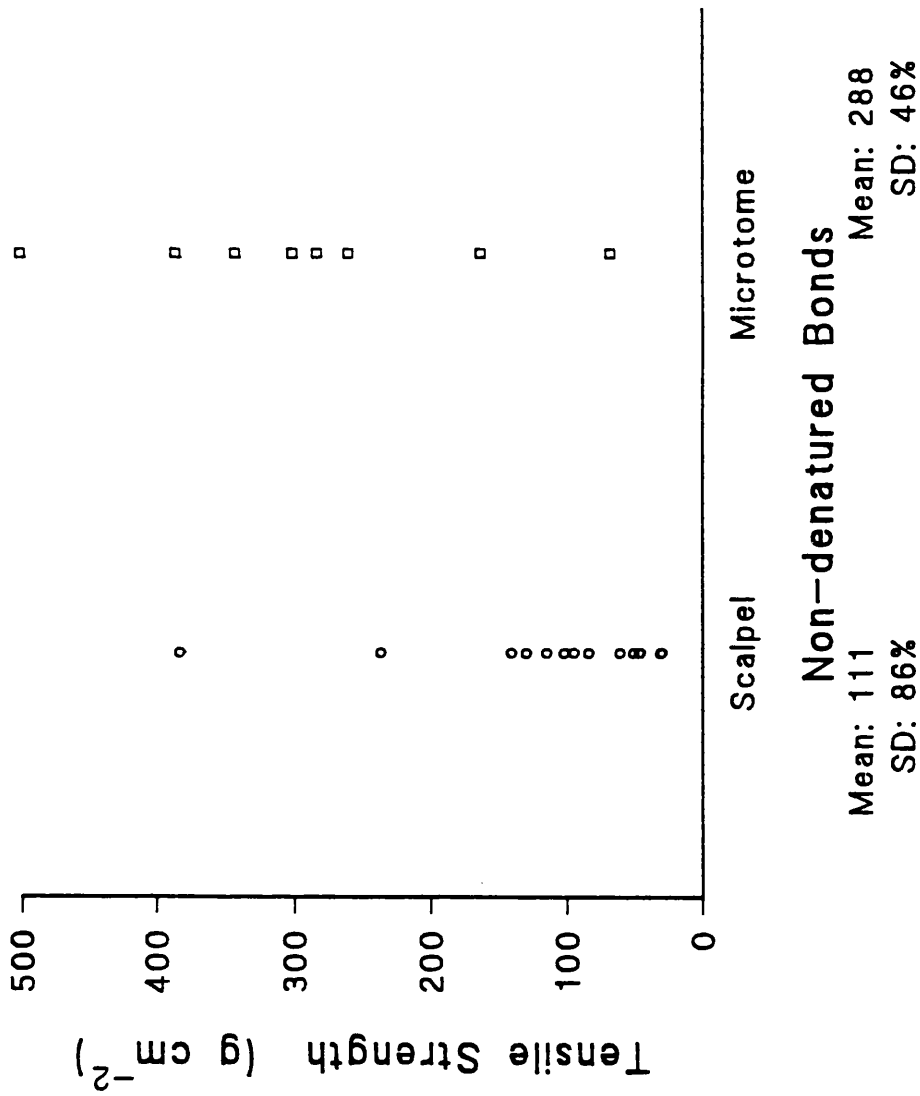


Figure 6.18 Comparison of dry bond strength under different cutting conditions. The bonding incision was created by scalpel blade or microtome blade.

the incision is lased, whereas the dry bonds require stability for 24 hours, further complicated by the more widespread shrinkage of the tissue during this period.

The oven bonded samples were visibly dehydrated in the bond area, observed as a change in tissue colour from an opaque white to a translucent brown/yellow. This was also frequently visible on a much smaller scale for laser bonded samples, along the path the laser beam had travelled.

6.5 CONCLUSION

This series of experiments has compared the properties of butt-jointed bonds created by laser and dehydration in an oven. The properties of these bonds have been shown to be the same as the overlapped dry bonds of Chapter 4. The similarity in properties between these laser and dehydrated bonds provides strong evidence that they are of the same type, and that the laser bond is thus mediated by dehydration. The presence of large scatter in the breaking strength of the natural unbonded tissue, indicates that biological variability may be a contributor to the scatter of the bonding results in addition to inadequate apposition.

Chapter 7

Laser Tissue Interactions

7.1 INTRODUCTION

Experimental data thus far has indicated that dehydration is primarily responsible for low temperature tissue bonding by Argon laser. However, earlier work by other groups has attempted to establish an explicit link between temperature and bonding since it was considered to be a temperature dependent process. The bonding mechanism was not known, but the presence of tissue denaturation at a readily achievable 60-65 deg.C. appeared a convenient focus for bonding. From our experience of the inconsistent nature of laser bonds produced in vivo, it appeared that a critical condition for bonding was not being consistently achieved. In the light of general opinion, it seemed reasonable to suggest that bonding temperature was this critical condition. If temperatures were too low, inadequate bonding would occur, and if temperatures were too high, destructive effects might be induced. The magnitude of the acceptable temperature range could only be estimated, but given our poor results, was perhaps only of the order of a few degrees Centigrade.

From a biological standpoint, it is clear that the ideal temperature is the lowest at which a satisfactory bond can be achieved in order to minimise damage to surrounding healthy tissue. It is known that healing effects propagate from undamaged tissue, suggesting that the greater its proportion within the lased area, the better the healing. This prompted the use of chromophore on the bonding faces to create locally increased absorption. The result is lower laser powers for the same bonding effect (43,44,45,51), with reduced exposure to surrounding tissue.

Whatever the mechanisms, knowledge of the temperature distribution during bonding appeared essential if the technique were to be improved. Various options were considered in the pursuit of detailed temperature information during lasing.

7.2 TEMPERATURE MEASUREMENT

7.2.1 Contact Probes

Under the lasing conditions employed, measurement of tissue temperature during bonding with a contact probe presents numerous difficulties, principally because of the small scale involved (volume of interest approximately 0.2mm^3). The probe must be small enough to leave the light distribution within the tissue unaltered. It must also be small enough to record spot temperatures in 0.15mm thick tissue in which steep temperature gradients may occur (17 deg.C. over $400\mu\text{m}$ has been quoted (111)). Larger probes would record an average temperature. A small thermal mass is required so that the presence of the probe does not alter the temperature distribution being measured. Investigations revealed that even a microthermocouple (RS component no. 158-913) presented significant inaccuracies at this scale since it represented a significant proportion of the volume being measured. It was concluded that a contact probe was unsuitable.

7.2.2 Remote Sensing

Remote sensing (eg. thermal camera) is an alternative approach, with the major advantage of requiring no contact with the sample. Even so, the small volume of interest exposes the limitations of this equipment.

A thermal camera determines temperature by monitoring the radiation emitted from a thermal source. A lens system focuses the infra-red scene onto a pyroelectric plate, the magnitude of induced charge at any point on the plate being proportional to infra-red intensity at that point. The charge distribution across the plate can be read by a raster scan and output to a monitor screen. The camera assumes that radiation is emitted from a perfect black-body (emissivity = 1) and measures the intensity in the $8\text{-}12\mu\text{m}$ region, from which it deduces the overall shape of the emission curve, and hence the black-body temperature. With careful calibration, referenced to black body sources, the camera is capable of accuracy of better than 0.5 deg.C.

The system has several limitations. Absorption of radiation emitted from the source (before it reaches the camera) is registered by the camera as reduced intensity and therefore displayed as a decreased temperature. Hence, a change of aperture affects recorded temperature since it alters intensity of radiation arriving at the charged infra-red sensitive plate. The strong absorption by water of radiation in the $8\text{-}12\mu\text{m}$ band, limits the depth of tissue that can be sensed. 90% of the observed emissions in the $8\text{-}12\mu\text{m}$ band from a heated tissue sample, come from the top $30\text{-}40\mu\text{m}$.

The camera also suffers from the usual limitations of any imaging system, summarised by the modulation transfer function (MTF), the angular resolution equating to approximately 15 milliradians. With a working focal distance of 30cm, a 2mm laser spot is at the limits of its resolution. Although the camera can 'see' such a source, its spatial frequency response is such that spots of this size are assigned temperatures below their true value.

For all its limitations, the camera appeared a better choice than the probe. It does not modify temperature within the tissue, and even though its indications will be incorrect under our conditions, it may be possible to correct the image by suitable calibration and compensation for the MTF with image processing techniques. This work is in progress.

Other groups (47,70,81,82) have used thermal cameras to assess bonding temperature, but often there is no suggestion that the limitations of the imaging equipment have been taken into account. It is important to quantify the errors since they may be large. The histological results from our in vivo work suggested that the camera may be in error may be as much as 20 deg.C. (tissue visibly denatured but camera registers 45 deg.C.). Our camera (without correction for the MTF) yielded results similar to those of White et al. and implies that his data may be inaccurate. In addition, temperatures at depths in excess of 40 μ m are not visible to the camera due to absorption of radiation by more superficial layers. Thus the camera can at best be expected to produce only an averaged picture of surface temperature. It certainly does not have the resolution to image localised hotspots of sub-millimetre diameter which might be denaturing tissue and possibly critical to bond strength.

7.2.3 Model

It is clear that neither contact probes, nor remote sensing is adequate alone for detailed investigation of the evolving temperature distribution within the tissue. Thus it was considered that a mathematical model might be appropriate, possibly providing detailed insight into the dynamic temperature evolution of the lased sample. Such a model could be validated against the thermal camera in those areas in which the camera was known to be correct, and by extension, the model could then be assumed to be correct at a detailed level beyond the resolution of the camera. However, given the experimental evidence that dehydration is the prime cause of tissue bonding, we would suggest that a model based on temperature alone would be unable to account for tissue bonding. Whereas, if it were extended to include dehydration it might satisfactorily account for the bonding effects observed.

7.3 MATHEMATICAL MODEL

7.3.1 Introduction

For the purposes of modelling the temperature distribution within the sample, detailed knowledge of the interactions between laser light and the sample are required. The absorbed light is treated as the energy source that heats the tissue. A typical sequence of events leading to tissue heating is outlined below:

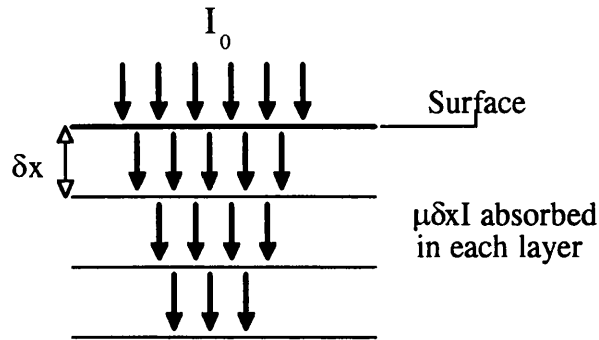
- i) Collimated light from the laser falls incident upon the tissue surface;
- ii) The refractive index change from air to tissue causes a proportion of the light to be reflected off the top surface, the remaining fraction entering it;
- iii) As the light travels through the tissue it is both scattered and absorbed;
- iv) That component which is absorbed, degrades into heat to diffuse into surrounding areas as dictated by heat transfer processes (principally conduction), from which a temperature distribution can be calculated.
- v) The tissue dehydrates at a rate defined by the temperature.

In detail the interactions are both many and complex, but can essentially be broken into two phases - (i) the evolving light distribution, and (ii) the resultant temperature distribution due to heating. A simplified approach to both is required, and each is taken in turn. The light distribution is discussed below, and heat flow discussed in the next chapter.

7.4 LIGHT DISTRIBUTION

7.4.1 Beer's Law

The traditional approach to modelling the intensity distribution within an absorbent medium is to imagine the light advancing through a 1-dimensional sample composed of multiple layers. With incident intensity I_0 , a fixed proportion $\mu\delta x I$ is absorbed as the light passes through each layer, μ being the absorption coefficient per unit length and δx the thickness of each layer.



The difference in intensity (δI) between successive layers is that which is removed by absorption:

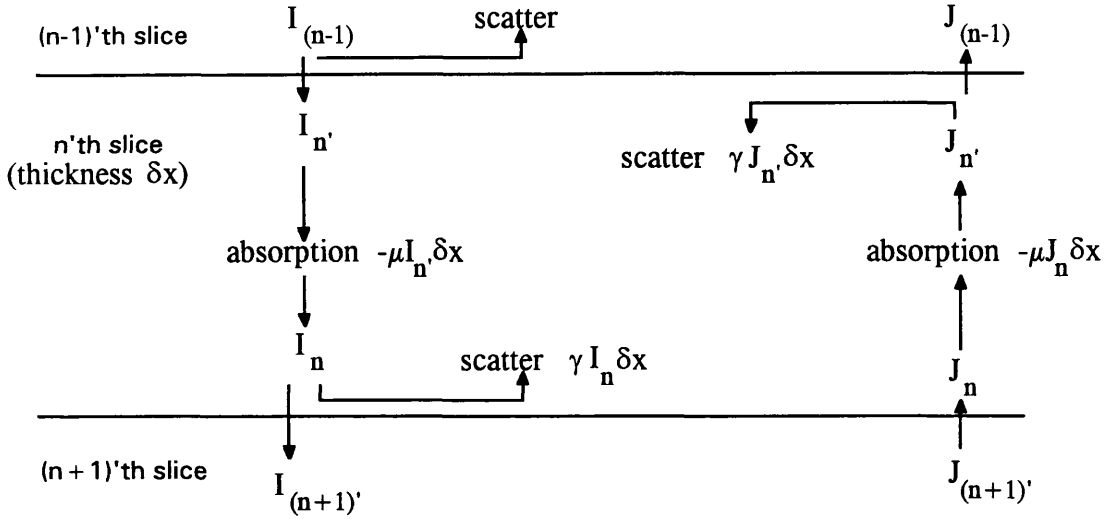
$$\begin{aligned} \delta I &= -\mu \delta x \\ \Rightarrow I &= I_0 \exp(-\mu x) \end{aligned}$$

This standard result gives exponential decay of intensity with depth - known as Beer's law. It agrees well with experiments in which successively thicker sample slices are irradiated with incident light and in which little scatter is present, the transmitted light intensity being measured as a function of sample thickness.

Compare this to a situation in which light is passing through a scattering material, where γ (the linear scattering coefficient) dictates the proportion scattered in each layer and μ is the linear absorption coefficient. In this instance, at each infinitesimal layer a proportion $I\gamma\delta x$ is removed from the intensity for subsequent scattering in addition to the $I\mu\delta x$ lost to absorption. However, the resultant transmitted intensity is not $\exp(-\alpha x)$ with $\alpha = \mu + \gamma$ as might be expected from a Beer's law type derivation, because that part of the light removed for scattering is itself partially scattered back into the incident beam. Hence the effective attenuation coefficient α , can be expected to lie somewhere between $\alpha = \mu$ and $\alpha = \mu + \gamma$.

7.5 THE KUBELKA-MUNK MODEL

The Kubelka-Munk model (112,113,114) is a well-established 1-dimensional approach to this problem and considers the light flux internal to the sample to consist of two independent opposing fluxes - the incident and backscattered fluxes. As before, light travels through a plane parallel medium, the intensity at the n^{th} slice before any absorption or scatter having occurred being I_n . On passing through the slice, a fraction $I_n\mu\delta x$ is absorbed, so that I_n remains. Thus $I_n\gamma\delta x$ is scattered at the boundary with the next slice. The incident or downward flux is derived forthwith:



Incident (downward) flux:

$$I_n = I_{(n-1)}(1 - \gamma\delta x) - I_{(n-1)}(1 - \gamma\delta x) \cdot \mu\delta x + J_{n'}(1 - \mu\delta x) \cdot \gamma\delta x$$

but

$$J_{n-1} = J_{n'}(1 - \gamma\delta x) + I_{(n-1)}\gamma\delta x$$

$$\Rightarrow J_{n'} = \frac{J_{n-1} - I_{(n-1)}\gamma\delta x}{1 - \gamma\delta x}$$

Substitute into the equation for I_n :

$$I_n = I_{(n-1)}(1 - \gamma\delta x)(1 - \mu\delta x) + \gamma\delta x(1 - \mu\delta x) \frac{(J_{(n-1)} - I_{(n-1)}\gamma\delta x)}{1 - \gamma\delta x}$$

so that

$$\Delta I = I_n - I_{n-1} = -I_{(n-1)}\gamma\delta x - I_{(n-1)}\mu\delta x + I_{(n-1)}\mu\gamma\delta x^2 + \frac{J_{(n-1)}\gamma\delta x}{1 - \gamma\delta x} - \frac{J_{(n-1)}\mu\gamma\delta x^2}{1 - \gamma\delta x} - \frac{I_{(n-1)}\gamma^2\delta x^2(1 - \mu\delta x)}{1 - \gamma\delta x}$$

In the limit as $\delta x \rightarrow 0$, terms of δx^2 or higher can be ignored, and since

$$\lim_{\delta x \rightarrow 0} \frac{1}{1 - \gamma\delta x} \rightarrow 1$$

the expression reduces to

$$dI = -\gamma I(x)dx - \mu I(x)dx + \gamma J(x)dx$$

ie. the change in incident flux is the sum of that lost to scattering and absorption plus a contribution scattered out of the opposing flux.

A similar argument considering the flux in the opposite direction yields

$$-dJ = -\gamma J(x)dx - \mu J(x)dx + \gamma I(x)dx$$

The result is two simultaneous first order linear differential equations called the Kubelka-Munk equations which define the Kubelka-Munk model:

$$\begin{aligned}\frac{dI}{dx} &= -\gamma I - \mu I + \gamma J \\ -\frac{dJ}{dx} &= -\gamma J - \mu J + \gamma I\end{aligned}$$

Solution of these equations yields fluxes that decay exponentially with depth

$$\begin{aligned}I &= I_0 \exp(-\alpha x) \\ J &= J_0 \exp(-\alpha x)\end{aligned}$$

where J_0 is independent of I_0 and

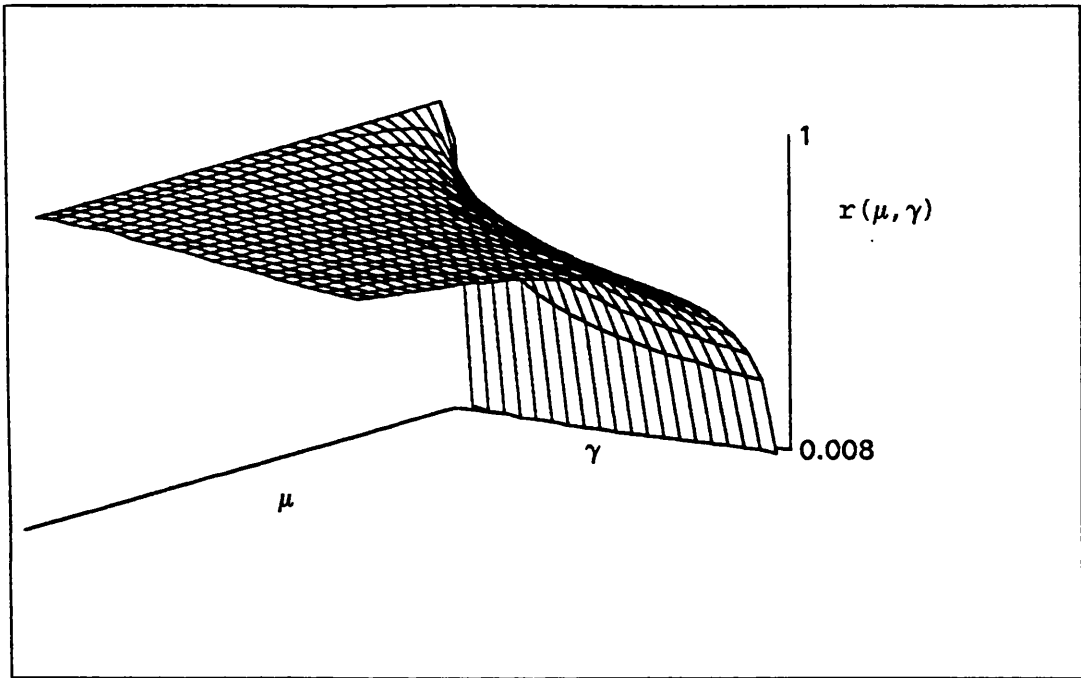
$$\alpha^2 = \mu(\mu + 2\gamma)$$

For no scatter, $\gamma=0$, $\alpha=\mu$ and the equation readily provides Beer's law. $\alpha = \sqrt{\mu(\mu + 2\gamma)}$ is a function whose value is always less than $(\mu + \gamma)$ and so as discussed above, the value of α lies between the extremes of $\alpha=\mu$ and $\alpha=\mu+\gamma$ (Fig. 7.1).

Development of the Kubelka-Munk theory (113) confirms the above to be an exact solution for a homogeneous material in which the illumination is perfectly diffuse, with the material transmitting and reflecting perfectly diffuse light only.

The reality of light interaction within a 3-dimensional scattering volume is infinitely more complex than the highly localised unidirectional scattering events considered here, and produces effects that deviate from the simple exponential behaviour derived above. One such example is the 'popcorn' effect, reported by Kroy et al. (115) and Langerholc (84) in relation to the lasing of tissue at relatively high powers. This referred to a circumstance in which the surface tissue appeared to rupture from beneath the surface, presumably due to a temperature maximum occurring beneath the surface, which produced expanding vapour pockets that ruptured the tissue - a process called 'decrepitation'. This action was later observed by Marchesini (82) who monitored the effect with a thermal camera, confirming the existence of a sub-surface temperature maximum. This is considered to be a scattering effect in which maximum light intensity occurs at a point beneath the surface because of the increased solid angle of scatterers available. However it must be close enough to the surface for the intensity to be high.

$$r(\mu, \gamma) = \frac{\sqrt{\mu(\mu + 2\gamma)}}{\mu + \gamma}$$



M

Figure 7.1 A 3-dimensional plot showing that $\sqrt{\mu(\mu + 2\gamma)} < \mu + \gamma$. The ratio function $r(\mu, \gamma) = \frac{\sqrt{\mu(\mu + 2\gamma)}}{\mu + \gamma}$ is always less than unity.

Various approaches have attempted to model these effects with varying degrees of success, utilising involved mathematics and frequently requiring a recourse to numerical techniques (87,89,90,116). Detailed consideration of these is beyond the scope of this thesis and is not necessary for our purpose, since the simpler model described below is more informative.

7.6 MODIFIED 1-DIMENSIONAL MODEL WITH SCATTERING

An instructive approach is to extend or modify the Kubelka-Munk model to include a more detailed examination of scattering events. We implement our own modification for this purpose.

Consider the scattering medium to consist of a large number of surface parallel planes or slices of infinitesimal thickness δx . Incident light advances through successive slices. A fraction of the intensity is removed at each level, for absorption (linear coefficient μ) and scattering (linear coefficient γ). The remainder simply advances through the sample. The portion removed for scatter is now considered a point source, freely able to irradiate the rest of the sample, to be further absorbed and scattered. We calculate the resultant absorption at each slice due to the unscattered (but attenuated) light, plus the contribution scattered into it from the rest of the sample. This process is described by considering the two components (unscattered and scattered contributions) independently as follows:

7.6.1 Contribution from Unscattered Component

A quantity $I(\mu + \gamma)\delta x$ is removed from each slice so that the intensity difference between successive slices is

$$\delta I = -I(\mu + \gamma)\delta x$$

and the advancing wavefront can be described as

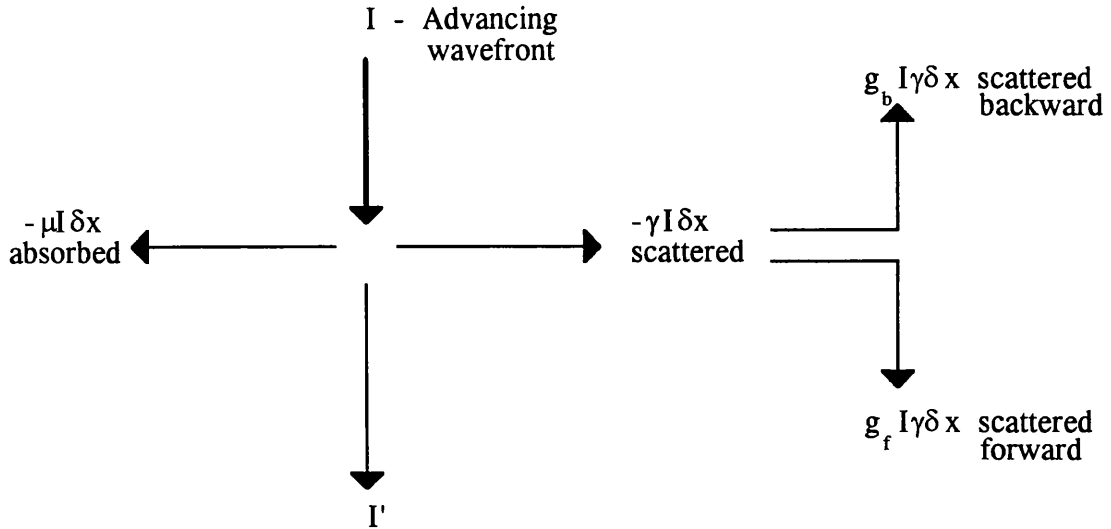
$$I(x) = I_0 \exp[-(\mu + \gamma)x]$$

with the absorption at a depth x being

$$A_w = I_0 (\mu + \gamma)\delta x \cdot e^{-(\mu + \gamma)x}$$

7.6.2 Contribution of Scatter to Absorption

The portion of the wavefront removed for scatter ($\gamma I(x)\delta x$) is available for absorption throughout the rest of the slice. The scattered component may be scattered backwards or forwards, the proportion scattered in either direction defined by the function $g = g_f + g_b = 1$. g_f is the fraction scattered forward, and g_b the fraction scattered backward.



For a sample of thickness D, the intensity at a depth x simply from the unscattered component is given by $I_0 \exp[-(\mu + \gamma)x]$, of which $\gamma \delta x I_0 \exp[-(\mu + \gamma)x]$ becomes available for scattering. This is now considered a secondary independent wavefront (exhibiting the same exponential decay as the main wavefront) spreading through the sample with attenuation, so that the absorption at a depth X (with $X > x$) due to the forward scattered component at x is

$$I_0 e^{-(\mu + \gamma)x} \cdot g_f \gamma \delta x \cdot e^{-(\mu + \gamma)(X - x)} \mu \delta x$$

For backscatter ($X < x$), the term becomes

$$I_0 e^{-\beta x} \cdot g_b \gamma \delta x \cdot e^{-\beta(x - X)} \mu \delta x \quad \text{where } \beta = \mu + \gamma.$$

The contribution $A_s(X)$ to the absorption at X from successive scattering layers within the sample as a whole (where D is the total sample thickness and $x = n\delta x$) is:

$$A_s(X) = \sum_{n=0}^{X/\delta x} g_f \gamma \delta x I_0 e^{-\beta(n\delta x)} \cdot e^{-\beta(X - n\delta x)} \mu \delta x + \sum_{n=X/\delta x}^{D/\delta x} g_b \gamma \delta x I_0 e^{-\beta(n\delta x)} \cdot e^{-\beta(n\delta x - X)} \mu \delta x$$

$$= \gamma \mu \delta x I_0 \left(\sum_{n=0}^{X/\delta x} g_f \delta x e^{-\beta X} + \sum_{n=X/\delta x}^{D/\delta x} g_b \delta x e^{-\beta(2n\delta x - X)} \right)$$

In the limit as $\delta x \rightarrow 0$, this becomes an integral

$$A_s(X) = \gamma \mu \delta x I_0 \left(\int_0^X g_f e^{-\beta x} dx + \int_X^D g_b e^{-\beta(2x - X)} dx \right)$$

$$\Rightarrow A_s(X) = \gamma \mu \delta x I_0 \left(g_f X e^{-\beta X} + \frac{g_b}{2\beta} \cdot e^{\beta X} (e^{-2\beta X} - e^{-2\beta D}) \right)$$

The total absorption in a slice of infinitesimal thickness dx at a depth x below the surface becomes

$$A(x) = A_W(x) + A_S(x) \\ = \mu dx I_0 e^{-\beta x} + \gamma \mu dx I_0 \left(g_f x e^{-\beta x} + \frac{g_b}{2\beta} \cdot e^{\beta x} (e^{-2\beta x} - e^{-2\beta D}) \right)$$

With zero scatter ($\gamma=0$) the equation reduces to Beer's law and the surface absorption at $x=0$ is $\mu dx I_0$. Normalising to this quantity, $A(x)$ becomes $A'(x)$

$$A'(x) = A'_W(x) + A'_S(x) \\ = e^{-\beta x} + \gamma \left(g_f x e^{-\beta x} + \frac{g_b e^{\beta x}}{2\beta} (e^{-2\beta x} - e^{-2\beta D}) \right)$$

The $A'_S(x)$ term is the modification to the absorption due to scatter and has the graphical form of figure 7.2. Note the sub-surface peak.

Remembering that $x = 1/(\mu + \gamma)$ corresponds to the e^{-1} point of the incident intensity, the next graph (Fig. 7.3) shows that the scattered contribution is affected by the thickness of the sample. Several points are worth noting about the scattered contribution.

- i) The scattered component provides a possible explanation for the sub-surface intensity maximum proposed in the decrepitation theorem.
- ii) Scattering can contribute a substantial fraction to the absorbed intensity

eg. in our 1-dimensional model, at $x=0$ with $g_b \gg g_f$ and $D \gg 1/(\mu + \gamma)$

$$A'_W(x) = 1$$

$$A'_S(x) = \frac{\gamma g_b}{4(\mu + \gamma)}$$

$$\text{For } \gamma \gg \mu \text{ and } g_b \approx 1 \quad \frac{A'_S(x)}{A'_W(x)} \approx 25\%$$

- iii) It is the forward scattered (g_f) component that provides the absorption peak at depth (Fig. 7.4).
- iv) The backward scattered (g_b) component is essentially exponential in nature (Fig. 7.5).

Although informative, a 1-dimensional model such as this has its limitations. In this case, the scattered contribution can never be sufficiently additive to alter the exponential decay of the main wavefront enough to create a sub-surface peak. This is readily seen by examining the gradient of $A'(x)$.

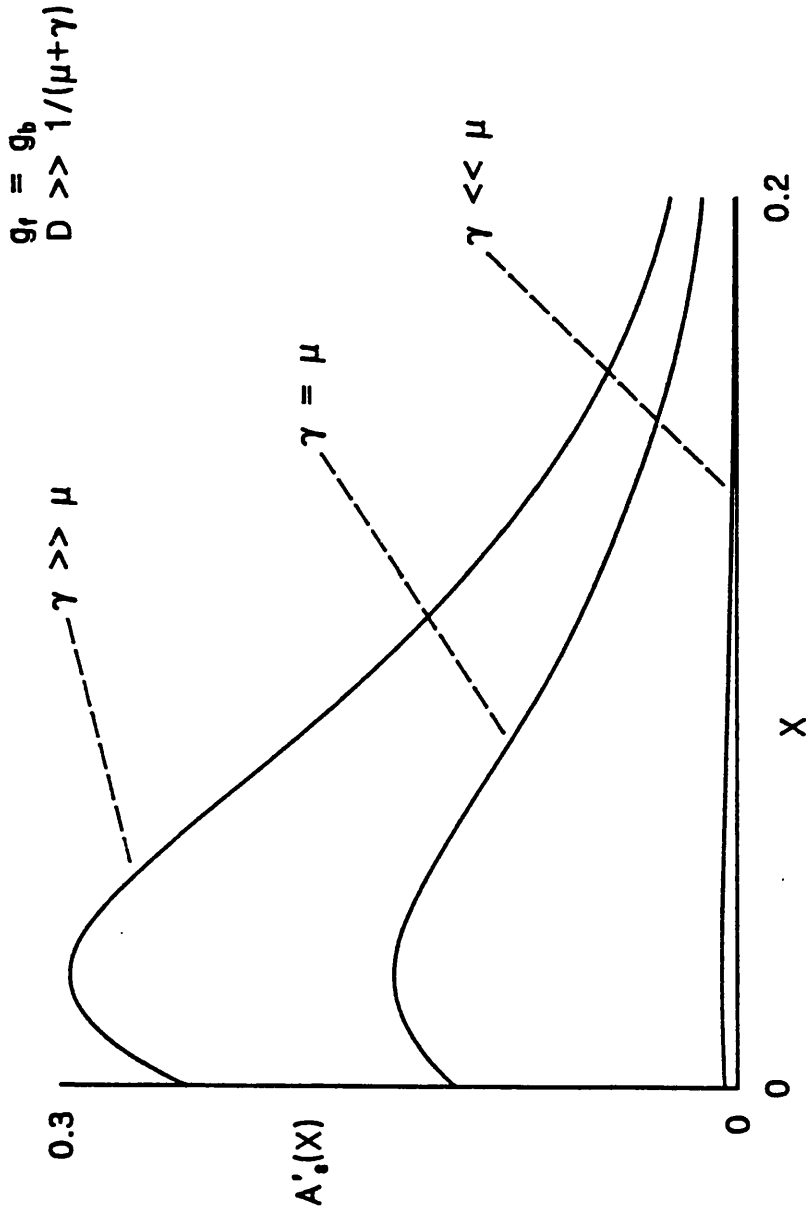


Figure 7.2 The scattering function $A'_s(X)$ plotted for different values of the linear scattering coefficient γ .

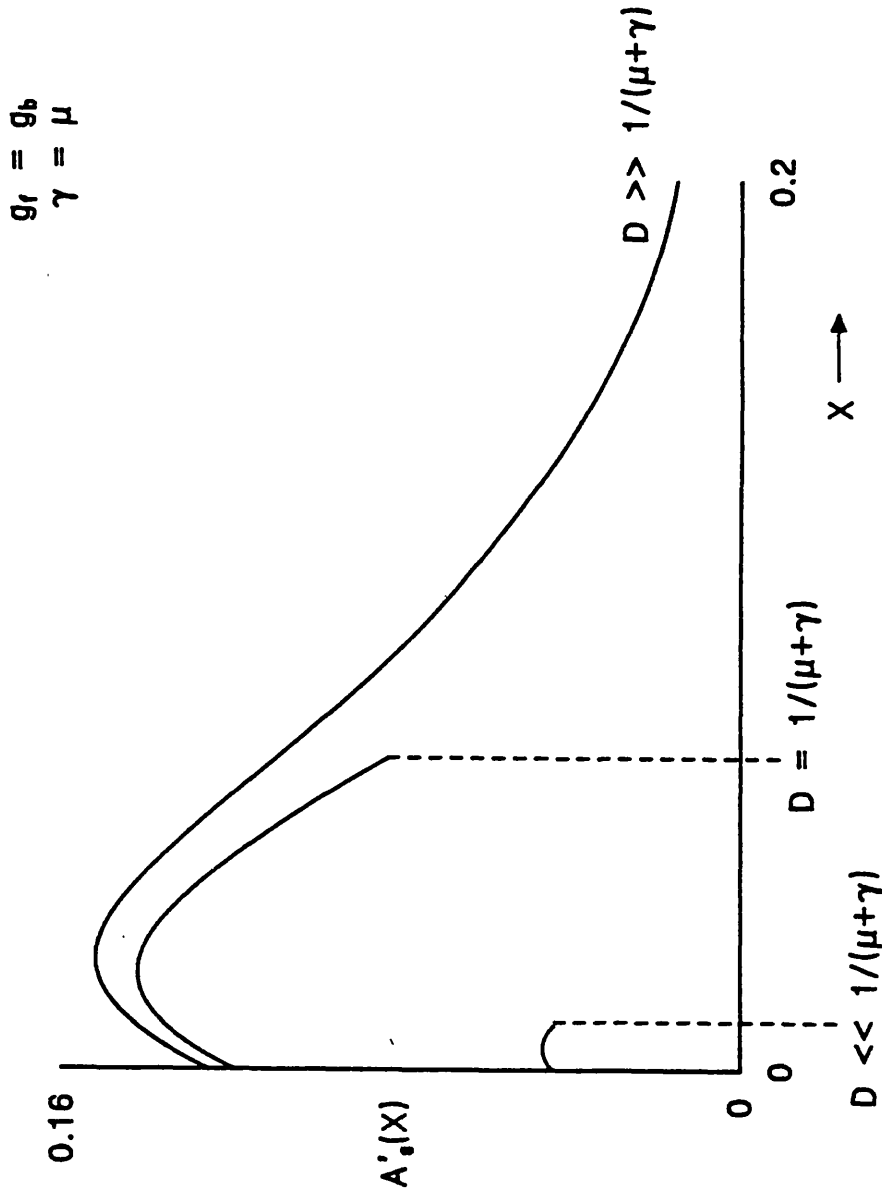


Figure 7.3 The function $A'_s(X)$ showing that the sub-surface maximum is related to the quantity of scatterers (ie. the thickness of tissue (D)).

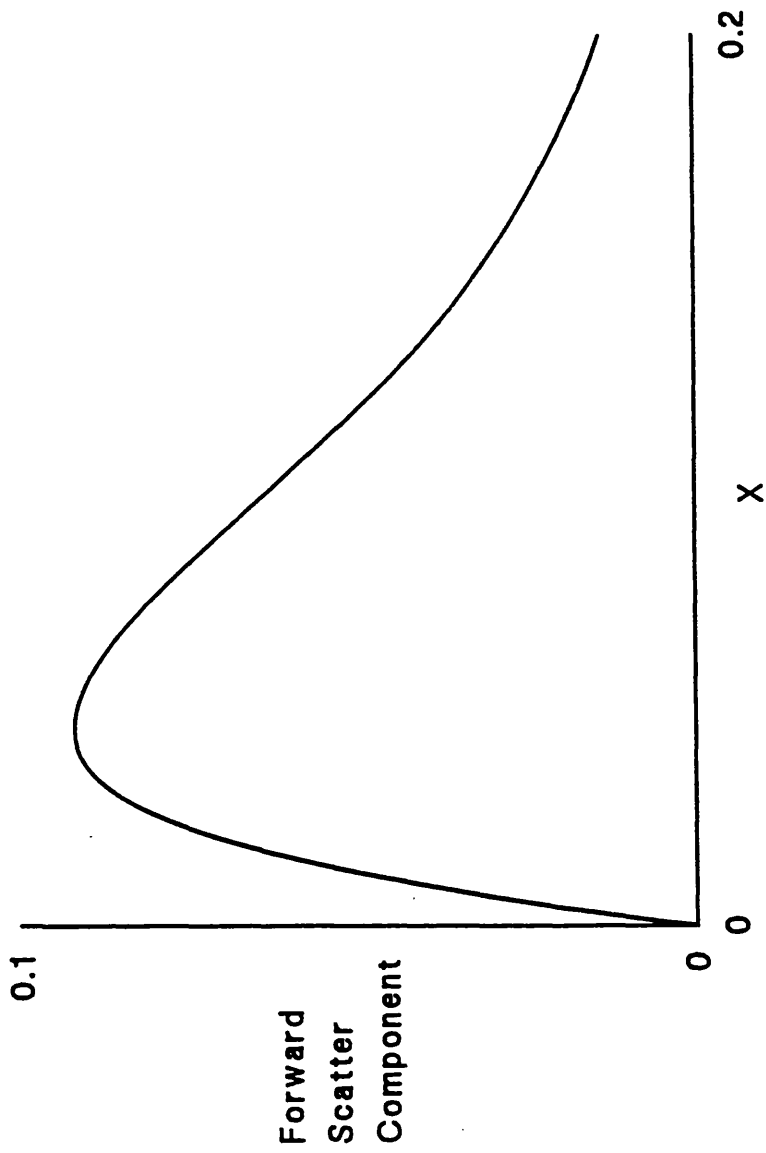


Figure 7.4 Typical shape of the forward scattered (gf) component of $A'_s(X)$.

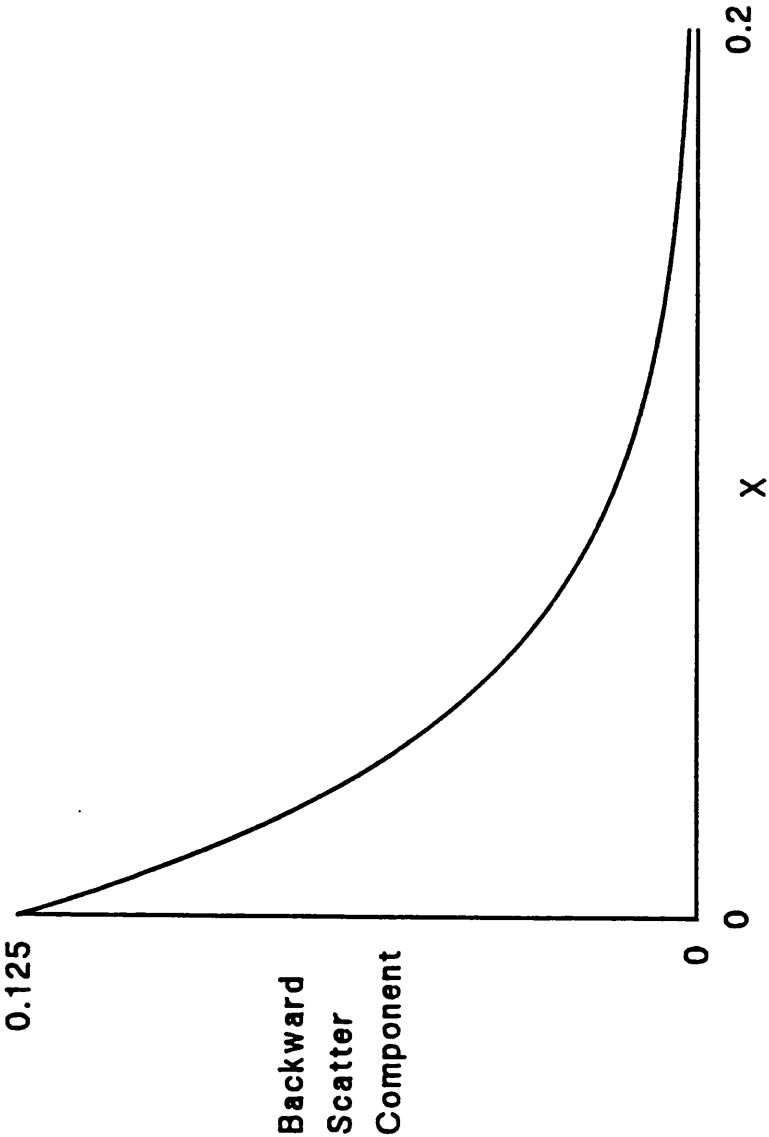


Figure 7.5 Typical shape of the backward scattered (g_b) component of $A'_s(X)$.

$$\frac{dA'(x)}{dx} = -\beta e^{-\beta x} + \gamma g_f e^{-\beta x} (1 - \beta x) - \frac{\gamma g_b}{2} (e^{-\beta x} + e^{\beta x} \cdot e^{-2\beta D})$$

To maximise the peak, let $D \rightarrow \infty$,

$$\begin{aligned} \frac{dA'(x)}{dx} &= -\beta e^{-\beta x} + \gamma g_f e^{-\beta x} (1 - \beta x) - \frac{\gamma g_b}{2} e^{-\beta x} \\ &= e^{-\beta x} \left(\gamma g_f (1 - \beta x) - \left(\beta + \frac{\gamma g_b}{2} \right) \right) \end{aligned}$$

For a peak, a positive gradient must exist beneath the surface:

$$\gamma g_f (1 - \beta x) \geq \beta + \frac{\gamma g_b}{2}$$

This is most likely at $x=0$ (minimising the effect of $-\beta x$) and by making g_f as large as possible ($g_f = 1, g_b = 0$). The required condition for a sub-surface intensity peak becomes

$$\begin{aligned} \gamma &\geq \beta \\ \text{ie. } \gamma &\geq \mu + \gamma \end{aligned}$$

a special condition true only for $\mu=0$. Clearly no sub-surface intensity peak is possible since the above condition requires $x=0$.

Figure 7.6 compares the absorbed intensity functions of both the unmodified and modified Kubelka-Munk models. They are very similar. In view of their similarity, the simpler unmodified model was chosen to calculate the absorbed energy distribution responsible for heating the tissue. The induced temperature distribution is discussed in the next chapter.

7.6.3 Three Dimensions

In the 3-dimensional situation, the number of scatterers contributing to the intensity at a point increases dramatically, because scattering occurs within the whole volume of the slice. It is not difficult to see that this increased volume of scatter could create sufficient additional sources to override the initial exponential decay at $x=0$ and create an irradiance maximum beneath the surface.

The values of the coefficients μ and γ basically remain unchanged in the move to 3-dimensions, although their interpretation changes slightly. In this case, g becomes a function of solid angle, determining the percentage of scattered light emitted in any direction with the obvious requirement that

$$\int_0^{2\pi} \int_0^{2\pi} g(\theta, \phi) d\theta d\phi = 1$$

where θ, ϕ are angles of azimuth and elevation in spherical polar co-ordinates. Equations can be written to describe light interactions in 3-dimensions (116,117),

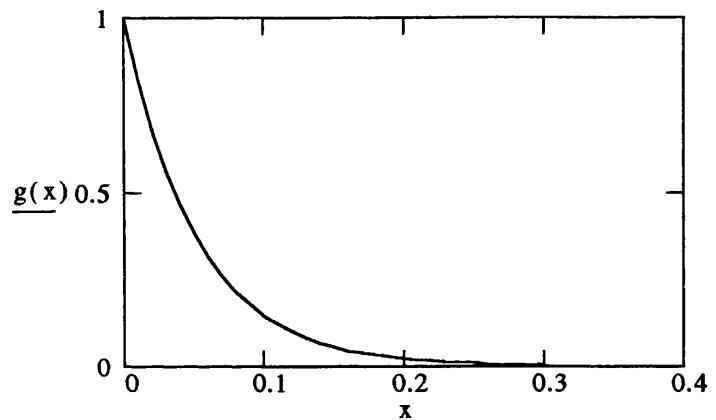
$$\mu := 11\text{cm}^{-1} \quad \gamma := 11\text{cm}^{-1} \quad D := 0.3\text{cm} \quad f := 0.5 \quad b := 1 - f$$

$$\alpha := \sqrt{\mu \cdot [\mu + 2 \cdot \gamma]}$$

$$\beta := \mu + \gamma$$

$$x := 0, 0.01 \dots 0.3$$

$$g(x) := \exp[-\alpha \cdot x]$$



$$A(x) := \exp[-\beta \cdot x] + \gamma \cdot \left[f \cdot x \cdot \exp[-\beta \cdot x] + \frac{b \cdot \exp[\beta \cdot x]}{2 \cdot \beta} \cdot [\exp[-2 \cdot \beta \cdot x] - \exp[-2 \cdot \beta \cdot D]] \right]$$

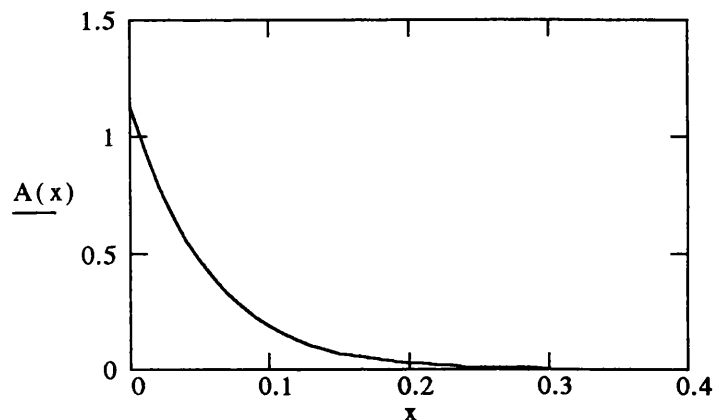


Figure 7.6

A comparison of the absorption of the standard $[g(x)]$ and modified $[A'(x)]$ Kubelka-Munk models. Both curves are normalised to the absorption of the standard model at the surface. The forward $[g_f]$ and backward $[g_b]$ scattered fractions are represented by f and b respectively.

but frequently prove analytically insoluble without gross oversimplification. Faced with such problems, the only recourse is to numerical methods. An example of this approach divides the volume of the sample into a regular array or matrix of discrete elements. It involves following the path of single light rays through the solid, recording the absorption of light rays along its path. Random number sequences (this is a stochastic technique) are used to simulate the probability of scattering or absorption events occurring at any interaction. After the passage of many rays (sufficient for statistical homogeneity within the sample - typically $\geq 10^6$ rays) a picture of absorption throughout the sample can be generated. A stochastic approach such as this is known as a Monte-Carlo technique. Results are in good agreement with experiment and do reveal an absorption maximum occurring beneath the surface in conditions where this might be expected.

7.7 CONCLUSION

The necessity of obtaining detailed temperature information during bonding has been stressed. This may provide insight into the mechanisms involved, particularly with respect to the contribution of dehydration. However, the accuracy of measurement required within the small volume of tissue being heated exceeds the resolution of available contact or remote sensing probes. Thus an alternative is to calculate the evolving temperature by modelling the heat flow, which can only be obtained from the absorbed light distribution. This has been explored in the form of an unmodified and modified 1-dimensional Kubelka-Munk model, and results of the application of the unmodified model to the modelling of heat flow is discussed in the next chapter.

Chapter 8

Numerical Model of Laser Bonding

8.1 INTRODUCTION:

8.1.1 Heat Flow and the Heat Equation

Having established a suitable distribution of absorbed intensity within the tissue (Kubelka-Munk model), it is possible to evaluate the resultant evolving temperature distribution. This is achieved through solution of the heat equation, a mathematical formulation describing heat flow through a body. It is derived from the fundamental hypothesis that the rate of heat flow across a boundary is proportional to the temperature gradient across it:

$$\frac{dQ}{dt} \propto \frac{du}{dx}$$

$Q = \text{Heat}$ $u = \text{Temperature}$
 $t = \text{Time}$ $x = \text{Distance}$

From it can be derived the differential heat equation (118)

$$\frac{1}{\kappa} \frac{\partial u}{\partial t} = \nabla^2 u + \frac{A}{K}$$

$u = \text{Temperature distribution}$
 $A = \text{Power distribution}$
 $K = \text{Thermal conductivity}$

where $\kappa = \frac{K}{\rho c}$

$\rho = \text{Density}$
 $c = \text{Specific heat capacity}$

This is of the same form as the diffusion equation. It was the diffusion process which inspired the derivation of the heat equation, since the diffusion hypothesis states that the rate of diffusion of a substance across a boundary is proportional to the concentration gradient across it.

The heat equation is very general, and correctly describes temperature and heat flow over a wide range of conditions. However, its complexity precludes

analytic solution except in the simplest of cases. This is true of our application (the lasing of tissue slices) and requires a recourse to numerical methods.

8.2 NUMERICAL EXPRESSION OF THE HEAT EQUATION

The numerical approach quantises the volume of interest so that it is broken into a large number of discrete elements, each uniquely identified by its coordinates. As an example, let $u(x,y,z,t)$ be the temperature function, whose derivatives in the x -dimension can be described as

$$\begin{aligned}\frac{\partial u}{\partial x} &\approx \frac{u(x + \delta x, y, z, t) - u(x, y, z, t)}{\delta x} \\ \frac{\partial^2 u}{\partial x^2} &\approx \frac{\frac{u(x + \delta x, y, z, t) - u(x, y, z, t)}{\delta x} - \frac{u(x, y, z, t) - u(x - \delta x, y, z, t)}{\delta x}}{\delta x} \\ &\approx \frac{1}{\delta x^2} [u(x + \delta x, y, z, t) - 2u(x, y, z, t) + u(x - \delta x, y, z, t)]\end{aligned}$$

Similarly, in the temporal domain

$$\frac{\partial u}{\partial t} \approx \frac{u(x, y, z, t + \delta t) - u(x, y, z, t)}{\delta t}$$

Before substituting these expressions into the heat equation, a considerable reduction in the complexity of notation can be achieved by mapping all points of the function $u(x,y,z,t)$ to the matrix elements U_{XYZT} where X, Y, Z, T are integers that define the points x, y, z, t by

$$x = X \cdot \delta x$$

$$y = Y \cdot \delta y$$

$$z = Z \cdot \delta z$$

$$t = T \cdot \delta t$$

The matrix heat equation now becomes

$$\begin{aligned}\frac{1}{\kappa} \frac{U_{XYZ,T+1} - U_{XYZT}}{\delta t} &= \frac{1}{\delta x^2} [U_{X+1,YZT} - 2U_{XYZT} + U_{X-1,YZT}] \\ &+ \frac{1}{\delta x^2} [U_{X,Y+1,ZT} - 2U_{XYZT} + U_{X,Y-1,ZT}] \\ &+ \frac{1}{\delta x^2} [U_{XY,Z+1,T} - 2U_{XYZT} + U_{XY,Z-1,T}] \\ &+ \frac{A_{XYZT}}{K}\end{aligned}$$

We proceed (with little loss of generality) to reduce the above to the 1-dimensional heat equation, a situation which exists when the temperature in one plane (eg. y-z plane) is constant, varying only with x, so that $\frac{\partial u}{\partial y^2} = 0$ and $\frac{\partial u}{\partial z^2} = 0$. Similarly,

A_{XYZT} is required to be a function of x and t only:

$$U_{x,T+1} = U_{x,T} + \frac{\kappa \delta t}{\delta x^2} (U_{x+1,T} - 2U_{x,T} + U_{x-1,T}) + \frac{\kappa \delta t}{K} A_{x,T}$$

Here, the temperature at the next time increment ($U_{x,T+1}$) is uniquely determined by the value of the function in the previous time frame. Hence, knowing the input energy A_{xT} and the initial temperature function U_{xT} , the temperature distribution at subsequent time points can be calculated by repeated application of the above formula with cyclic substitution of $U_{x,T+1}$ in the main body of the equation. The one condition governing convergence of the solution is that the term $\frac{\kappa \delta t}{\delta x^2} < 0.5$ (119). We define δt_{\max} as that value of δt that makes the convergence expression equal to 0.5. If this condition is not fulfilled, the solution becomes unstable, and repeated iterations create a solution which oscillates wildly.

An initial temperature distribution is required before any solution is possible. Hence this is known as a boundary value problem because the boundaries of the solution have to be defined before the solution in general can be obtained. This property applies equally to the analytic solution. To illustrate these points, a simple example relevant to our cause is considered below.

8.2.1 Simple Analytical Validation: - The Hotspot Problem

A problem that has caused concern during laser bonding is the possible presence of undetected hotspots that may be being generated within the tissue. The presence of these may be critical to the success or failure of a bond. It is recognised that their existence may depend upon the inhomogeneity of the tissue sample, but for our purposes we simply assume the tissue to be a homogeneous medium.

A small hotspot embedded within an infinite cooler solid is considered. This represents an adequate approximation of those situations in which the size of the hotspot is small in comparison to the dimensions of the surrounding tissue. The rate at which the hotspot cools can be calculated and thus the energy loss from its volume. Maintenance of such a hotspot would require an inhomogeneity in the incident laser power density capable of sustaining this loss of energy. The magnitude of the beam inhomogeneity required will determine whether such a hotspot is within the bounds of possibility or not.

The 3-dimensional analytical solution of the heat equation governing cooling of a hotspot cube of side length $2a$ with an initial temperature U_0 above that of the surrounding volume, is given by

$$u(t) = U_0 \left[\operatorname{erf} \left(\frac{a}{2\sqrt{\kappa t}} \right) \right]^3 \quad \text{where } \operatorname{erf}(x) = \frac{2}{\sqrt{\pi}} \int_0^x e^{-u^2} du$$

Applying this to the lasing of a 0.15mm thick tissue slice by a 1.5mm diameter beam, we evaluate a relatively large hotspot of dimension 0.1x0.1x0.1mm. Consider a hotspot 10 deg.C. above that of the surrounding tissue, which could be significant given that in vivo bonding temperatures appear to be ~50 deg.C (denaturation occurs at about 60 deg.C.). A temperature graph of the analytic function above, describing temperature at the centre of the hotspot as it cools by conduction, is shown in figure 8.1. The graph superimposes the numerical solution, showing excellent agreement throughout. The oscillations of the solution in which δt exceeds δt_{\max} are clearly evident, even though it is exceeded in this case by only 1%.

Obviously a finite solution matrix can only approximate an infinite solid, and so boundary conditions were implemented to define how points at the boundary of the matrix should respond. In this case, the temperature should continue undisturbed beyond the edge of the matrix, approximated by smoothly extrapolating the curve beyond the edge of the boundary.

The graphical solution reveals that the half cooling time of the hotspot is approximately 5.5 milliseconds. For the hotspot of volume 10^{-12} m^3 , the initial average rate of energy loss (dQ/dt) can be approximated by

$$\frac{dQ}{dt} = mc \frac{du}{dt} = \rho Vc \frac{du}{dt}$$

where ρ = density (1000 kg m^{-3})

V = volume (10^{-12} m^3)

c = specific heat ($4.2 \times 10^3 \text{ J kg}^{-1} \text{ }^\circ\text{C}^{-1}$)

$$\begin{aligned} &= 1000 \times 10^{-12} \times 4.2 \times 10^3 \times \frac{5}{5.5 \times 10^{-3}} \\ &= 3.8 \text{ mW} \end{aligned}$$

This energy can be considered to be leaving the 6 faces of the cube, and represents an outgoing power density at each face of

$$P_d = \frac{3.75 \times 10^{-3}}{6 \times (0.1 \times 10^{-3})^2} = 62.5 \text{ kWm}^{-2}$$

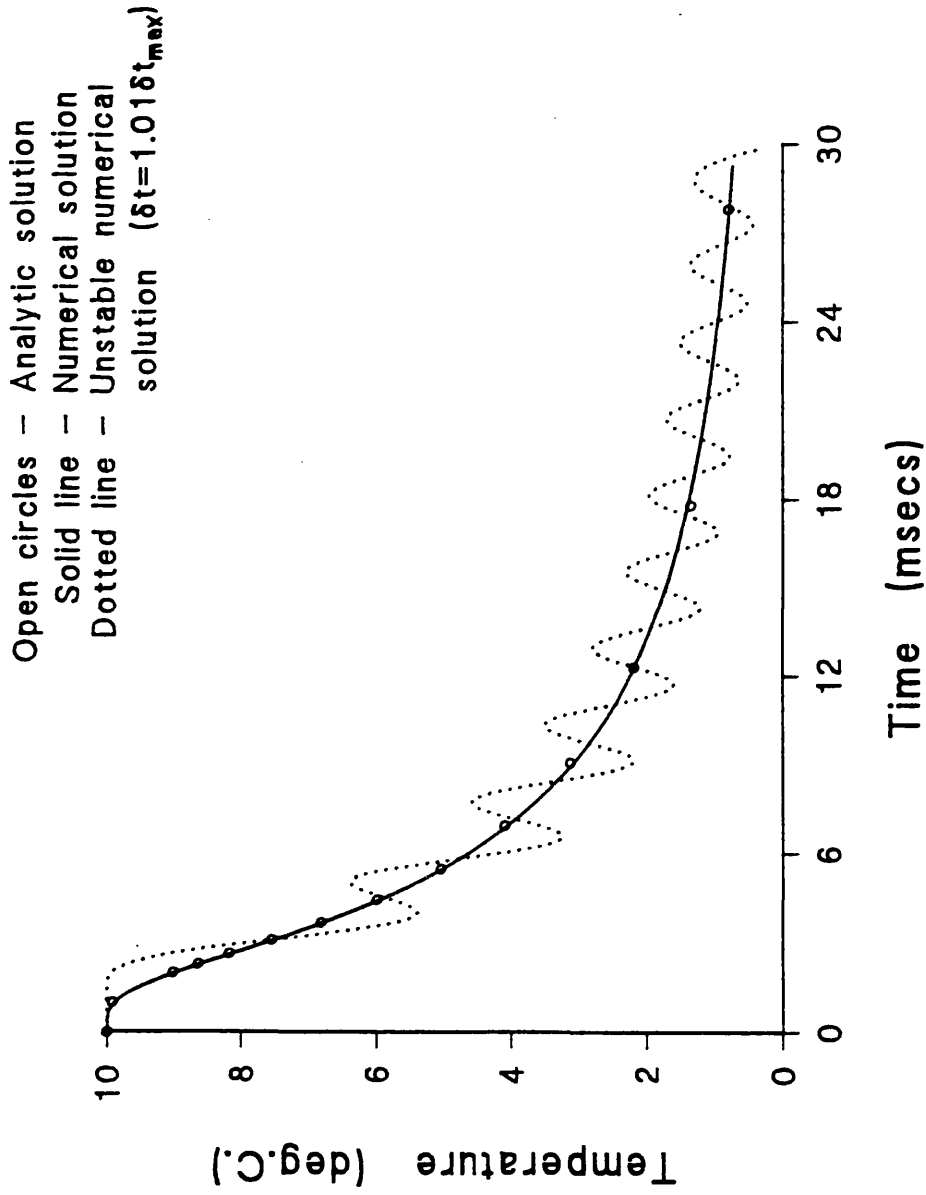


Figure 8.1 Mathematical solution to the cooling of a hotspot in an infinite cooler medium. The 10 deg.C. hotspot has dimensions of a cube of side length 0.1mm.

Compare this to the average incident power density of the beam itself (typically 80mW with 0.8mm beam radius - Chapter 3)

$$P_d' = \frac{80 \times 10^{-3}}{\pi \times (0.8 \times 10^{-3})^2} = 39.8 \text{ kWm}^{-2}$$

It can be seen that maintenance of such a hotspot would require localised incident power density fluctuations over 0.1mm in excess of 50%. This figure is very large in comparison to the homogeneity of a laser beam and indicates that such hotspots do not occur. In relation to tissue slices of thickness 0.15mm, a 0.1mm hotspot is quite big. However, the figure of 50% increases for hotspots of smaller size and therefore are even less likely. We therefore conclude that hotspots of 10 deg.C. or more are not generated within the lased tissue.

8.2.2 Cylindrical Polar Co-ordinates

Thus far, only Cartesian co-ordinates have been considered, but other co-ordinate systems can be used where appropriate. In cylindrical polar co-ordinates, the 3-dimensional heat equation becomes

$$\frac{1}{\kappa} \frac{\partial u}{\partial t} = \frac{\partial^2 u}{\partial r^2} + \frac{1}{r} \frac{\partial u}{\partial r} + \frac{1}{r^2} \frac{\partial^2 u}{\partial \theta^2} + \frac{\partial^2 u}{\partial z^2} + \frac{A}{K}$$

8.3 CALCULATION OF TISSUE TEMPERATURE DISTRIBUTION

We now consider in more detail, application of these numerical techniques to the problem in hand, namely evaluation of the evolving temperature distribution at the bonding faces of lased tissue, ultimately relating to the bonding of carotid vessels in vivo (Chapter 3). Our in vitro experimental work (Chapter 6) involved the lasing of thin slices of sheep aorta approximately 140 μ m thick. This forms a useful and appropriate body of data with which to compare the theoretical results, since bonding was performed under well defined conditions in terms of lasing power, distance, tracking speed etc. The abundance of available data will lend itself to interpretation of the model's results.

8.3.1 Matrix Granularity

The granularity of the solution matrix (ie. the size of the increments δx , δy , δz , δt) must be chosen so that the temperature function is evaluated at a sufficient number of points for the data to be useful. We consider the problem in Cartesian co-ordinates. A minimum of 10 points was chosen in any axis. With a tissue thickness of approximately 0.15mm, and a beam diameter of the order of 1.5mm, spatial increments are

$$\delta x = 0.15 \text{ mm}$$

$$\delta y = 0.15 \text{ mm}$$

$$\delta z = 0.014 \text{ mm}$$

(Tissue thickness = 0.14mm)

The result is a 1000 point array that must be evaluated for every increment of δt seconds. The convergence condition defines the maximum value of δt that is possible for a convergent solution

$$\kappa \delta t \left(\frac{1}{\delta x^2} + \frac{1}{\delta y^2} + \frac{1}{\delta z^2} \right) < 0.5$$

With a value of $\kappa = 1.407 \times 10^{-7} \text{ m}^2 \text{ s}^{-1}$ for water (a reasonable approximation for tissue since ~80% by weight is water (Chapter 6)) and substituting the values for δx , δy , δz the condition becomes

$$\delta t_{\max} = \frac{0.5}{\kappa} \left[\frac{1}{\delta x^2} + \frac{1}{\delta y^2} + \frac{1}{\delta z^2} \right]$$

$$\approx \frac{0.5 \delta z^2}{\kappa} \quad \text{since } \delta z \ll \delta x, \delta y$$

$$\Rightarrow \delta t_{\max} \approx 8 \times 10^{-4} \text{ secs.}$$

Given that non-denatured full bond strength in our experiments was only achieved at a tracking speed of 30sec/mm (65mW incident power - Chapter 6), solutions for periods greater than 30 seconds may be necessary. Thus a 1000 point matrix must be generated for every 0.8 milliseconds, and the solution at $t = 30$ requires solving the matrix 37500 times. This is all at a coarse spatial and temporal resolution, and with a little more detail could easily involve generating over 100000 matrices. With a rough assessment of approximately 20 multiplications per matrix element a 30 second solution may involve 750×10^6 multiplications! This equates to many hours (if not days) of computation on a personal computer (PC).

Under suitable conditions, the use of symmetry can dramatically reduce the computational overhead by decreasing the number of elements within the matrix. In the case of a stationary beam incident upon a flat tissue slice, cylindrical symmetry about the axis of the beam is present. Using cylindrical polar co-ordinates, and temperature no longer a function of θ (cylindrical symmetry), the heat equation becomes

$$\frac{1}{\kappa} \frac{\partial u}{\partial t} = \frac{\partial^2 u}{\partial r^2} + \frac{1}{r} \frac{\partial u}{\partial r} + \frac{\partial^2 u}{\partial z^2} + \frac{A}{K}$$

with z describing the dimension of thickness.

Using matrix granularity similar to that of the Cartesian discussion above, δz is left unchanged with δr taking the place of δx or δy . Since $\delta z \ll \delta r$, the

convergence criterion remains mainly dependent upon δz so that δt_{\max} is still approximately 0.8ms. However, symmetry has reduced the matrix from 3-dimensions (1000 point matrix) to 2-dimensions (100 point matrix). Not only is less computation involved per matrix element, but the size of the matrix is reduced by an order of magnitude. This makes the solution much more manageable and dramatically reduces computation time.

8.3.2 Boundary Conditions

The numerical solution of the heat equation with cylindrical symmetry is given by

$$U_{RZ,T+1} = U_{RZT} + \kappa \delta t \left(\frac{U_{R+1,ZT} - 2U_{RZT} + U_{R-1,ZT}}{\delta r^2} + \frac{1}{r} \frac{U_{R+1,ZT} - U_{RZT}}{\delta r} + \frac{U_{R,Z+1,T} - 2U_{RZT} + U_{R,Z-1,T}}{\delta z^2} \right) + \frac{\kappa \delta t}{K} A_{RZT}$$

This will be used to model the heat flow within a thin tissue slice whose extension in the r-plane is much greater than that of the beam, as per the experiments of Chapter 6. This is adequately modelled by a tissue of infinite radial extent. Solution of the equation requires boundary conditions to be defined. In this case they are rather more involved than those of the simple hotspot example quoted earlier. Conditions governing behaviour of the heat flow around the entire boundary of the matrix need to be established, which includes an approximation of heat flow at large r, as well as the energy exchange between top and bottom surfaces of the slice and the surrounding atmosphere. Each is taken in turn below.

8.3.3 Conditions at Tissue Surface

At each exposed surface, behaviour of heat flow within the tissue is modified by the heat lost to the surrounding cooler atmosphere. The proportion lost from the tissue, is dictated by the fundamental equation

$$\frac{dQ}{dt} \propto \frac{du}{dz}$$

which states that the heat flow across a boundary is proportional to the temperature gradient. This readily provides Newton's law of cooling

$$\frac{dQ}{dt} = h(u_a - u_s) \quad u_a = \text{air temperature}$$

$$u_s = \text{tissue surface temperature}$$

Numerical solution of this defining boundary condition enables the change of temperature at the top and bottom surfaces of the tissue to be calculated. The constant of proportionality (h) is called the surface heat transfer coefficient and controls the rate at which the body as a whole cools.

8.3.4 Symmetry Condition at Beam Axis ($r=0$)

The symmetry axis of the incident beam is defined as the radial origin ($r=0$). The apparent singularity that occurs with the $\frac{1}{r} \frac{\partial u}{\partial r}$ term of the cylindrical heat equation at $r=0$, was resolved by relying on symmetry about $r=0$, so that $U_{-RZT} = U_{+RZT}$. A quadratic function was fitted to the points and gradients at U_{-1ZT} and U_{1ZT} to estimate the value of the temperature function at $r=0$.

8.3.5 Boundary Condition for Large r

In a manner similar to the hotspot example given earlier, intelligent extrapolation of the temperature function was used to provide continuity of heat flow at the matrix edge (for large r), approximating heat flow in a slice of infinite radial extent. This approximation is improved by making the radius of the matrix as large as possible.

8.3.6 Energy Distribution

The heating energy distribution A_{RZT} is obtained from the absorbed light distribution discussed in the previous chapter (simple Kubelka-Munk model). However, it requires modification since energy density is not only a function of depth (ie. due to absorption and scatter etc.) but is also a function of radius in accordance with the beam profile of the incident laser light. Beam profile was measured along two orthogonal axes in the radial plane intersecting at the beam axis, by tracking the beam across a 0.17mm diameter aperture linked to a power meter. Power density as a function of position was calculated and the results shown in figure 8.2. Note that the beam is not perfectly symmetric. The most likely cause is imperfections or unevenness of the imperfectly cleaved fibre faces, which distorts the emerging light distribution. In addition, co-axial alignment of the fibre with the optic axis of the handpiece focusing lens is critical because of its small radius of curvature (~ 2 mm). These two points in combination readily account for the degradation of beam symmetry.

The profile closely resembles that of a cone, and is represented in the model this way. Derivation of the function used to describe the incident power density is given below. Knowledge of the total beam power P_T , and the beam radius ρ is required.

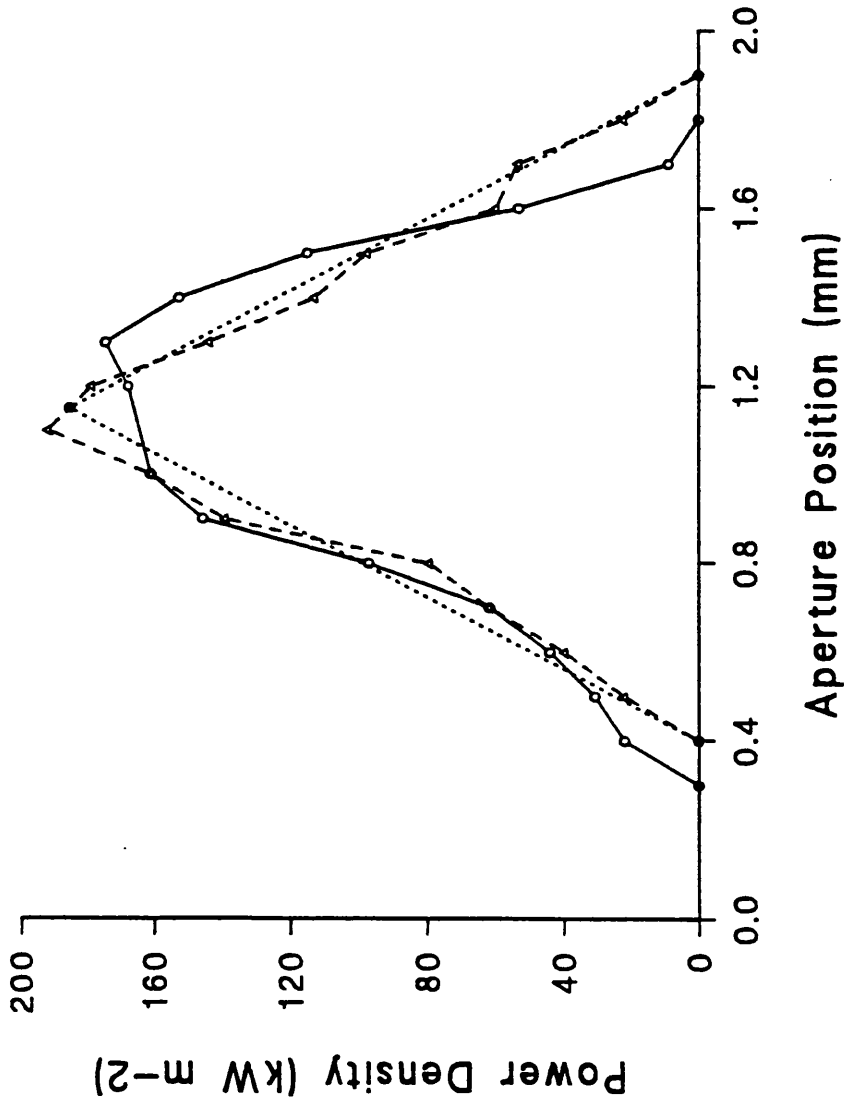
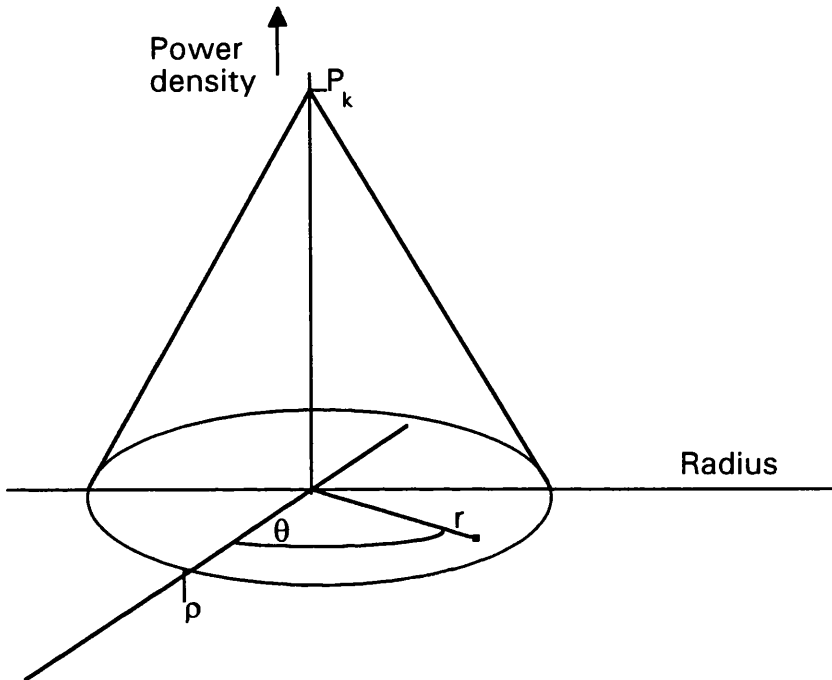


Figure 8.2 Beam profile measured with a 0.17mm diameter aperture. The solid and dashed lines (open circles and triangles) depict the profile on two orthogonal axes intersecting at the beam centre. The conical dotted profile represents the mathematical approximation used in the model.

8.3.7 Conical Beam Profile:



Power density function = $P(r, \theta)$

$$\begin{aligned}
 \text{Total Power} = P_T &= P[r_0, \theta_0] r_0 \delta r \delta \theta + P[r_0, \theta_1] r_0 \delta r \delta \theta + P[r_0, \theta_2] r_0 \delta r \delta \theta + \dots \\
 &+ P[r_1, \theta_0] r_1 \delta r \delta \theta + P[r_1, \theta_1] r_1 \delta r \delta \theta + P[r_1, \theta_2] r_1 \delta r \delta \theta + \dots \\
 &+ P[r_2, \theta_0] r_2 \delta r \delta \theta + P[r_2, \theta_1] r_2 \delta r \delta \theta + P[r_2, \theta_2] r_2 \delta r \delta \theta + \dots \\
 &+ \dots \\
 &= \delta r \delta \theta \sum_j \sum_k r_j P[r_j, \theta_k] \\
 &= \int_0^\rho \int_0^{2\pi} r P(r, \theta) dr d\theta
 \end{aligned}$$

(In the limit as $\delta\theta$, δr tend to zero.)

(2ρ = Beam diameter)

For a conical beam profile of diameter 2ρ , the power density $P(r, \theta)$ reduces to

$$P(r, \theta) = (\rho - r) \frac{P_k}{\rho} \quad (P_k = \text{Power density at } r = 0)$$

Substitution yields:

$$\begin{aligned}
 P_T &= \int_0^\rho \int_0^{2\pi} \frac{P_k}{\rho} (\rho - r) r dr d\theta \\
 &= \frac{\pi}{3} P_k \rho^2
 \end{aligned}$$

from which P_k can be evaluated, producing the equation describing the conical beam profile of radius ρ and power P_T

$$P(r, \theta) = \frac{3P_T (\rho - r)}{\pi \rho^3}$$

The energy deposited within each element of the matrix in time δt can be calculated to first order using the Kubelka-Munk attenuation coefficient α (where $\alpha = \sqrt{\mu(\mu + 2\gamma)}$). Absorption in any element is $\alpha I \delta z$ (see Chapter 7). Empirical data was used to modify this highly collimated exponential decay to introduce a degree of scatter. This was obtained from other work (111) which has shown that a 75% increase in the diameter of a 0.8mm radius beam occurs over a depth of $400\mu\text{m}$. The diameter increase was modelled as a linear function of depth. Thus the power density decreases with depth in proportion to the square of the increasing radius.

The resulting semi-empirical power distribution A_{RZT} decreases with depth due to attenuation, and also decreases due to an increase in irradiated area related to the scatter.

8.3.8 Chromophore

The absorption coefficient was modified where necessary to accommodate the effects of increased absorption by chromophore. This equates to absorption of approximately 50% of the incident radiation (43,111) at the chromophored surface.

8.3.9 Parameters

The numerous constants that require definition have been assigned values appropriate for water. Given that 80% of the tissue by weight is water, this is a reasonable approximation.

$$K = 0.591 \text{ Wm}^{-1}\text{K}^{-1}$$

$$\rho = 1000 \text{ kgm}^{-3}$$

$$c = 4.2 \times 10^3 \text{ Jkg}^{-1}\text{K}^{-1}$$

$$\kappa = K/\rho c = 1.407 \times 10^{-7} \text{ m}^2\text{s}^{-1}$$

$$h = 825 \text{ WK}^{-1}$$

The value for h was determined empirically by monitoring the cooling of a lased tissue sample with the thermal camera. The laser was switched off, and the time required for the peak temperature to cool to a specified temperature - as recorded by the camera - was measured. Using an initial temperature distribution in the model similar to that recorded by the camera (corrected for imaging artefacts and inaccuracies, thus accurate to $\approx \pm 10\text{deg.C.}$) just prior to switching off the

laser, the mathematical model was repeatedly run with different values of h until the cooling time matched with experiment.

Substituting these conditions and parameters into the model, tissue temperature as a function of time over a wide range of conditions can be calculated. The solution involves evaluation of the boundary conditions first, following which the main body of the equation is solved.

8.4 VALIDATION OF MODEL

As a simple test, the numerical technique was set up to model the stationary lasing of a chromophored $140\mu\text{m}$ thick tissue slice - conditions very similar to those used in Chapter 6, but without tracking movement of the beam. Applying 65mW, the model calculated a peak tissue temperature of 59 deg.C. at the centre of the beam at the lased surface. With 100mW applied, the model calculated a peak temperature of 80 deg.C. The figures (Figs. 8.3-8.10) show that the time taken to reach thermal equilibrium is of the order of 5 seconds, indicating that at a tracking speed of 30 seconds per mm (as per Chapter 6), the sample can be expected to attain thermal equilibrium, thus closely approximating the conditions of this model. A set of graphs presenting temperature as a function of radius is shown in figures 8.4 and 8.8.

These results are in agreement with the experimental findings of Chapter 6 in which histology showed that the 65mW samples were not denatured, and the 100mW samples were denatured. However the model exhibits an omission since no account was taken of the fact that the samples were sitting on a glass slide during lasing. Since glass is a better conductor than air, this would reduce the calculated temperatures. Although peak temperatures occur at the lased (top) surface, the model indicates little drop in temperature with tissue depth - of the order of 4 deg.C. over $140\mu\text{m}$ (Figs. 8.5 & 8.9).

8.4.1 Detailed Experimental Validation of Model

The spatial resolution of the infra-red camera is inadequate for accurate verification of the model at 0.1mm resolution. As an alternative, we chose to analyse the histological effects of lasing, and use this to infer the temperatures achieved throughout the sample, which could then be correlated with the model. In particular, the denaturation temperature represents a well defined temperature threshold that can act as a temperature reference. As explained in Chapter 2, the collagen content of a tissue sample can be observed by staining with picosirius and examining under a microscope with polarised light. The enhanced birefringence

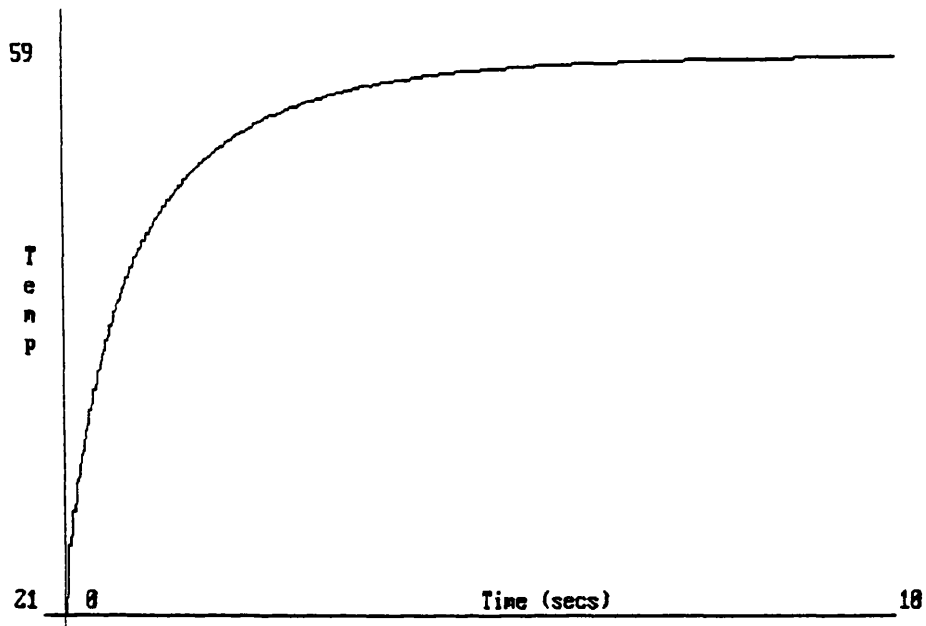


Figure 8.3 Solution of temperature rise at chromophored tissue surface when lased with stationary 65mW beam. Tissue slice modelled as 140 μ m thick.

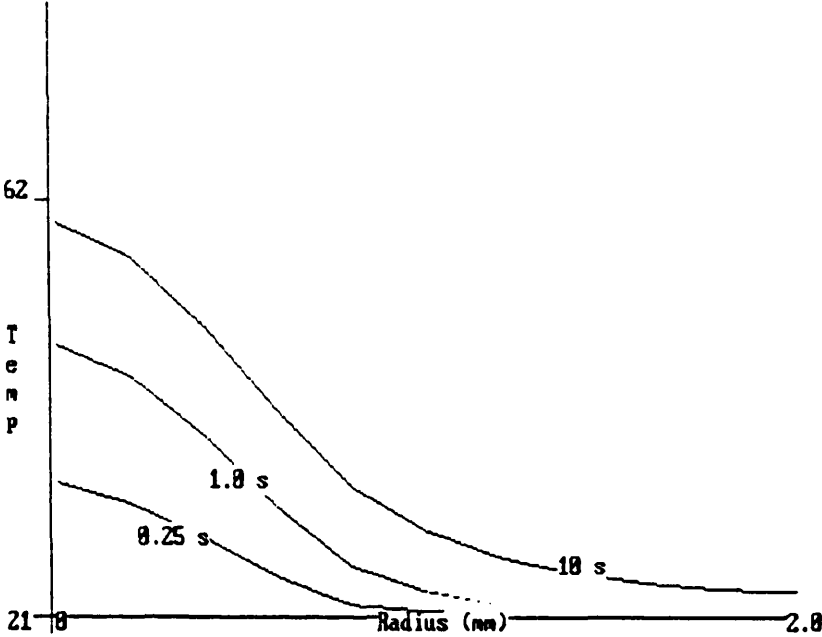


Figure 8.4 Radial temperature distribution at different time points (secs.) at chromophored tissue surface when lased with stationary 65mW beam. Tissue slice modelled as 140 μ m thick.

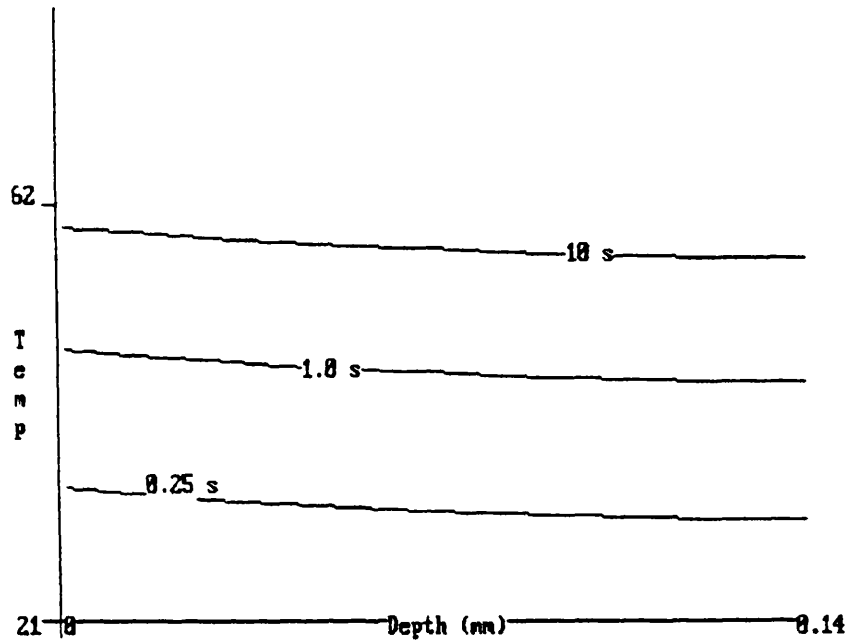


Figure 8.5

Temperature as a function of tissue depth at the beam centre of chromophored tissue when lased with stationary 65mW beam. Tissue slice modelled as 140 μ m thick.

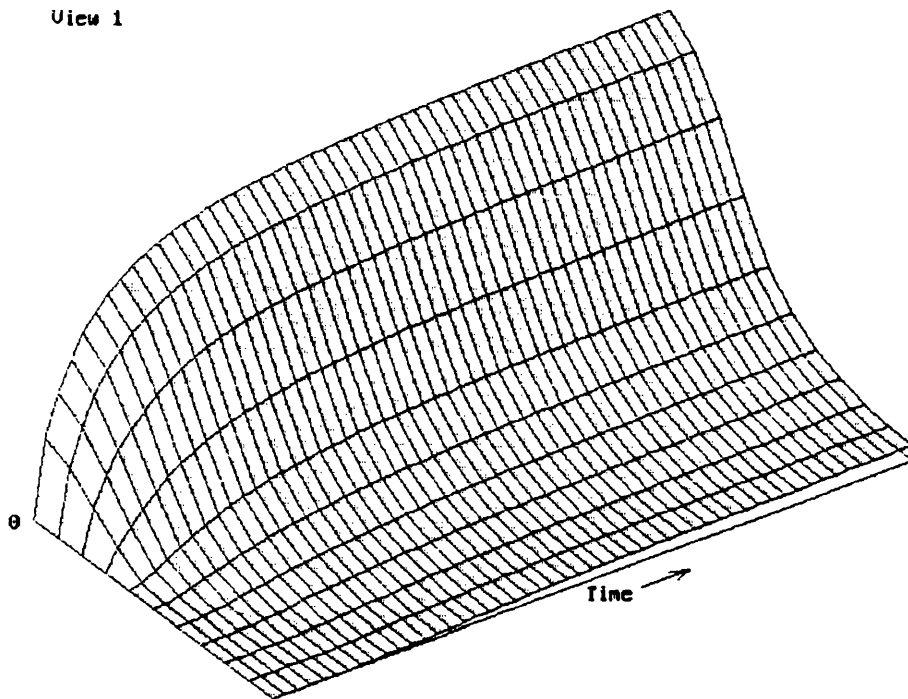


Figure 8.6 3-dimensional representation showing radial temperature evolution with time. The vertical axis shows temperature. Chromophored tissue was modelled as $140\mu\text{m}$ thick, irradiated with a stationary 65mW beam.

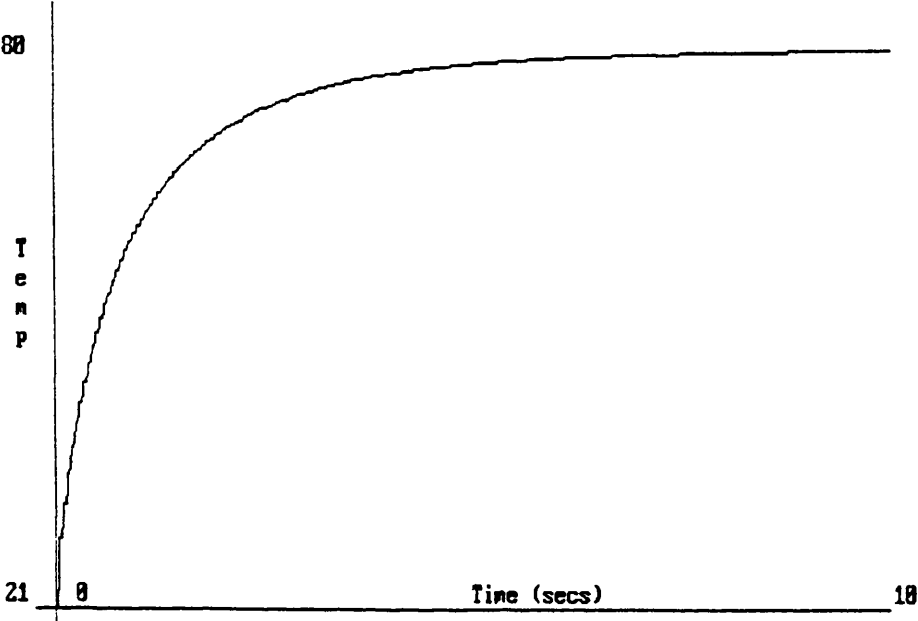


Figure 8.7 Solution of temperature rise at chromophored tissue surface when lased with stationary 100mW beam. Tissue slice modelled as 140 μ m thick.

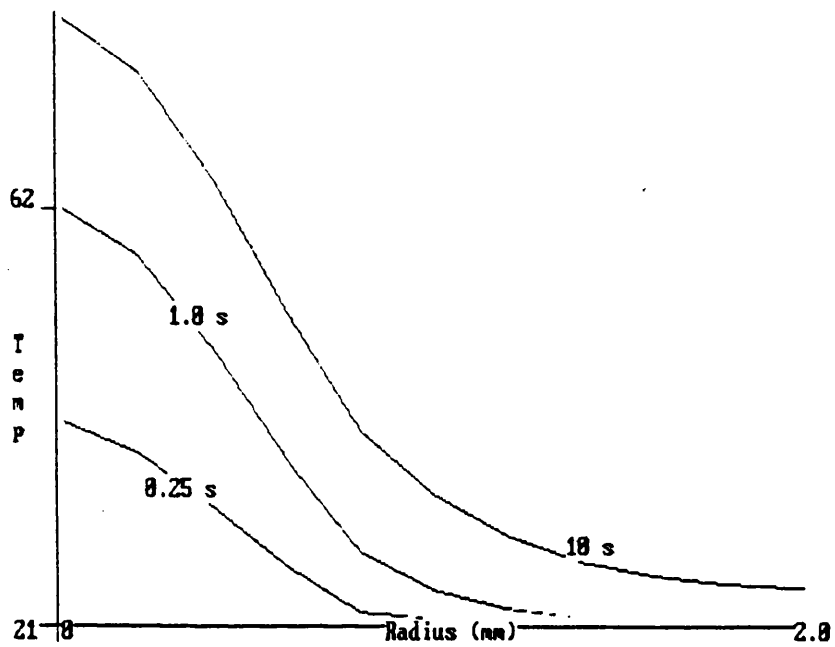


Figure 8.8 Radial temperature distribution at different time points (secs.) at chromophore tissue surface when lased with stationary 100mW beam. Tissue slice modelled as $140\mu\text{m}$ thick.

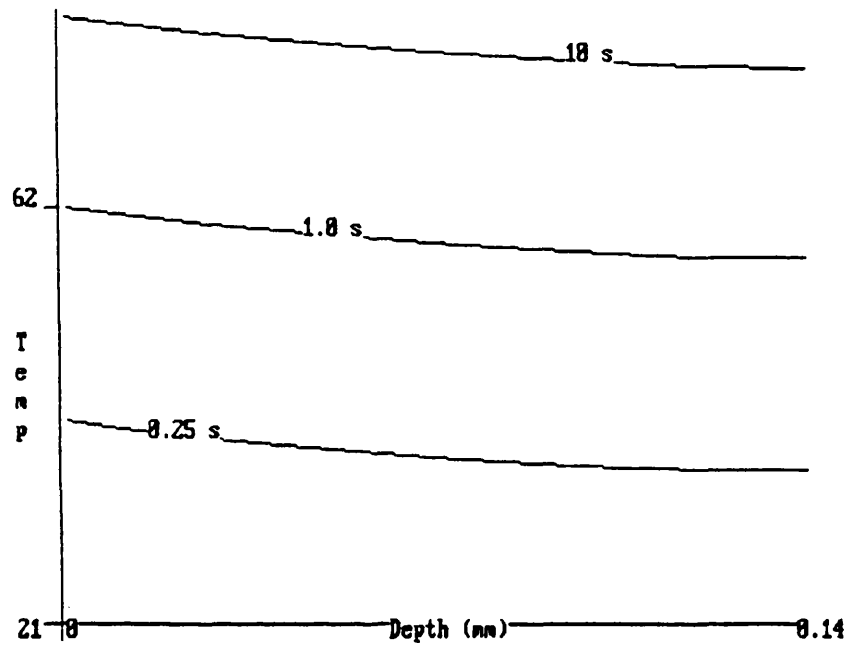


Figure 8.9 Temperature as a function of tissue depth at the beam centre of chromophored tissue when lased with stationary 100mW beam. Tissue slice modelled as $140\mu\text{m}$ thick.

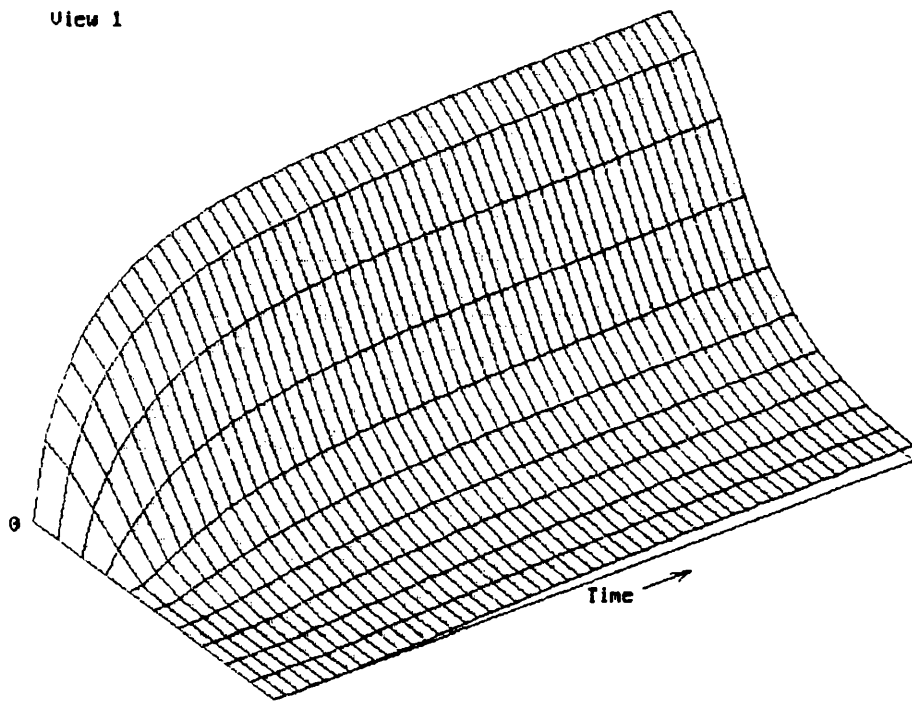


Figure 8.10 3-dimensional representation showing radial temperature evolution with time. The vertical axis shows temperature. Chromophored tissue was modelled as $140\mu\text{m}$ thick, irradiated with a stationary 100mW beam.

of the collagen fibres causes them to 'shine' strongly above the crossed-polarised blackness of the background. However, denatured collagen does not exhibit this property and thus areas of denatured collagen within a sample can be easily identified.

A proposed experiment using this technique, consists of irradiating a tissue slice under well defined conditions. After lasing, the slice is sectioned and stained with picosirius. Those regions of tissue that have been thermally denatured (ie. in which temperatures have exceeded ~ 62 deg.C.) will provide dark patches against surrounding bright areas in which the collagen remains unaffected. The boundary between the two areas represents a temperature boundary of 62 ± 2 deg.C. This isotherm can be compared to that predicted by the model.

8.5 VALIDATION EXPERIMENT

The validity of the model was tested against lased pericardial slices approximately $600\mu\text{m}$ thick, whose lasing surface had been painted with chromophore.

8.5.1 Lasing $\sim 600\mu\text{m}$ Thick, Chromophored Tissue Sections

Fresh sheep pericardium was cut into rectangular slices ($\sim 1.5 \times 1$ cm) and thickness measured with a Mitutoyo tissue gauge. A slice was held around its perimeter by a supporting horizontal frame and a thin layer of chromophore applied to the upper (lasing) surface. The laser handpiece was placed 11 ± 2 mm above the sample, the laser power and spot diameter having been previously determined. The beam was held stationary, and the sample lased for a specified period up to a maximum of approximately 25 seconds. During this period, tissue temperature was monitored with the thermal camera. The lasing time was controlled accurately by an electronic shutter. After lasing, the slice was fixed in 10% formol saline and transverse $10\mu\text{m}$ sections were taken and stained with picosirius. Examined under a polarised microscope, both the undamaged collagen and the blacker thermally denatured regions were easily identified. Figure 8.11 shows a typical selection of successive sections. The denatured area can be seen to progressively increase to a maximum, corresponding to that section which intersects the axis of the beam. Further sections show a diminished area of denaturation eventually fading to nothing as the slices extend beyond the perimeter of the beam.

The model was used to calculate the co-ordinates of the 62 deg.C. isotherm, to be compared with the denaturation boundary seen histologically. The central tissue section intersecting the beam axis was used as the section for comparison with the model because it represents the plane of symmetry used in

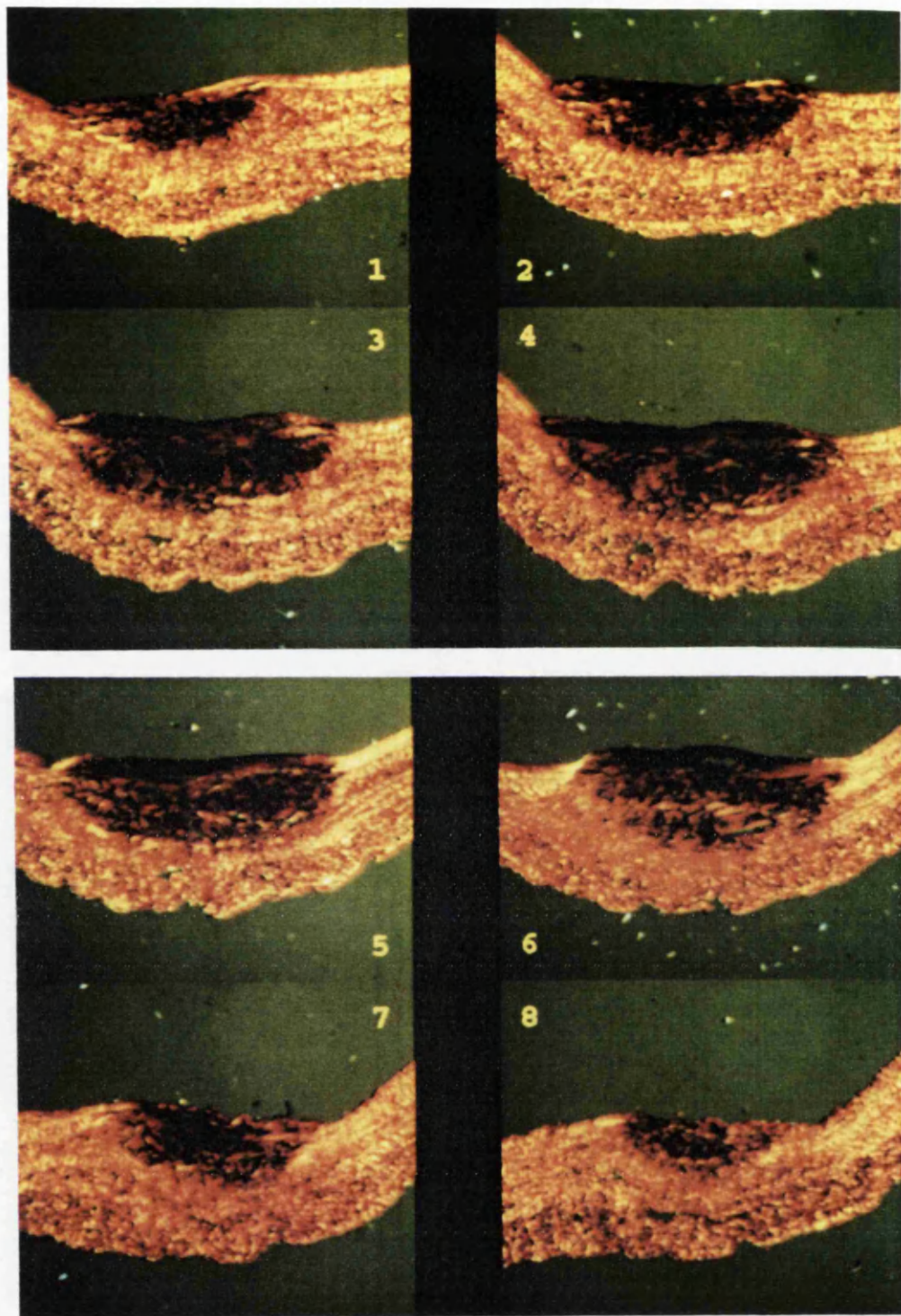


Figure 8.11 Serial sections of 660µm thick tissue lased at 230mW for 17.1 seconds. The tissue was stained with picosirius red and viewed under polarised light. The area of denaturation (dark areas) increases to a maximum at the centre of the beam (sections 4&5).

the mathematical model. Figures 8.12-8.15 show the theoretical prediction of the denatured area superimposed in yellow. The mapping of the theoretically denatured area onto the tissue section was complicated by the deformations induced in tissue shape and thickness by lasing. However, it can be seen that areas within the compass of the beam beneath the denatured region appear undisturbed, and look no different to surrounding tissue that has not been exposed to the beam at all. On this basis, the undistorted non-lased surface of the slice was taken as the surface from which measurements relevant to the model should be made. Hence, the 62 deg.C. isotherm was plotted with respect to this surface, and all areas beyond the isotherm considered to be at a higher temperature, and thus denatured. Table 8.1 shows a comparison of peak theoretical and experimental temperature as recorded by the camera (without correction). The depth of denaturation in the centre of the beam matches the histology well. However the width of the denaturation zone nearer the surface is consistently underestimated and perhaps reflects poor implementation of the scattered component. It is recognised that the denaturation boundary is not always sharply defined, but general agreement with the theoretical results is good.

8.5.2 Discussion

Given the large number of approximations used for the model parameters, the resulting agreement with the histology measurements over the range of conditions tested, is encouraging. On this basis, the model temperature distribution can be assumed to be correct. When correlated with the thermal camera used to monitor tissue temperature during lasing of the thicker samples, the results of the model indicate camera temperature errors to be in excess of 30 deg.C (Table 8.1). Considering the *in vivo* laser bonds discussed in Chapter 3, it must be concluded that the indicated temperatures of 40-50 deg.C. in reality must have been some 30-40 deg.C. higher. This is in a agreement with the associated histology which showed widespread tissue damage. The model has also shown that no local hotspots are likely. It is thus safe to assume that the temperature within the lased area rises steadily from the onset of lasing until it reaches equilibrium some 5 or 10 seconds later. The implication for a moving spot is that if the tracking speed is slow enough the lased area will simply attain equilibrium temperature, and slowly cool as the beam moves on. However, at higher tracking speeds, the rise to thermal equilibrium is interrupted, the maximum temperature being somewhat less than the equilibrium temperature, in accordance with the time the tissue is illuminated by the beam.

Such information, although useful, does not provide further insight as to

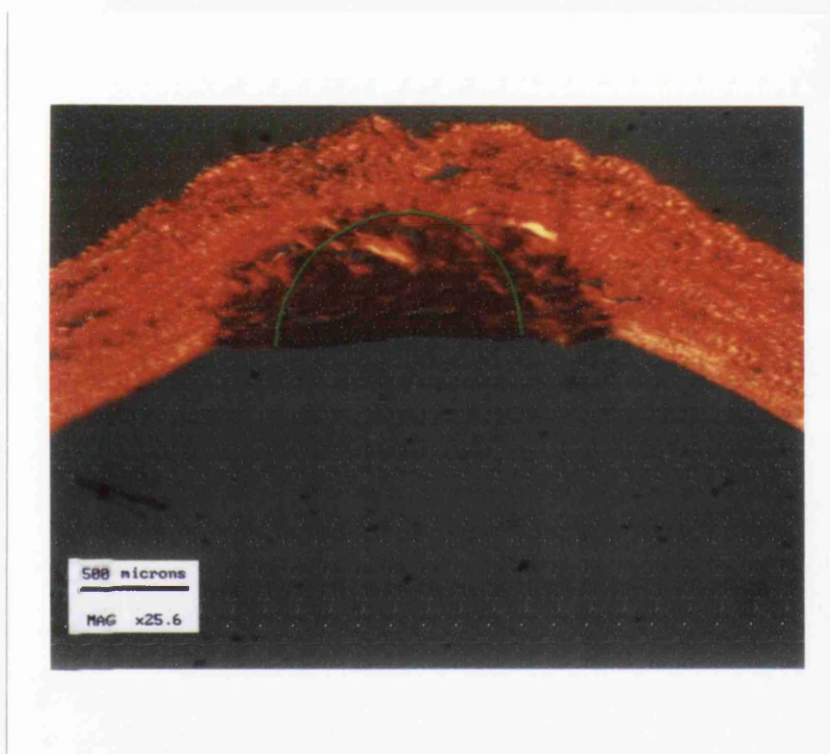


Figure 8.12 Central section of 660 μm thick tissue lased for 17.1 seconds at 230mW. The theoretically predicted boundary (~62 deg.C.) between denatured (dark areas) and non-denatured tissue is shown by the green line.

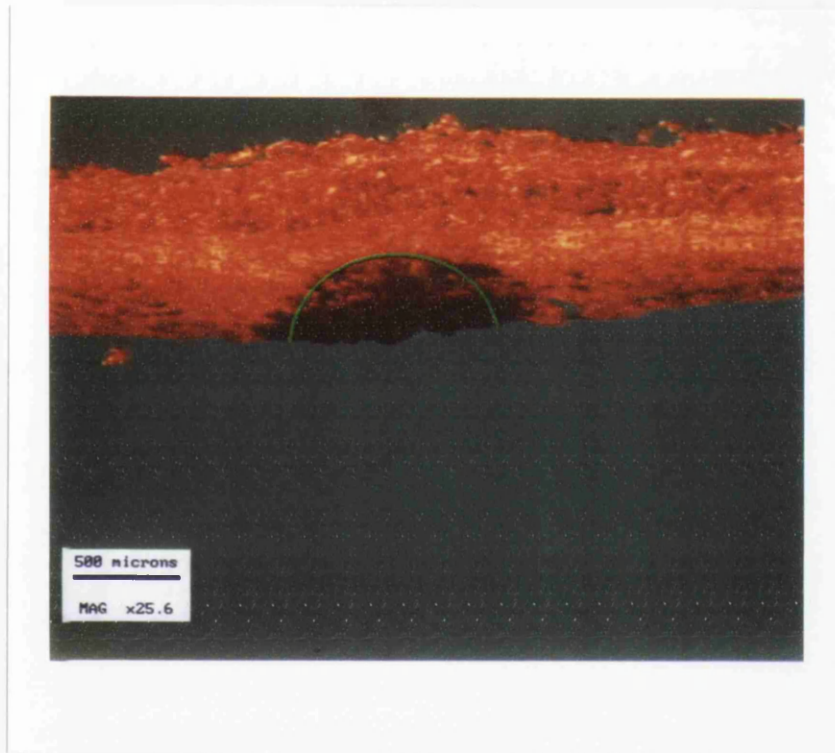


Figure 8.13 Central section of $800\mu\text{m}$ thick tissue lased for 13.4 seconds at 215mW. The theoretically predicted boundary (~ 62 deg.C.) between denatured (dark areas) and non-denatured tissue is shown by the green line.

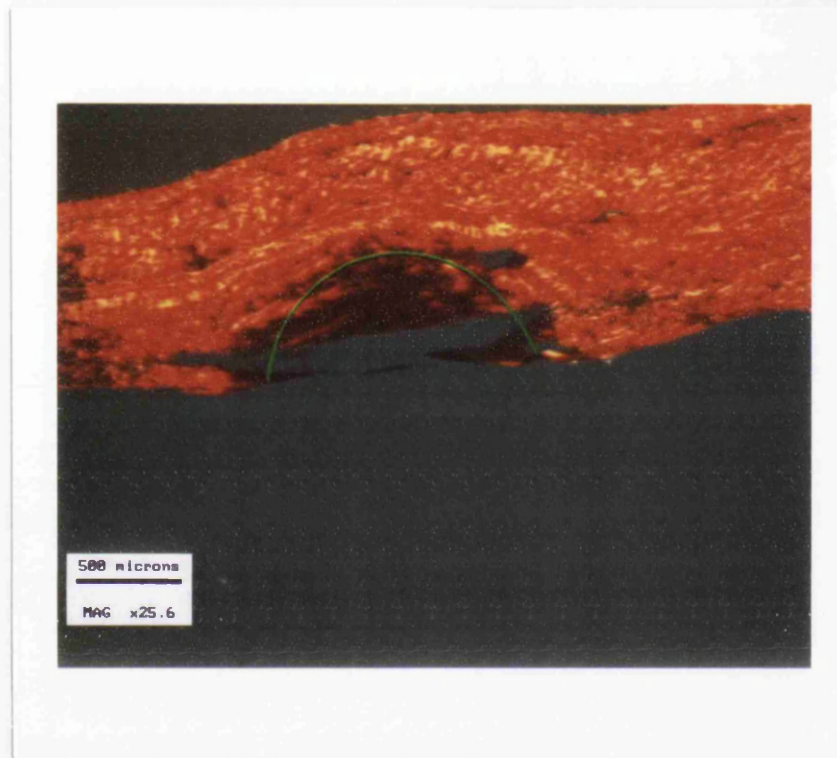


Figure 8.14 Central section of $950\mu\text{m}$ thick tissue lased for 21.6 seconds at 230mW. The theoretically predicted boundary (~ 62 deg.C.) between denatured (dark areas) and non-denatured tissue is shown by the green line.

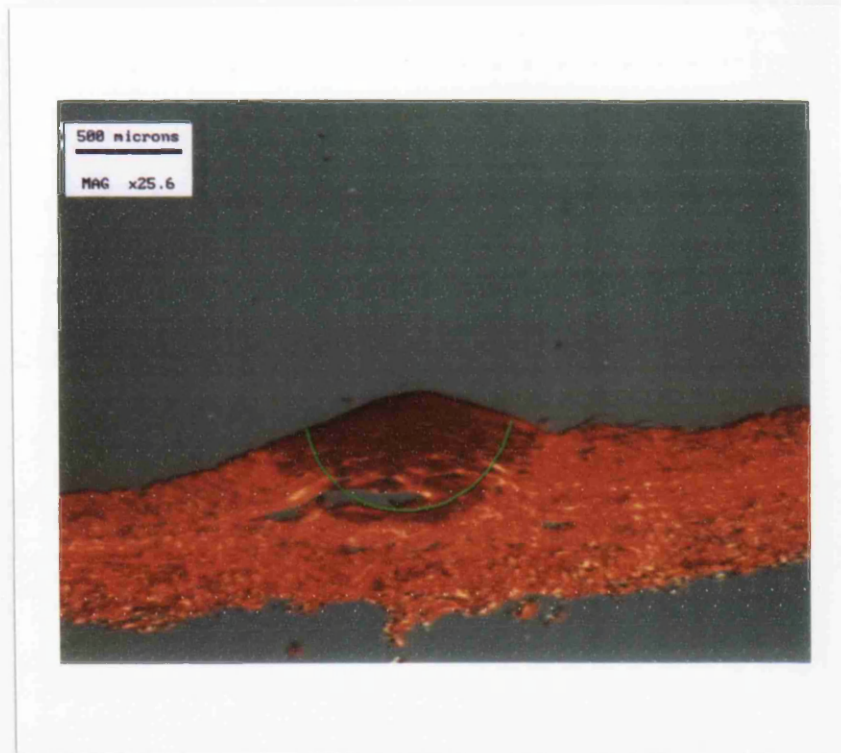


Figure 8.15 Central section of $640\mu\text{m}$ thick tissue lased for 17.7 seconds at 215mW. The theoretically predicted boundary (~ 62 deg.C.) between denatured (dark areas) and non-denatured tissue is shown by the green line.

		<i>Beam Centre</i>	
	Peak camera	Peak model	Peak model
	temperature	temperature at	temperature at
	(deg.C. ± 2)	$r=0\text{mm}$ (deg.C.)	$r=0.1\text{mm}$ (deg.C.)
Power, Time, Thickness			
230mW, 17.1secs, 660 μm	50	87.3	80.3
215mW, 13.4secs, 800 μm	35	83.5	76.9
230mW, 21.5secs, 950 μm	45	87.9	80.9
215mW, 17.6secs, 640 μm	42	83.3	76.7

Table 8.1 Calculated and recorded peak temperatures of tissue of variable thickness for a range of lasing times. The temperature obtained with the theoretical model is given at the radial symmetry axis ($r=0\text{mm}$) and at a radius of 0.1mm.

why Argon laser bonding does or does not occur, except to say that hotspots cannot be blamed for inconsistencies in bond strength. Temperature is believed to be an important parameter, but the evidence of the *in vivo* bonds of Chapter 3 in which tissue was denatured even though information from the thermal camera suggested otherwise, implores caution in the interpretation of temperature data, including that presented by other groups (47,79). On the other hand, this data must be considered in the light of our own experimental work (Chapter 6) in which bonds were successfully created at temperatures above and below denaturation, indicating that temperature is not as important as was first thought.

8.6 DEHYDRATION

The above exploration has revealed little about the bonding mechanism and thus prompts extension of the model to include dehydration. The experimental work of previous chapters has strongly implicated dehydration as the prime mechanism of Argon laser tissue bonding. It has been proposed that (120) bond strength is related to the proportion of water driven out of the bonding faces. With knowledge of the power distribution within the tissue it is possible to calculate the lasing time and hence the tracking speed required to achieve full bond strength (ie. the time required to evaporate all the water from the bonding faces). The numerical model has proven itself reliable, and therefore data provided by it is suitable for the dehydration calculation. The model will be used to determine the tracking speed required to achieve full bond strength with a 65mW beam incident upon apposed tissue faces 140 μ m thick (Chapter 6), based on dehydration. However, the distribution of power at the bonding faces is complicated by the presence of chromophore - it is very difficult (as a result of multiple scattering events) to estimate the power distribution at these faces. Rather, as an alternative, the distribution is inferred from the cooling characteristics of the tissue when the laser is switched off.

Consider the tissue slice heated to thermal equilibrium by a stationary beam of 65mW. At thermal equilibrium, the energy entering the system equals that leaving it. Hence the energy lost from the tissue at the instant of 'switch-off' must equal the power being absorbed from the laser. Such an approach makes few assumptions about the power distribution and absorption at the chromophore faces. Furthermore, tissue temperature is confined to be below 62 deg.C. according to the histology (65mW did not cause tissue denaturation).

The model was used to obtain the temperature distribution just prior to switch-off and in the ensuing period. Model parameters appropriate to the 65mW

bonding experiments of Chapter 6 were used. A graph of tissue temperature as a function of time is shown in the figures 8.16 and 8.17. The sharp negative temperature gradient at the point of switch-off is clearly visible. However before proceeding further, a small issue relating the model to the 65mW laser experiment needs to be addressed. The bond incision is not perfectly straight and thus the centre of the beam naturally wanders away from and back to the incision as it progresses along the length of the bond. A realistic estimate of the accuracy of delivery places the centre of the beam within $\pm 0.25\text{mm}$ of the incision. For this reason, a temperature gradient corresponding to the average temperature gradient over a central 0.25mm radius is used to calculate the absorbed power. A table of tissue temperatures showing cooling at the instant of switch-off is provided (Table 8.2).

The absorbed power at switch-off (ie. thermal equilibrium) is given by

$$\frac{dQ}{dt} = mc \frac{du}{dt}$$

Average temperature drop in 0.1 seconds (immediately after switch-off) = 3.8 deg.C. in a radius of 0.25mm. Tissue thickness = 0.14mm, with density $c = 1000 \text{ kgm}^{-3}$

$$\begin{aligned} \frac{dQ}{dt} &= mc \frac{du}{dt} = \rho Vc \frac{du}{dt} \\ &= 1000 \cdot \pi \cdot (0.25 \times 10^{-3})^2 \times 0.14 \times 10^{-3} \times 4.2 \times 10^3 \times \frac{3.8}{0.1} \\ &= 4.4 \text{ mW} = \text{Absorbed power} \end{aligned}$$

Dehydration:

The energy required to raise the same mass of water to 100 deg.C. and evaporate it is given by:

$$\begin{aligned} E_e &= mcdu + ml \\ &\quad (l = \text{latent heat} = 2.3 \times 10^6 \text{ Jkg}^{-1}) \\ &= m(cdu + l) \\ &= 2.75 \times 10^{-8} (4.2 \times 10^3 [100 - 20] + 2.3 \times 10^6) \\ &= 72.5 \text{ mJ} \end{aligned}$$

Applying a constant 4.4mW to this volume to dehydrate the water takes

$$\frac{72.5}{4.4} = 16.5 \text{ seconds}$$

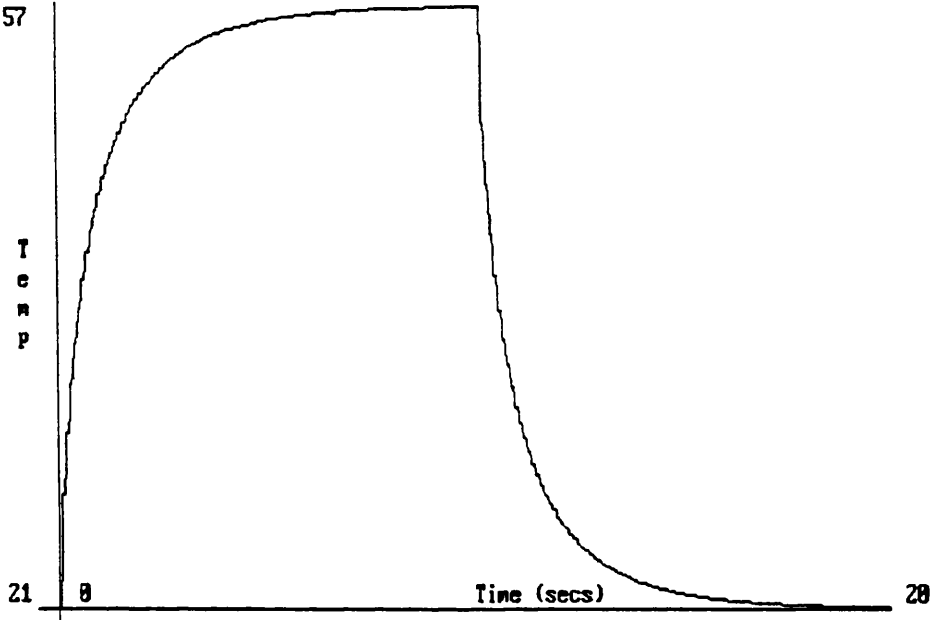


Figure 8.16 Tissue temperature as a function of time when lased with a stationary 65mW beam for 10 seconds before being switched off. Tissue slice modelled as 140 μ m thick.

View 2

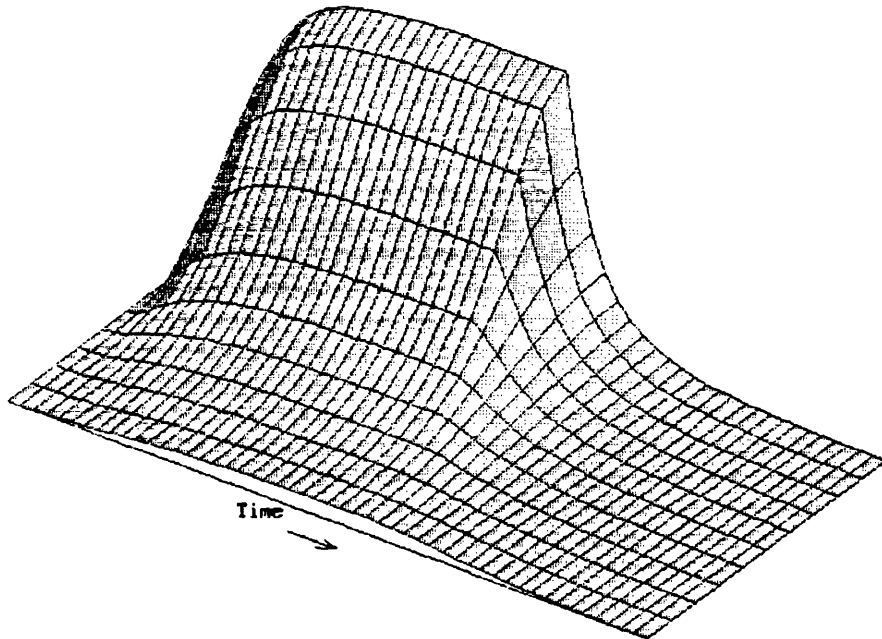


Figure 8.17 3-dimensional representation showing radial temperature evolution with time. The vertical axis shows temperature. Tissue was modelled as $140\mu\text{m}$ thick, and irradiated with a stationary 65mW beam for 10 seconds before being switched off.

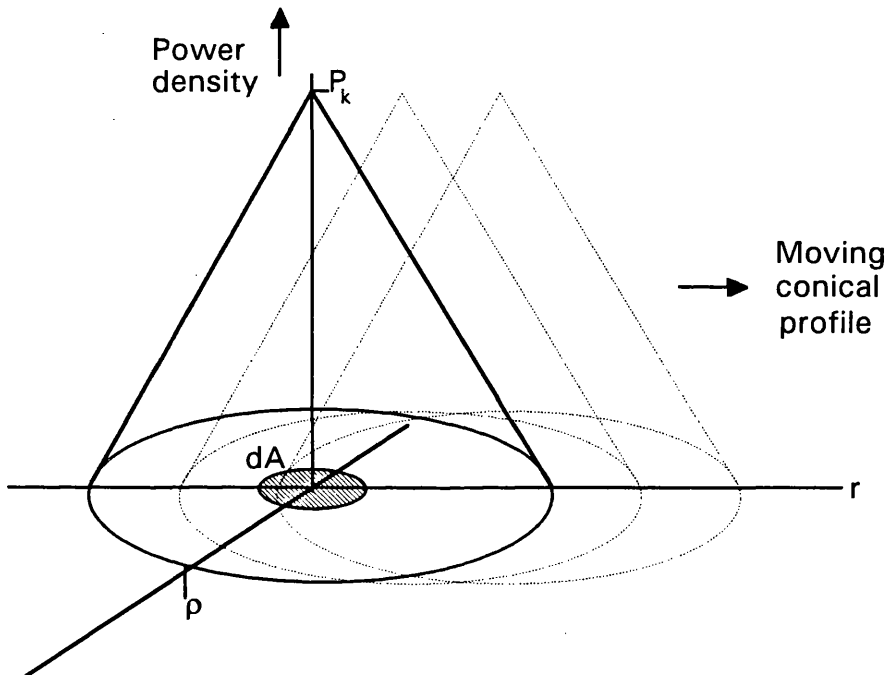
		<i>Beam Centre</i>		
	Time	Temp (deg.C) @	Temp (deg.C)	Temp (deg.C)
	(Seconds)	radius (r) = 0mm	at r=0.1mm	at r=0.2mm
	9.8	58.701	55.991	49.651
	9.9	58.705	55.995	49.656
'Switch-Off' here...	10	53.719	51.821	46.876
	10.1	49.715	48.259	44.375
	10.2	46.478	46.328	42.222
	10.3	43.803	42.878	40.352
	10.4	41.555	40.799	38.715
	10.5	39.64	39.014	37.274
	10.8	35.294	32.915	33.842
	11.5	29.563	29.415	28.321
	13	24.82	24.82	24.562

Table 8.2

A table of tissue temperatures (65mW beam, 140 μ m slice) at different radii (from the stationary beam centre) as a function of lasing time. The table begins after 9.8 seconds of lasing and the tissue has achieved thermal equilibrium. At 10 seconds the laser is switched off and the tissue cools rapidly.

However, the beam is not stationary but moves along the length of the incision. Therefore 4.4mW only represents the absorbed power at one point as the peak power passes by. We therefore sum the energy delivered to that spot by a single pass of the conical energy profile of radius 0.75mm. The average peak power density absorbed (P_k) in the 0.14mm depth is given by:

$$P_k = \frac{4.4 \times 10^{-3}}{\pi \cdot (0.25 \times 10^{-3})^2} = 22.4 \text{ kWm}^{-2}$$



With the beam moving at $v \text{ mms}^{-1}$ it can be considered to spend a period of $\frac{dr}{v}$ secs. on each elemental length before moving an increment dr . Thus the energy absorbed (dE_s) throughout the tissue depth in elemental area dA is

$$dE_s = P \left(1 - \frac{r}{\rho}\right) dA \frac{dr}{v}$$

and the energy from a single pass is given by

$$\begin{aligned} E_s &= 2PdA \frac{1}{v} \cdot \int_0^\rho \left(1 - \frac{r}{\rho}\right) dr \\ &= \frac{PdA}{\rho} \\ &= \frac{22.4 \times 10^3 \times \pi (0.25 \times 10^{-3})^2 \times 0.75 \times 10^{-3}}{v} \end{aligned}$$

$$E_s = \frac{3.3 \times 10^{-6}}{v}$$

In order to evaporate all water in a single pass, E_s must equal E_e (72.5mJ), so that

$$\begin{aligned} 72.5 \times 10^{-3} &= \frac{3.3 \times 10^{-6}}{v} \\ &= 4.55 \times 10^{-5} \text{ ms}^{-1} \\ &= 0.0455 \text{ mm s}^{-1} \\ v &= 22.0 \text{ sec mm}^{-1} \end{aligned}$$

Applying this result to the graph of figure 8.18 the calculated tracking speed correlates well with the position of the knee of the curve. This is where maximum bond strength is just achieved and corresponds to the point at which complete dehydration of the bonded area is calculated to occur. Based on the simple premise that bond strength is in direct proportion to the percentage dehydration of the bond line, the strength/tracking-speed curve might be expected to increase linearly with inverse tracking speed up to a maximum where the beam moves slowly enough to fully dehydrate the tissue. Such a curve would be expected to cut the origin (zero offset) but is not seen in the graph. This may be attributable to free water lying on the tissue surface which is also dehydrated in addition to that within the tissue. It could be argued that this calculation over estimates the inverse tracking speed required for complete dehydration since only 80% of the tissue by weight is water, however this must be balanced against the fact that tissue temperature is also probably overestimated since the model takes no account of the lased slice sitting on a cooler glass slide.

Given the vagaries of the model, agreement with the tracking speed graph is remarkably good. Certainly this line of investigation has proved more fruitful than that of temperature alone and further indicates that dehydration is the mechanism behind Argon laser bonding.

8.7 CONCLUSION

Using empirical data to establish values for parameters in the mathematical model, the evolving temperature distribution during lasing was calculated. The results of the model compare favourably with the results of experiment and indicate a large error (~30-40 deg.C.) in the thermal camera measurements used for the in vivo work. The model reveals the presence of localised hotspots to be highly unlikely, and so these cannot be blamed for the inconsistency of laser bonds. Rather, the

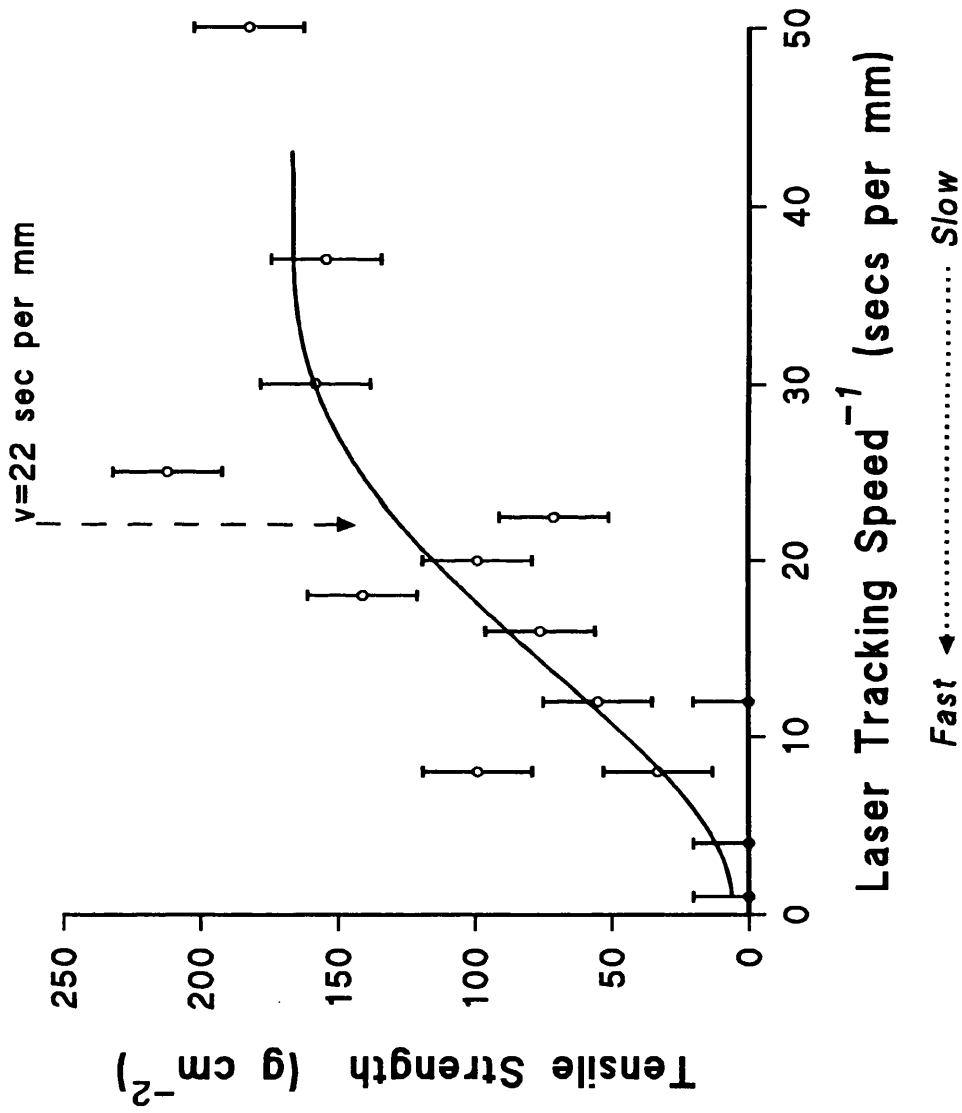


Figure 8.18 Bond strength as a function of laser tracking speed. The curve is a least squares 4th order polynomial fit to the data. The theoretically predicted minimum tracking speed⁻¹ required for maximum bond strength (65mW beam, 140µm thick tissue) is also shown (v).

result of lasing is a steady temperature rise to a maximum, followed by temperature decay as the beam moves on. For slow enough tracking speeds the maximum temperature equates to thermal equilibrium appropriate to the lasing conditions, but higher tracking speeds provide insufficient time for this temperature to be established, and hence maximum temperature decreases with increased tracking speed. However, of itself, the temperature information has proved inconclusive in so far as explaining the bonding mechanism is concerned. But if extended to include dehydration, the theoretical prediction of inverse tracking speed required for maximum bond strength coincides well with that shown experimentally - a compelling indication that Argon laser bonding is mediated by dehydration.

Chapter 9

Laser Bonding - Conclusions

9.1 INTRODUCTION

Laser assisted vessel anastomosis represents a potentially attractive alternative to sutured anastomosis. Its apparent simplicity is alluring, only requiring that a laser beam be directed along the apposed joint. In theory this would permit anastomosis of small vessels not possible with sutures, with improved precision and reduced operation time. Results have shown that such bonds can be of very high quality (to the extent that it is difficult to identify the position of the bond after lasing) with improved long term patency. Knowledge of the mechanism responsible for bonding has been sought in order to optimise bonding conditions and thus create consistently strong bonds. However despite investigation by many groups the mechanism remained unknown in detail, although it was attributed to the thermal effects of lasing. Thermal denaturation was considered necessary for a satisfactory bond - a conclusion drawn from work with the CO₂ laser. However White et al. (47,79) cast doubt on these claims since they created bonds at temperatures below the denaturation temperature of the tissue. This prompted the suggestion that a different mechanism was in evidence at the low temperatures encountered by White.

It was against this background that the work of this thesis was undertaken. The quantity of data that has since been accumulated is considerable and thus a summary of the salient points of each chapter is presented below, followed by a discussion of the work as a whole and implications for future investigation.

9.1.1 Chapter 3 - Laser Bonding In Vivo

Laser anastomosis of rabbit carotid arteries in vivo used a chromophore dye (1% fuchsin in alcohol) to locally increase Argon absorption at the apposed faces. No stay sutures were used. A thermal camera monitoring the proceedings recorded typical bonding temperatures of 40 - 50 deg.C. Although successful bonds were made, many ruptured several hours after the operation. Histology revealed extensive thermal damage in the bond area. Additional use of cyanoacrylate glue to

reinforce the laser bond saved the vessels from rupture, but created a very high incidence of fatal thrombosis.

9.1.2 Chapter 4 - Dry Bonds In Vitro

Overlapped tissue bonds were created without the use of a laser at temperatures encompassing those induced by the Argon laser (20 - 90 deg.C., error ± 3 deg.C.). The results of this work revealed:

- i) Bonds can be created at temperatures above and below denaturation;
- ii) Bonds created by dehydration (ie. dry bonds) are much stronger than those created under wet conditions;
- iii) Bond strength is temperature dependent. A jump in bond strength occurs as bonding temperature exceeds the denaturation temperature of the tissue;
- iv) Dry bond strength decreases after a period of rehydration;

9.1.3 Chapter 5 - Scatter of Dry Bonds

The dependence of the scatter of dry bond strength on bonding conditions was explored at a bonding temperature of 55 deg.C. Results showed that:

- i) Scatter in bond strength was reduced with improved quantification and removal of inter-surface air gaps;
- ii) Scatter in bond strength was reduced with increased pressure applied to the apposed surfaces;
- iii) Bond strength increased at high apposing pressures.

9.1.4 Chapter 6 - Laser/Dry Bonding Equivalence

The properties of butt-jointed laser and dry bonds were compared. In vitro bonding conditions similar to that found in the rabbit in vivo were used.

- i) Dry and laser bonds were successfully created at temperatures above and below denaturation.
- ii) No difference in bond strength between dry and laser bonds was recorded with bonding temperatures below denaturation.

- iii) Both laser and dry bonds demonstrated a jump in bond strength as the bonding temperature exceeded denaturation.
- iv) Strength of bonds created at temperatures above denaturation were significantly greater for dry bonds as compared to laser bonds.
- v) Both dry and laser bond strength decreased following a period of rehydration.
- vi) No difference in bond histology was observable between dry and laser groups created below the denaturation temperature of the tissue.
- vii) No difference in bond histology was observable between dry and laser groups created above the denaturation temperature of the tissue. Histology confirmed tissue denaturation in the bond area.
- viii) A large scatter (coefficient of variation = 30%) in breaking strength of natural tissue slices of comparable dimension to the bonded slices was demonstrated.
- ix) The properties of these bonds were similar to the overlapped dry bonds of Chapter 4.

9.1.5 Chapters 7 & 8 - Theory

In combination with empirical data a theoretical description of the laser bonding process was developed which:

- i) Excluded the possibility of highly localised areas of denaturation due to micro-hotspots within the lased tissue;
- ii) Adequately described the denatured region within a lased tissue sample;
- iii) Indicated a thermal camera error of 30-40 deg.C.
- iv) Qualitatively accounted for the shape of the bond strength/tracking speed graph, and when extended to include dehydration successfully indicated the point at which maximum bond strength was achieved.

9.2 OVERALL ASSESSMENT OF WORK

The *in vivo* laser bonding work of Chapter 3 demonstrated the difficulty of producing long term tissue bonds of consistent strength. The hitherto accumulated evidence of the CO₂ bonding work indicated that tissue denaturation was a necessary condition for successful laser bonding. However, the non-laser overlap bonding work of Chapter 4 (in agreement with the claims of White et al.) showed that denaturation was not a prerequisite for a tissue bond. Furthermore, in our experiment a laser was not used, thus excluding any photochemical explanation. The importance of dehydration in the creation of the overlapped tissue bonds led to the proposal of a mechanism based on dehydration to describe the bonding process. The nature of the short range bonding forces described in the model implicated surface apposition as a possible cause of scatter in bond strength. The resultant reduction in scatter due to improved apposition (Chapter 5) appeared to confirm this.

Applying the proposed mechanism to laser bonds required that bonding be the result of localised tissue dehydration within the beam at the apposed tissue faces. However, the bonding work carried out so far had only been performed on large slices of overlapped tissue under conditions rather different from the delicate butt-jointed bonds encountered with the laser *in vivo*. Thus the relevance of the overlap dry bonding work to that of the laser *in vivo* was in doubt. It was suggested that if dehydration was responsible for bonds created by both methods, the properties of the bonds should be the same. The work of Chapter 6 explored their similarities. All results (except one) showed no significant difference in the properties of bonds created by laser or dehydration. The exception refers to dry bonds created at temperatures above denaturation, which were significantly stronger than those created by laser at a similar temperature. That apart, the properties of the butt-jointed bonds (laser and dry) closely followed those of the overlap bonds.

The mathematical model (Chapters 7 & 8) used to describe the bonding temperature, satisfactorily depicted the area of tissue denaturation as observed histologically. In addition, extension of the model to include dehydration produced a good estimate of the laser exposure time required to obtain maximum bond strength.

The evidence provided above indicates that the mechanism responsible for tissue bonding by Argon laser or dehydration is the same. We therefore conclude that low temperature Argon laser bonding as practised by White et al. and ourselves is mediated by dehydration.

9.3 IMPLICATIONS

According to our proposed mechanism, the inconsistent bond strength and postoperative bond disruption of our *in vivo* work can be interpreted as the result of poor tissue apposition and subsequent bond rehydration. *In vivo*, there is little that can be done about natural rehydration. Thus tissue apposition becomes the appropriate focus of attempts to improve the laser bond. Our experimental work has shown that tissue apposition is critical to bond strength. Careful apposition of butt-jointed bonds was achieved in the laboratory using a microscope, but the scatter in bond strength remained large (standard deviation approximately 50%). A significant proportion of this may be due to natural tissue variability (standard deviation of breaking strength of natural unbonded tissue of similar dimensions was 30%). Given that 50% scatter was the minimum achievable under carefully controlled laboratory conditions, results in a clinical setting can be expected to be much worse, as indicated by our *in vivo* experiments.

This problem of inconsistency is the greatest stumbling block to clinical acceptance of the laser bonding technique. The interaction between bond consistency and apposition needs to be further explored. This would involve correlating bond strength against the percentage of tissue actually apposed (ie. in contact) along the length of a joint. The latter parameter is difficult to obtain since it requires detailed sectioning of the bond to estimate the contact area. However, a sectioned bond is clearly unfit for strength testing. A possible solution involves the use of a confocal microscope which can 'optically section' the bond region (no fixing of the tissue is required), to build up a 3-dimensional digital representation (121,122) of the state of the mating faces along the length of the joint. The bond can then be strength tested as per normal.

If apposition is the root cause of bond inconsistency, a mechanical jig might help to create the high quality apposition required for strong reproducible bonds. However, it is difficult to imagine what form such a device might take, given that it must be simple and small enough to be used *in vivo*, creating accurately aligned butt-joints with vessels of varied size down to less than 1mm diameter. In contrast, the overlap bond offers several advantages, in particular the large surface contact area available in comparison to that of butt-jointed bonds. End-to-end anastomoses may be possible with an overlap bond if one vessel was inserted inside the other (Fig. 9.1) and good apposition achieved by expanding the diameter of the overlapped vessels with a biodegradable stent. The vessel walls would need to be thin for adequate Argon laser penetration and the overlap joint would be pre-coated with chromophore for good laser absorption at the bonding surfaces.

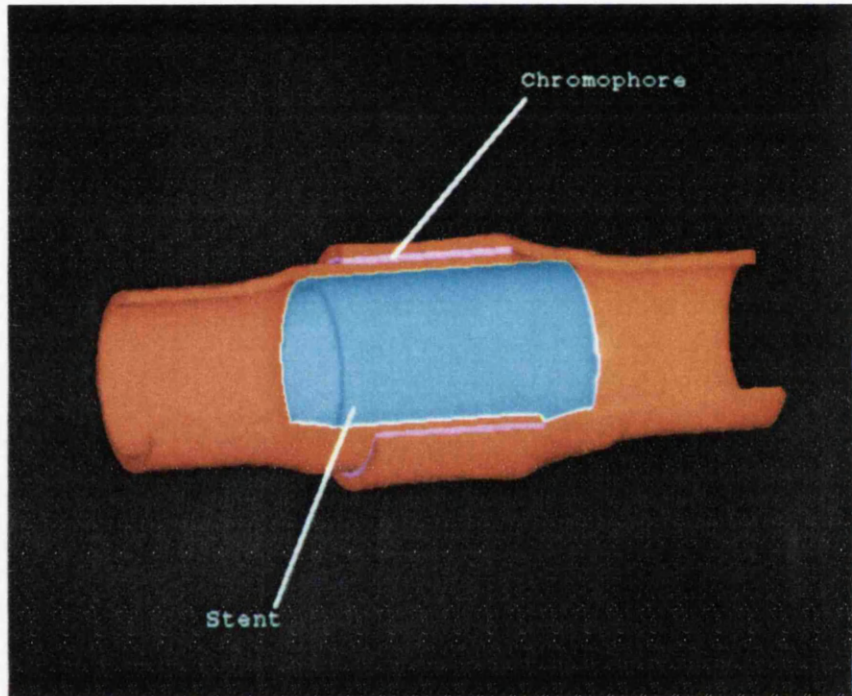


Figure 9.1 Cut-away showing proposed overlap bonding technique. Overlapped vessels are held in contact with the help of an intravascular stent.

The use of a chromophore is not widely reported in laser bonding circles, perhaps because the majority of work is performed with the CO₂ laser where no chromophore is required. Chromophores have been used in conjunction with the Nd:YAG laser (44,45) and its utility with respect to our work has been previously established (42,43). The chromophore we used was a solution of 1% fuchsin in 100% alcohol. Fuchsin is the coloured component (a deep purple), the alcohol simply acting as convenient carrier of the dye crystals in solvent form. The alcohol is known to help disperse water content in the bond area (111). On reflection this helps to explain the results of incidental unreported work carried out by ourselves in which dry and laser tissue bonds were created without chromophore. As expected, the lasing time required to create a bond increased significantly, but surprisingly so did the bonding time of the dry bonds in which no laser was used. This was confusing at the time, but it now seems likely that this is related to the water dispersing (ie. dehydrating) effect of the alcohol in the chromophore. By dissolving the same quantity of dye in an alcohol-water solution it might be expected that lasing times would increase in relation to the water content of the solvent. This is certainly worthy of further investigation. It also has bearing on the extreme case of White et al. who used no chromophore and poured water onto the bond while lasing. Under these conditions it is not surprising that he required high laser power to create the tissue bond, in view of the large quantity of water present.

As for tissue bonding and the CO₂ laser, this thesis represents a sound base from which to explore the mechanism of CO₂ laser bonding. Perhaps CO₂ bonds are mediated by dehydration? The properties of in vitro CO₂ bonds created at temperatures above and below the denaturation temperature of the tissue should be compared with Argon laser and dry bonds at the same temperature. However, assessment of bond strength would also need to be extended to bonding temperatures typical of the CO₂ bond - in excess of 100 deg.C. If maximum bond strength occurred just above the denaturation temperature, it would indicate that the higher temperatures are causing excessive tissue damage. This would imply that no new mechanism is active, the bonding being the result of dehydration. Other issues: Are CO₂ bonds weakened following rehydration? What form does the bond strength/tracking speed graph take, and can it be explained by a dehydration effect? Answers to the above questions would provide considerable insight into the nature of the CO₂ bonding process.

Finally, returning to laser bonding in vivo several questions remain. The biggest problem - apposition - has already been discussed. But what of bonding temperature? What temperature provides optimum durability? This is more than simply a question of bond strength, since in vivo the weld is merely a temporary

measure holding the tissue together until the healing process is adequately established. At temperatures above denaturation a stronger bond occurs, but tissue damage is considerable (denatured) and it is likely that healing will take longer. Alternatively the faster healing of a non-denatured bond must be balanced against the weaker bonds that are created. An additional factor is that bond strength is constantly weakened *in vivo* by natural rehydration. It must also be considered to what extent tissue is damaged by the dehydration process alone.

Looking forward to the next chapter, the action of laser balloon angioplasty supposedly fixes or bonds a stenosed vessel in an expanded state. The bonding of tissue planes of the vessel wall are involved which possibly parallels the action of our overlap bonds. From our experience of bonding to date, we are well placed to investigate the processes involved.

9.4 CONCLUSION

There is much work to do before the technique of laser bonding can become clinically acceptable. The greatest problem is apposition. The quality of surface intimacy required for consistent bonding apparently exceeds that which we were able to achieve in the laboratory. This problem alone suggests that the future of laser anastomosis is far from certain. We are not in a position to recommend what the optimal *in vivo* bonding conditions are, but we have been able to propose and validate a mechanism for Argon laser bonding and can point to those areas now in need of further investigation.

The potential similarity between the bonding process and laser balloon angioplasty now permits us to consider the latter in detail.

Chapter 10

Laser Balloon Angioplasty

10.1 INTRODUCTION

The subject of balloon angioplasty briefly referred to in the introductory chapter of this thesis will now be considered in detail.

Percutaneous transluminal coronary balloon angioplasty (PTCA) rapidly established itself in clinical practice during the early 1980's, having been introduced in the latter half of the previous decade (123,124). It has dramatically affected the treatment of coronary disease, being used as an alternative to coronary artery bypass surgery. The procedure involves crossing an atheromatous lesion with a deflated balloon which is then inflated (Fig. 10.1). The plaque is compressed by the inflation which opens the bore of the artery. Although less expensive to perform than bypass surgery, its principle shortcoming is the high rate of restenosis with some 30% of treated patients requiring further treatment within 6 months (125).

The role of the laser in angioplasty is recanalisation of stenotic or occluded arteries by ablation of atheroma. This produces channels with smooth walls (126). A more recent innovation is the simultaneous irradiation of plaque during balloon inflation (126,127). It is claimed that this can thermally remodel the vessel wall, fixing it in its expanded state. Investigation of the latter technique forms the subsequent chapters of this thesis.

10.2 HISTORY

Balloon catheters have a long history, James Arnott describing the use of a urethral dilatation catheter (128) as early as 1819. Cardiac catheterisation was utilised in 1929 by Werner Forssman (129) to infuse nutrients and drugs to the heart. Mason Sones (1959) pioneered coronary catheterisation with injection of contrast medium and cineangiography (130). Dotter and Judkins (1964) used a balloon catheter to treat atherosclerotic obstructions of the femoral artery (131). However it was not

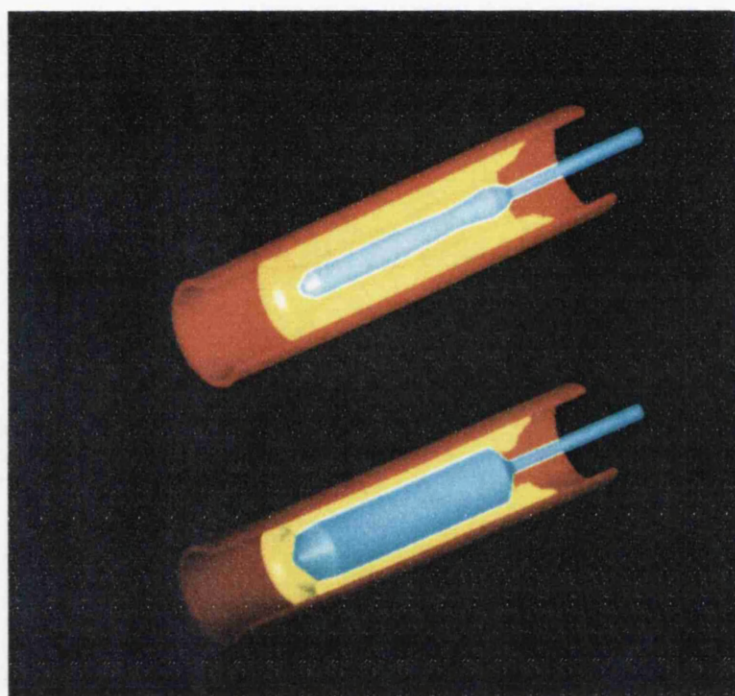


Figure 10.1 Diagrammatic action of angioplasty balloon. The bore of the vessel is increased by application of the expanded balloon to the yellow plaque.

until 1979 that Gruntzig described the potential therapeutic advantages of coronary balloon angioplasty in the treatment of coronary disease (123).

The standard procedure has changed little since its inception, but indications for treatment then were rather more restrictive than today (132), namely:

- i) Angina pectoris sufficient to compromise quality of life;
- ii) History of pain less than 1 year - indicates the presence of soft compressible atheroma;
- iii) Single vessel disease of a dominant artery;
- iv) Readily accessible atheroma.

As confidence with the technique has grown, the selection criteria have broadened. It is now estimated that between 10% and 20% of revascularisation candidates are suitable for PTCA. The list of conditions considered includes multivessel coronary disease, unstable angina, isolated main coronary disease, anastomotic stenosis and revascularisation during the acute phase of evolving myocardial infarction. Intraoperative dilatation during bypass surgery has also been used, dilating a constriction distal to the anastomosis if the vessel in this area is unsuitable for grafting (133,134,135).

The minimally invasive approach of angioplasty as compared to bypass surgery is much appreciated by the patient, and other advantages include reduced morbidity and cost (136,137). However, the procedure is not applicable to patients with extensive disease and it is not without risk. There was a period when it was believed that PTCA represented a 'no lose' situation, because at its worst, failure simply required a resort to the established technique of bypass surgery. However, it has since emerged that the mortality of failed coronary angioplasty patients undergoing emergency bypass is some 10 times higher than that of a comparable bypass group. Mortality jumps from 1% to 11% (138).

10.3 BALLOON ANGIOPLASTY IN PRACTICE

It is appropriate to consider a typical angioplasty procedure to place the role of the laser in context.

A small cannula inserted into the femoral artery of the patient permits passage of a soft tipped flexible wire (guidewire) through the vascular network to the diseased coronary artery. Visualisation of the procedure is provided by angiography. Once the guidewire has been placed across the lesion, the deflated catheter balloon is manoeuvred to the same spot by sliding the catheter over the guidewire. A thin metal ring at the centre of the balloon permits radiographic

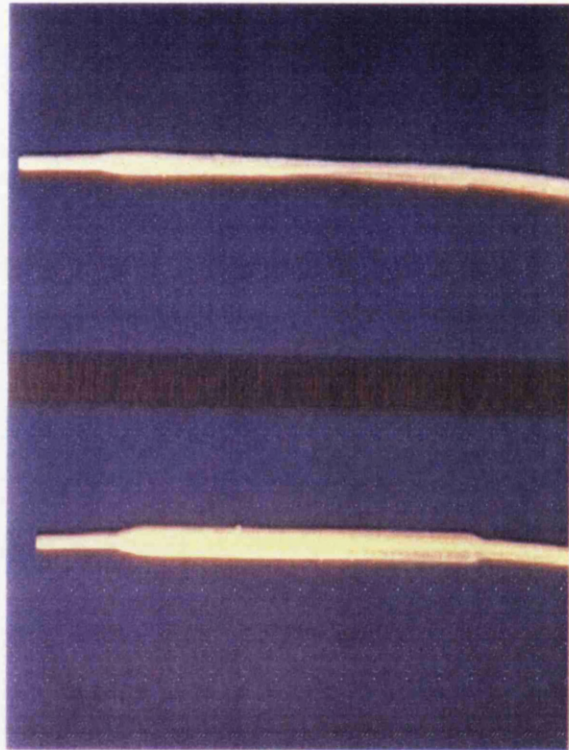


Figure 10.2 Deflated (top) and inflated (bottom) angioplasty balloon.

identification of its position in vivo. The balloon expands cylindrically to a specified diameter when inflated under pressure (Fig. 10.2). It is inflated for up to 30 seconds, compressing the plaque and stretching the vessel wall. The inflation pressure (typically between 4 and 10 atmospheres - ie. 0.4 to 1MPa) determines the forces applied to the plaque face. Repeat inflations may be necessary to achieve the desired increase in vessel diameter as observed by arteriography with the balloon deflated.

Temporary occlusion of the vessel by the balloon can cause angina, but these symptoms disappear rapidly after balloon deflation. Of more concern is the occurrence of total coronary occlusion which may result from the mechanical insult to the vessel wall. In extreme cases this may persist, requiring emergency coronary artery bypass surgery to bridge the lesion.

10.3.1 Complications

Platelets can initiate thrombus formation and therefore heparin and anti-platelet drugs are administered to reduce the risk of clotting. Transient effects of inflation include angina and possible arrhythmias which are dealt with as they arise. More damaging effects arise from direct stimulation of the vessel wall, the most serious of which is acute coronary occlusion. This occurs as the result of vessel spasm, thrombus, or haemorrhage into the plaque. Thrombus occlusion can be dealt with by further balloon inflations. Spasm rarely occurs if calcium channel blockers and nitrates are used.

Balloon inflation can produce splitting of the vessel wall to produce intimal flaps and dissections. A review of failed PTCA patients placed for emergency bypass surgery revealed that nearly 90% were the result of arterial dissection and/or occlusion (138). In this group of patients, the most common cause of post-operative death was low cardiac output.

In the longer term, the principal limitation of balloon angioplasty - even after an apparently successful procedure - is restenosis (139,140), the condition typically being manifested by the return of angina symptoms. The mechanism of restenosis is poorly understood but appears to be associated with intimal hyperplasia (141), the eventual bulk of the lesion being determined by the vigour of the smooth muscle reaction (142). Antithrombotic agents are administered on the basis that restenosis is a form of accelerated thrombosis. It has also been suggested that elastic recoil of the stretched coronary wall contributes to restenosis of the vessel (143).

10.4 MODIFICATIONS

Various modifications to the technique of angioplasty have been implemented to circumvent the complications outlined above.

Coronary stenosis is graded as a percentage constriction of lumen diameter as obtained radiographically. However, between the extremes of 10% and 90% constriction, its relevance as an indicator of graded physiological impairment has been questioned (144). Thus some groups are investigating alternative visualisation techniques (145-149). These attempt to obtain information about the structure and content of the plaque as well as luminal shape and diameter.

Nonetheless, general improvement in the quality of the radiographic image is useful since it improves visualisation of catheter position and permits better interpretation of the effects of angioplasty on the vessel wall. Thinner catheters with a steerable guidewire and variable stiffness enable better negotiation of arteries. Stronger balloons allow higher pressures to be used with greater expanding forces applied to the plaque (150). Vascular stents, acting as an internal circumferential scaffold to support the lumen, open the possibility of preventing abrupt vessel closure, and constructed of appropriate biocompatible materials may inhibit restenosis (151-154). Initial attempts in this area were poor, the stents performing unpredictably. Modern variants however, are flexible, biocompatible and thrombosis resistant. Flexibility of a stent is important because it is required to have an initially small diameter in order to pass through the vessel network before being expanded to its full size. Nitinol is a metal stent which achieves the expansion by heating (151). Other stents are expanded beyond their elastic limit by balloon, at which point they are unable to collapse. However, such techniques are currently rather experimental and little *in vivo* human data is available.

Mechanical recanalisation, beyond punching a hole through the thrombus with a guidewire, can utilise rotational catheters which wind the thrombus matrix tightly round the shaft to be later expelled from the system (155).

10.5 THE LASER IN ANGIOPLASTY

The technique of coronary balloon angioplasty was rapidly accepted after its introduction in 1979. Within a few years a PTCA registry had been established, containing several thousand patients by 1982 (156,157). The availability of this growing body of formal data certainly encouraged acceptance of the technique. The next few years provided a learning period during which its limitations became apparent, particularly the problem of restenosis. So it was that the laser was introduced, being applied in two areas: principally recanalisation, but also laser

assisted balloon angioplasty. Both utilise the thermal component of laser radiation and are discussed below.

10.5.1 Recanalisation

Laser recanalisation relies on the thermal ability of the laser to ablate tissue (126,158). At its most crude, it involves placing an optical fibre at an occlusion and mechanically pushing it through the plaque, aided by the ablative radiation from the fibre tip. The fibre is subsequently withdrawn and replaced by a balloon, angioplasty being performed to augment final lumen diameter.

The most widely used lasers for the procedure are Argon and Nd:YAG. The list does not include the CO₂ laser, since its radiation is currently unable to be transmitted by optical fibre. High power, short exposure irradiations are recommended. With short enough pulses the tissue does not have time to conduct the heat away from the target site, resulting in more efficient ablation with reduced thermal injury to surrounding tissue (159,160).

It has been argued that the Argon laser is unsuitable for plaque ablation since absorption of Argon wavelengths by the natural vessel lies between that of fatty and fibrous plaques (161,162). A possible solution involves differentiating the material being irradiated by an in vivo spectroscopic technique, analysing the return signal from the laser irradiated tissue (163,164). A logical extension of this involves the injection of chromophore which localises in atheroma (165). This locally increased absorption for Argon wavelengths would improve the specificity and efficiency of plaque ablation. The output of the Nd:YAG laser encounters more suitable absorption characteristics (166,167,168). It has greater penetration than the Argon laser, is less absorbed by blood, resulting in deeper ablation.

In recognition of the danger of vessel perforation by a bare fibre tip, numerous modified tips have been designed. The metal capped fibre tip absorbs all the radiation and is heated to a high temperature (169,170). Like a thermic lance, it bores its way through the occlusive material. Although perforation is reduced, and a channel of larger diameter than a bare fibre is cut, associated thermal damage is relatively large. The sapphire tip attempts to reduce this by being heated to much higher temperatures (in excess of 2000 deg.C.), producing similarly large channels but with reduced thermal injury (171). Another alternative is to retain the direct ablative effect of the radiation by replacing the cap with a silica lens. This produces a more predictable and uniform beam than the bare fibre, and keeps thermal damage to a minimum because of radiative ablation (172,173).

Such techniques reduce the chances of perforation, but other complications remain. These include haematoma at the puncture site, pseudoaneurysm,

thrombosis distal to the target area and acute reocclusion within 24 hours of the procedure (174-177). It has been argued that different lasers rather than modified probes are required, and this line of investigation has met with limited success. The Excimer laser has shown promise, having successfully recanalised stenotic coronaries, and superficial and popliteal arteries in man (178,179,180). Its ultraviolet output appears to cleanly ablate tissue with remarkably little thermal damage and appears to relax the vessel. This contrasts with the Argon and Nd:YAG lasers which induce vascular spasm at extended exposures (181,182). The Erbium-YAG laser is claimed to be superior to the Excimer laser because it acts in much the same way but produces fewer toxic fumes during ablation (183).

The primary success rate of laser angioplasty applied to totally occluded vessels is between 65% and 90%, and in stenotic vessels it is 90%. Reports show that these figures are improving (126). Failure most commonly occurs in those vessels that have long lesions or poor distal vessel run-off. Heavily calcified lesions present a problem since it is not always possible to get the fibre through the atheroma (184,185,186). In spite of these problems, the laser remains a useful tool in recanalisation of total occlusions or long stenotic lesions, but in truth its future role is not established. Currently it must be used in conjunction with balloon angioplasty to enable the small ablated channels to be expanded. The balloon increases channel diameter and creates a smooth luminal surface. Proponents of the laser suggest that this may not be necessary (187) if a fibre with a large diameter sapphire tip was used (eg. 3mm). This would bore a channel of adequate diameter without the need for additional balloon treatment and would establish the laser as a treatment modality in its own right, particularly if it could be shown that improved long term patency was the result.

10.5.2 Laser Balloon Angioplasty

The introduction of the laser has improved recanalisation but data indicates that restenosis remains a problem. This is considered to result from the creation of a thrombogenic surface by both balloon and laser (endothelial denudation, mural tears) the contours of which encourage local flow separation (188,189,190) leading to platelet aggregation, microthrombi and lipoprotein deposition. Smooth muscle cell proliferation and visco-elastic recoil of the vessel wall are also important factors (139-143,191-193).

A combined laser-balloon has been developed by Spears et al. to address these problems (127,194), laser irradiation taking place during balloon inflation. The dilatation catheter contains a fibre whose uniformly dispersive tip is centred within the transparent balloon. The balloon is inflated as for a normal angioplasty

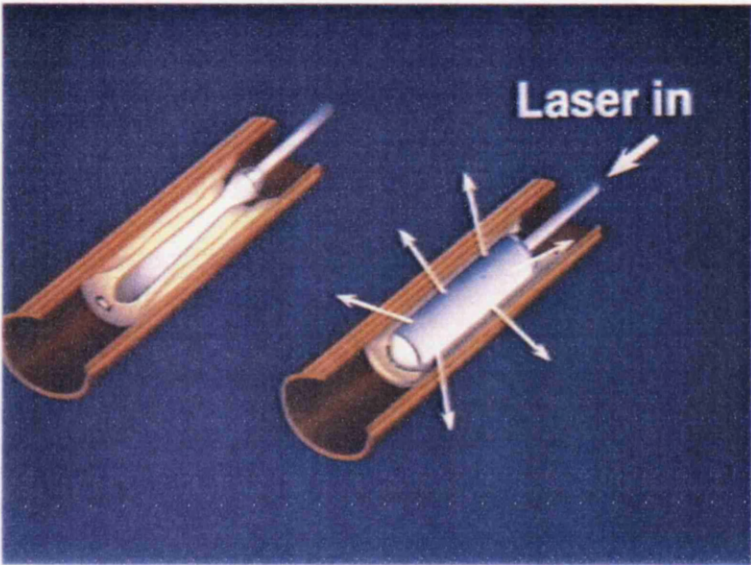


Figure 10.3 The Spears laser balloon is used to irradiate the expanded vessel during balloon inflation.

procedure, but the final inflation includes irradiation of the vessel lumen during balloon inflation (Fig. 10.3). This heats the vessel wall to temperatures of between 80 and 120 deg.C. It is suggested that the treatment dehydrates thrombi, smoothes the luminal surface and alters the elastic properties of the wall in such a way as to impede visco-elastic recoil (introducing the concept of a biological stent) and thus reducing restenosis. It was the *in vitro* work of Jenkins and Spears which revealed that intimal flaps and dissections could be welded back onto the vessel wall if temperatures in the region of 100 deg.C. were applied (109,195-197). This was an important finding given that many PTCA failures are attributed to occlusion as a result of arterial dissection. Several clinical trials have been initiated to evaluate the technique, but results to date have been equivocal (177,198,199).

Despite the obvious differences in bonding conditions, the sealing of arterial dissections has strong overtones of laser tissue bonding. The theoretical framework of laser tissue interactions is already available and much is applicable to laser balloon angioplasty with little or no changes (117,200,201). As with laser bonding the tissue absorbs light, which degrades into heat, and raises tissue temperature. Mathematically, thermal damage can be associated with the denaturation temperature, and at temperatures in the region of 100 deg.C. allowances must be made for phase transitions (84). The bonding mechanism is more clearly thermal in the case of laser balloon angioplasty, the laser simply acting as convenient, controllable source of energy. Other energy sources have been utilised, such as heating by microwaves (202). Heating the balloon with hot saline has also been tried (203,204) with results comparable to the laser, but none of this work has systematically evaluated the effect of balloon temperature on the diseased artery. Rather these techniques tend to be applied *in vivo* to be evaluated radiographically and histologically (where possible) in the follow-up period (months to years). Acutely expanded vessel diameter in excess of that achievable with the normal balloon procedure is a common experience, but restenosis usually becomes evident in the following months.

The investigative work that has been performed on laser balloon angioplasty, has not accurately characterised the temperatures induced in the vessel wall. (The problem of assessing temperature is not dissimilar to that encountered in the laser bonding work). Furthermore, it is not clear what the immediate objectives of the procedure are in detail, other than expansion of the lumen and reduction of restenosis. We would suggest the problem presents itself in two parts, namely (i) the sealing of intimal flaps (investigated by Jenkins et al. (109,195)) and (ii) modification of vessel wall characteristics (eg. lumen diameter, elasticity) to stop restenosis.

In response to (i), the parallels between laser sealing of dissections and laser tissue bonding (as discussed earlier in this thesis) raise the question of whether the high temperatures quoted for successful sealing are actually required. Is it possible that the sealing is mediated by dehydration? However, lower temperature bonding may not be appropriate since the increased length of time to achieve the seal may prohibitively increase thermal damage due to conduction of heat to neighbouring areas.

In response to (ii), temperatures of 100 deg.C. must affect the physical characteristics or properties of the vessel wall - this has not been investigated. It must be asked to what extent the applied heat cause thermal shrinkage, or how denaturation affects the bore of the treated vessel? Also, how is the elastic modulus of the vessel modified, if at all? - and all such effects are likely to be temperature dependent.

In the light of this (and the difficulty of obtaining temperature information from the laser balloon), a fluid-driven balloon was developed, capable of simulating the thermal effects of the laser balloon whilst providing accurate temperature information. The equipment was used to implement thermal angioplasty to investigate the effect of balloon temperature on lumen diameter. This information is essential if creation of a viable biological stent is to be achieved in the hope of reducing restenosis, and is the concern of the remaining chapters of this thesis.

Chapter 11

Thermal Simulation of Laser Balloon

11.1 INTRODUCTION

Simulating the effects of a laser balloon angioplasty catheter (LBAC) raises particular and detailed questions about its mode of action. For instance, what mechanical or physical effects is it achieving, and by what mechanism? Should the balloon system be treating plaque, the vessel wall or both? What is the effect of the various parameters - inflation time, inflation pressure, temperature, energy, intensity etc. - on the outcome of the treatment? Unfortunately, very little is known about the interactions of the laser balloon with tissue and this makes it an uncharacterised tool in the context of augmenting balloon angioplasty.

As with the laser bonding work, advantageous effects are reported to occur at certain temperatures, but detailed examination reveals that little is known about the actual conditions being generated by the laser. Thermal response of the tissue during lasing is very difficult to measure, and therefore current understanding relies heavily on insights from the theoretical world. The answering of fundamental questions regarding the interactions required for successful laser angioplasty requires an approach in which parameters are measured, and outcomes predicted and confirmed. From work already undertaken, it seems highly unlikely that the major effects of laser balloon angioplasty result from a photochemical response. Indications are that the principal causative factor is thermal, in which tissue response is a function of temperature (109). If this is correct, emulation of the laser balloon is reduced to imposing specified temperatures on the vessel wall during balloon inflation.

Vessels can be heated in several ways, through conduction, convection or radiation. The laser relies on the latter, and temperature information is difficult to acquire. In contrast, heating the vessel wall by conduction (through application of a constant temperature balloon to the vessel) permits better evaluation of temperature and its effects during balloon angioplasty. Since standard angioplasty procedure uses fluid to inflate the balloon, measurement of fluid temperature

provides a fairly direct and reliable way of assessing the temperature of the vessel. This approach to simulation of the laser balloon is now explored in detail.

11.2 A MODIFIED BALLOON TO SIMULATE THERMAL EFFECTS OF LASER BALLOON ANGIOPLASTY

The construction of a standard balloon catheter is described, followed by a description of the laser device. Modification of the standard balloon to permit thermal emulation of the laser balloon is then outlined with a detailed comparison of the merits of each.

11.2.1 Standard Balloon Angioplasty Catheter

The standard balloon catheter is a simple device which has changed little over the years since its introduction in 1979 (123). Its basic construction is shown in figure 11.1 (eg. Cordis coronary dilatation catheter: balloon diameter 3.0mm, balloon length 2.0cm, maximum guidewire 0.014 inches). The catheter consists of two coaxial cylindrical channels. The outer channel terminates as a balloon, the end of which is sealed onto the inner guidewire channel. Its plastic construction is resistant to heat, being both flexible and yet non-distensible. Fluid pumped into the outer channel inflates the balloon to its natural diameter, and being non-distensible, balloon diameter varies little with increased internal pressure, up to and beyond 10 atmospheres (1MPa). The central guidewire sheath is simply a flexible hollow cylinder through which a guidewire may be pushed. A small metal ring attached to the guidewire sheath within the balloon identifies balloon position during angiography.

11.2.2 Laser Balloon Angioplasty Catheter

The laser balloon angioplasty catheter is a three channel version of the standard balloon catheter. Separate channels are provided for the guidewire and balloon with the addition of another for an optical fibre which takes the laser light to the balloon. The fibre terminates in a dispersive tip which wraps around the guidewire channel and irradiates the vessel wall through the balloon. Laser balloon catheters tend to be driven by a Nd:YAG laser, the output of which can be transmitted through a fibre and has certain desirable properties with respect to interaction with diseased tissue (eg. good tissue penetration with large scatter coefficient). In operation, the balloon is inserted into the diseased vessel and inflated as for standard balloon angioplasty. It is only at the final inflation that the laser is activated and used to 'seal' or 'fix' the vessel and plaque in its new position.

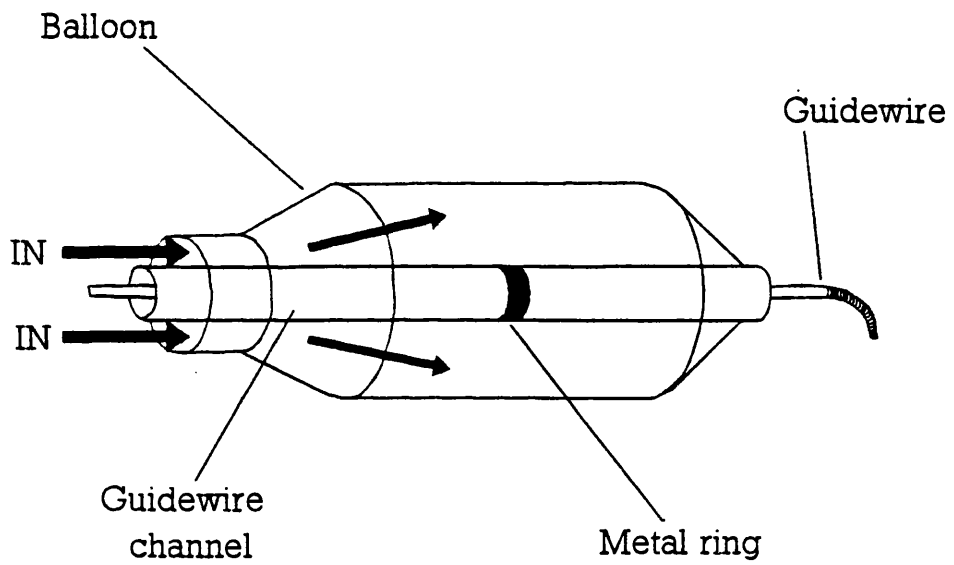


Figure 11.1 Construction of a standard angioplasty balloon catheter. Arrows indicate fluid flow for balloon inflation.

11.2.3 Modified Balloon Angioplasty Catheter - 'Thermal Balloon'

The modified thermal balloon angioplasty catheter was designed to simulate the temperature conditions generated by the laser balloon and was constructed from a standard balloon catheter.

The guidewire sheath of a standard 3.0mm balloon catheter was perforated in the area of the balloon. This was done by cutting off the end of the guidewire sheath to break the seal between it and the balloon (but still keeping the balloon intact). The balloon was pulled back 1-2 cm, to expose the guidewire sheath. A hypodermic needle just large enough to fit within the bore of the guidewire channel was inserted (to support it when being cut), and a scalpel used to cut 3 or 4 evenly spaced holes, approximately 1mm in length, along the length of the exposed sheath. This permits free flow of fluid between guidewire and balloon channels. With the supporting needle removed, the balloon was returned to its original position, encompassing the holes, and resealed to the guidewire sheath with superglue. The end of the guidewire channel was plugged with superglue and 1-2mm of guidewire.

The modified catheter works as follows. Water pumped through the guidewire channel is forced into the balloon and inflates it (Fig. 11.2). The water leaves through the outer channel and drips from the balloon port of the catheter (the exit port). However, the fine passage presented by the outer channel restricts the exiting flow, and the back pressure inflates the balloon. The higher the flow rate into the guidewire channel, the greater the back pressure and hence the pressure within the balloon. Pressures in excess of 10 atmospheres (1MPa) can be generated this way. The balloon can be heated by pumping hot water through it. Thermocouples monitor the entrance and exit temperature of the water (ie. the temperatures at the catheter guidewire and balloon ports respectively) and provide a fairly accurate estimate (± 5 deg.C.) of balloon temperature. The constant replenishment of hot water within the balloon keeps its temperature stable. Higher flow rates not only increase balloon pressure but effectively increase its thermal mass since water of a constant temperature replenishes the balloon at a faster rate. Pressure sensors placed at the entrance and exit ports enable balloon pressure to be monitored.

11.3 SUPPORTING EQUIPMENT

The mode of operation of the thermal balloon dictates the nature of supporting equipment required to drive it. A powerful pump is needed to circulate water through the catheter at a constant flow rate, capable of generating pressures

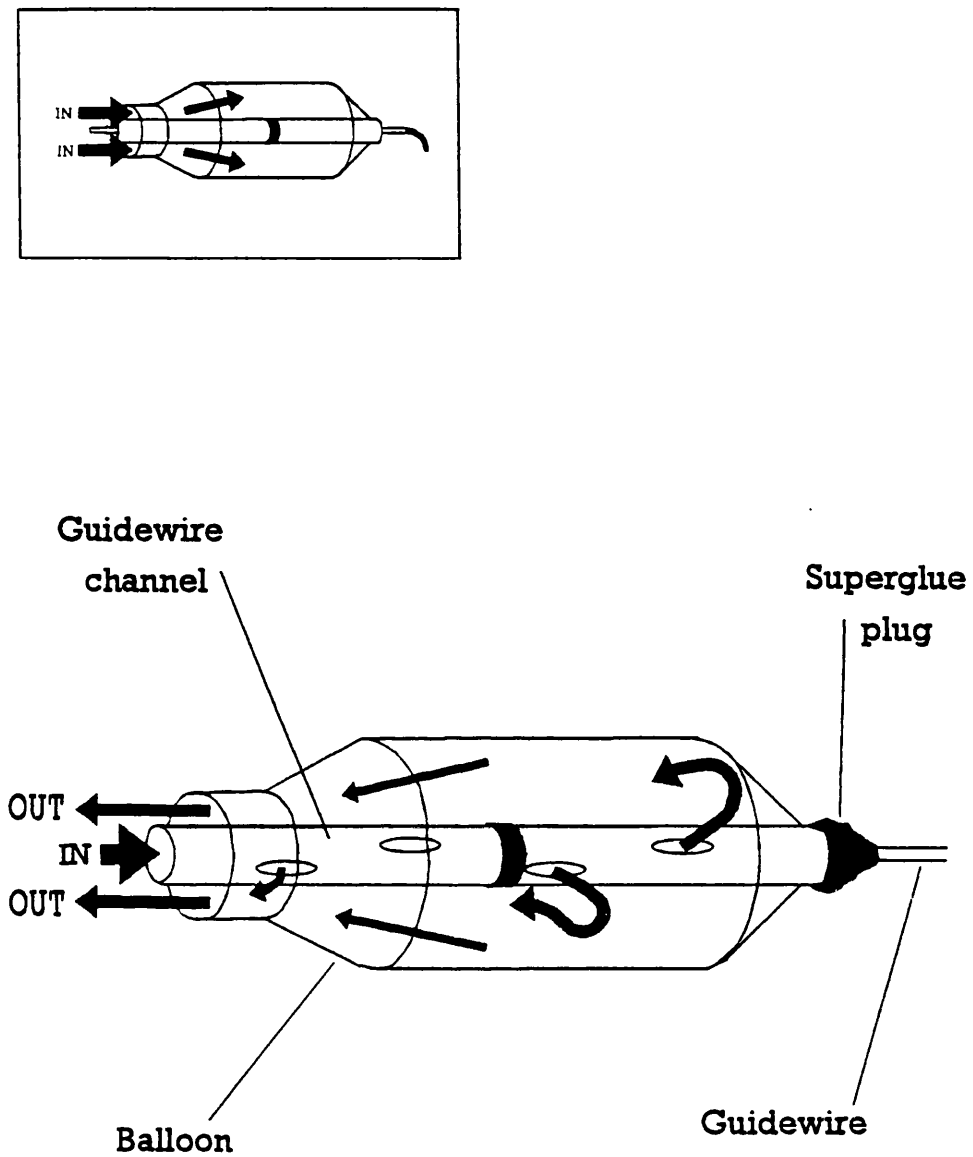


Figure 11.2 The modified balloon accepts fluid through the guidewire channel which exits through the outer balloon channel. Arrows indicate direction of fluid flow. The inset displays the standard balloon for comparison.

typical of balloon angioplasty - up to 10 atmospheres (1MPa). In addition a temperature stabilised heat exchanger is required to heat the circulating water (and hence the balloon) to a specified temperature. The arrangement is shown in figure 11.3.

11.3.1 Peristaltic Pump

The only pump available in our laboratory with enough power to drive the water at 10 atmospheres (1MPa) was a large peristaltic unit, operated under optimised conditions. The force required from the vanes of the pump is related to the bore of the tube being subjected to peristalsis (Fig. 11.4). The pump was unable to supply the force necessary to generate high balloon pressures if the tube bore exceeded approximately 5mm or more. Thus the tube bore was reduced so that a lesser force was required. The speed of the pump (revolutions per minute) set the flow rate, which pressurised the balloon.

11.3.2 Heat Exchanger

The heat exchanger was placed after the pump to reduce tube fatigue. If placed in front of the pump, those parts of the tubes subjected to direct peristaltic action, rapidly fatigued when pumped at high temperature and pressure. At 90 deg.C. they consistently ruptured within minutes. A long lasting tube appeared to require an unusual mix of properties, being heat resistant and strong enough to withstand high pressure for long periods, and yet flexible enough to be pumped by peristaltic action. Trial and error showed that PVC tubes were more durable than most. The temperature at the pump was reduced by moving the heat exchanger. Thus pumping was performed cold, after which the high pressure water was heated in the heat exchanger as shown (Fig. 11.4). This resulted in a system whose tubes could supply the balloon at high temperature and pressure for over 30 minutes before failing.

11.3.3 Non-Return Valve and Compliance Chamber

Balloon pressure was monitored via a T-piece connected to the entrance (guidewire) port of the catheter. The non-return valve and compliance chamber were introduced to keep balloon pressure constant. Without either, the pressure gauge revealed large rhythmic pressure fluctuations of the order of 3-4 atmospheres (0.3-0.4MPa) synchronised to the motion of the pump. It was noted that as one peristaltic vane began to compress the tube, the other vane released the tube at high pressure. The pressure was sufficient to drive the water back into the pump onto the oncoming compressing vane. The result was a periodic rapid

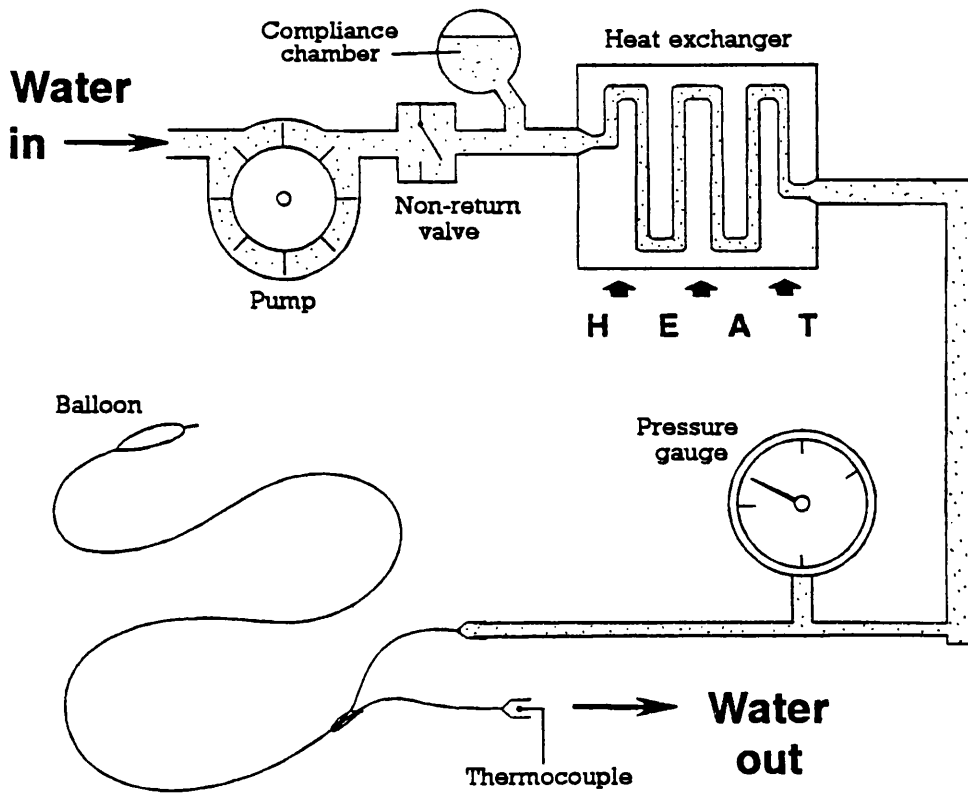
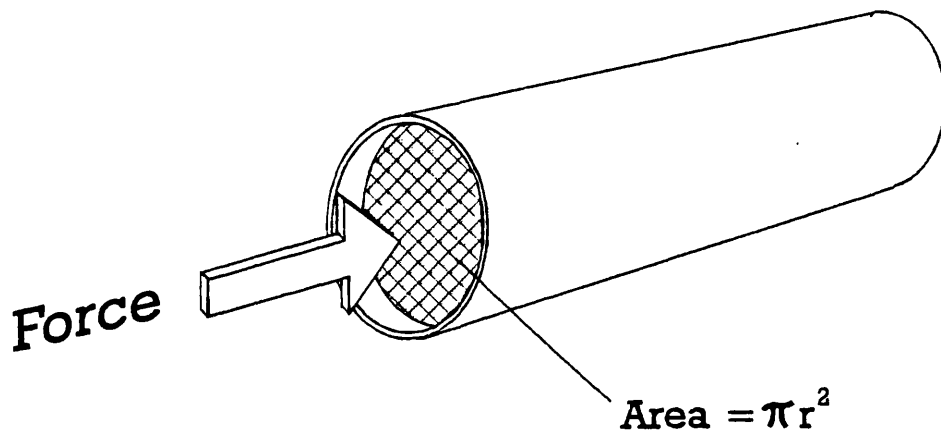


Figure 11.3 Equipment required to drive the thermal balloon angioplasty catheter.



$$\text{Force} = \text{Pressure} \times \text{Area} \propto r^2$$

Figure 11.4 The force required from the peristaltic pump to pressurise the balloon is proportional to the square of the tube radius.

pressure drop (several atmospheres) followed by a slow ramped pressure increase as the compressing vane continued its sweep until it released the tube and the cycle was repeated.

A non-return valve was acquired and placed at the output of the pump, which reduced the sharp pressure drop at vane crossover by 50%, but the pressure fluctuations were still considered a little too large. This was due to the low compliance of the water/balloon system. Small changes in bulk volume were accompanied by large changes in internal pressure because of the inelastic walls of the tube and incompressibility of the water. When the non-return valve shut, the internal pressure continued to force water out of the balloon exit port. The loss in volume created a significant pressure drop which was only restored when the pump delivered a fresh charge of water. An auxiliary pump was introduced to keep the system fully pressurised during the period in which the peristaltic pump was unable to supply sufficient pressure and the valve was closed. The auxiliary pump was placed after the valve, and took the form of a large compliance chamber (essentially a small cylinder of compressed air). The large compliance means that the small volume changes that occur result in minimal drop in pressure. Clearly, the larger the chamber, the lower the pressure drop. The system (Fig. 11.5) operates as follows:

- i) The peristaltic pump draws water from the reservoir at low pressure.
- ii) The water is pressurised and forced past the valve.
- iii) The valve shuts.
- iv) The high pressure compliance chamber expands and continues to drive water into the balloon with minimal pressure drop.
- v) The peristaltic pump delivers a new charge of high pressure water (valve open) which pressurises the balloon and recharges the compliance chamber.
- vi) GOTO (iii)

This arrangement produces much gentler pressure oscillations, of the order of $\pm 15\%$.

11.3.4 General Notes

Work with hot liquids at high pressures, requires careful consideration of safety. In our case, if a tube containing boiling water at 10 atmospheres (1MPa) ruptures, the

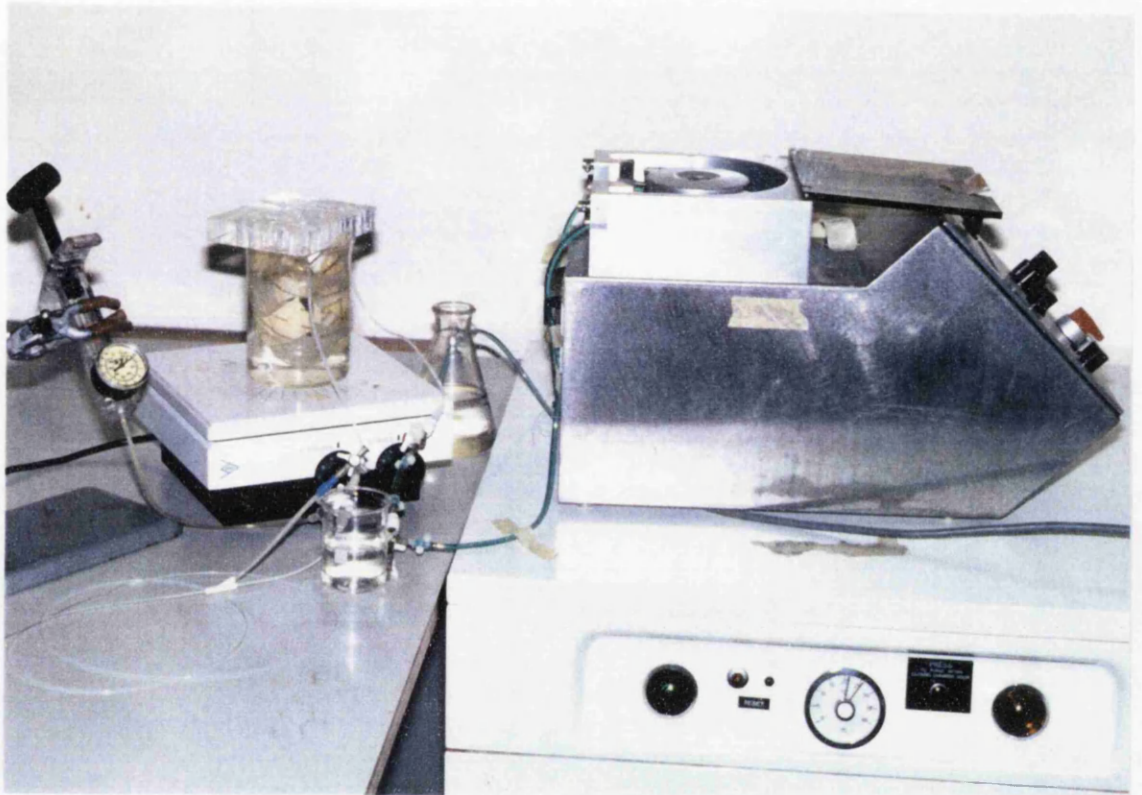


Figure 11.5 Equipment required to drive the thermal balloon angioplasty catheter. The peristaltic pump is visible on the right, with the jar of water on the hot plate acting as the heat exchanger. A pressure gauge is to its left and the balloon catheter on the bench beneath.

system compliance combined with the low flow rates used ($0.2 \text{ cm}^3\text{sec}^{-1}$), causes boiling water to leak rather than explode from the tube. The extent of damage is localised and this minimises the hazard to surrounding equipment and observers.

Balloon parameters (temperature, pressure) are not measured directly, but are inferred from the data provided by sensors placed at the catheter entrance and exit ports. These confirm the presence of pressure and temperature drops across the length of the catheter. The temperature difference between entrance and exit ports will be greatest when balloon temperature is high, and particularly when the balloon is under load (ie. heating something). Under these conditions (balloon sandwiched between heart muscle, inflated to 5 atmospheres (0.5MPa) at 95 deg.C.) the measured temperature drop was 10 deg.C., indicating that temperature within the balloon can be known to $\pm 5\text{deg.C.}$

The internal balloon pressure is more difficult to assess. Our observations suggest that balloon pressure is close to that measured at the entrance port, as most of the pressure drop occurs across the narrow bore of the outer balloon channel. This is supported by the fact that under pressure the balloon is highly non-compliant (ie. it feels hard). However if the catheter is connected back to front so that water enters through the balloon channel and leaves through the inner guidewire channel, the balloon is 'squashy' to the touch, needing little external force to compress it. This indicates that most of the pressure drop must occur across the balloon channel.

In reality, accurate knowledge of the internal pressure of the balloon is not critical. What does matter is that the balloon reach its full diameter when inflated inside a vessel. The diameter can be known since the balloon is very non-compliant when inflated. For example, under a low power microscope, the diameter of a 3.0mm balloon was observed to change by less than 10% over a pressure range of 4 to 10 atmospheres (0.4-1MPa). The small pressure variations caused by the pumping equipment can be expected to have negligible effect on inflated balloon diameter.

11.4 COMPARISON OF THERMAL AND LASER BALLOON CATHETERS

The object of the laser balloon is to apply heat to an atheromatous vessel during balloon inflation without damaging surrounding muscle. The direct effect of this heating is unclear, but ideally it should (permanently) expand the internal diameter of the treated vessel. The reasons for this process are unknown, suffice to say that there is evidence to suggest that expanding the vessel under heat for a certain period can produce the desired result (194). With so many unknowns, it is

important that the thermal balloon should emulate the behaviour of the laser balloon as closely as possible. Their similarities are discussed forthwith.

In terms of balloon pressure and inflation time there is little to distinguish the laser balloon from the thermal balloon, except for small pressure fluctuations in the latter. This should be of little significance since the balloon inflates to its full diameter. The lack of compliance means that pressure fluctuations from the pump will cause virtually no change in diameter.

The thermal balloon catheter is at a disadvantage where the guidewire is concerned, because of the lack of an available channel down which to feed it. This is not expected to cause problems during in vitro work because a guidewire was glued into the end of the guidewire channel.

The remaining comparison concerns vessel temperature, and here the two modalities differ. Delivery of energy by laser light is convenient and laser output is highly controllable. This enables Jenkins, Spears et al. (127,196) to rapidly achieve a working temperature of about 120 deg.C. within 5 seconds, by starting with a high intensity beam, which is subsequently reduced in a step-like fashion thereafter to stop the temperature rising further. Increased absorption of Nd:YAG wavelengths by plaque, in comparison to the vessel, is considered a useful property that could be exploited to produce localised heating within the plaque rather than the vessel wall. This could be further modified by the application of chromophore to the area of interest.

The incident Nd:YAG energy is widely scattered by interaction with tissue and absorbed over a depth of several millimetres. This is greater than the thickness of the vessel wall (several hundred μm). Thus a relatively uniform energy distribution is produced which minimises conductive temperature gradients across the thickness of the vessel. However, this information has been gleaned more from mathematical models than experiment. It highlights the principal problem of the laser balloon catheter at its current stage of development: the actual temperatures being generated are not well established.

In contrast, the thermal balloon applies a known, highly uniform temperature to the surrounding plaque and vessel faces. In this respect it is superior to the laser device. Thermal balloon temperature is accurately controllable, although its response time cannot equal that of the laser, as it requires 10 to 20 seconds to reach a stable temperature. The current set-up has a maximum working temperature of about 90 deg.C., limited by the boiling point of the pumped water. This need not be a limit however. Exchanging the pumping fluid for oil would allow temperatures in excess of 100 deg.C. to be generated, and inflation temperature

would simply be limited by the temperature resistance of the balloon. The laser balloon suffers from the same limitation.

The major difference between the two systems is the method used to heat the vessel. The laser balloon catheter applies radiant energy to the vessel, whereas the thermal balloon applies heat at a known temperature. This heat is applied to the vessel or plaque surface and penetrates the tissue by conduction. The temperature gradient will be higher than that of the laser since the laser distributes its energy throughout its absorption depth. Over the thickness of thin walled vessels, the temperature distributions of both modalities will differ little. This will not be the case for thicker vessels and plaque, where the temperature profile with thickness can be expected to be appreciably different.

As has been shown, the thermal balloon catheter can simulate the action of the laser balloon in many respects, but there are also important differences which may cause discrepancies, particularly in the case of thick walled vessels. Nevertheless, knowing the temperature applied to the vessel wall justifies its use as an investigative tool. A comparison between the two modalities raises particular questions about what the laser balloon is trying to achieve and how it does it. This equipment gives us the opportunity to answer some of these questions.

11.5 APPLICATION

The eventual aim of a proposed study involving the thermal balloon would be to obtain and optimise the balloon parameters (inflation time, pressure, temperature) necessary to permanently increase the bore of the diseased vessel. This information defines the conditions that must be achieved by a laser balloon catheter if angioplasty is to be successful. The laser represents a flexible, controllable source of energy that must be considered the medium of choice in the clinical setting. However, at present the values of some of the parameters are not known (principally vessel temperature). It is the function of the thermal balloon to help determine these. As such, the thermal balloon is not intended for clinical use at this stage, but simply as an *in vitro* tool to illuminate the thermal effects of laser balloon angioplasty.

Whole, diseased coronary hearts are difficult to obtain. In contrast, diseased sections of such hearts are available. This produced a requirement to work on diseased heart sections *in vitro*, involving measurement of vessel parameters (eg. vessel diameter) before and after thermal angioplasty. A notional experiment consists of the following:

- i) Obtain a myocardial section containing coronary vessels.
- ii) Measure vessel diameter from coronary angiogram.
- iii) Apply balloon.
- iv) Measure new vessel diameter from coronary angiograms and investigate histological changes.

Vessel diameter can be directly measured radiographically, and involves infusing an X-ray opaque dye into the coronary vessel during angiography. Since vessel diameter will be a function of intravascular pressure, the infusion pressure of the dye needs to be carefully specified. This approach also demands that the heart section be sealed in such a way that contrast medium can pass through the coronary vessel at a specified pressure, but not leak from the sidebranches and degrade the X-ray image.

After much trial and error a satisfactory technique was developed to enable angiography of a coronary heart section as described. This is now discussed in detail.

11.6 A TECHNIQUE FOR THE SEALING OF MYOCARDIAL SECTIONS TO PERMIT IN VITRO ANGIOGRAPHY OF THE CORONARY VESSELS

Work described here was performed on normal sheep hearts, because of their availability and similarity in size and shape, to human hearts.

A fresh sheep heart was obtained from the abattoir. The left anterior descending coronary artery (LAD) was identified and a section of myocardium containing the LAD and aortic root was excised (Figs. 11.6 & 11.7). A typical section was 4cm wide by 2cm deep by 10cm long, with the LAD running down the middle of the top face. A 3mm coronary perfusion cannula was sutured into the left main stem at the aortic root with 3-0 Ethibond sutures. The heart section was gently squeezed and washed to remove excess blood and dabbed dry on a paper towel. The cut faces of the section were examined for large exposed vessels, and these were plugged with short lengths (several millimetres) of cocktail stick and superglue. In general, about 5 vessels would be plugged in this way. Each of the cut faces were evenly smeared with superglue and bonded to sheets of double thickness paper towel. The towel acts like blotting paper to the superglue, which sets hard within the tissue matrix while bonding it to the tissue face. The action is not unlike that of resin with glass fibre, and seals the heart section in a hardened paper towel shell. This level of sealing is sufficient for injection of contrast medium

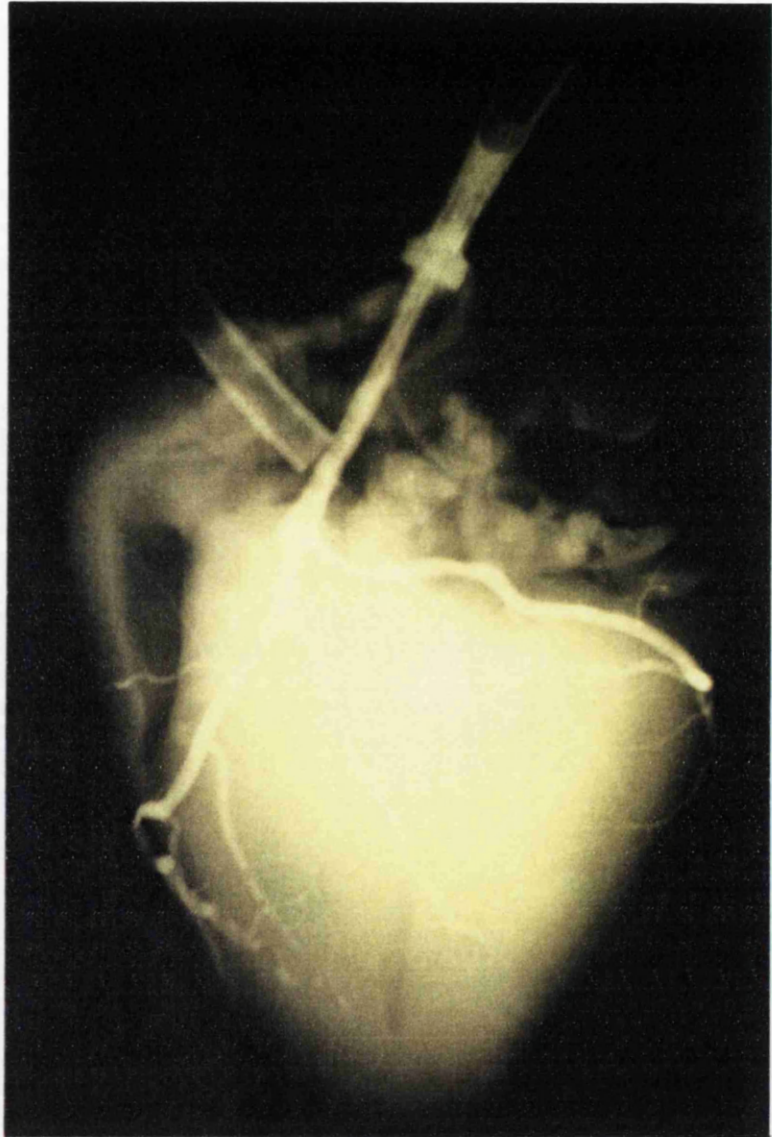


Figure 11.6 Angiogram of heart showing coronary vessels.

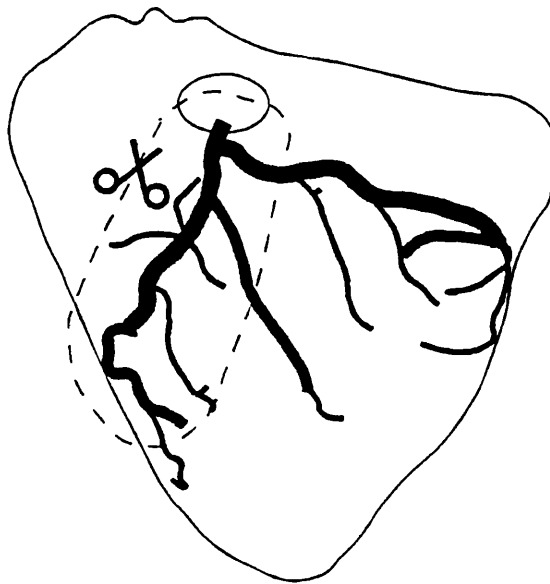


Figure 11.7 A section of myocardium containing the left anterior descending coronary artery is excised from the heart.

through the LAD at low intravascular pressure (< 100 mmHg), but is unsatisfactory as the pressure is raised to 300 mmHg. In consequence, the sealing was augmented by an additional technique (the use of contrast-gel), which when used in combination with the glued paper towel, proved to be an effective sealant at these higher pressures (Fig. 11.8).

Contrast-gel consists of a near-saturated solution of gelatin in hot water mixed with a large proportion of a powdered contrast medium (E-Z-HD, E-Z-EM Inc., Montreal Canada). The important property of the gel is that it sets to a thick rubbery consistency at room temperature, but as it is heated above (approximately) 37 deg.C., it melts to become a liquid. This change of state is quite reversible, and simply requires a shift of temperature across 37 deg.C.

Prior to injecting liquid contrast-gel through the LAD, a fine 1.02mm intravenous cannula (with luer nozzle removed) was threaded through the vessel until it protruded from both ends. Experience has shown that feeding the cannula from the exit (non-cannulated) end of the vessel is preferable, since the fine cannula is less likely to be diverted from its course by the side branches of the LAD. The intravenous cannula was plugged at the aortic end with a piece of cocktail stick and superglue. A 50ml syringe was used to pump the liquid contrast-gel (40 deg.C.) through the aortic cannula into the LAD and sidebranches. Moderate hand pressure was required, and the opaque gel could be seen spreading through the vessel network. It soon dribbled from the exit end of the LAD, and after several seconds the end was pinched shut and held there for 3 minutes. This stopped the flow and the gel cooled and set. Pressure was applied to the syringe throughout this period to ensure that the gel was properly filling the vessel network. On release, the gel had set and blocked the LAD and all sidebranches, with the intravenous cannula set in gel inside the LAD. An angiogram was performed to show the details.

The remainder of the procedure unblocks the LAD, but leaves all sidebranches still occluded. The 50ml syringe was removed from the aortic cannula, and the plug that blocked the fine cannula cut off, to make it patent. 40 deg.C. water was continually injected through the fine cannula, which loosened surrounding gel within the LAD enough to allow the cannula to be moved around and free more of the surrounding gel. When loose enough, the cannula was slowly withdrawn (still injecting water) from the exit end of the vessel while 40 deg.C. water was injected through the aortic cannula to melt remaining gel and flush it out of the LAD. An angiogram at this stage reveals a heart section, all of whose vessels are blocked with thick contrast-gel except for the LAD which is patent. The

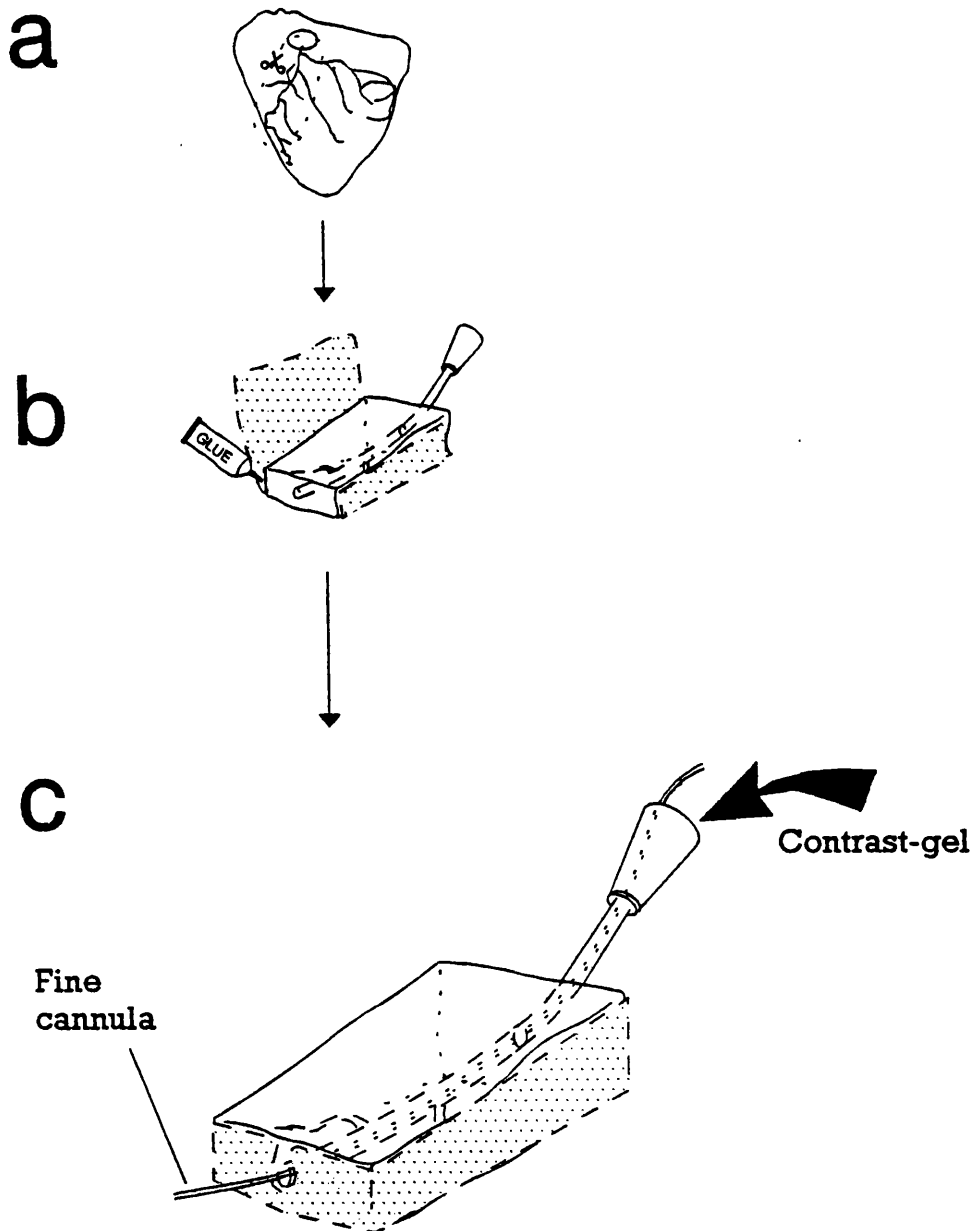


Figure 11.8 Following preliminary sealing of excised section (a) with glue and paper towel (b), injection of liquid contrast-gel (c) seals all vessels when set. Infusion of 45 deg.C. water through the embedded fine cannula melts only the surrounding gel leaving the LAD patent and all other vessels still occluded.

section is highly resistant to leaks, even after multiple infusions at 300mmHg.

There are two particular points that should be noted. Care must be taken to ensure that the intravenous cannula is not flushed out of the vessel when the contrast-gel is first injected into the vessel. If this should happen, no patent channel exists within the LAD and therefore the gel cannot be flushed out. Also, it is anticipated that temperatures of 40 deg.C. are too low to cause damage to surrounding tissue and thus it can be assumed that the technique does not interfere with the state of the vessel.

11.7 CONCLUSION

The work of this chapter describes:

- i) The creation of a thermal balloon capable of simulating the effects of a laser balloon.
- ii) A technique to seal all vessels in a heart section except the vessel of interest.

Both are essential requirements if in vitro investigation of the thermal effects of laser balloon angioplasty is to be possible. The sealed heart section allows balloon access to the vessel of interest, followed by quantitation of its effects through angiography and histology. These ideas are more fully explored in the experiment of the next chapter.

Chapter 12

In Vitro Application of Thermal Balloon

12.1 INTRODUCTION

The water heated, thermal balloon catheter of the previous chapter was developed to induce a similar vessel response to the laser balloon catheter, while providing a direct indication of temperature. There is evidence that vessel response during angioplasty is temperature dependent (109,195,196), and correlating vessel changes with balloon temperature and other parameters will hopefully indicate the conditions required to achieve desirable results. However, before detailed correlations can be undertaken, it is necessary to establish the stability of vessel diameter in the face of repeated investigations. In addition the limitations of the measurement technique must be established.

The experiments of this chapter establish these limitations, utilising the experimental suggestions of Chapter 10. In the light of the techniques described there, it is possible to apply a thermal balloon to a vessel of interest under known temperature conditions and to evaluate its effects. Sheep hearts, readily available from the local abattoir, were an obvious choice on which to test the system. The sheep heart is a reasonable analogue of the human heart, and the lack of coronary disease in the samples was considered advantageous since it provided a simple starting model. It must also be remembered that the elasticity of the normal vessel wall is held at least partially responsible for the high incidence of restenosis following coronary balloon angioplasty (143,194).

An experiment was organised to subject the left anterior descending coronary artery (LAD) of the sheep heart to normal or thermal balloon angioplasty, thus allowing direct comparison of their effects. In addition this experiment permits assessment of overall experimental technique, which if proved successful would indicate further application to fundamental questions regarding the acute mechanism of thermal or laser balloon angioplasty.

12.2 METHOD

Six fresh sheep hearts without coronary disease were obtained from the abattoir and the following experimental procedure applied to each in turn.

A section of the heart approximately 10cm long by 4cm wide by 2cm deep, containing the LAD and aortic root was excised. The section was cannulated at the aortic root. The 5 or 6 larger exposed vessels visible on the cut faces of the section were plugged with superglue and short pieces of cocktail stick. The myriad of smaller vessels exposed at the cut faces were stopped by bonding double thickness paper towel to each face with superglue. The section was further sealed with the introduction of thick-setting contrast-gel. A fine cannula had been introduced into the LAD prior to the procedure and was thus set within the gel inside the LAD.

The patency of the LAD alone was restored by pumping 45 deg.C. water through the fine cannula, loosening surrounding gel. Water (at the same temperature) was then pumped through the aortic cannula as the fine cannula was removed, and the gel flushed out to produce a patent LAD. This patency was restricted to the LAD and was evident from the angiogram, with all of the side branches remaining blocked by contrast-gel.

12.2.1 Standard X-ray Procedure

Angiograms, subsequent to the above, were used to establish the diameter of the LAD. Vessel diameter was measured at 4 defined intravascular pressures for a simple assessment of diameter as a function of pressure. The procedure is detailed below.

A fine 1.02mm intravenous cannula was taken and inserted several centimetres into the distal end of the LAD. The vessel was bound by 3 loops of 4-0 Prolene suture at the vessel exit, closing the end of the vessel tightly around the cannula. The cannula was carefully withdrawn until only a few millimetres of it extended beyond the sutures into the vessel, leaving as much of the LAD as undistorted as possible. The cannulated heart section was placed in the X-ray machine - a small self-contained radiographic unit that exposes a volume of approximately 1m³ (Hewlett Packard Faxitron Series, Model 43855A) - and a T-piece connected to the aortic cannula. One end of the T-piece was connected through several feet of tubing to a pressure gauge. The other end of the T-piece connected a similar length of tubing to a 50ml syringe containing contrast medium - Urografin 325. The Urografin was gently infused by hand at an observed pressure of less than 50mmHg, pushing out all of the air in the system. The Urografin left the LAD through the fine exit cannula and was collected in a jar.

The design of the X-ray machine was such that the syringe and pressure gauge could remain external to the machine with the radiation door shut, without squashing the several feet of tubing connecting them to the heart section. Hence, with the door closed, Urografin was infused at a steady pressure (accurate to ± 5 mmHg as observed on the pressure gauge), during which the heart section was angiographically exposed at 30kV, 3mA for 3 seconds. These settings provided good angiographic images. Early experiments in which an additional pressure gauge had been connected to the exit cannula via another T-piece, revealed exit pressures in all cases of less than 5mmHg. Thus the intravascular pressure was simply taken as that recorded at the aortic cannula. Contrast angiograms were taken (Fig. 12.1) at 4 defined infusion pressures representing a broadly physiological range - 100, 150, 200, 250mmHg.

These angiograms provided images from which vessel diameter was subsequently obtained by direct measurement. Since they were obtained before any manipulations with a balloon, they were designated the 'pre-balloon' results. The radiographic procedure was repeated after balloon angioplasty (described below) to allow direct comparison of balloon effects on vessel diameter.

12.2.2 Application of the Cold Balloon

The pre-balloon X-rays were examined to establish the area of the LAD most suitable for diameter measurement. Ideally, this consisted of a straight length of vessel, approximately 5-10mm long, containing no side vessels or kinks. Deviation of the vessel from these conditions complicates diameter measurement since a straight unkinked length of vessel provides the least room for subjective errors in the determination of vessel edges and width. The chosen site was marked on one of the X-rays and the distance from the exit end of the vessel to the point of interest measured.

The exit sutures were loosened and the fine cannula removed. The LAD was flushed with saline to remove any remaining Urografin. An intravenous cannula (luer fitting removed) was coaxed through the LAD so that it protruded from both the exit end of the vessel and the aortic cannula. The guidewire of the balloon was inserted into the aortic end of the intravenous cannula and threaded through it. Both cannula and guidewire were then pulled out of the exit end of the vessel, dragging the attached collapsed balloon behind until half of the balloon protruded from the vessel exit. (This procedure was found to be easier than sending the guidewire through the vessel without the aid of the fine intravenous cannula, since the fine cannula was more easily manipulated through the potentially collapsed

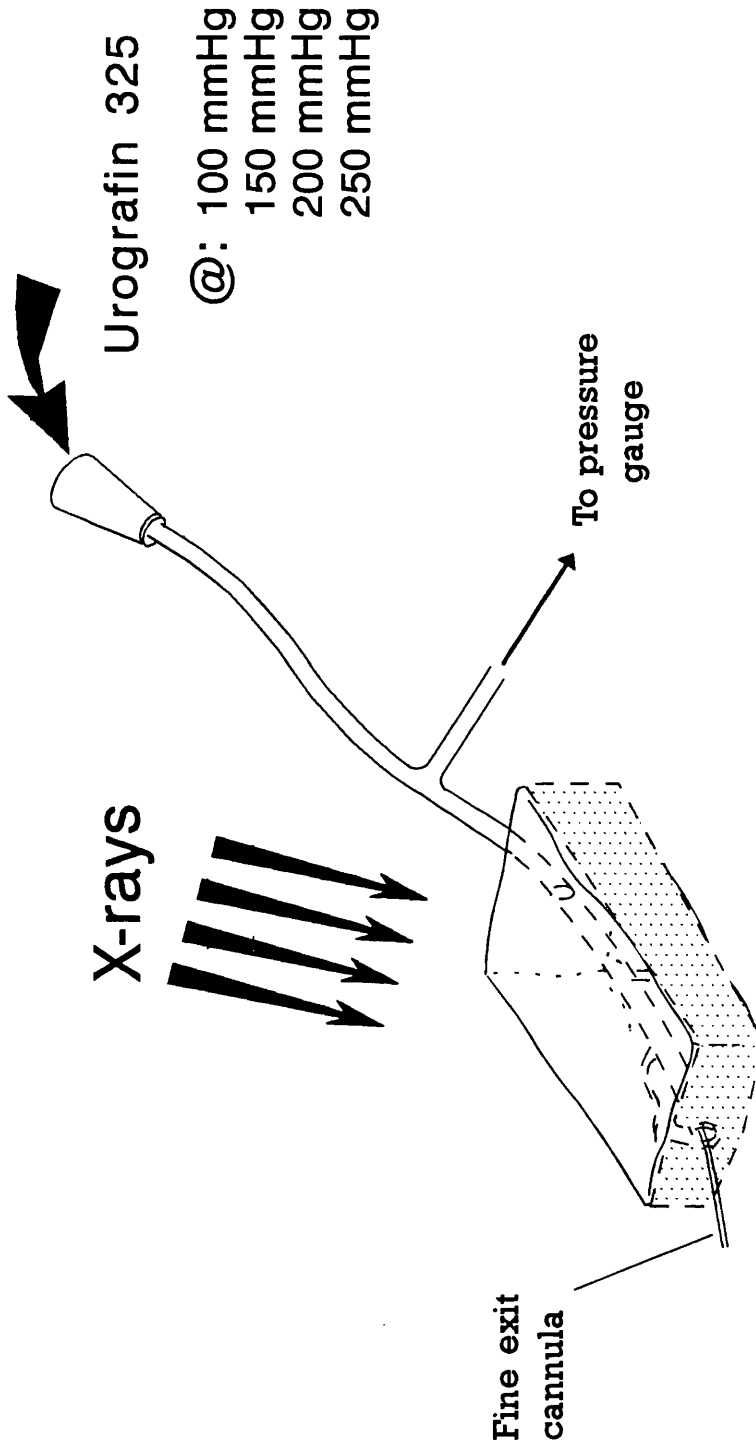


Figure 12.1 X-rays are taken while the sealed myocardial section is infused with contrast medium (Urografin) under pressure.

pathways of the vessel). The balloon was now pulled back into the section by the distance necessary to place the centre of the balloon at the area of interest. Great accuracy was not necessary as the balloon itself was 2cm long, allowing a large margin of error over which the area of interest would still be subjected to the full diameter of the balloon. The balloon diameter when inflated was 3.0mm. With the balloon correctly centred within the LAD, it was inflated to 5 atm. (0.5MPa) with room temperature water (21 ± 2 deg.C.) for 90 seconds. After this period, the pump was switched off, the balloon was sucked into collapse with a syringe (by sucking water out of the exit channel of the balloon) and the balloon gently pulled free of the heart section.

To evaluate the effects on vessel diameter, the heart section was immediately imaged (Fig. 12.2) according to the standard X-ray procedure at 100, 150, 200, 250mmHg. This set of images formed the 'cold balloon' results.

12.2.3 Application of Hot Balloon

The exit sutures of the heart section were loosened, following angiography, and the exit cannula withdrawn. The LAD was flushed with room temperature saline to remove any remaining Urografin. Using the technique described above, the balloon was reinserted in the LAD and centred on the area of interest. The balloon was inflated to 5 atm. (0.5MPa) with boiling water, inducing a balloon temperature of 90 ± 5 deg.C. After 90 ± 10 seconds, the pump was switched off, the balloon sucked into collapse and withdrawn from the vessel. Again the standard X-ray procedure was immediately performed for subsequent assessment of vessel diameter (Fig. 12.3). These angiograms constituted the 'hot balloon' results.

12.2.4 X-ray Analysis

Vessel diameter was measured directly off the angiograms using a low power microscope with a computer. The selected point of interest marked on the pre-balloon image was accurately transferred to all other angiograms by placing it on a light box and overlying the other angiograms in turn, overlapping each over the reference image as closely as possible. The marked point could be seen through the overlying X-ray image and was marked on it. The same reference angiogram was used throughout since this eliminated any cumulative systematic drift in the position of the point between angiograms.

The measuring equipment consisted of a digitising tablet with mouse, placed under a camera lucida attached to a low power microscope (x10). The lucida projected a faint image of the tablet and mouse onto the microscope field of view.

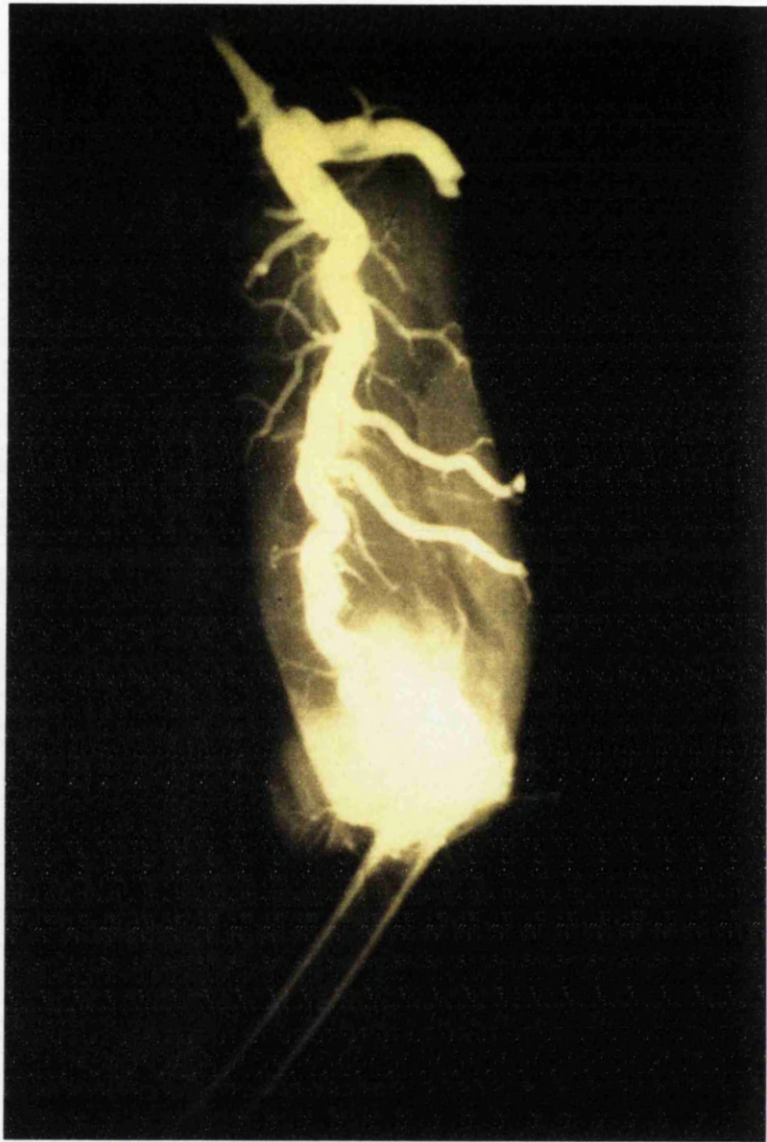


Figure 12.2 Typical angiogram of myocardial section (following cold balloon angioplasty), taken during infusion of Urografin at 200mmHg.

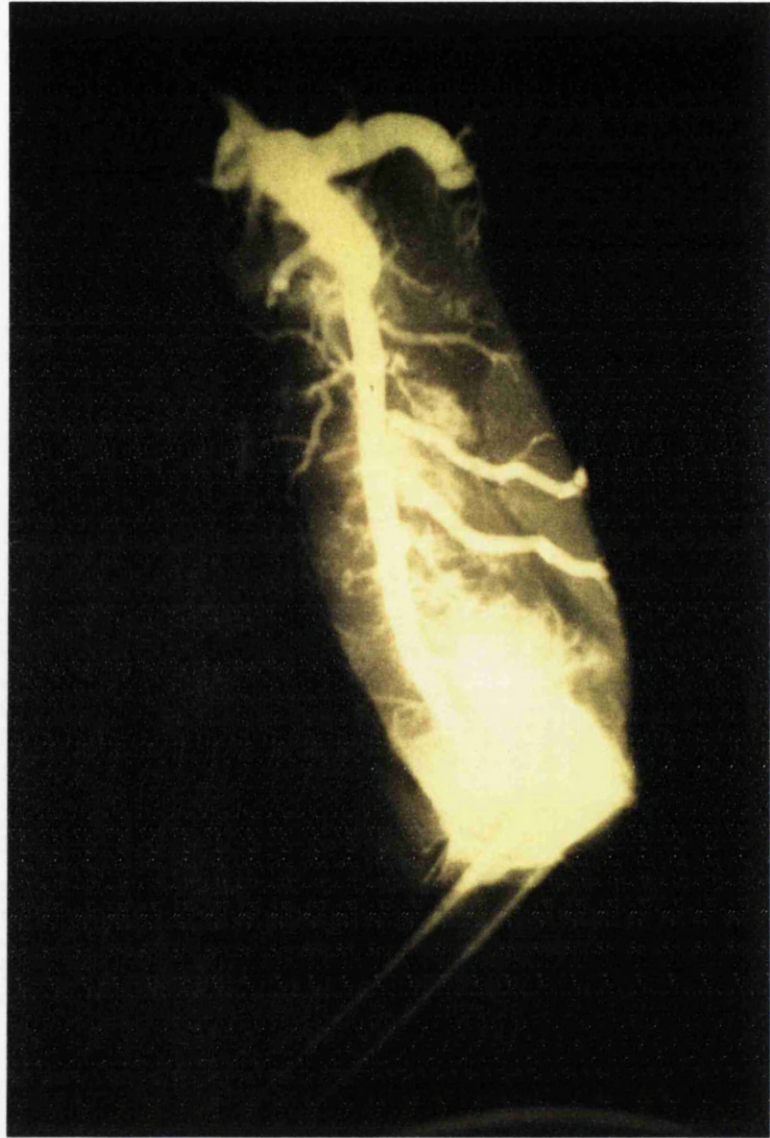


Figure 12.3 Typical angiogram of myocardial section (following hot balloon angioplasty), taken during infusion of Urografin at 200mmHg. Note that the kinks in the LAD have been removed.

The mouse had a small light emitting diode on its top surface, which could easily be seen as a bright spot within the field of view and acted as an effective mouse pointer. Both mouse and tablet were interfaced to an (old) Hewlett Packard microcomputer (Z80 4MHz CPU, 128kB RAM, 2 floppy drives, 256x256 monochrome screen) which recorded the x,y position of successive mouse clicks and was thus able to calculate the distance between any two points. It was calibrated in millimetres as seen through the microscope, providing an overall system resolution of better than 0.05mm.

For each X-ray image, the region of interest was centred within the field of view of the microscope. The bright mouse pointer was placed at the edge of the vessel and the mouse clicked. It was then moved perpendicular to the vessel axis, across to the other vessel edge, and the mouse clicked again. The computer returned the distance between the two points (ie. vessel diameter), correctly calibrated in millimetres. This procedure was repeated 7-10 times at different points along the length of the vessel over a 5-10mm stretch centred on the point of interest. This resulted in 7-10 measured vessel diameters from which an average diameter could be calculated. The standard deviation represents a combination of the mouse positioning error and the variability of vessel diameter as a result of kinks and bends.

No sophisticated computer edge detection algorithms were used - vessel edges were simply determined by eye. The procedure was performed on all X-ray images produced with the standard X-ray procedure, to yield vessel diameter as a function of intravascular pressure over a range of balloon conditions.

12.3 HISTOLOGY

The region of the LAD that had been subjected to balloon angioplasty was identified on the heart section with the help of the angiograms. Excision biopsies (forming a cube of side 10mm approximately) containing the LAD and surrounding muscle, were taken. As a control, biopsies were also taken from anatomically similar untreated vessels. The samples were fixed in 10% formol saline, to be cut as serial paraffin wax sections 4 μ m thick. Sections were stained with Elastic van Gieson and Picrosirius Red to permit detailed investigation of the connective tissue components of the vessel wall.

12.4 ADDITIONAL EXPERIMENTS

12.4.1 Reproducibility

The following experiment was undertaken to establish the reproducibility of repeated measurements on the same vessel,

A heart section was sealed as previously described to leave a patent LAD with all side branches blocked. The section was subjected to the standard X-ray procedure, imaging at intravascular pressures of 100, 150, 200, 250mmHg. For reproducibility, this was repeated 4 times on the same section. Finally, for purposes of comparison, a balloon was inserted and inflated at room temperature for 90 seconds at 5 atm. (0.5MPa). A final set of X-rays was taken in accordance with the standard X-ray procedure.

The angiograms were subsequently analysed under the microscope to measure vessel diameter as a function of infusion pressure.

12.4.2 Vessel Response to Heat (No Balloon)

In contrast to the main experiment in which the vessel was heated during balloon inflation, this experiment established the natural response of the vessel when heated without the presence of a balloon.

The heart section was sealed, with the LAD remaining patent as before. A pre-balloon set of X-ray images was taken using the standard X-ray procedure. A 50cm³ syringe filled with boiling water was steadily infused into the aortic cannula at low pressure through the LAD for 40 ± 10 secs. (approximate flow rate 0.5cm³ sec⁻¹). A thermocouple inserted into the exit end of the vessel recorded temperatures of 80-85 deg.C. The section was imaged again using the standard X-ray procedure. The whole experiment was repeated with a fresh heart to obtain an indication of the reproducibility of the result.

Subsequent analysis of the angiograms permitted measurement of vessel diameter before and after heating with hot water.

12.5 STATISTICAL ANALYSIS

The averaged vessel diameter and associated standard deviation are quoted throughout. Data was plotted as averaged vessel diameter as a function of intravascular infusion pressure. Where appropriate, vessel diameters were compared before and after the balloon procedures. Comparison of data groups was aided by linear regression analysis and the non-parametric Mann-Whitney U test.

12.6 RESULTS

12.6.1 Reproducibility

Figure 12.4 plots averaged vessel diameter as a function of intravascular infusion pressure for the sheep heart on which the standard X-ray procedure was repeated 4 times (solid lines). At 100mmHg reproducibility is seen to be poor ($n=5$, mean diameter = 1.50mm, SD = 0.37mm), but this improves considerably at 150mmHg and above, with the smallest standard deviation occurring at 250mmHg ($n=5$, mean diameter = 2.16mm, SD = 0.04mm). These results indicate that direct comparison of vessel diameters is best performed at pressures of 150mmHg and above.

The dashed line on the graph shows vessel diameter after angioplasty with a 3.0mm balloon at room temperature for 90 seconds. It is clear in the case of this vessel that the properties of the vessel wall have remained unchanged.

12.6.2 Vessel Response to Heat (No Balloon)

Averaged vessel diameter is plotted as a function of infusion pressure (Fig. 12.5), showing diameter before (solid line) and after (dotted line) flushing with near boiling water for 40 secs. The vessel has shrunk in response to the heat, the vessel diameter having been reduced by 39% at 250mmHg from 3.16mm to 1.82mm. The repeat of this experiment with a different sheep heart yielded a similar shrinkage of 41% at 250mmHg (diameter before flushing = 3.7mm, after flushing = 2.1mm).

12.6.3 Vessel Response to Cold and Hot Balloon Angioplasty

The graph (Fig. 12.6) shows typical results from one of the hearts examined. As above, average vessel diameter was plotted as a function of intravascular pressure over the 100-250mmHg pressure range. The 3 lines show vessel diameter prior to angioplasty (solid line), after cold balloon angioplasty (dashed line - 3.0mm diameter balloon inflated room temperature to 5atm. for 90 secs.), and after hot balloon angioplasty (dotted line - 3.0mm diameter balloon inflated to 90 deg.C., 5 atm. for 90 secs.). Although initial diameter of the vessel prior to the angioplasty was similar to that of the previous example in which flushing hot water was used, the diameters after heating were considerably different. The thermal balloon induced shrinkage of 20% (3.4mm reduced to 2.7mm as measured at 250mmHg) as opposed to the 40% of the flushed vessel. Clearly the presence of the inflated balloon has modified the natural response of the vessel to heat. In addition, it is equally apparent that initial application of the cold balloon to the vessel (dashed

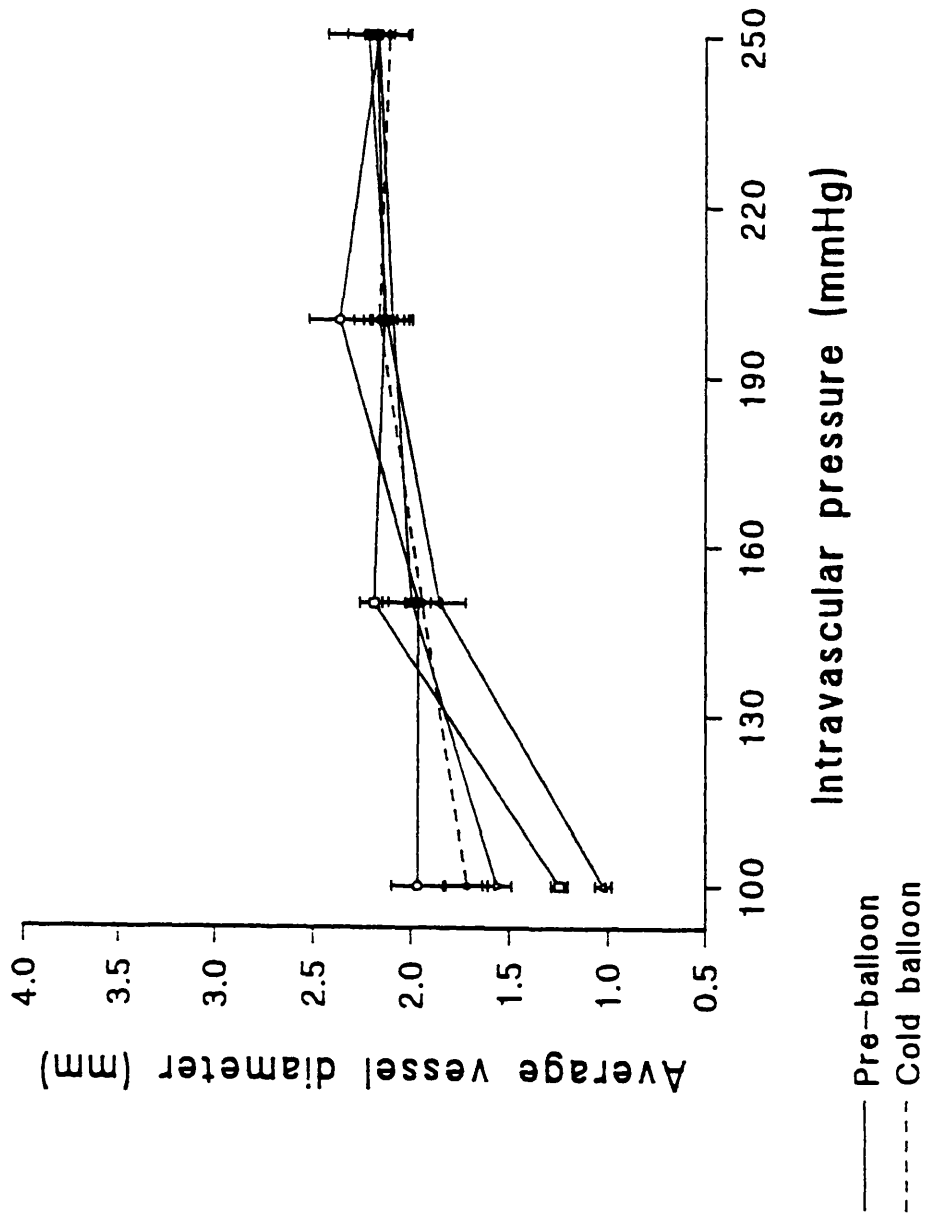


Figure 12.4 Reproducibility of vessel diameter as a function of intravascular pressure. Each point shows mean vessel diameter over a 5mm length of vessel and associated standard deviation. Solid lines refer to results prior to angioplasty, and the dashed line is the result following cold balloon angioplasty.

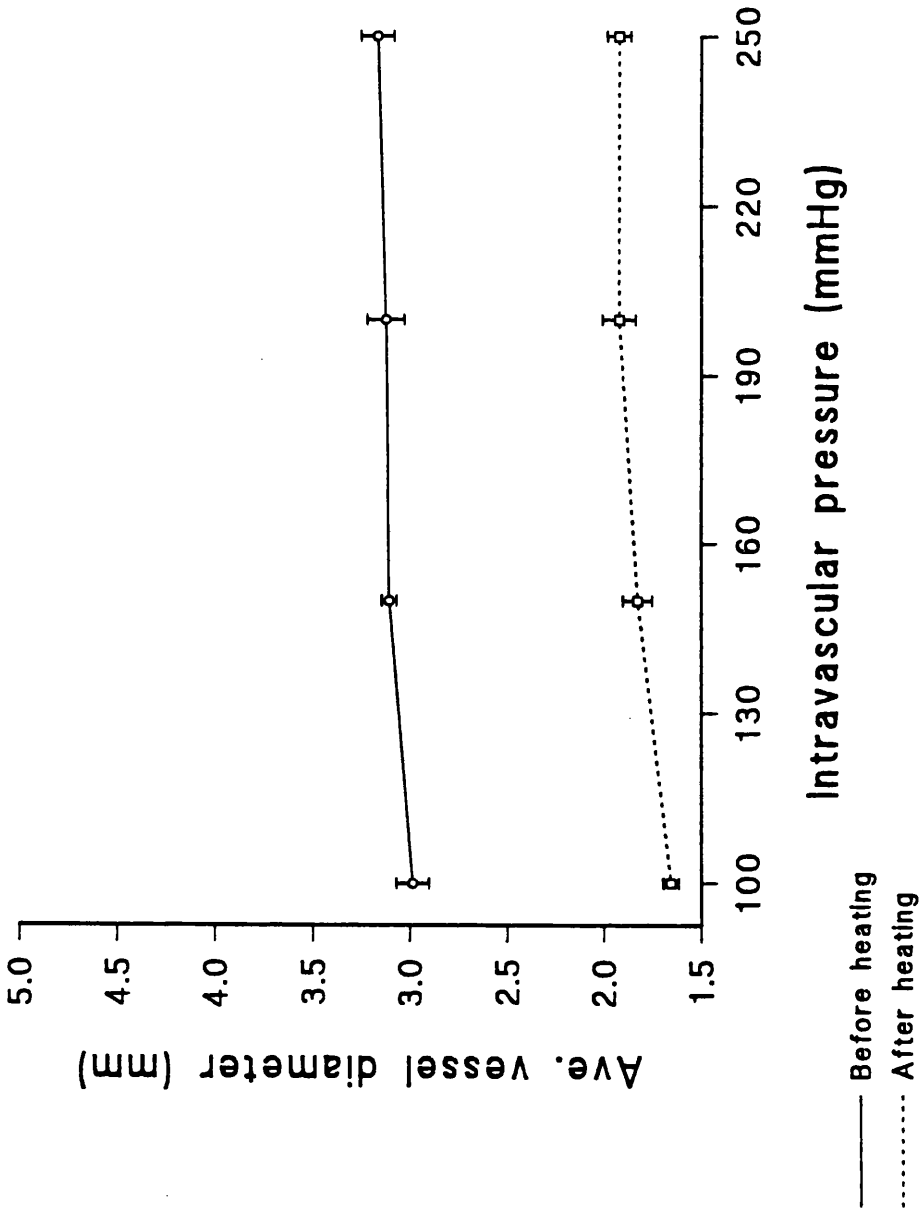


Figure 12.5 Vessel diameter as a function of intravascular pressure before (solid line) and after (dotted line) flushing with 80-85 deg.C. water. Points show mean vessel diameter over a 5mm length of vessel and associated standard deviation.

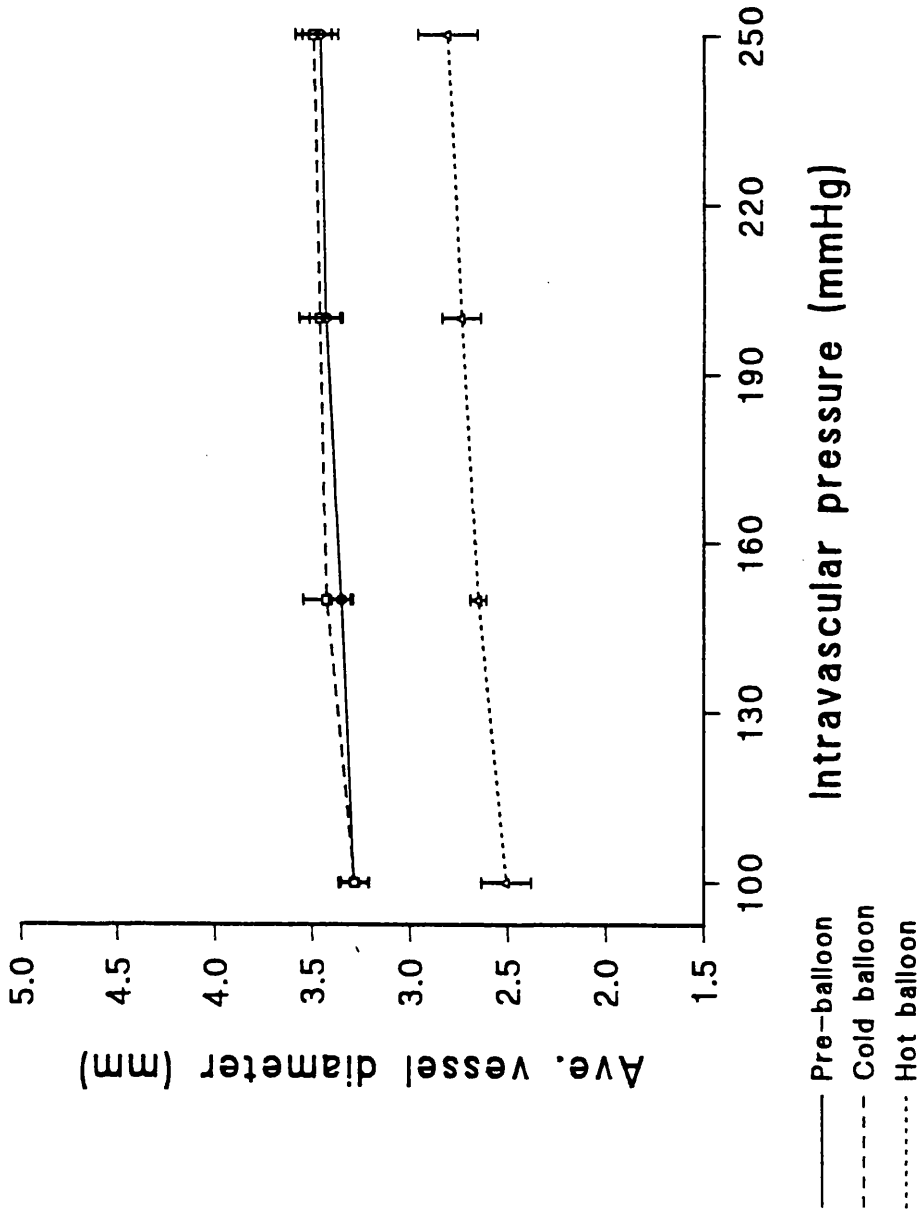


Figure 12.6 Vessel diameter as a function of intravascular pressure prior to angioplasty (solid line), following cold balloon angioplasty (dashed line), and following hot (90°C) balloon angioplasty (dotted line). Points show mean diameter over a 5mm length of vessel and associated standard deviation.

line) left the properties of the natural vessel wall unchanged since the solid and dashed lines closely overlap.

The data from all 6 hearts has been summarised in the next two graphs of figures 12.7 and 12.8 (see also Table 12.1). The first of the graphs (Fig. 12.7), plots vessel diameter after cold balloon angioplasty against that prior to the procedure. For improved clarity, error bars are not shown but estimated to be ± 0.1 mm. The data has been grouped according to infusion pressure, interpretation of the data being aided by linear regression analysis, the lines of which are superimposed on the graph. Each line relates vessel diameter before and after cold balloon angioplasty at one of the 4 pressures - 100, 150, 200, 250mmHg. All the lines overlap to a considerable extent, indicating little change in diameter with the change of intravascular pressure. All have gradients within 3% of unity with near zero intercepts (0 ± 0.1 mm) on the y-axis. The correlation coefficient of all was close to unity ($r \geq 0.98$) and highly significant ($p < 0.001$). These results indicate that the properties of the natural vessel wall in the range of diameters tested (1.6-3.5mm), remained unchanged following angioplasty with the 3.0mm cold balloon. As a consequence of this, the pre and cold balloon diameters of a vessel at each pressure were averaged for use in the next graph.

Figure 12.8 shows vessel diameter following hot balloon angioplasty compared with the averaged pre and cold balloon vessel diameters. Again for clarity, error bars on the x-axis have not been shown, but are estimated to equate to ± 0.1 mm. The regression lines relate to all points evaluated at the same pressure, the 4 lines representing measurements at 100, 150, 200, 250mmHg. Apart from the wayward line at 100mmHg, the lines are fairly tightly grouped. In all cases the gradients are well below unity (0.62, 0.43, 0.40, 0.37 at 100, 150, 200, 250mmHg respectively) with non-zero intercepts (0.69, 1.28, 1.36, 1.46mm at 100, 150, 200, 250mmHg respectively). The regression coefficient was less significant at 100mmHg ($r = 0.82$, $p < 0.05$) than at 150mmHg and above ($r \geq 0.95$, $p < 0.01$).

12.6.4 Histology

Figures 12.9 and 12.10 demonstrate the typical histological changes induced in the vessel wall following thermal angioplasty. The sections were stained with Elastic van Gieson (EVG) and Picrosirius (PSR). Degradation of the intima is apparent with areas of endothelial denudation, combined with medial compression containing sites of vacuolation. These are probably the result of expanding pockets of vapour created by the near boiling temperatures. Loss of staining in the adventitia and beyond is indicative of a zone of heat induced

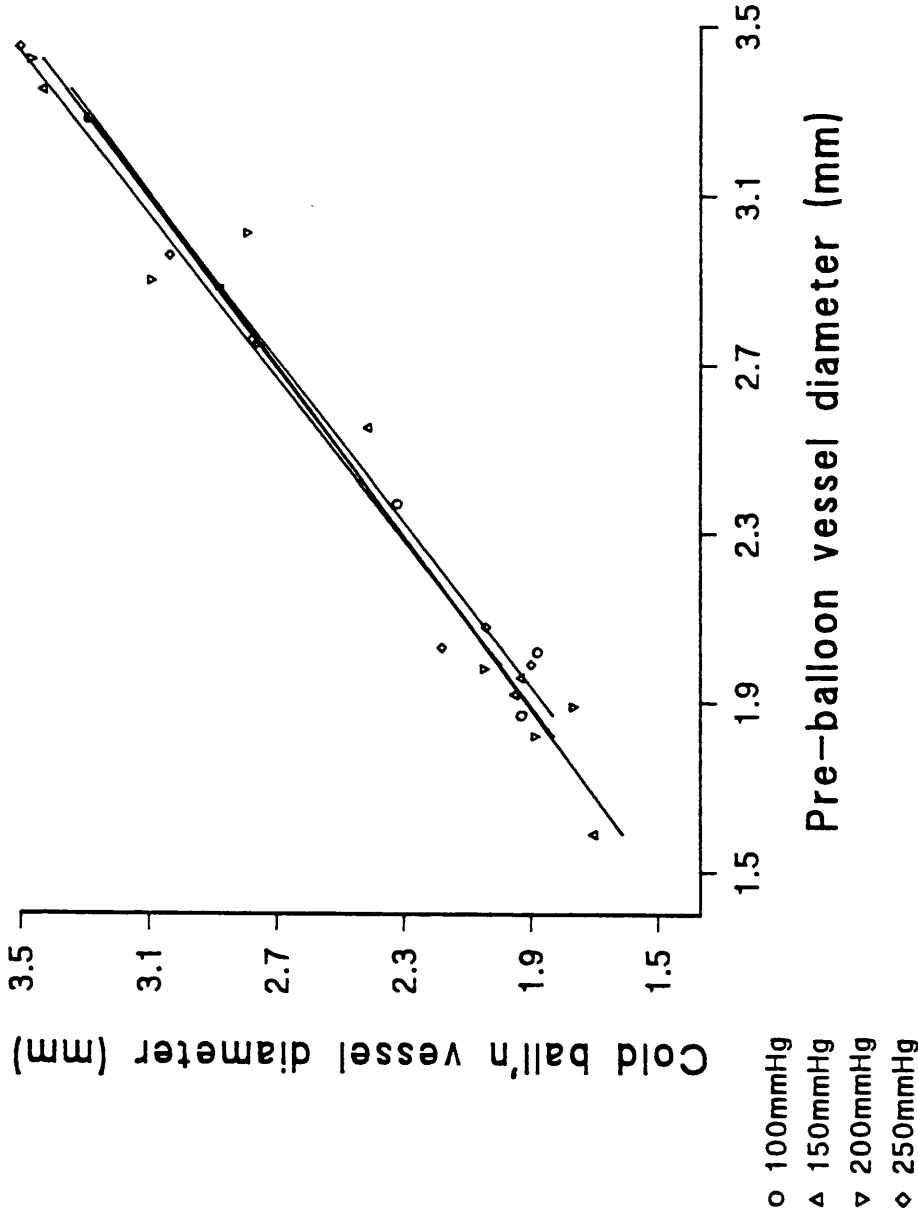


Figure 12.7 Vessel diameter following cold balloon angioplasty as a function of vessel diameter prior to angioplasty. Data has been grouped according to intravascular infusion pressure. Linear regression:

100mmHg: $y = 1.03x - 0.09$ $r = 0.99$ $n = 5$ 150mmHg: $y = 0.98x + 0.06$ $r = 0.99$ $n = 6$

200mmHg: $y = 1.00x + 0.02$ $r = 0.98$ $n = 6$ 250mmHg: $y = 1.03x - 0.06$ $r = 0.99$ $n = 6$

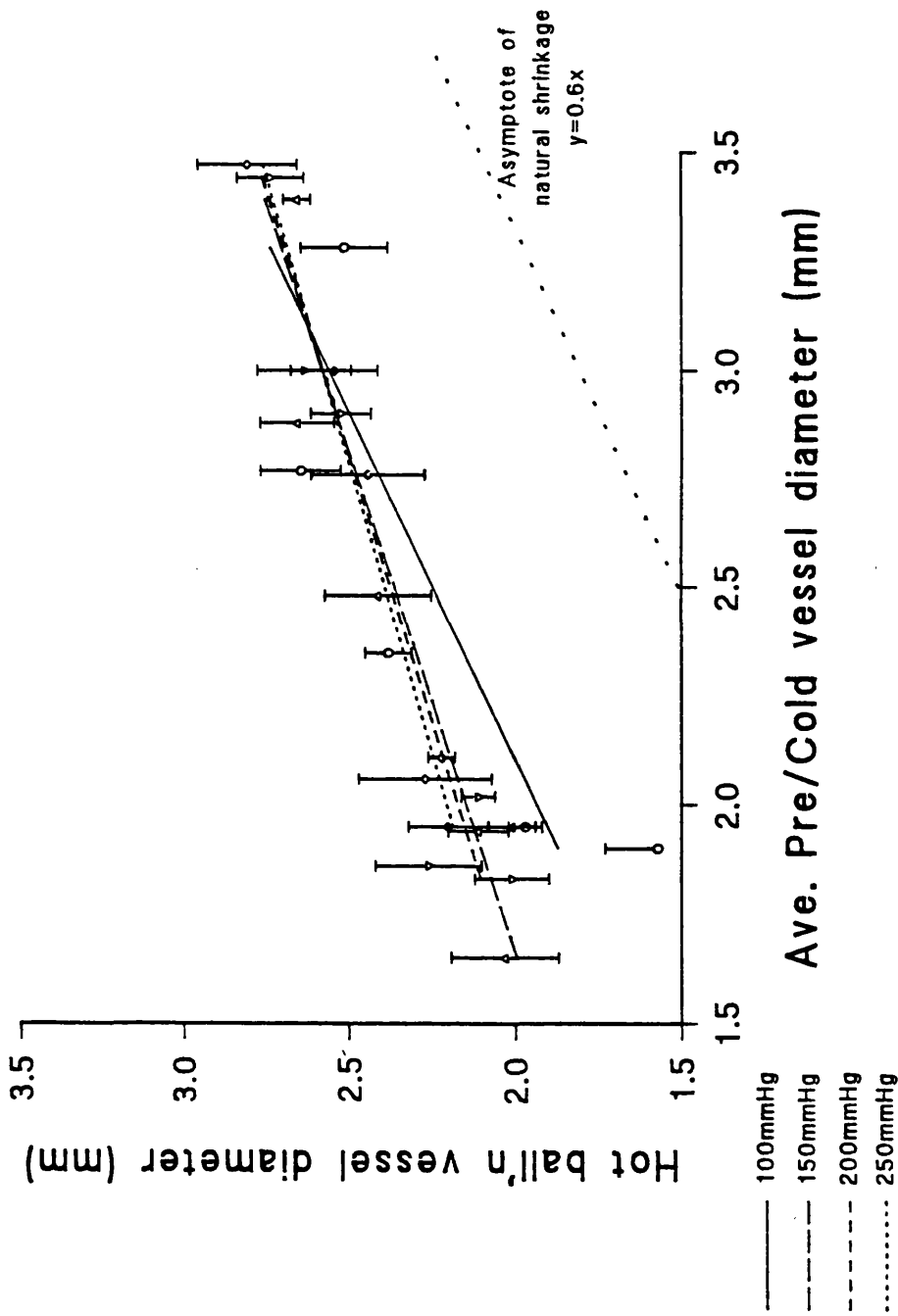


Figure 12.8 Vessel diameter following hot (90°C) balloon angioplasty as a function of averaged pre and cold vessel diameter. Data has been grouped according to intravascular infusion pressure. Linear regression

100mmHg: $y = 0.62x + 0.69$	$r = 0.82$	$n = 5$	150mmHg: $y = 0.43x + 1.28$	$r = 0.95$	$n = 6$
200mmHg: $y = 0.40x + 1.36$	$r = 0.95$	$n = 6$	250mmHg: $y = 0.37x + 1.46$	$r = 0.98$	$n = 6$

	Pre-balloon vessel diameter (mm ± 0.1)	Cold balloon vessel diameter (mm ± 0.1)	Hot balloon vessel diameter (mm ± 0.1)
100 mmHg	2.37	2.32	2.38
	1.87	1.93	1.57
	2.02	1.88	1.97
	2.76	2.77	2.64
	3.28	3.28	2.51
150 mmHg	2.55	2.41	2.41
	1.96	1.93	2.01
	1.92	1.95	2.11
	1.59	1.7	2.03
	2.88	2.87	2.65
	3.35	3.42	2.65
200 mmHg	3.01	2.79	2.52
	1.89	1.77	2.01
	1.98	2.05	2.11
	1.82	1.89	2.26
	2.9	3.09	2.63
	3.42	3.46	2.73
250 mmHg	2.75	2.76	2.44
	1.99	1.9	2.2
	2.03	2.18	2.22
	2.08	2.04	2.27
	2.96	3.03	2.54
	3.45	3.49	2.8

Table 12.1 Vessel diameter as a function of intravascular infusion pressure before and after angioplasty with the thermal balloon angioplasty catheter. The 'cold' balloon generates a temperature of 22 deg.C. The hot balloon applies a temperature of 90 deg.C. to the vessel wall.

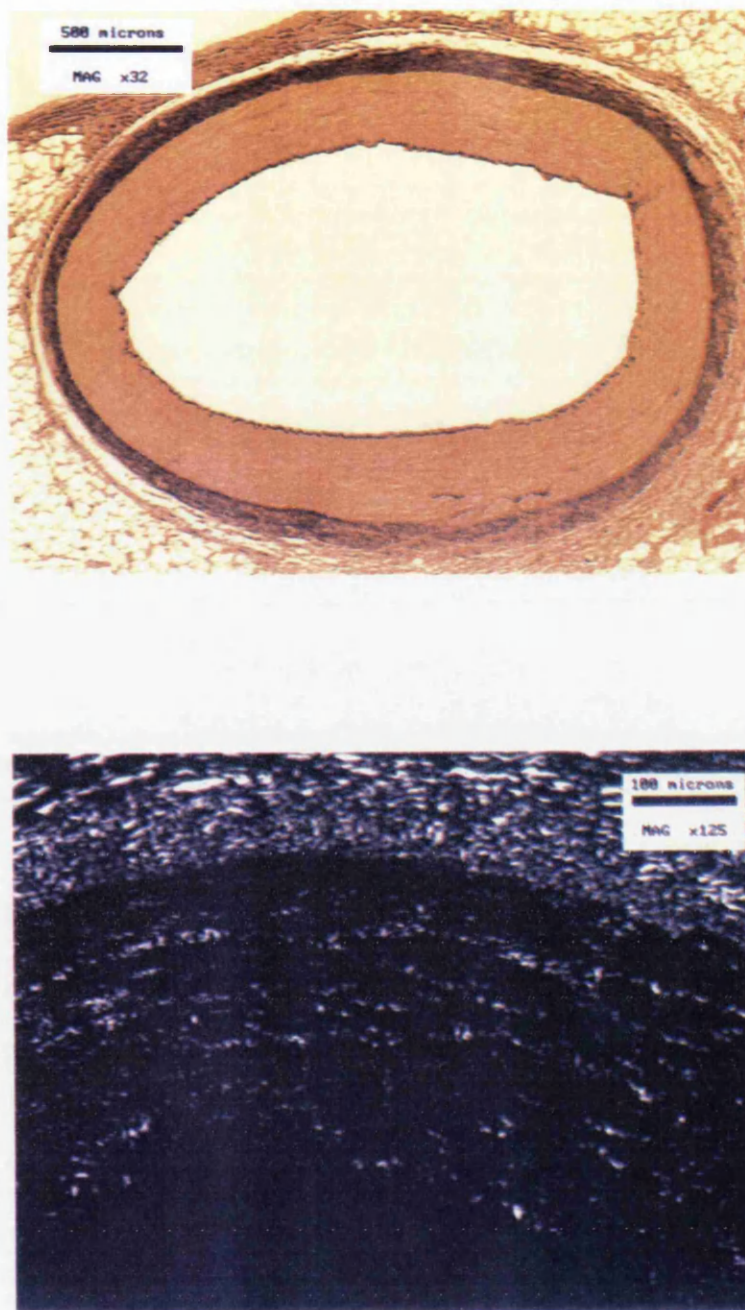


Figure 12.9 EVG stained vessel section (top) prior to thermal angioplasty. A close-up of the vessel wall stained with PSR is shown below - collagen is clearly evident.

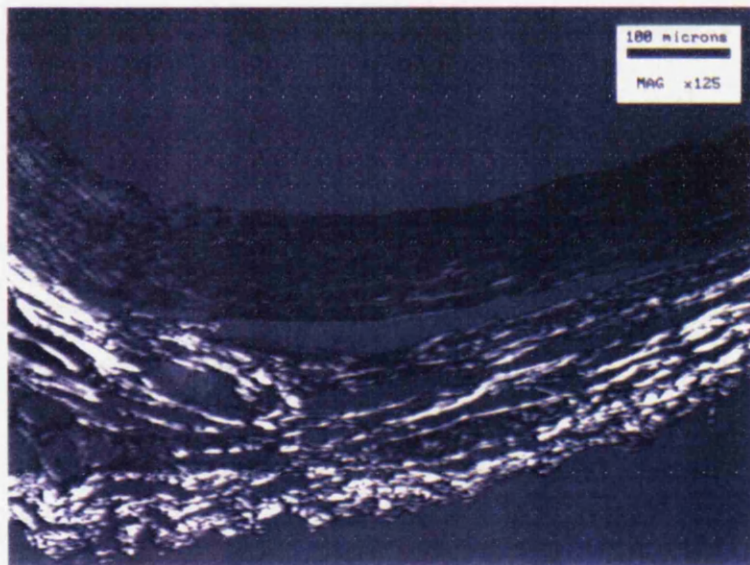
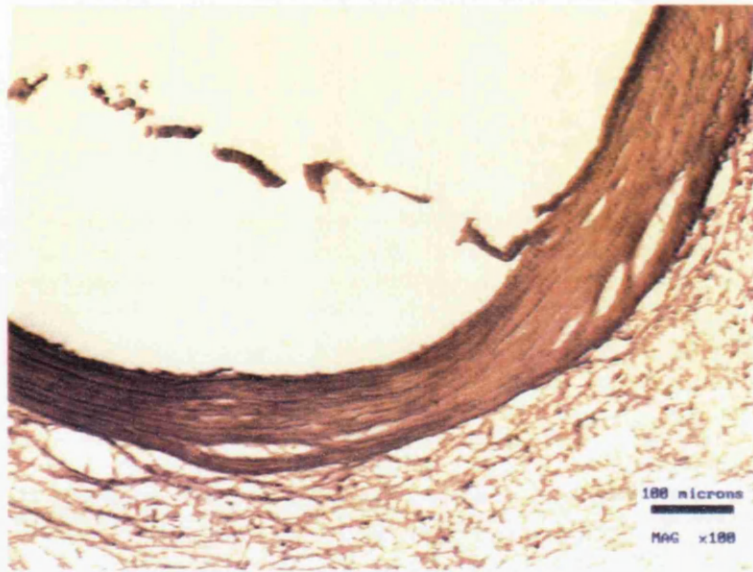


Figure 12.10 Vessel section following hot (90 deg.C.) balloon angioplasty (EVG - top image; PSR - bottom image). Disruption of wall integrity is evident, with endothelial denudation. Note the lack of birefringence (collagen denatured) in the wall of the PSR stained vessel.

degradation expanding beyond the immediate confines of the balloon. The Picosirius stained section reveals extensive collagen denaturation in the thermally treated vessel.

12.7 DISCUSSION

12.7.1 Technique

A critical factor in obtaining accurate results was X-ray image quality. Good contrast between vessels and heart muscle provides sharp visible vessel edges which encourage reproducible, well defined results. This was dependent on both X-ray technique and the quality of sealing of the heart section. Effective sealing was of paramount importance to the success of the experiment, since if this was not achieved, Urografin leaked out of the section during angiography creating an X-ray opaque pool in which the section sat, 'whiting out' the X-ray image to obscure the detail of the vessels. Although in our experiments sealing was good, it was never quite 100% effective. Leaks did occur, especially at an infusion pressure of 250mmHg, but they were small enough to interfere only rarely with the relevant region of the angiogram.

A slow degradation in X-ray image quality was observed with sequential angiograms, the contrast between vessel and muscle steadily reducing as muscle became increasingly underexposed. This was presumably due to seepage of contrast medium under repeated angiography, from the small vessel ends into the muscle.

Early attempts at imaging used a contrast medium consisting of a barium powder suspension in water. It soon became apparent however, that the powder was settling out and silting up the vessels with repeated use, distorting our results (eg. high pressures were required for inordinately low flow rates in which vessels had nearly silted up completely). This prompted the use of Urografin, which transformed the angiographic results. Urografin is an iodine solution, and thus silting did not occur, resulting in improved contrast with reduced image degradation over time.

Measurement of vessel diameter from the X-ray images did not make use of computer edge detection algorithms because the computer hardware was not available (a framegrabber would be required). Other groups have used such an approach, detecting edges as particular gradients of image intensity, mapped as a polynomial function (145). Claimed precision was in the region of $10\mu\text{m}$. For all the relative simplicity of our approach, the results are encouragingly accurate, revealed by the high level of reproducibility and the strongly significant linear correlation

coefficient obtained with only 6 data points. It is also a reflection of the uniformity of vessel response - the shrinkage effect is well defined.

12.7.2 Results

Reproducibility of measured vessel diameter was good at 150mmHg and above. The poorer reproducibility at 100mmHg suggests that this internal pressure was insufficient to properly inflate the vessel.

A consistent finding with the 3mm cold balloon was failure to alter the characteristics of the natural vessel wall. With heat alone (no balloon), vessel characteristics did change - vessel diameter shrank by approximately 40%. The point at which the vessel shrank while infusing the hot water was noticeable, sensed as increased resistance to the injected water flow due to the newly diminished bore of the vessel. This kind of shrinkage is reminiscent of work performed by Gorisch et al. in which *in vivo* vessel diameter was monitored as it shrank in response to heat (205). He concluded that shrinkage was primarily due to thermal denaturation of collagen. Such a conclusion is supported by our histological results in which the collagen of the heated vessel was seen to be denatured when stained with picosirus under polarised microscopy. Also consider that the endothelium and muscle contribute little to the elasticity of the wall (94,206,207), and that the elastin component is more stable and remains largely unaffected by the heat (205). The only remaining major component is collagen. Thus the evidence points to collagen denaturation as the determining factor of vessel response to heat *in vitro*.

Introduction of an inflated balloon while heating (hot balloon) modified the natural thermal shrinkage of the vessel to the extent that vessels of initial diameter less than 75% that of the balloon did not shrink but were expanded by the treatment. Those vessels of initial diameter greater than 75% that of the balloon, shrank by varying degrees, determined by the initial diameter of the vessel. The crossover between shrinkage and expansion occurred at approximately 75% the diameter of the 3.0mm balloon (ie. approximately 2.3mm) suggesting that a vessel of this initial size remains unchanged in diameter following thermal angioplasty. In the extreme case of very large vessel diameters, the 3.0mm balloon is unlikely to modify the natural thermal shrinkage of the vessel because it will be too small to do so. In this case the vessel might be expected to shrink by its natural 40%. Thus it can be argued that the lines of regression represent the first order approximation of a larger curve which approaches the asymptote of natural shrinkage at large vessel diameters, described by the simple expression $y=0.60x$. It is proposed that the

lines of regression more correctly represent the gradient of the larger curve in the region in which they are drawn.

In relation to vessel elasticity, the regression lines of figures 12.7 and 12.8 are similarly tightly overlapped indicating that no reduction in vessel distensibility has occurred. If vessel elasticity has changed, the effect is not observable with the resolution of our technique.

Concerning figure 12.8, all lines appear to intersect at the x-y coordinate of (3.1,2.6). The x-coordinate of the intersection is equal to the diameter of the balloon, but we are unable to interpret the significance of this, or give any reason why the intersection should occur.

Clearly, shrinkage of a vessel you are trying to expand is undesirable, and awareness of such an effect would be necessary in the clinical setting. Either other effects (which may exist with atheromatous vessels) must overcome this, or a balloon approximately 30% larger than the natural vessel diameter should be used when treating the vessel to stop shrinkage. The shrinkage demonstrated here is an acute effect which may be temporary *in vivo*. In the experiment recorded by Gorisch et al. (205), acutely diminished vessel diameters expanded with time. At 85deg.C. Gorisch recorded acute shrinkage of approximately 50% which relaxed after 10-15 minutes to a shrinkage of only 25%.

The outlying data of figure 12.8 at 100mmHg, is consistent with earlier observations that vessel diameter may not be fully attained at this intravascular pressure. This is further confirmed by the increased scatter of the data points as indicated by the reduced correlation coefficient ($r=0.86$ as opposed to $r \geq 0.95$ for the higher pressure data). However, additional issues are raised, since it has been assumed throughout that the vessel is cylindrically symmetric so that measurement of diameter from one X-ray projection is sufficient. This assumption is likely to be partially responsible for the error in diameter measured at 100mmHg, where the vessel may not have assumed a cylindrical shape at this low pressure. Multiple projections are required to obtain a true estimate of vessel cross-section. It is reasonable to assume substantial symmetry in the healthy natural vessel lumen, but highly unlikely in atheromatous vessels. In that instance, a second X-ray at 90 degrees to the first would be required (at the very least) for a reasonable estimate of lumen diameter.

In general, issues grow more complex when atheromatous vessels are considered, for instance it is known that atheromatous plaque is rarely homogeneous, consisting of both fatty and calcified deposits (208). It is likely that the conditions required for successful angioplasty will differ according to whether

fatty or calcific deposits form the predominant component. Thus characterisation of the plaque would be required in order to be matched to the treatment.

Whatever the complications, the response of the atheromatous vessel will be better understood if the contribution of the natural vessel wall to its behaviour is known, as has been established in this experiment.

In practice, a better model of the human heart *in vitro* is required than the sheep heart used in this experiment. The pig seems a suitable candidate, and may prove useful as a model of coronary disease, the eventual aim being to apply thermal balloon techniques to human atherosclerosis *in vitro*.

12.8 CONCLUSION

This experiment has attempted to assess the viability of the thermal balloon in conjunction with quantitative techniques, as a platform for the investigation of the effects of thermal balloon angioplasty *in vitro*. The balloon system has shown itself able to apply defined temperatures to the vessel wall *in vitro*. In combination with techniques used for quantifying balloon effects on the vessel, novel information has been obtained. This work has been sufficiently successful to merit further investigation.

Chapter 13

Laser Balloon Angioplasty - Conclusions

13.1 INTRODUCTION

Percutaneous transluminal coronary angioplasty has in recent years proved a valuable adjunct to bypass surgery in a limited set of patients with coronary artery disease. However, restenosis remains a significant problem with approximately 30% of patients requiring further intervention within 6 months. There have been varied attempts to reduce restenosis but success has been limited, reflecting the poorly understood mechanisms involved. Lasers applied to angioplasty have generated considerable interest, their primary application being in the recanalisation of occluded vessels, but restenosis remains largely unaffected. An alternative technique developed by Spears, involves irradiating the balloon expanded vessel by laser from within the balloon during inflation. It has been proposed that this bonds the tissue planes in the expanded state by action of the laser (primarily thermal in nature) providing a "biological stent" that prevents collapse of the vessel wall and provides a scaffold for the natural healing process. The expected result is a reduction in restenosis, but results to date are equivocal.

13.2 EXPERIMENTS

Successful implementation of laser augmented balloon angioplasty requires detailed study of mechanical and histological changes induced in the vessel wall during dilatation and heating. The experiments described in the latter chapters of this thesis represent a first step in the closer examination of these processes, revealing that:

- i) Preparation of an in vitro heart section suitable for repeat angiographic investigations permits direct comparison of vessel diameter pre- and post angioplasty;
- ii) Development of a water heated balloon that simulates the thermal effect of a Spears laser

- balloon permits application of known uniform temperature distributions to the vessel during angioplasty;
- iii) The angiographic measurement of vessel diameter was shown to be accurate, reproducible and reliable;
 - iv) Properties of the natural vessel wall were seen to remain unchanged following standard angioplasty (ie. cold balloon);
 - v) The natural shrinkage of the vessel in response to heat was modified in a well defined manner by the use of a 3.0mm diameter thermal balloon. Vessels of natural diameter 2.3mm or less were expanded by the treatment, while those of greater diameter shrank;
 - vi) Histology revealed extensive collagen denaturation in those samples subjected to the 90 deg.C. balloon. It seems likely that the change in collagen state is responsible for the change in vessel diameter.

13.3 FUTURE STUDY

It is important that the temperature range of the thermal balloon be extended to more realistically include temperatures used in the laser technique (120 deg.C.). This may improve its efficacy. Other areas for further study include:

13.3.1 Vessel Elasticity

Although changes in vessel diameter were recorded following thermal angioplasty, it would be useful to obtain associated changes in vessel elasticity since both affect the visco-elastic recoil of the vessel wall. However the small size of the vessels involved makes this difficult. It is possible that in conjunction with a video camera the strength testing rig of the laser bonding experiment could be adapted to measure vessel elasticity (Young's modulus). The length of the stretched sample could be recorded by a video camera connected to an image analysis system.

Providing the vessel diameter after thermal angioplasty was increased, a stiffer vessel wall might be advantageous since the vessel lumen would be less

likely to collapse. In addition it seems probable that the Young's modulus will be a function of the induced thermal dilation.

13.3.2 Atheromatous Vessels

Atheromatous vessels introduce many complications to our experiments, especially since the composition of atheroma can vary widely. It is already generally appreciated that different types of atheroma require different treatment regimes. Thus it is important in our case that the structure of atheroma be characterised before balloon treatment so that it might be included with subsequent correlations of vessel diameter and balloon parameters. Radiography offers limited characterisation - calcified deposits are radio-opaque. Angioscopy enables visual inspection of the luminal plaque surface, permitting possible identification of plaque types. Intravascular ultrasound provides the most comprehensive assessment, obtaining structural information at depth. Such characterisation would be referenced to histological findings. It seems likely in the long term that the nature of the plaque would determine the treatment technique.

13.3.3 In Vivo

The success of laser assisted balloon angioplasty will be determined by its ability to reduce restenosis. Therefore an in vivo series of experiments must be performed. The atheromatous pig is a good candidate and the in vivo results could be readily correlated with earlier in vitro work also performed on pig hearts.

13.4 CONCLUSION

The eventual aim of these investigations is to establish which balloon parameters are required to effectively reduce restenosis following the balloon angioplasty procedure. Although a water heated balloon has been described because of experimental advantages, the controllability and flexibility of the laser assisted balloon makes it the modality of choice for the generation of conditions required for effective treatment within the atheromatous vessel.

References

- 1 Bertolotti M. 1983 Masers and lasers: An historical approach. Published by *Adam Hilger*
- 2 Gordon JP. 1958 The MASER. *Sci Amer* December 42;199
- 3 Maiman TH 1960 Stimulated optical radiation in ruby. *Nature* 187;493
- 4 Schawlow AL 1961 Optical MASERS. *Sci Amer* 204(6);52
- 5 O'Shea DC, Callen WR, Rhodes WT 1978 Introduction to lasers and their applications. Published by *Addison-Wesley*
- 6 Moseley H, Haywood JK 1987 Medical Laser Safety. *IPSM Report 48*
- 7 DHSS 1984 Guidance on the safe use of lasers in medical practice. *HMSO*
- 8 BS 4803. Radiation safety of laser products and systems. 1983 *London: British Standards Inst.*
- 9 ANSI Z-136.1. Safe use of lasers. 1986 *New York: American National Standards Inst.*
- 10 DIN 58215. Eye protectors against laser radiation: safety requirements and testing. 1982 *Deutches Institute Fur Normung*
- 11 Fenner J, Moseley H 1989 Damage thresholds of CO2 laser protective eyewear. *Lasers Med Sci* 4;33-39
- 12 Goldrath MH, Fuller TA, Segal S 1981 Laser photovaporization of endometrium for the treatment of menorrhagia. *Am J Obstet Gynecol* 140;14

- 13 Bown SG 1985 Controlled studies of laser therapy for haemorrhage from peptic ulcers. *Acta Endosc* 15;1
- 14 MacLeod IA, Mills PR, MacKenzie JF, Joffe SN, Russell RI, Carter DC 1983 Neodymium yttrium aluminium garnet laser photocoagulation for major haemorrhage from peptic ulcers and single vessels. *Br Med J* 286;345
- 15 Diabetic retinopathy study 1978. Photocoagulation treatment of proliferative diabetic retinopathy. *Ophthalmol* 85;82
- 16 Macular photocoagulation study 1982. Argon laser photocoagulation for senile macular degeneration. *Arch Ophthalmol* 100;912
- 17 Maser MR, Apfelberg DB, Lash H 1983 Clinical applications of the argon and carbon dioxide lasers in dermatology and plastic surgery. *World J Surg* 7;684
- 18 Moseley H 1988 Medical Physics Handbooks 18: Non-ionising radiation. Published by *Adam Hilger*
- 19 Warwick R, Williams PL (Eds) 1973 Gray's Anatomy Published by *Longman*
- 20 Fisher J, Wheatley DJ 1987 An improved pericardial bioprosthetic heart valve: design and laboratory evaluation. *Eur J Cardio-thorac Surg* 1;71-79
- 21 Cooper DKC, Novitzky D 1990 The transplantation and replacement of thoracic organs. Published by *Kluwer Academic Publishers*
- 22 Swerdlow CD, Winkle RA, Mason JW 1983 Determinants of survival in patients with ventricular tachyarrhythmias. *N Engl J Med* 308;1436
- 23 Meier B 1992 Recanalization of chronically occluded arteries. *Herz* 17(1);27-39
- 24 Jain KK, Gorisch W 1979 Repair of small blood vessels with the Neodymium-YAG laser - a preliminary report. *Surgery* 85;684

- 25 Neblett CR, Morris JR, Thomsen S 1986 Laser-assisted microsurgical anastomosis. *Neurosurgery* 19(6);914-933
- 26 Sigel B, Acevedo FJ 1963 Electrocoaptive union of blood vessels - a preliminary experimental study. *J Surg Res* 3(2);90-96
- 27 Sigel B, Dunn MR 1965 The mechanism of blood vessel closure by high frequency electrocoagulation. *Surg Gynecol Obstet* 121;823-831
- 28 White RA, Abergel RP, Lyons R, Klein SR, Kopchok G, Dwyer RM, Uitto J 1986 Biological effects of laser welding on vascular healing. *Lasers Surg Med* 6;137-141
- 29 Quigley MR, Bailes JE, Kwaan HC, Cerullo LJ, Block S 1986 Comparison of myointimal hyperplasia in laser-assisted and suture anastomosed arteries. A preliminary report. *J Vasc Surg* 4(3);217-219
- 30 Ashworth EM, Dansing MC, Olson JF, Hoagland WP, Baughman S, Glover JL 1987 Large-artery welding with a milliwatt CO2 laser. *Arch Surg* 122(6);673-677
- 31 Quigley MR, Bailes JE, Kwaan HC, Cerullo LJ, Brown JT 1986 Aneurysm formation after low power carbon dioxide laser-assisted vascular anastomosis. *Neurosurgery* 18(3);292-299
- 32 Oishi J 1986 Microvascular anastomosis with a low-output CO2 laser. (I) Laser device, techniques and conditions of anastomosis. *J Jpn Orthop Ass* 60(7);801-811
- 33 Krueger RR, Almquist EE 1985 Argon laser coagulation of blood for the anastomosis of small vessels. *Lasers Surg Med* 5;55-60
- 34 Schober R, Ulrich F, Sander T, Durselen H, Hessel S 1986 Laser-induced alteration of collagen substructure allows microsurgical tissue welding. *Science* 232;1421-1422

- 35 Sartorius CJ, Shapiro SA, Campbell RL, Klatte EC, Clark SA 1986
Experimental laser-assisted and end-to-side microvascular anastomosis.
Microsurg 7(2):79-83
- 36 Badeau F, Lee CE, Morris JR, Thompson S, Malk EG, Welch AJ 1986
Temperature response during microvascular anastomosis using milliwatt CO2
laser. *Lasers Surg Med* 6;179
- 37 Godlewski G, Pradal P, Rouy S, Charras A, Dauzat M, Lan O, Lopez FM
1986 Microvascular carotid end-to-end anastomosis with the argon laser.
World J Surg 10(5);829-833
- 38 White RA 1987 Technical frontiers for the vascular surgeon: laser
anastomotic welding and angioscopy-assisted intraluminal instrumentation.
J Vasc Surg 5(4);673-680
- 39 Jain KK 1984 Sutureless extra-intracranial anastomosis by laser.
Lancet 2;816-817
- 40 White RA, Kopchok G, Peng S-K, Fujitani R, White G, Klein S, Uitto J 1987
Laser vascular welding - how does it work? *Ann Vasc Surg* 1;461-464
- 41 Jacobowitz IJ, Wang S, Basu S, Baumann G, Marini C, Cunningham JN
1990 Influences of laser pulse duration and anastomotic disruption on laser-
assisted microvascular anastomoses. *Microsurgery* 11(2);85-90
- 42 Vance CA, Evans JH, Wheatley DJ 1986 Laser assisted vessel
anastomosis in coronary artery surgery. *Lasers Surg Med* 6; 271
- 43 Vance CA, Fisher J, Wheatley DJ, Evans JH, Spyt TJ, Moseley H, Paul JP
1988 Laser assisted vessel anastomosis of coronary arteries in vitro:
optimization of bonding conditions. *Lasers Med Sci* 3;219-227
- 44 Chuck RS, Oz MC, Delohery TM, Johnson JP, Bass LS, Nowygrod R, Treat
MR 1989 Dye-enhanced laser tissue welding. *Lasers Sur Med*
9;471-477

- 45 Mozami N, Oz MC, Bass LS, Treat MR 1990 Reinforcement of colonic anastomoses with a laser and dye-enhanced fibrinogen. *Arch Surg* 125(11);1452-1454
- 46 Kopchok G, Grundfest WS, White RA, Donayre C, Fujitani R, Litvack F, White GH, Klein SR, Morgenstern L 1986 Argon laser vascular welding: the thermal component. *Proc Soc Photooptical Instr Eng* 712;260-263
- 47 Kopchok G, White RA, Grundfest WS, Fujitani RM, Litvack F, Klein SR, White GH 1988 Thermal studies of in-vivo vascular tissue fusion by argon laser. *J Invest Surg* 1;5-12
- 48 Ashton RC, Oz MC, Lontz JF, Matsumae M, Taylor R, Lemole GM Jr, Shapira N, Lemole GM 1991 Laser-assisted fibrinogen bonding of vascular tissue. *J Surg Res* 51(4);324-328
- 49 Fried MP, Caminear DS, Sloman-Moll ER, Samonte BR 1991 The use of absorbable sutures in laser-assisted microvascular anastomoses. *Laryngoscope* 101(4 Pt1);389-394
- 50 White RA, Kopchok GE, Vlasak J, Hsiang Y, Fujitani RM, White GH, Peng S-K 1990 Experimental and early clinical evaluation of vascular anastomoses with argon laser fusion and the use of absorbable guy sutures: a preliminary report. *J Vasc Surg* 12;401-408
- 51 Libutti SK, Oz M, Forde KA, Auteri JS, Johnson JP, Bass LS, Treat MR 1990 Canine colonic anastomoses reinforced with dye-enhanced fibrinogen and a diode laser. *Surg Endosc* 4(2);97-99
- 52 Samonte BR, Fried MP 1991 Laser-assisted microvascular anastomosis using CO2 and KTP/532 lasers. *Lasers Surg Med* 11(6);511-516
- 53 Bailes JE, Quigley MR, Kwaan HC, Cerullo LJ, Brown JT 1985 Fibrinolytic activity following laser-assisted vascular anastomosis. *Microsurg* 6(3);163-168

- 54 McCarthy WJ, Hartz RS, Yao JST, Sottiurai VS, Kwaan HC, Michaelis LL 1986 Vascular anastomoses with laser energy. *J Vasc Surg* 3(1);32-41
- 55 Jain KK 1983 Sutureless end-to-side microvascular anastomosis using Neodymium-YAG laser. *Vasc Surg* 17;240-243
- 56 Vale BH, Frenkel A, Trenka-Benthin S, Matlaga BF 1986 Microsurgical anastomosis of rat carotid arteries with the CO2 laser. *Plast Reconst Surg* 77(5);759-766
- 57 Kuroyanagi Y, Taguchi M, Yano T, Jones DN, Shionoya S 1991 Argon laser-assisted anastomoses in medium size vessels: one year follow-up. *Lasers Surg Med* 11(3);223-231
- 58 White RA, Kopchok G, Donayre C, Abergel RP, Lyons R, Klein SR, Dwyer RM, Uitto J 1986 Comparison of laser welded and sutured arteriotomies. *Arch Surg* 121;1133-1135
- 59 Negro A, Rogers DW, Naim JO, Parry FW 1986 A comparison of microsurgical suture and CO2 laser welded anastomosis of rabbit uterine cornua. *Lasers Surg Med* 6;212
- 60 Ulrich F, Durselen R, Schober R 1988 Long-term investigations of laser-assisted microvascular anastomoses with the 1.318- μ m Nd:YAG laser. *Lasers Surg Med* 8;104-107
- 61 Frazier OH, Painvin A, Morris JR, Thomsen S, Neblett CR 1985 Laser-assisted microvascular anastomoses: Angiographic and anatomopathologic studies on growing microvascular anastomoses: Preliminary report. *Surg* 97(5);585-589
- 62 Gennaro M, Ascer E, Mohan C, Wang S 1991 A comparison of CO2 laser-assisted venous anastomoses and conventional suture techniques: patency, aneurysm formation, and histologic differences. *J Vasc Surg* 14(5);605-613

- 63 Quigley MR, Bailes JE, Kwaan HC, Cerullo LJ, Brown JT, Fitzsimmons J
1985 Comparison of bursting strength between suture- and laser-
anastomosed vessels. *Microsurg* 6(4);229-232
- 64 Burger RA, Gerharz CD, Seitzmayer M, Engelmann U, Hohenfellner R 1991
Bursting strength of the rat aorta: comparison of suture and laser
anastomoses. *Urol Int* 47(1);48-52
- 65 Ruiz-Razura A, Lan M, Hita CE, Khan Z, Hwang NHC, Cohen BE 1988
Bursting strength in CO2 laser-assisted microvascular anastomoses.
J Reconstr Microsurg 4;291-296
- 66 Hartz RS, Locicero J, Shih SR, McCarthy WJ, Michaelis LL 1985
Mechanical properties of end-to-end laser-assisted and sutured arterial
anastomoses under axial loading. *Surg Forum* 36;457-459
- 67 Dew DK 1983 Laser microsurgical repair of soft tissue: an update and
review. *Lasers Surg Med* 3;134
- 68 White R, Kopchok G, Peng S-K, Fujitani R, White G, Klein S, Grundfest W
1987 Mechanism of laser vascular tissue welding. *Lasers Surg Med*
5;84
- 69 White RA comments on McCarthy WJ, Hartz RS, Yao JST, Sottiurai VS,
Kwaan HC, Michaelis LL 1986 Vascular anastomoses with laser energy.
J Vasc Surg 3(1);32-41
- 70 Frazier GH, Shehab SA, Radovancevic B, Parnis S 1987 Anastomosis of
bypass grafts using low powered CO2 lasers. *Lasers Surg Med* 5;84
- 71 Quigley MR, Bailes JE, Kwaan HC, Cerullo LJ, Brown JT, Lastra C, Monma B
1985 Microvascular anastomosis using the milliwatt CO2 laser. *Lasers
Surg Med* 5;357-365
- 72 Oishi J 1986 Microvascular anastomosis with a low-output CO2 laser.
(II) Histopathological features. *J Jpn Orthop Ass* 60(7);813-824

- 73 White RA, Kopchok G, Donayre C, Lyons R, White G, Klein SR, Abergel RP, Uitto J 1986 Laser welding of large diameter arteries and veins. *Trans Am Soc Artif Intern Organs* 32;181-183
- 74 Lim KH, Wang S, Kaplan P, Rose DM, Cunningham JN 1986 Factors that affect bursting strength of intestinal anastomosis with CO2 laser. *Lasers Surg Med* 6;202
- 75 Sauer JS, Rogers DW, Hinshaw JR 1986 Bursting pressure of CO2 laser-welded rabbit ileum. *Lasers Surg Med* 6;106-109
- 76 Flemming AF, Bown SG, Colles MJ, Brough MD 1990 Comparison of laser-assisted and conventionally sutured microvascular anastomoses by bursting pressure: a reanalysis and further studies. *Microsurgery* 11(1);25-33
- 77 Epstein M, Cooley BC 1986 Electron microscopic study of laser dosimetry for microvascular tissue welding. *Lasers Surg Med* 6;202
- 78 Acland RD, Trachtenberg L 1977 The histopathology of small arteries following experimental microvascular anastomosis. *Plast Reconstruct Surg* 59;868-875
- 79 White RA, Kopchok GE, Donayre CE, Peng S, Fujitani RM, White GH, Uitto J 1988 Mechanism of tissue fusion in argon laser-welded vein-artery anastomoses. *Lasers Surg Med* 8;83-89
- 80 Godlewski G, Rouy S, Pradal P 1986 Scanning electron microscopy of microarterial anastomoses with the argon laser. *Lasers Med Sci* 1;111-115
- 81 Torres JH, Springer TA, Welch AJ, Pearce JA 1990 Limitations of a thermal camera in measuring surface temperature of laser-irradiated tissues. *Lasers Surg Med* 10;510-523
- 82 Marchesini R, Andreola S, Emanuelli H, Melloni E, Schirotti A, Spinelli P, Fava G 1985 Temperature rise in biological tissue during Nd:YAG laser irradiation. *Lasers Surg Med* 5;75-82

- 83 van Gemert MJC, Lee CE, Denham CR, Welch AJ 1985 Modeling of laser-tissue welding during vessel anastomosis. *Lasers Surg Med* 5;171
- 84 Langerholm J 1979 Moving phase transitions in laser-irradiated biological tissue. *Appl Opt* 18(13);2286-2293
- 85 Welch AJ 1984 The thermal response of laser irradiated tissue. *IEEE J Quant Elect* QE20;1471-1481
- 86 Halldorsson T, Langerholm J 1978 Thermodynamic analysis of laser irradiation of biological tissue. *Appl Opt* 17(24);3948-3959
- 87 Sluzalec A 1987 Finite element model of heat flow in biological tissue undergoing laser irradiation. *J Biomech* 20(10);937-941
- 88 Welch AJ, Yoon G, van Gemert MJC 1987 Practical models for light distribution in laser-irradiated tissue. *Lasers Surg Med* 6;488-493
- 89 Jacque SL, Prah SA 1987 Modeling optical and thermal distributions in tissue during laser irradiation. *Lasers Surg Med* 6;494-503
- 90 Keijzer M, Jacques SL, Prah SA, Welch AJ 1989 Light distributions in artery tissue: monte carlo simulations for finite-diameter laser beams. *Lasers Surg Med* 9;148-154
- 91 Okada M, Shimizu K, Ikuta H, Horii H, Nakamura K 1985 A new method of vascular anastomosis by low energy CO₂ laser: experimental and clinical study. *Kobe J Med Sci* 31;151-168
- 92 Tulleken CA, van Dieren A, Verdaasdonk RM, Berendsen W 1992 End-to-side anastomosis of small vessels using an Nd:YAG laser with a hemispherical contact probe. Technical note. *J Neurosurg* 76(3);546-549
- 93 Warwick R, Williams PL (Eds) 1973 *Gray's Anatomy - Chapter 6*
Published by *Longman*
- 94 Burton AC 1954 Relation of structure to function of the tissues of the wall of blood vessels. *Physiol Rev* 34;619-642

- 95 Baer E, Cassidy JJ, Hiltner A Hierarchical structure of collagen and its relationship to the physical properties of tendon. In *Collagen: biochemistry, biomechanics, biotechnology*. Vol 2:Chap 9;177-99 (Ed. Nimni ME) CRC Press, Boca Raton, 1988
- 96 Parry DAD 1988 The molecular and fibrillar structure of collagen and its relationship to the mechanical properties of connective tissue. *Biophys Chem* 29;195-109
- 97 Pruet CW 1987 The microstructure of collagen and elastin. *Ear Nose Throat J* 66;431-435
- 98 Nimni ME 1980 The molecular organization of collagen and its role in determining the biophysical properties of the connective tissues. *Biorheology* 17;51-82
- 99 Parry DAD, Craig AS
Collagen fibrils during development and maturation and their contribution to the mechanical attributes of connective tissue. In *Collagen: biochemistry, biomechanics, biotechnology*. Vol 2:Chap 1;1-23 (Ed. Nimni ME) CRC Press, Boca Raton, 1988
- 100 Elden HR 1968 Physical properties of collagen fibers. *Int Rev Connect Tissue Res* 4;283-348
- 101 Flory PJ, Garrett RR 1958 Phase transitions in collagen and gelatin systems. *J Am Chem Soc* 80;4836-4845
- 102 Junqueira LCU, Bignolas G, Brentani RR 1979 Picrosirius staining plus polarization microscopy, a specific method for collagen detection in tissue sections. *J Histochem* 11;447-455
- 103 Vidal BC, Mello MLS, Pimental ER 1982 Polarisation microscopy and microspectrophotometry of Sirius Red, Picrosirius and Chlorantine fast red aggregates and of their complexes with collagen. *Histochem J* 14;857-878

- 104 Junqueira LCU, Cossermelli W, Brentani R 1978 Differential staining of collagens type I, II and III by sirius red and polarization microscopy. *Arch Histol Jap* 41(3);267-274
- 105 Brooks SG, Ashley S, Wright H, Davies GA, Kester RC, Rees MR 1991 The histological measurement of laser-induced thermal damage in vascular tissue using the stain picosirius red F3BA. *Lasers Med Sci* 6;399-405
- 106 Travers V, Trevidic P, Jagueux M, Apoil A, Nicoletis C 1988 Experimental microvascular anastomosis with a CO2 laser. A series of 240 anastomoses. *Ann Chir Main* 7(3);202-209
- 107 Ruiz-Razura A, Branfman GS, Lan M, Cohen BE 1990 Laser-assisted microsurgical anastomoses in traumatized blood vessels. *J Reconstr Microsurg* 6(1);55-59
- 108 Nakata S, Campbell CD, Pick R, Replogle RL 1989 End-to-side and end-to-end vascular anastomoses with a carbon dioxide laser. *J Thorac Cardiovasc Surg* 98;57-62
- 109 Jenkins RD, Sinclair IN, Anand R, Kalil AG, Schoen FJ, Spears JR 1988 Laser balloon angioplasty: effect of tissue temperature on weld strength of human postmortem intima-media separations. *Lasers Surg Med* 8;30-39
- 110 Eley DD, Tabor D 1961 Fundamentals of Adhesive Joints In *Adhesion* Chapter 1;1-18 Eley DD (Ed) Published by Oxford University Press
- 111 Vance CA 1988 (April) Laser assisted vascular anastomosis. Phd Thesis - Glasgow University, Scotland
- 112 Kubelka P, Munk F 1931 *Zeits. f. tech. Physik* 12;593
- 113 Kubelka P 1948 New contributions to the optics of intensely light-scattering materials. Part1. *J Opt Soc Am* 38(5);448-457
- 114 Kubelka P 1954 New contributions to the optics of intensely light-scattering materials. Part II: Nonhomogeneous layers. *J Opt Soc Am* 44(4);330-335

- 115 Kroy W, Halldorsson T, Langerholm J 1980 Laser coagulation: practical advice from a theoretical viewpoint. *Applied Optics* 19(1);6-9
- 116 Prah SA 1988 (December) Light transport in tissue. Phd Thesis - University Of Texas At Austin
- 117 Yoon G, Welch AJ, Motamedi M, van Gemert MCJ 1987 Development and application of three-dimensional light distribution model for laser irradiated tissue. *IEEE J Quant Elect* QE-23(10);1721-1733
- 118 Carslaw HS, Jaeger JC 1959 Conduction of heat in solids. Published by *Clarendon Press*
- 119 Smith GD 1985 Numerical solution of partial differential equations. Published by *Oxford University Press*
- 120 Fenner J, Martin W, Moseley H, Wheatley DJ 1992 Shear strength of tissue bonds as a function of bonding temperature: a proposed mechanism for laser-assisted tissue welding. *Lasers Med Sci* 7;39-43
- 121 Shotton DM 1989 Confocal scanning optical microscopy and its applications for biological specimens. *J Cell Sci* 94:175-206
- 122 Wilson, Tony (Eds.) 1990 Confocal microscopy. Published by *Academic Press*
- 123 Gruntzig A, Senning A, Siegenthaler WE 1979 Non-operative dilatation of coronary artery stenosis: percutaneous transluminal coronary angioplasty. *N Engl J Med* 301;61
- 124 Vlietstra RE, Holmes DR 1983 Coronary balloon angioplasty: has its importance been overinflated? *Cardiovasc Rev Reports* 4(2);245-252
- 125 Holmes DR, Vlietstra RE, Smith HC et al. 1984 Restenosis after percutaneous transluminal coronary angioplasty (PTCA): a report from the PTCA registry of the National Heart, Lung, and Blood Institute. *Am J Cardiol* 53 (suppl);77C-81C

- 126 Yang XM, Manninen H, Soimakallio S 1990 Percutaneous transluminal laser angioplasty: progress over the last two years. *Acta Radiol* 31;3-12
- 127 Jenkins RD, Spears JR 1990 Laser balloon angioplasty: a new approach to abrupt coronary occlusion and chronic restenosis. *Circulation* 81(Suppl4);101-108
- 128 Arnott J 1841 On dilatation by fluid pressure in stricture of the urethra. *Lond M Gaz* 28;343-346
- 129 Forssman W 1929 Die sonderung des rechten herzens. *Klin Wochenschr* 8;2085-2087
- 130 Sones FM, Shirey EK, Proffit WL et al. 1959 Cine-coronary arteriography. *Circulation* 20;773-774
- 131 Dotter CT, Judkins MP 1964 Transluminal treatment of arteriosclerotic obstruction. *Circulation* 30;654-670
- 132 Gruntzig A, Fischer M, Goebel N, Schlumpf M 1981 Percutaneous transluminal coronary angioplasty (PTCA). Study of 147 patients. *Ann Radiol (Paris)* 24(5);377-379
- 133 Stertzner SH, Wallsh E, Bruno MS 1983 Evaluation of transluminal coronary angioplasty in left main coronary artery stenosis. *Am J Cardiol* 51;676
- 134 Douglas JS, Gruntzig AR, King SB 1982 Results of percutaneous transluminal coronary angioplasty in patients with angina pectoris following coronary bypass surgery. *Am J Cardiol* 49;904
- 135 Topol EJ, Califf RM, George BS et al. A randomized trial of immediate versus delayed elective angioplasty after intravenous tissue plasminogen activator in acute myocardial infarction. *N Engl J Med* 317;581
- 136 Reeder JS 1987 Angioplasty and the cost of myocardial revascularization: has its promise been fulfilled? *Int J Cardiol* 15;287

- 137 Reeder GS, Vlietstra RE, Mock MB et al. 1986 Comparison of angioplasty and bypass surgery in multivessel coronary artery disease. *Int J Cardiol* 10;213
- 138 Naunheim KS, Fiore AC, Fagan DC, McBride LR, Barner HB, Pennington G, Willman VL, Kern MJ, Deligonul U et al. 1989 Emergency coronary artery bypass grafting for failed angioplasty: risk factors and outcome. *Ann Thorac Surg* 47;816-823
- 139 Nobuyoshi M, Kimura T, Ohishi H, Horiuchi H, Nosaka H, Hamasaki N, Yokoi H, Kim K 1991 Restenosis after percutaneous transluminal coronary angioplasty: pathologic observations in 20 patients. *J Am Coll Cardiol* 17(2);433-439
- 140 Vlietstra RE, Holmes DR, Rodeheffer RJ, Bailey KR 1991 Consequences of restenosis after coronary angioplasty. *Int J Cardiol* 31;143-148
- 141 Liu MW, Roubin GS, King SB 1989 Restenosis after coronary angioplasty: potential biologic determinants and role of intimal hyperplasia. *Circulation* 79(6);1374-1387
- 142 Liu MW, Berk BC 1991 Restenosis following coronary balloon angioplasty: role of smooth muscle cell proliferation. *Trends Cardiovasc Med* 1(3);107-111
- 143 Waller BF, Orr CM, Pinkerton CA, VanTassel JW, Pinto RP 1990 Morphologic observations late after coronary balloon angioplasty: mechanisms of acute injury and relationship to restenosis. *Radiology* 174;961-967
- 144 Marcus ML, Skorton DJ, Johnson MR, Collins SM, Harrison DG, Kerber RE 1988 Visual estimates of percent diameter coronary stenosis: "A battered gold standard". *J Am Coll Cardiol* 11(4);882-888
- 145 Spears JR, Sandor T, Als AV, Malagold M, Markis JE, Grossman W, Serur JR, Paulin S 1983 Computerized image analysis for quantitative measurement of cineangiograms. *Circulation* 68(2);453-461

- 146 Demer LL, Kirkeeide LL, Jain A, Hartley CJ, Raizner AE, Gould KL 1987 Quantitation of lumen enlargement during coronary angioplasty using pressure-volume curves vs. arteriography. *J Am Coll Cardiol* 9(2);105A
- 147 Merickel MB, Carman CS, Brookeman JR, Ayers CR 1991 Image analysis and quantification of atherosclerosis using MRI. *Computerised Medical Imaging And Graphics* 15(4);207-216
- 148 Mallery JA, Tobis JM, Griffith J, Gessert J, McRae M, Moussabeck O, Bessen M, Moriuchi M, Henry WL 1990 Assessment of normal and atherosclerotic arterial wall thickness with an intravascular ultrasound imaging catheter. *Am Heart J* 119(6);1392-1400
- 149 Gussenhoven EJ, Essed CE, Lancee CT, Mastik F, Frietman P, van Egmond FC, Reiber J, Bosch H, van Urk H, et al. 1989 Arterial wall characteristics determined by intravascular ultrasound imaging: an in vitro study. *J Am Coll Cardiol* 14(4);947-952
- 150 Abele JE 1980 Balloon catheters and transluminal dilatation: Technical considerations. *Am J Radiol* 135;901-906
- 151 Cragg A, Lung G, Rysavy J, Castaneda F, Castaneda-Zuniga W, Amplatz K 1984 Nonsurgical placement of arterial endoprostheses: A new technique using nitinol wire. *Radiology* 147;261
- 152 Schatz RA 1989 A view of vascular stents. *Circulation* 79(2);445-457
- 153 Soulen MC, Bonn J, Shapiro MJ 1991 Recanalization of an occluded aortoiliac bypass graft with Palmaz stents. *J Vasc Interv Radiol* 24(2);497-501
- 154 White CJ, Ramee SR, Banks AK, Mesa JE, Chokshi S, Isner JM 1992 A new balloon-expandable tantalum coil stent: angiographic patency and histologic findings in an atherogenic swine model. *J Am Coll Cardiol* 9(4);870-876

- 155 Ritchie JL, Hansen DD, Vracko R, Auth DC 1986 Mechanical thrombolysis: a new rotational catheter approach for acute thrombi. *Circulation* 73(5);1006-1012
- 156 Kent KM, Bentivoglio LG, Block PC, Bourassa MG, Cowley MJ, Dorros G, Detre KM, Gosselin AJ, Gruentzig et al. 1984 Long-term efficacy of percutaneous transluminal coronary angioplasty (PTCA): report from the national heart, lung and blood institute PTCA registry. *Am J Cardiol* 53;27C-31C
- 157 Holmes DR, Vlietstra RE, Mock MB, Smith HC, Cowley MJ, Kent KM, Detre KM 1982 Follow-up of patients undergoing percutaneous transluminal coronary angioplasty (PTCA): a report from the NHLBI PTCA registry. *Am J Cardiol* 49;917
- 158 Doyle DL 1990 Update on laser angioplasty. *Can Med Assoc J* 142;1391
- 159 Strikwerda S, Silverman CB, Ratliff NB et al. 1988 Effects of varying argon ion laser intensity and exposure time on the ablation of atherosclerotic plaque. *Lasers Surg Med* 8;66
- 160 Welch AJ, Valvano JW, Pearce JA, Hayes LJ, Motamedi M 1985 Effect of laser radiation on tissue during laser angioplasty. *Lasers Surg Med* 5;251-264
- 161 Torres JH, Motamedi M, Levine AB, Welch AJ, Pearce JA 1989 Disparate absorption of argon laser irradiation by fatty versus fibrous atheromata. Implications for laser angioplasty. *Lasers Surg Med* Suppl 1;13
- 162 Orme EC, McClane RW, Straight RC 1989 Absorption coefficient analysis of in vitro human normal and atherosclerotic arteries. *Lasers Surg Med* Suppl 1;12

- 163 Sartori M, Henry PD, Roberts R 1986 Characterisation of intimal structure and thickness in normal and atherosclerotic vessels by argon ion laser induced fluorescence. *Lasers Surg Med* 6;176
- 164 Prince MR, Deutch TF, Matthews-Roth M, Margois R, Parish JA, Oseroff AR 1986 Preferential light absorption in atheromas in vitro: implications for laser angioplasty. *J Clin Invest* 78;295-302
- 165 Orme EC, Spikes BE, Straight RC, McClane RW, Vincent GM 1989 An in vitro survey of photosensitizers which may be taken up by atherosclerotic plaque. *Lasers Surg Med* 1;12
- 166 Eichler J, Knof F, Lenz H 1977 Measurements on the depth of penetration of light (0.35-1.0 μ m) in tissue. *Rad Environm Biophys* 14;239-242
- 167 Normann S, Cohen D, Feldman RL, Geiser A, Conti CR 1982 Effects of carbon dioxide, Nd-YAG, and argon laser radiation on coronary atheromatous plaques. *Amer J Cardiol* 50;1199
- 168 Litvack F, Papaioannou T, Mohr FW, Jakubowski AT, Forrester JS 1986 Role of laser and thermal ablation devices in the treatment of vascular diseases. *Amer J Cardiol* 61;81G
- 169 Sanborn TA, Faxon DP, Kellett MA, Jacobs AK, Ryan TJ 1987 Percutaneous coronary laser thermal angioplasty with a metallic capped fibre. *J Am Coll Cardiol* 9(2);104A
- 170 Lammer J, Kleinert R, Pilger E, Schmidt-Kloiber H, Reichel E 1989 Contact probe for intravascular laser recanalization experimental evaluation. *Invest Radiol* 24(3);190-195
- 171 Geschwind HJ, Blair JD, Mongkolsmal D et al. 1987 Development and experimental application of contact probe catheter for laser angioplasty. *J Amer Coll Cardiol* 9;10
- 172 Geschwind HJ 1988 Laser angioplasty. Newer modalities. *Ann Radiol (Paris)* 31;69

- 173 Decker-Dunn D, Christensen DA, Vincent GM 1990 Multifiber gradient-index lens laser angioplasty probe. *Lasers Surg Med* 10;85-93
- 174 Linnemeier TJ, Cumberland DC, Rothbaum DA, Landin RJ, Ball MW 1989 Human percutaneous laser-assisted coronary angioplasty. Efforts to reduce spasm and thrombosis. *J Amer Coll Cardiol* 13;61A
- 175 Nordstrom LA, Haugland JM, Strauss GS, Peterson CR, Monson BK, Dyrud P 1989 Direct laser angioplasty. Clinical results of 53 consecutive human peripheral and 5 coronary cases. *Lasers Surg Med Suppl* 1;7
- 176 Mitty HA, Sanborn TA, Dan SJ, Train JS 1988 Large, 2.5-mm laser probe for sole thermal angioplasty and laser-assisted balloon angioplasty. *Radiology Suppl* 169P;140
- 177 Spears JR, Reyes V, Sinclair IN et al. 1989 Percutaneous coronary laser balloon angioplasty. Preliminary results of a multicenter trial. *J Amer Coll Cardiol* 13;61A
- 178 Grundfest WS, Litvack IF, Goldenberg TSVI, Sherman T, Morgenstern L, Carroll R, Fishbein M, Forrester J, et al. 1985 Pulsed ultraviolet lasers and the potential for safe laser angioplasty. *Amer J Surg* 150;220-226
- 179 Gijsbers GHM, Sprangers RLH, Keijzer M, de Bakker JMT, van Leeuwen TGV, Verdaasdonk RM, Borst C, van Gemert MJC 1990 Some laser-tissue interactions in 308nm excimer laser coronary angioplasty. *J Interven Cardiol* 3(4);231-241
- 180 Duda SH, Karsch KR, Haase KK, Huppert PE, Claussen CD 1990 Laser ring catheters in excimer laser angioplasty. *Radiology* 175;269-270
- 181 Steg PG, Rongione AJ, Gal D, DeJesus ST, Clarke RH, Isner JM 1989 Excimer laser irradiation induces endothelium-independent relaxation of vascular smooth muscle. *J Amer Coll Cardiol* 13;141A

- 182 Rongione AJ, Gal D, DeJesus ST, Chokshi S, Clarke RH, Isner JM 1989 The mechanism responsible for laser-induced photorelaxation of vascular smooth muscle is limited to ultraviolet and visible wavelengths. *J Amer Coll Cardiol* 13;142A
- 183 Wolbarsht ML, Gomes E 1989 A fiber optic delivery of Er:YAG laser radiation. *Lasers Surg Med Suppl* 1;4
- 184 Geschwind HJ, Dubois-Rande JL, Poirot G, Boussignac G 1989 Guided percutaneous pulsed laser angioplasty. Results and follow-up. *J Amer Coll Cardiol* 13;13A
- 185 Lammer J, Kleinert R 1988 Laser angioplasty by sapphire contact probe. Experimental and clinical results. *J Intervent Radiol* 3;53
- 186 Sanborn TA, Cumberland DC, Greenfield AJ, Welsh CL, Guben JK 1988 Percutaneous laser thermal angioplasty. Initial results and 1-year follow-up in 129 femoropopliteal lesions. *Radiology* 168;121
- 187 Sanborn TA, Greenfield AJ, Guben JK, Menzoian JO, LoGerfo FW 1987 Human percutaneous and intraoperative laser thermal angioplasty. Initial clinical results as an adjunct to balloon angioplasty. *J Vasc Surg* 5;83
- 188 Black LD, Radbill JR, Crawford DW 1977 Analysis of pulsatile, viscous blood flow through diseased coronary arteries of man. *J Biomechanics* 10;339-353
- 189 Mohandas N, Hochmuth RM, Spaeth EE 1974 Adhesion of red cells to foreign surfaces in the presence of flow. *J Biomed Mater Res* 8;119-136
- 190 Logan SE 1975 On the fluid mechanics of human coronary artery stenosis. *IEEE Trans Biomed Eng* 22;327-334
- 191 Hardoff R, Shefer A, Gips S, Merdler A, Flugelman MY, Halon DA, Lewis BS 1990 Predicting late restenosis after coronary angioplasty by very early (12 to 24h) thallium-201 scintigraphy: implications with regard to mechanisms of late coronary restenosis. *J Am Coll Cardiol* 15(7);1486-1492

- 192 Swartz SM, Campbell GR, Campbell JH 1986 Replication of smooth muscle cells in vascular disease. *Circ Res* 58;427-444
- 193 Ku DN, Giddens DP, Zarins CK, Glagov S 1985 Pulsatile flow and atherosclerosis in human carotid bifurcation: positive correlation between plaque location and low and oscillating shear stress. *Arteriosclerosis* 5;265-276
- 194 Spears JR Sealing. In *Cardiovascular Laser Therapy* Chapter 6;177-199 (Eds Isner J, Clarke R) Published by Raven Press Ltd
- 195 Jenkins RD, Sinclair IN, Anand RK, James LM, Spears JR 1988 Laser balloon angioplasty: effect of exposure duration on shear strength of welded layers of postmortem human aorta. *Lasers Surg Med* 8;392-396
- 196 Jenkins RD, Sinclair IN, McCall PE, Schoen FJ, Spears JR 1989 Thermal sealing of arterial dissections and perforations in atherosclerotic rabbits with laser balloon angioplasty. *Lasers Life Sci* 3(1);13-30
- 197 Spears JR, James LM, Leonard BM, Sinclair IN, Jenkins RD, Motamedi M, Sinofsky EL 1988 Plaque-media rewelding with reversible tissue optical property changes during receptive cw Nd:YAG laser exposure. *Lasers Surg Med* 8;477-485
- 198 Safian RD, Reis JG, Pomerantz RM 1990 Laser balloon angioplasty: potential clinical applications. *Herz* 15(5);299-306
- 199 Ischinger T, Coppenrath K, Weber H, Enders S, Ruprecht L, Unsold E, Hessel S 1990 Laser balloon angioplasty: technical realization and vascular tissue effects of a modified concept. *Lasers Surg Med* 10;112-123
- 200 Miller JC, Haglund RF (Eds) 1991 Laser ablation: mechanisms and applications: proceedings of a workshop held in Oak Ridge, Tennessee, USA, 8-10 April Published by *Springer Verlag*
- 201 van Gemert MJC, Schets GACM, Stassen EG, Bonnier JJ 1985 Modeling of (coronary) laser-angioplasty. *Lasers Surg Med* 5;219-234

- 202 Smith DL, Walinsky P, Martinez-Hernandez A, Rosen A, Sterzer F, Kosman Z
1992 Microwave thermal balloon angioplasty in the normal rabbit. *Am Heart J* 123(6);1516-1521
- 203 Gleason T, Cragg AH, Smith TP, Landas SK, DeJong SC 1990
Preliminary results of thermal balloon angioplasty in a canine model. *J Vasc Intervent Radiol* 1;121-126
- 204 Cragg AH, Smith TP, Landas S, Nakagawa N, Barnhart W, DeJong SC
1991 Six-month follow-up after thermal balloon angioplasty in canine iliac arteries. *Cardiovasc Intervent Radiol* 14(4);230-232
- 205 Gorisch W, Boergen K-P 1982 Heat induced contraction of blood vessels. *Lasers Surg Med* 2;1-13
- 206 Peterson LH, Jensen RE, Parnell J 1960 Mechanical properties of arteries in vivo. *Circ Res* 8;622-639
- 207 Boucek RJ 1988 Contributions of elastin and collagen organization to passive mechanical properties of arterial tissue. In *Collagen: biochemistry, biomechanics, biotechnology*. Vol 2:Chap 10;201-221 (Ed. Nimni ME) CRC Press, Boca Raton, 1988
- 208 Waller BF 1989 "Crackers, breakers, stretchers, drillers, scrapers, shavers, burners, welders and melters" - the future treatment of atherosclerotic coronary artery disease? A clinical-morphological assessment. *J Am Coll Cardiol* 13(5);969-987